Integration of Noise Modelling into RF Receiver Design

Benjamin Klein

A thesis submitted to the Faculty of Engineering and the Built
Environment, University of the Witwatersrand, Johannesburg, in
fulfilment of the requirements for the degree of Doctor of Philosophy.

Johannesburg, 2017

DECLARATION

I declare that this thesis is my own unaided work. It is being submitted for the Degree of Doctor of Philosophy at the University of the Witwatersrand, Johannesburg. It has not been submitted before for any degree or examination to any other University.

....
(Signature of Candidate)

...............day of..................year....2017....

Abstract

The scientific requirements for Radio Frequency (RF) receivers especially for Radio Astronomy have become more demanding, requiring: compact, low-profile, multi and wideband antennas and more sensitive receivers. Integration of the antenna into the receiver system is often critical to meet these demands.

Noise theory to model these more complex systems is well developed but is not implemented in commercial solvers, given the niche market of the receivers it is only available using specialised software. If the system is closely coupled, it becomes necessary for design to incorporate Electromagnetic (EM) and Microwave (MW) modelling into the multi port noise modelling. `CAESAR`, a combined noise and EM/MW modelling code is available, but to use it requires the exclusive use of the `CAESAR` software, which is impractical given the utility and wide use of commercial solvers.

Mathematical methods are developed to incorporate commercial solvers into the more specialised `CAESAR`, validated using a folded dipole and applied to a wideband Eleven antenna system, a compact form of a log periodic dipole array. The Eleven antenna consist of eight single ended or four differential ports, with a closely coupled feeding arrangement. Cryogenic measurements are done to verify the modelling, the measured sensitivity matches with the model closely in amplitude and shape, giving confidence to the approach, and allowing modelling but not system optimisation.

Optimising the antenna based on receiver design and still being able to use commercial code requires the external scripting of a commercial solver. The `EDITFEKO` (card based) module of `FEKO` (a powerful and versatile solver) is used along with the meshing software `GMSH` and `GNU Octave`. Optimisation of system sensitivity is demonstrated on a choke horn fed reflector system at 1420 MHz.

This optimisation method is applied to a practical application, an octave band system (4.5 GHz to 9 GHz) for the Hartebeesthoek Radio Observatory. The design is split into smaller simulations using waveguide modes and the associated S–parameters, the techniques are presented and checked on a truncated system. Initial design and optimisation are given.

The combining of specialised multiport noise modelling design and optimisation within commercial EM/MW solvers allows more sensitive and specialised receivers to be built.

Index terms— noise modelling, wideband, multiport, corrugated horn, octave band receiver, EM/MW optimisation

Acknowledgements

The degree of Doctor of Philosophy is long and not always direct, it requires much assistance and collaboration. In retrospect it would have been impossible without the help of many individuals, too many to thank individually, but it would not be complete without thanking a few specific persons.

First thanks to my supervisor, Alan Clark, for overseeing this work and giving me time and guidance. Renier Dreyer, for the use of his cluster. The Wits electrical engineering department for being such a warm and stimulating place to work.

The Chalmer's Antenna group, overseen by the now late Per Simon Kildal, for introducing me to wideband antennas and systems. Jian Yang, for discussions on beam patterns and port definitions. Rob Maaskant, for his help with his software, and adapting it for commercial solvers. Marianna Ivashina, for help with noise modelling, and definitions.

At the Onsala observatory, Leif Helldner for technical expertise. Miroslav Pantaleev, for help with measurements and the use of his laboratory. Roy Booth, for introducing me to the observatory and Sweden.

The Wits physics department, for work on their prototype, specifically Andreas Faltenbacher for overseeing the project and Siobhan Reddy for her work in measuring the antenna patterns.

At the Hartebeesthoek observatory, the late Mike Gaylard for his suggestion of a wideband receiver. The workshop staff for helping with the technical design, specifically Keith Jones and Pieter Stronkhorst. George Nicolson, for keeping in touch and the many discussions on receivers.

Finally to my family, friends and girlfriend, for all your love and support.

Contents

List of Figures

List of Tables

Acronyms

ANT Antenna.

BOR1 Body of Revolution–Type 1.

Caltech The California Institute of Technology.

Chalmers Chalmers University of Technology.

DL Descriptive Language.

DTU Technical University of Denmark.

EM Electromagnetic.

FDTD Finite Difference Time Domain.

FEM Finite Element Method.

GaAs Gallium Arsenide.

HartRAO Hartebeesthoek Radio Astronomy Observatory.

HE Hybrid, with a dominate Electrical mode.

HEMT A High-electron-mobility Transistor.

HM Hybrid, with a dominate Magnetic mode.

LNA Low Noise Amplifier.

MMIC A Monolithic Microwave Integrated Circuit.

MOM Method of Moments.

MW Microwave.

OMT Orthomode Transducer.

TE Transverse Electrical.

TM Transverse Magnetic.

UWB Ultra–Wideband.

VLA Very Large Array.

VSWR Standing Wave Ratio.

List of Symbols

A Aperture.

A_{phy} Physical aperture.

B Bandwidth.

E electric field strength in $[V/m]$.

e_{ap} Aperture efficiency.

e_{mis} Mismatch efficiency.

e_{ohmic} Aperture efficiency.

$e_{\pi/2}$ spillover efficiency, over $\pi/2$.

e_{rad} Radiation efficiency.

$E_{s,n}$ Ergodic noise source present at the n^{th} port.

F Noise figure.

$\boldsymbol{f}_n$ embedded element pattern of the n^{th} port.

$\Gamma_{\textbf{act},n}$ Active input impedance of n^{th} LNA.

$G_{\textbf{co}}$ Co antenna gain pattern.

$G_{\textbf{LNA}}$ LNA gain.

$\Gamma_{\textbf{opt},n}$ Optimium noise match for the n^{th} LNA.

$G_{\textbf{xp}}$ Cross antenna gain pattern.

H magnetic field strength in $[A/m]$.

k Boltzman's constant.

N_z Characteristic noise matrix.

$P_{ex,n}$ Exchangable power at the n^{th} port.

ϕ_r Illumination angle for feed.

ϕ_v Illumination angle for the main reflector.

P_L Power delivered to the load.

P_N Noise power.

$\mathbf{S}$ Scattering matrix.

T	Noise temperature.
T_{AP}	Antenna temperature, due to T_p.
α	Loss factor.
T_a	Antenna temperature, as seen by the receiver.
T_A	Antenna temperature, as seen by the terminal.
T_{bg}	Brightness temperature.
$T_{\mathbf{LNA}}$	LNA noise temperature.
T_p	Physical temperature.
T_r	Receiver temperature.
W_m^*	Beam former weighting.
Y_{cor}	Correlation admittance.
Y_{opt}	Optimium input admittance.
Y_s	Source input admittance.
Z_{Feed}	Feed input impedance.
Z_{LNA}	LNA input impedance.
Z_L	Load input impedance.
Z_s	Source input impedance.

Chapter 1

Introduction

1.1 Background

Traditional antenna design has focused purely on the antenna: the radiation pattern, bandwidth, beam angle and radiation efficiencies. Aperture antennas have aperture and illumination efficiencies, and arrays of antennas the concept of array patterns and feeding phase [1]. In this approach the impedance of the antenna as seen by the source or receiver is looked at in general as a matching criteria and characterised as a matching efficiency. For maximum power transfer and to minimise standing waves this is as in classical circuit theory conjugate matched to the receiving circuitry [2]. There exists a classic separation between the microwave circuitry and the antenna as can be seen in the standard texts of *Pozar* [3] which focuses almost completely on the circuitry and *Balanis* [4] on antennas. This separation is sensible the abstraction of modelling an antenna or microwave receiver as a transmission line and load simplifies design significantly. This allows antennas to be classically modelled either using a mathematical approach, for example taken by *Elliot* [5] or more intuitively by *Kraus* [1]. In the last fifty years microwave and antenna design has increasingly relied on full Electro Magnetic (EM) computer modelling and optimisation [6].

The most popular modelling methods are: Method of Moments (MOM), Finite Element Method (FEM) and Finite Difference Time Domain(FDTD). These methods have been developed with many implementations and commercial packages, for example `FEKO` [7] (now under `Altair`), `CST` [8] and `ANSYS HFSS` [9]. This has allowed the modelling of more complex specialised antennas and systems. In addition to the commercial solvers many free and open source solvers have been built, one of the most well know being `NEC`, which was first available in 1965 [10]. The latest version is `NEC4` but many spin-offs and alternative versions have been developed, for example `SuperNEC` [11] and more recently `NEC2++` [12]. In order to survive in the long run code requires support, maintenance and, particularly in the case of free software, an active community of dedicated users to troubleshoot and contribute. `SuperNEC` is no longer available partially because it didn't get this support.

Most free EM software has been discontinued for two principle reasons: given the wide range of available solvers and methods and the relatively small community, no single code base has been given enough support. Secondly EM is complex and many of the authors who understand the physics have not had the experience in writing code for large communities.

In recent years these problems have diminished somewhat. Managing large software has become easier, for example `NEC2++`, which uses the collaborative Github structure for developing code [13]. The development of general solvers has also widened communities and helped with getting broader support and funding. The `FENICS` project [14–16] a general partial differential equations (PDE) solver, is well supported and funded and has because of its a wide applicability, a large community. The barrier to using it easily for EM is still high however, as can be seen in the example of application to a rectangular waveguide problem by *Davidson et al.* [17]. A slightly different approach to this problem is the very powerful multi physics code `GetDP` developed by *Patrick Dular* and *Christophe Geuzaine* [18–20], which does not require a large software community to maintain, as the core code is minimal. `GetDP` uses the meshing program `GMSH` [21] as the interface and the user is required to write (or copy from examples) the modules of the solver, including the Galerkin [22]. The learning curve is very steep especially as the solver is written in its own custom programming language. The great advantage is that the code is very simple to maintain and because the interface is so close to the solver the user has almost complete control. A similar rectangular waveguide example to that cited for `FENICS`, developed by the author and *Geuzaine* is available [23].

This leaves the current state of EM modelling dominated by commercial software which has the funds and expertise to produce and maintain well documented packages. For specialised problems and academics these are often limiting hence the existence of so many custom solvers. Commercial code is written primarily for industry so flexibility in describing the structure, simulating and optimisation is restricted to what is has been allowed within the program and the desires of the general community. Radio Astronomy in particular and specialised research in general, does not have the user base to justify large time being invested in adapting software for these problems. One particular limitation is the input `CAD` software of most commercial solvers; complex structures can be tricky to describe. Most solvers have some scripting ability, for example the `LUA` language [24] for `FEKO`, however it requires the user to be familiar with the language and is only available to run in the post processing stages. `CST` has some very limited `Visual Basic` scripting. `ANSYS HFSS` allows scripting via Microsoft Visual Basic Scripting (`Vbscript`) natively. There is an open source (BSD licensed) Python wrapper [25] which looks more promising but is not available for `GNU Linux` and is not currently being maintained.

At the same time that antenna design has been moving to more commercial simulations requirements have become more demanding. This is due to the demands for compact, low-profile, multiband and wideband antennas for industrial and scientific uses. For example fractal [26] and self–complementary antennas [27]. The field of Radio Astronomy is a typical example of this change.

Radio Astronomy particularly as applied to geodesy requires wider band receivers [28], as do software defined radios often requiring Ultra–Wideband (UWB) antennas. Here wideband is considered octave band and higher 2:1 or a 66% percentage bandwidth, where percentage bandwidth is the ratio between the bandwidth and the centre frequency:

$$BW_{\%} = \frac{BW}{F_c}$$

Most antennas are optimised for narrow bandwidths, dipoles have a 10% bandwidth for example. UWB has a definition in communications but for antennas is considered here to be a bandwidth of 3:1 (133%) or greater, often referred to as frequency independent antennas. Prominent examples of UWB antennas being considered for future radio telescopes are the Eleven antenna [29] quasi self-complementary antennas [30] and the Quadridge horn [31]. Correspondingly amplifiers [32, 33] for Radio Astronomy have been developed and thus wideband systems have become increasingly interesting both for economic reasons and for wideband observations [28, 34]. In the design of a wideband system compromises are inevitable and it is important to be able to accurately model and provide comparisons between existing and possible system sensitivities for different wideband options. This is particularly important in large arrays when systems require cryogenic cooling and therefore where the costs of large wideband systems become significant.

The usefulness of a radio receiver normally expressed as its sensitivity is given by A/T, where A is the effective area of the antenna and T is the noise of the receiver expressed as a temperature (often known as the Johnson–Nyquist noise). The noise is calculated as a power using $P = kTB$, where k is Boltzman's constant and B is the fractional bandwidth, often normalised to $1\ Hz$. In the past the limiting factor for T was the Low Noise Amplifier (LNA). Early generations of radio astronomy systems were to a first degree limited by the noise temperature of the amplifiers and the design of the system was conscious of noise but not optimised for it. As the technology of LNAs and associated cooling has been improved, the LNA has become a more equal contributor to the noise of systems. It has become increasingly important to consider the noise contribution of all parts of the system before the LNA which has led to more complex noise models and techniques. The noise modelling of multi port closely coupled antenna systems however, are non trivial and at the extreme requires full EM modelling. Specialised EM code has been written to take this into account, specifically the `CAESAR` solver [35] and a PAF–reflector toolbox [36, 37]. These codes are highly specialised and limited compared to the wide range of available commercial solvers.

For Radio Astronomy receiver design, the incorporating of specialised software and noise modelling into commercial software is highly desirable given the central usefulness of the receiver's sensitivity or A/T, and the wide availability and power of commercial solvers. There are two principal reasons for this: firstly it allows better noise modelling of systems with existing antenna designs, better predicting the final sensitivity given reflector and LNA choices. Secondly it allows the incorporating of noise into optimisation and design for new antennas. This Ph.D. focuses on the problem: *Incorporating multiport noise modelling into RF receiver design.*

1.2 Goals and outline

For specialised highly sensitive systems there is clearly a need to expand the current open source solvers and to customise available commercial solvers. The first step is to gain an understanding and be able to accurately noise model these systems.

Multiport wideband modelling To investigate and apply current noise modelling theory and techniques to a real world highly sensitive, wideband, multiport system. To verify the model a wideband highly sensitive system is modelled and measured. The background theory of noise modelling is presented in chapter 2 using a circuit and network modelling approach. Both single and multiport noise modelling is presented and the noise models for LNAs are analysed. The theory is applied to the Eleven antenna connected to cryogenically cooled LNAs in chapter 3, the noise is measured and compared to the theory.

The second step is to integrate the output from commercial EM code into custom specialised noise modelling code.

Integration with specialised noise modelling code With the wide use of commercial solvers it is not practical to remodel all of the available wideband antennas using specialised noise modelling solvers. Rather the results of the commercial solvers are integrated into a specialised solver and the noise computed and verified with measurements. The network theory is given along with an example in chapter 4, which is verified by just using the specialised noise modelling software and using it combined with a commercial solver.

The third step is to modify the existing EM solvers so as to be able to run them as a component in a design and optimisation loop.

Modifying commercial solvers Commercial EM software contains powerful numerical solvers. For specialised research and sensitivity optimisation in particular, it would be useful to be able to use these solvers as a component in a wider design. A commercial solver is investigated and code is written and tested to be able to run it externally. The plausibility of using this to design a practical receiver is investigated using noise modelling and overall sensitivity as the goal function. The software approach and code outline is given in chapter 5, along with some examples of how it can be used. Finally a simple example is given.

The fourth and final step is to apply the software to a practical receiver design.

System wide design It is inefficient to run EM modelling on a whole receiver therefore the simulation needs to be broken up into components. It is necessary to be able to predict the effects of the antenna on the overall noise however, so simulations are split in the standard way while demonstrating that it is still possible to calculate the overall system sensitivity. This is given in chapter 6 along with some preliminary results.

Conclusions are presented in chapter 7.

1.3 Scope

This work is focused on noise modelling and the application of software to receiver design rather than on a specific receiver, LNA or antenna. The goal of this work is to primarily model and verify the accuracy of the model for existing systems and secondly to show how this can be applied to optimising and designing new receivers. Verification is done using existing methods and measurements.

The software used to run the commercial solver is written to be as adaptable and customizable as possible. It is written to be expandable by a general user rather than as a complete package. For this reason the focus is not on implementing a particular optimisation, but on optimisation in general. Various geometries are demonstrated.

The building and full optimisation of the complete receiver is considered future work. Tools are verified and a simple design is built, a paper design is demonstrated for a larger receiver system.

Chapter 2

Noise Theory

2.1 Introduction

The following chapter goes through the noise theory for RF receivers. This establishes a firm base of noise theory and application which can be incorporated into receiver design.

The fundamentals of thermal noise was first investigated, as it related to circuits and circuit theory, by *N Nyquist* [38] and *J Johnson* [39] in the late 1920s. The formal definition for a passive network, is given by *Friis* in the 1944 [40]. Later this was linked to network theory and generalised, by *R Twiss* [41] *H Rothe, W Dahlke* [42] and probably most formally by *H. Haus* [43, 44] in the 1950s. A good summary of the early work done can be found in an IRE review [45].

2.2 Single channel receiver noise modelling

It is convenient to model a single channel radio receiver as a simple circuit. Each component is replaced as an equivalent resistor at a physical temperature, where the noise power P_N is converted to an equivalent temperature T by using eq. (2.1), where k is Boltzman's constant and Δ_{BW} is the bandwidth, normally normalised to per unit bandwidth of 1 Hz. In the case of the feed this temperature is the physical temperature of the antenna and the resistance is the ohmic losses in the feed. Which immediately shows how cooling the feed or reducing its ohmic losses, translate to a reduced system temperature. The temperature does not have to be a physical temperature, in general it is not for any other components in the feed chain. It holds for any component regardless of how the noise is generated, as long as the noise is white over the time periods the signal is integrated over. A simple single channel receiver is shown in fig. 2.1.

$$P_N = kT_s\Delta_{\text{BW}} \tag{2.1}$$

where:

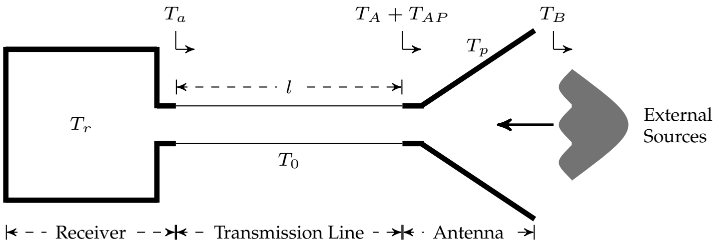

Figure 2.1: Single channel noise model, adapted from [46, figure 2.35].

T_p = Antenna's physical temperature
T_0 = Line's physical temperature
l = Line length
T_r = Receiver temperature
T_B = Brightness temperature
T_a = Antenna temperature seen by the receiver
T_A = Antenna temperature seen at the terminal
T_{AP} = Antenna noise temperature, due to T_p

The simple single channel circuit model of this receiver is shown in fig. 2.2, where the receiver is modelled as a single low noise amplifier (LNA) and load.

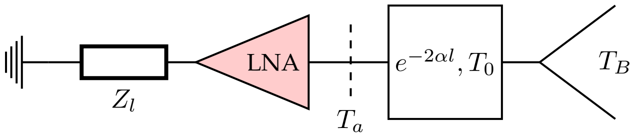

Figure 2.2: Referenced noise model, for a simple single channel receiver.

Given that all the noise impedances are matched, all the noise temperatures can be referred to any plane within the model by considering the losses and gains. For single dish antennas this model, although simple is normally sufficient to model the noise characteristics. If the amplifier noise dominates the system the brightness and thermal temperatures can be estimated accurately enough by using the feeds beam and ohmic characteristics. It is noted that this is at a modelling stage, however if one is designing an antenna and the first LNA has a comparable low noise temperature, then the brightness and thermal characteristics must be accounted for in the design. It also should be noted that the brightness temperature is a function of pointing angle of the antenna. The noise temperature as seen by the receiver is calculated in eq. (2.2) [46, equation 2-14r], where α is the loss per unit length.

$$T_a = T_A e^{-2\alpha l} + T_{AP} e^{-2\alpha l} + T_0(1 - e^{-2\alpha l}) \tag{2.2}$$

The receiver noise is calculated by summing up the noise of each component, divided by the gain preceding the component. Shown in eq. (2.3), a variation of the one given in [40, equation 16]. If the gain of the first LNAs are high clearly they dominate the receiver's noise, which justifies the simple model of the receiver.

$$T_r = T_{\text{LNA1}} + \frac{T_{\text{LNA2}}}{G_{\text{LNA1}}} + \frac{T_{\text{mixer}}}{G_{\text{LNA1}} G_{\text{LNA2}}} + \cdots \tag{2.3}$$

The total system noise temperature is then $T_s = T_r + T_a$, which is related to the noise power using eq. (2.1). Incorporating the radiation efficiency and mismatch efficiency is relatively simple. The radiation efficiency e_{rad} is a measure of the feed's ohmic losses, The mismatch factor, e_{mis} is the mismatch between the antennas input impedance, Z_{feed} and LNA input impedance, Z_{LNA}, calculated as:

$$e_{mis} = 1 - \left| \frac{Z_{feed} - Z_{LNA}}{Z_{feed} + Z_{LNA}} \right|^2 \tag{2.4}$$

This mismatch represents the power mismatch loss and not the increased noise temperature of the LNA due to the mismatch to the optimum noise impedance. The model is then modified as shown in fig. 2.3, and described by eq. (2.5).

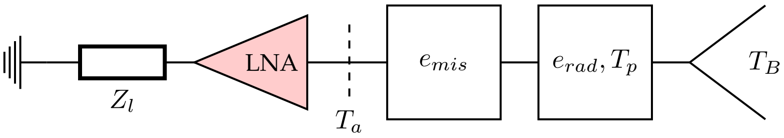

Figure 2.3: Referenced noise model, equivalent receiver model.

$$T_a = \left[T_B e_{rad} + \left(1 - e_{rad}\right) T_p\right] e_{mis} \tag{2.5}$$

2.3 Atmospheric contribution

The antenna temperature seen at the terminals of the antenna T_A is calculated in eq. (2.6) by integrating the brightness temperature T_{bg} over the gain pattern of the antenna [2, equation 2.116], here considering the cross and co gain patterns G_{xp} and G_{co}. Mathematically, T_a is solved as follows [47]:

$$T_a = \frac{\iint\limits_{4\pi} T_{bg}\left(\alpha\left(\theta, \varphi\right)\right) \left[\left|G_{\text{co}}\left(\theta_f\right)\right|^2 + \left|G_{\text{xp}}\left(\theta_f\right)\right|^2\right] \sin\theta d\theta \, d\varphi}{\iint\limits_{4\pi} \left[\left|G_{\text{co}}\left(\theta_f\right)\right|^2 + \left|G_{\text{xp}}\left(\theta_f\right)\right|^2\right] \sin\theta d\theta \, d\varphi} \tag{2.6}$$

Where T_{bg} is the brightness distribution as seen by the feed. The presence of reflectors are taken into account by the brightness temperature and not the beam pattern. The antenna picks up background radiation from the sky, sky brightness T_b,and ground, ground noise T_g. This is a general calculation, and sophisticated model for specific sky views and ground is not useful here. The sky brightness is given by [48, 49]:

$$T_{bg}\left(f\right) = T_{b0}\left(f\right) e^{-\tau_\nu\left(s_0\right)} + \int_0^s k_a\left(f, s\right) T\left(s\right) e^{-\tau_\nu\left(s\right)} ds \tag{2.7}$$

Where k_a is the zenith opacity, T_{b0} is the sum of cosmic microwave background and galactic emission and τ_ν is:

$$\tau_\nu(\theta) = \int_0^\infty \frac{k_a(f,s)}{\sqrt{1-\left[\sin\theta/(1+s/R)\right]^2}} ds \tag{2.8}$$

The sky brightness temperature for various look angles ϕ is plotted in figure 2.4, the results are as expected, and fairly constant across the band.

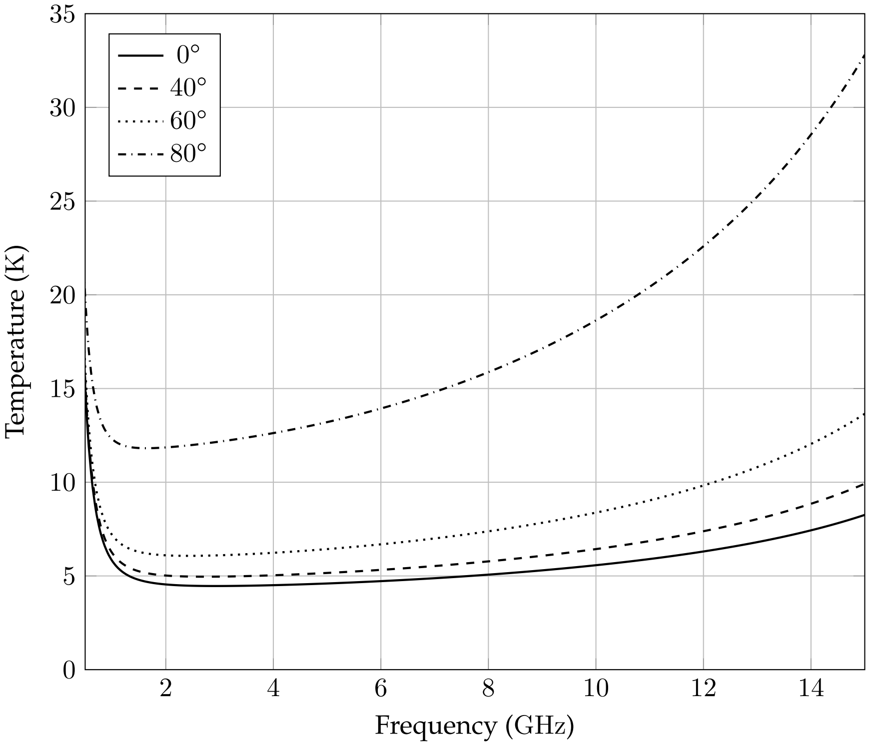

Figure 2.4: Brightness Temperature vs Frequency, for various pointing angles.

The system noise contribution of the atmosphere is now calculated by: integrating the sky brightness across the beam, assuming the ground temperature to be a constant 293 K from $\phi > 90°$, using equation 2.6. The result can be verified by calculating the illumination efficiency of the beam over the sky and ground. This can be considered as the spillover efficiency over a $\theta_0 = \pi/2$ illumination. Calculated as, (following the form in [46]):

$$e_{\pi/2} = \frac{\int_0^{\pi/2} G_f(\theta')\sin(\theta')\, d\theta'}{\int_0^{\pi} G_f(\theta')\sin(\theta')\, d\theta'} \tag{2.9}$$

The brightness distributions are estimated assuming averaged ground and sky temperatures. Calculated for the sky as $T_{Sky}(1 - e_{\pi/2})$ and the ground $T_{Ground}(1 - e_{\pi/2})$. The results are found to be consistent.

2.4 Multiport modelling

Antennas with more complex feeding networks or arrays cannot simply be represented as a single channel receiver and present some complications for modelling. There are multiple approaches to solving this problem, a summary is presented here:

2.4.1 Parametric model

One simple example is thinking of the beam forming network as part of the antenna; if it is matched to make the contributions of reflections small enough, then this looks to the noise model as a pure resistive loss, exactly as equivalent to the resistive loss in the antenna. This then reverts to the single channel case. If however the reflections cannot be discounted it is still possible to find the equivalent single channel model. A beam forming array is shown in fig. 2.3, in cases where cross coupling is insignificant it is possible to calculate an equivalent single channel receiver.

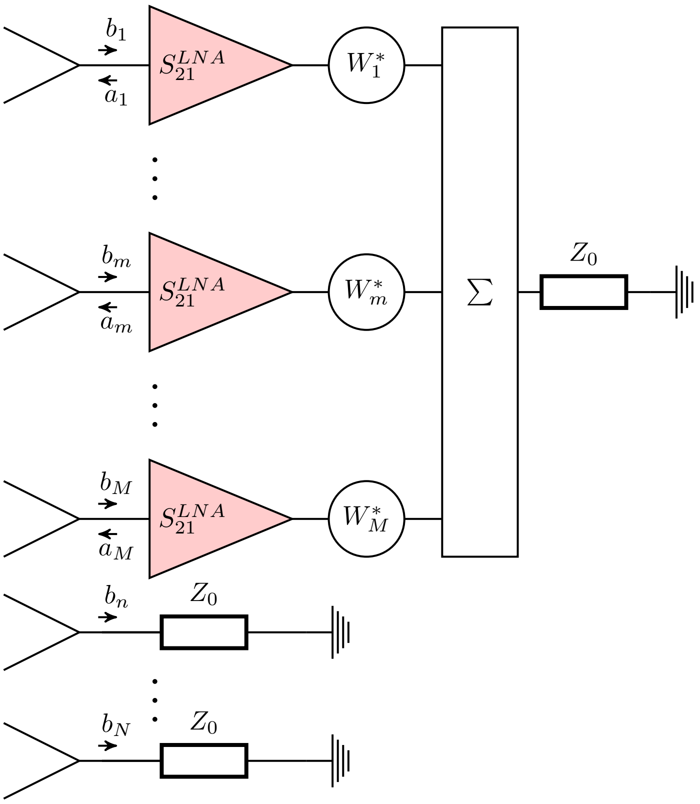

Figure 2.5: Beam forming network, adapted from [50].

The technique is presented by *M V Ivashina,R Maaskant*, and *B Woestenburg* in [50]. The method sums up the contributions through the beam forming network into a single equivalent system, as follows:

$$G_m^{av} = \left(\frac{1}{M}|S_{2,1}^{\mathrm{LNA}}|^2|w_m|\right)\left(1-|\Gamma_{\mathrm{act},m}|^2\right) \tag{2.10}$$

$$T_m^{\mathrm{LNA}} = T_{min} + \frac{4R_nT_0}{Z_0}\frac{|\Gamma_{\mathrm{act},m}-\Gamma_{\mathrm{opt}}|^2}{|1+\Gamma_{\mathrm{opt}}|^2\left(1-|\Gamma_{\mathrm{act},m}|^2\right)} \tag{2.11}$$

$$T_{\text{out}}^{\text{LNA}} = \sum_{m=1}^{M} G_m^{\text{av}} T_m^{\text{LNA}} \tag{2.12}$$

$$e_{\text{rad}} = \frac{\mathsf{W}^\dagger \left(\mathsf{I} - \left[S_{act,act}^H S_{act,act} + S_{pas,act}^H S_{pas,act}\right]\right) \mathsf{W}}{\mathsf{W}^\dagger \left(\mathsf{I} - S_{act,act}^H S_{act,act}\right) \mathsf{W}} \tag{2.13}$$

$$e_{\text{mis}} = \frac{\mathsf{W}^\dagger \left(\mathsf{I} - S_{act,act}^H S_{act,act}\right) \mathsf{W}}{\mathsf{W}^\dagger \mathsf{W}} \tag{2.14}$$

Where $S_{act,act}^H$ and $S_{pas,act}^H$ are the hermitian matrices of the active and passive feeds and eq. (2.11) is the standard amplifier model derived in section 2.4.3. In the simplest case of multiple identical channels being summed the noise would be equivalent to only one of the channels. For example two linearly polarised channels X and Y summed through a hybrid to form a circularly polarised receiver are most often considered a single circularly polarised channel with the equivalent noise performance of either channel, assuming that the coupling between the channels is low.

2.4.2 Deriving the characteristic noise matrix

Given the resistor model it is intuitive to approach the noise modelling from a circuit perspective. The following theory is based on the approach taken by *Haus* and *Adler* in [51] and the summary of this work found in [44].

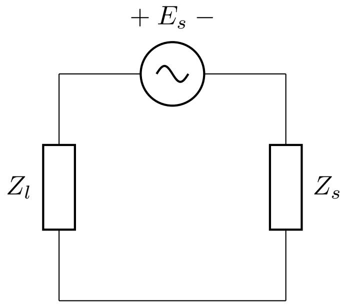

Figure 2.6: Equivalent circuit of a source attached to a load.

Considering an ergodic noise source E_s which when averaged contains the power as given by a resistor at temperature T so that $\langle |E_s|^2 \rangle = 4RkTB$, where k is Boltzman's constant and B is the bandwidth. If this source is connected to a load as seen in fig. 2.6 it is easy to derive that the power delivered to this load is:

$$P_L = \frac{\langle |E_s|^2 \rangle \mathrm{Re}(Z_L)}{|Z_s + Z_L|^2} \tag{2.15}$$

The maximum amount of power that can be delivered to the load as defined by *Haus* as the exchange power P_{ex} to solve problems with negative source impedances, occurs when $Z_L = Z_s^*$ which follows from eq. (2.15) to give:

$$P_{ex} = \frac{\langle |E_s|^2 \rangle}{2(Z_s + Z_s^*)} \tag{2.16}$$

Expanding this to a N–port impedance matrix Z shown in fig. 2.7, we can apply this per channel, so that the exchangeable power from an individual port is:

$$P_{ex,i} = \frac{\langle|E_i E_i^*|\rangle}{2(Z_{ii} + Z_{ii}^*)} \tag{2.17}$$

This can be expressed in a more convenient matrix form using the column vector a, where $a_j = 0$ for $j \neq i$ and $a_i = 1$. So that:

$$P_{ex,i} = \frac{\mathsf{a}^\dagger \langle|\mathsf{E}\mathsf{E}^\dagger|\rangle \mathsf{a}}{2\mathsf{a}^\dagger[\mathsf{Z} + \mathsf{Z}^\dagger]\mathsf{a}} \tag{2.18}$$

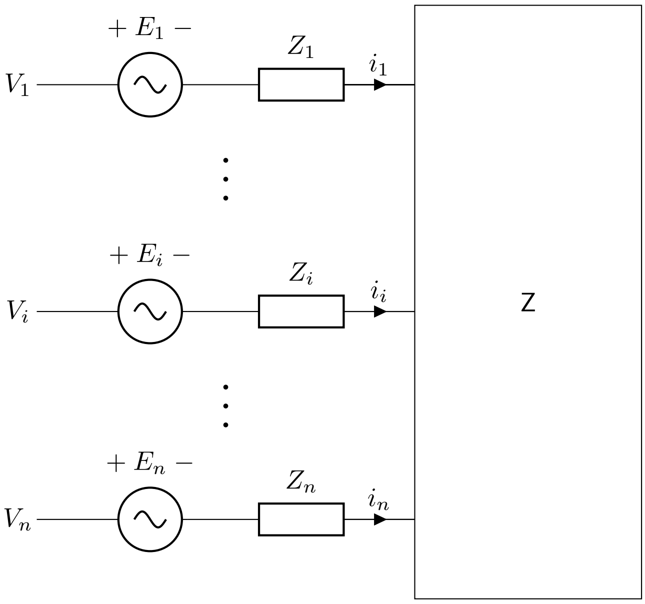

Figure 2.7: Linear noisy n-port, adapted from [44].

In order to derive the noise matrix first this N–port Z matrix is embedded into a lossless 2N–port impedance matrix Z_T, shown in fig. 2.8.

Dividing the Z_T into sub matrices we can express the voltages at both ports as:

$$\mathsf{V}_a = \mathsf{Z}_{aa}\mathsf{I}_a + \mathsf{Z}_{ab}\mathsf{I}_b \tag{2.19}$$

$$\mathsf{V}_b = \mathsf{Z}_{ba}\mathsf{I}_a + \mathsf{Z}_{bb}\mathsf{I}_b \tag{2.20}$$

Applying the lossless condition [1] for the embedding network gives:

$$\mathsf{I}^\dagger(\mathsf{Z}_T + \mathsf{Z}_T^\dagger)\mathsf{I} = 0 \tag{2.21}$$

Implying that $(\mathsf{Z}_T + \mathsf{Z}_T^\dagger) = 0$, expanding out gives:

$$\begin{bmatrix} \mathsf{Z}_{aa} + \mathsf{Z}_{aa}^\dagger & \mathsf{Z}_{ab} + \mathsf{Z}_{ba}^\dagger \\ \mathsf{Z}_{ba} + \mathsf{Z}_{ab}^\dagger & \mathsf{Z}_{bb} + \mathsf{Z}_{bb}^\dagger \end{bmatrix} = 0 \tag{2.22}$$

The voltage at the input of the Z is given by $\mathsf{V} = \mathsf{Z}\mathsf{I} + \mathsf{E}$, substituting $\mathsf{I} = -\mathsf{I}_a$ and

---

[1] Z version of $I^2R = 0$, and † is the conjugate transpose, or Hermitian operator.

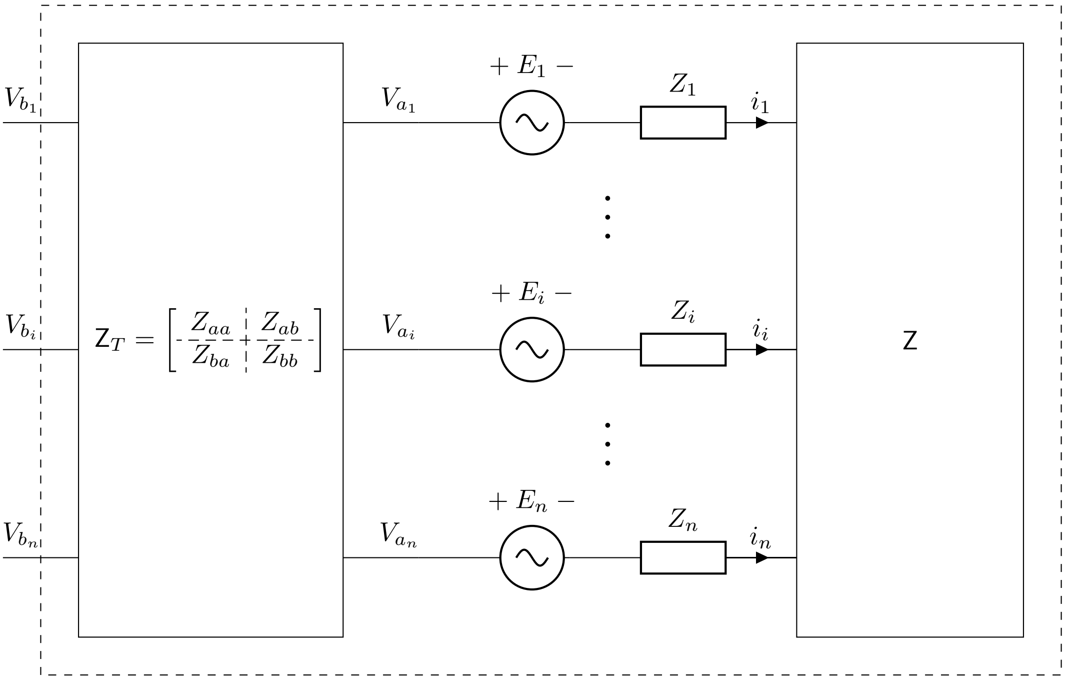

Figure 2.8: Embedded Linear noisy n-port, adapted from [44].

equating to eq. (2.19):

$$
\begin{aligned}
-\mathsf{Z}\mathsf{I}_a + \mathsf{E} &= \mathsf{Z}_{aa}\mathsf{I}_a + \mathsf{Z}_{ab}\mathsf{I}_b \\
\mathsf{I}_a &= -(\mathsf{Z} + \mathsf{Z}_{aa})^{-1}\mathsf{Z}_{ab}\mathsf{I}_b + (\mathsf{Z} + \mathsf{Z}_{aa})^{-1}\mathsf{E} \qquad (2.23)
\end{aligned}
$$

Defining the new combined matrix as Z' with associated noise sources E'. Then the output voltage is:

$$
\mathsf{V}_b = \mathsf{Z}'\mathsf{I}_b + \mathsf{E}' \qquad (2.24)
$$

We can now equate this voltage with eq. (2.20):

$$
\begin{gathered}
\mathsf{Z}'\mathsf{I}_b + \mathsf{E}' = \mathsf{Z}_{ba}\mathsf{I}_a + \mathsf{Z}_{bb}\mathsf{I}_b \\
\text{substituting in eq. (2.23) and setting } \mathsf{E}', \mathsf{E} = 0 \\
\mathsf{Z}'\mathsf{I}_b = \mathsf{Z}_{ba}(-(\mathsf{Z} + \mathsf{Z}_{aa})^{-1}\mathsf{Z}_{ab}\mathsf{I}_b) + \mathsf{Z}_{bb}\mathsf{I}_b \\
\mathsf{Z}' = -\mathsf{Z}_{ba}(\mathsf{Z} + \mathsf{Z}_{aa})^{-1}\mathsf{Z}_{ab} + \mathsf{Z}_{bb} \qquad (2.25)
\end{gathered}
$$

Setting the input current $\mathsf{I}_b = 0$ we can then solve for the noise matrix E':

$$
\mathsf{E}' = \mathsf{Z}_{ba}(\mathsf{Z} + \mathsf{Z}_{aa})^{-1}\mathsf{E} \qquad (2.26)
$$

Considering the denominator and numerator of eq. (2.18) seperably, we can solve for:

$$\begin{aligned}\mathsf{Z}' + \mathsf{Z}'^{\dagger} = &- \mathsf{Z}_{ba}(\mathsf{Z} + \mathsf{Z}_{aa})^{-1}\mathsf{Z}_{ab} + \mathsf{Z}_{bb} \\ &- \mathsf{Z}^{\dagger}_{ab}(\mathsf{Z}^{\dagger} + \mathsf{Z}^{\dagger}_{aa})^{-1}\mathsf{Z}^{\dagger}_{ba} + \mathsf{Z}^{\dagger}_{bb}\end{aligned}$$

Applying eq. (2.22) conditions, $\mathsf{Z}_{aa} = -\mathsf{Z}^{\dagger}_{aa}$, $\mathsf{Z}_{bb} = -\mathsf{Z}^{\dagger}_{bb}$, $\mathsf{Z}_{ab} = -\mathsf{Z}^{\dagger}_{ba}$ and $\mathsf{Z}_{ba} = -\mathsf{Z}^{\dagger}_{ab}$.

$$\begin{aligned}\mathsf{Z}' + \mathsf{Z}'^{\dagger} &= \mathsf{Z}_{ba}[(\mathsf{Z} + \mathsf{Z}_{aa})^{-1} + (\mathsf{Z}^{\dagger} + \mathsf{Z}^{\dagger}_{aa})^{-1}]\mathsf{Z}^{\dagger}_{ba} \\ &\text{Which can be simplified to:} \\ &= \mathsf{D}^{\dagger}(\mathsf{Z} + \mathsf{Z}^{\dagger})\mathsf{D} \qquad (2.27)\end{aligned}$$

Where $\mathsf{D} = \mathsf{Z}_{ba}(\mathsf{Z} + \mathsf{Z}_{aa})^{-1}$. Which is the form from eq. (2.26), so that $\mathsf{E}' = \mathsf{DE}$. Which then can be used to solve for the numerator in eq. (2.18) to give the transform:

$$\langle \mathsf{E}'\mathsf{E}'^{\dagger}\rangle = \mathsf{D}^{\dagger}\langle \mathsf{EE}^{\dagger}\rangle\mathsf{D} \qquad (2.28)$$

We can now rewrite eq. (2.18) as:

$$P'_{ex,i} = \frac{\mathsf{a}^{\dagger}\mathsf{D}^{\dagger}\langle|\mathsf{EE}^{\dagger}|\rangle\mathsf{Da}}{2\mathsf{a}^{\dagger}\mathsf{D}^{\dagger}[\mathsf{Z} + \mathsf{Z}^{\dagger}]\mathsf{Da}} \qquad (2.29)$$

Given D is a function of the embedding network it can be chosen to diagonalise both matrices and set the matrix $\langle \mathsf{EE}^{\dagger}\rangle$ to the identity matrix. The sum simplifies to a singular value such that:

$$P'_{ex,i} = b_i \qquad (2.30)$$

Where b_i is an eigenvalue of the matrix:

$$\frac{1}{2}(\mathsf{Z} + \mathsf{Z}^{\dagger})^{-1}\langle \mathsf{EE}^{\dagger}\rangle$$

This represents the extreme of the noise power from the noise sources and the negative of it is known as the characteristic noise matrix.

$$\mathsf{N}_z = -\frac{1}{2}(\mathsf{Z} + \mathsf{Z}^{\dagger})^{-1}\langle \mathsf{EE}^{\dagger}\rangle \qquad (2.31)$$

For a purely resistive network this becomes:

$$\mathsf{N}_z = -kTB\mathsf{I} \qquad (2.32)$$

Where I is the identity matrix.

2.4.3 Two Port noise model

Noisy networks can be represented conveniently as a port model as shown in fig. 2.9. *H Rothe, W Dahlke* [42] show how the noise in the network can be modelled using two equivalent correlated noise sources and leaving the port network noiseless. The equivalent circuits are show in fig. 2.10.

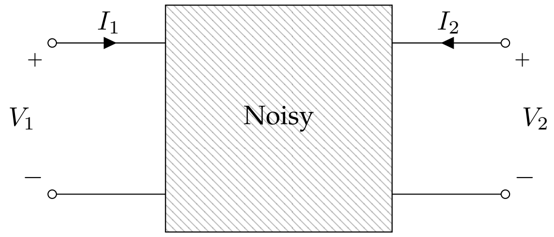

Figure 2.9: Noisy two port network.

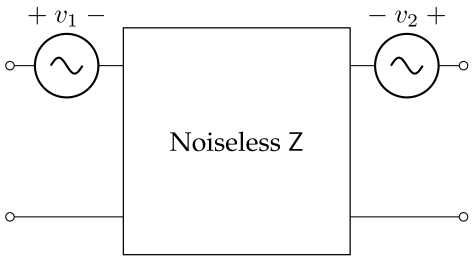

(a) Equivalent Z network.

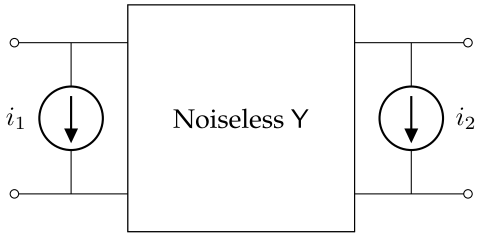

(b) Equivalent Y network.

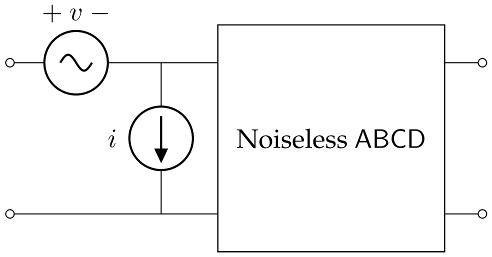

(c) Equivalent ABCD network.

Figure 2.10: Equivalent circuits with external noise sources.

The network equations can now be expressed as:

$$
\begin{aligned}
\mathsf{I} &= \mathsf{Y}_N \mathsf{V} + \mathsf{i} \\
\mathsf{V} &= \mathsf{Z}_N \mathsf{I} + \mathsf{i} \\
{}^{\mathsf{V}}\!/_{\mathsf{I}} &= \mathsf{ABCD}_N {}^{\mathsf{V}}\!/_{\mathsf{I}} + {}^{\mathsf{v}}\!/_{\mathsf{i}}
\end{aligned}
\tag{2.33}
$$

Where i and v are the noise sources and the correlation between any individual noise source is given by $C; i, j = \langle i_i v_k^* \rangle$. $C_i; i, j = \langle i_i i_j^* \rangle$, $C_v; i, j = \langle v_i v_j^* \rangle$ and $C_m; i, j = \langle i_i v_j^* \rangle$. The matrices C_i,C_v and C_m are the characteristic noise matrices.

Following the nomenclature and approach presented by *S A Maas* in [52]. Considering the two port model in fig. 2.10c because the $^{Z}/_{Y}$, ABCD is noiseless it can be removed from the analysis and represented as shown in fig. 2.11. Where the Y_s is the input admittance.

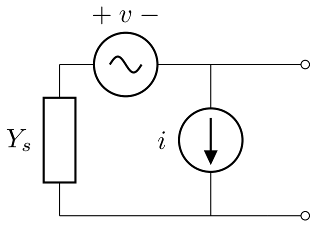

Figure 2.11: Equivalent circuit with ABCD matrix removed.

We can represent the noise source current i as a sum of correlated and uncorrelated components as:

$$i = i_u + vY_{cor} \tag{2.34}$$

Where:

$$Y_{cor} = \Gamma\sqrt{\frac{\langle|i|\rangle^2}{\langle|v|\rangle^2}} = \frac{\langle iv^*\rangle}{\langle|v|\rangle^2} \tag{2.35}$$

The circuit perspective is shown in fig. 2.12:

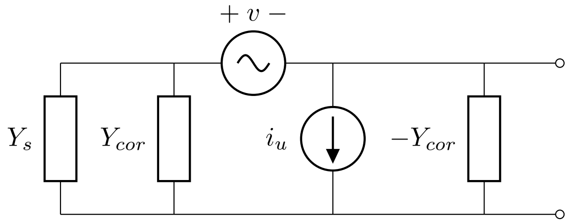

Figure 2.12: Equivalent circuit with uncorrelated sources.

Considering the equivalent circuit in fig. 2.12, we can calculate the mean square short circuit current $\langle|i_{\text{tot}}|\rangle$, simply by summing the currents as they are now uncorrelated [2]:

$$\langle|i_{\text{tot}}|\rangle = \langle|i_u|\rangle^2 + \langle|i_s|\rangle^2 + \langle|v|\rangle^2\langle|Y_s + Y_{cor}|\rangle^2 \tag{2.36}$$

All of these currents can be replaced by equivalent sources:

$$R_n = \frac{\langle v\rangle^2}{4KT_0B} \tag{2.37}$$

$$G_n = \frac{\langle i_u\rangle^2}{4KT_0B} \tag{2.38}$$

$$G_s = \frac{\langle i_s\rangle^2}{4KT_0B} \tag{2.39}$$

Where G is the real part of Y

Therefore:

$$\langle i_{\text{tot}}\rangle^2 = (4KT_0B)\left(G_s + G_n + R_n\langle Y_s + Y_{cor}\rangle^2\right) \tag{2.40}$$

---

[2] $|a+b|^2 = |a|^2 + |b|^2 + |a^*b| + |ab^*|$; if a and b are uncorrelated $|a^*b| = |ab^*| = 0$

The noise figure F, defined purely in terms of the current is $F = \langle i_{\text{tot}} \rangle^2 / \langle i_s \rangle^2$. Where i_{tot} is the total short circuited current at the output and $\langle i_s \rangle$ is the current coming from an impedance Z_s at the input. Intuitively this is the ratio of the total current out given an input current, equivalent to $F = (290 + Te)/290$ so dividing eq. (2.40) by $\langle |i_s| \rangle^2$ (or the equivalent G_s).

$$F = \frac{\langle i_{\text{tot}} \rangle^2}{\langle i_s \rangle^2} = 1 + \frac{G_n}{G_s} + \frac{R_n}{G_s} \langle |Y_s + Y_{cor}| \rangle^2 \tag{2.41}$$

To find the minimum noise figure F_{min} we set $\text{Im}\{Y_s\} = -\text{Im}\{Y_{cor}\}$ and solve for $\mathrm{d}F(G_0)/\mathrm{dG_s} = 0$, where G_0 is the optimium input impedance to obtain:

$$F_{min} = 1 + \frac{G_n}{G_s} + \frac{R_n}{G_s} \langle |G_s + G_{cor}| \rangle^2 \tag{2.42}$$

By definition $Y_{s,opt} = G_{s,opt} - \text{Im}\{Y_{cor}\}$ and $Y_{cor} = G_{cor} + \text{Im}\{Y_{cor}\}$, so $Y_{cor} = G_{cor} + G_{s,opt} - Y_{s,opt}$. Substituting this and eq. (2.42) back into eq. (2.41), gives us:

$$\begin{aligned} F =& 1 + \frac{G_n}{G_s} + \frac{R_n}{G_s} \langle |Y_s - Y_{s,opt} + G_s + G_{cor}| \rangle^2 && (2.43) \\ =& 1 + \frac{G_n}{G_s} + \frac{R_n}{G_s} \langle |G_s + G_{cor}| \rangle^2 + \frac{R_n}{G_s} \langle |Y_s - Y_{s,opt}| \rangle^2 && (2.44) \\ =& F_{min} + \frac{R_n}{G_s} \langle |Y_s - Y_{s,opt}| \rangle^2 && (2.45) \end{aligned}$$

Which is the familiar form. Even though differential amplifiers are three port devices if the admittance Y_s is considered as the differential impedance, and the common mode noise is low they can still be modelled using eq. (2.45), however in the case that it is not we develop the three port model below:

2.4.4 Three port differential amplifier model

J. Randa in [53] derives the form for a general multiport amplifier, with the noise figure at the i_{th} port is given by:

$$F_i(\Gamma, \mathsf{A}) = 1 + \frac{1}{k_B T_0} \left(\frac{([\mathsf{I} - \mathsf{S}\Gamma]^{-1} \hat{\mathsf{N}} [\mathsf{I} - \mathsf{S}\Gamma]^{-1})^\dagger}{([\mathsf{I} - \mathsf{S}\Gamma]^{-1} \mathsf{S}\mathsf{A}\mathsf{S}^\dagger [\mathsf{I} - \mathsf{S}\Gamma]^{-1})^\dagger} \right)_{ii} \tag{2.46}$$

Where Γ is the input matching and A is the input correlation matrix. In order to derive this form we follow the method of the two port case, consider the three port ABCD model in fig. 2.13.

As before we can separate out the currents into correlated and uncorrelated terms:

$$\begin{aligned} i_1 =& i_{u1} + i_2 + C_{12} + v_1 Y_{cor11} + v_2 Y_{cor12} && (2.47) \\ i_2 =& i_{u2} + i_1 + C_{21} + v_1 Y_{cor21} + v_2 Y_{cor22} && (2.48) \end{aligned}$$

Given that this is a three port model the correlation matrix should be 3×3 so eq. (2.48) has a redundant term. We can consequently set $C_{12} = C_{21} = 0$, this correlation term can be easily accounted for later. The equivalent circuit model is then shown in fig. 2.14.

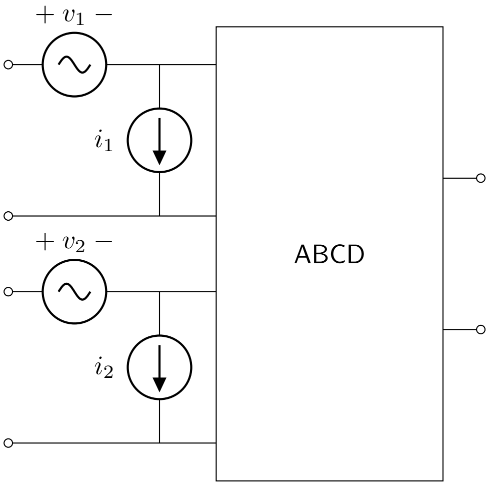

Figure 2.13: Three port ABCD network, with external noise sources.

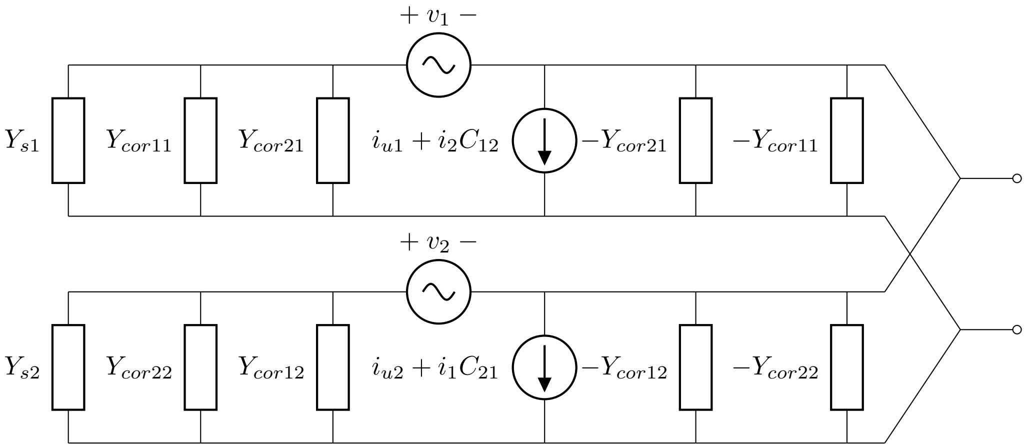

Figure 2.14: Equivalent circuit of three port differential amplifier noise model.

As before:

$$\begin{aligned}|i_{stot}|^2 =&|i_{s1}+i_{s2}|^2+|i_{u1}+i_{u2}|^2\\&+|v_1|^2|Y_{s1}+Y_{cor11}+Y_{cor21}|^2\\&+|v_2|^2|Y_{s2}+Y_{cor22}+Y_{cor12}|^2\end{aligned} \tag{2.49}$$

Defining:

$$Rn_1=\frac{|V_1|^2}{4k_BT_0\Delta_f} \qquad Rn_2=\frac{|V_2|^2}{4k_BT_0\Delta_f}$$

$$Gs_1=\frac{|i_{s1}|^2}{4k_BT_0\Delta_f} \qquad Gs_2=\frac{|i_{s2}|^2}{4k_BT_0\Delta_f}$$

$$Y_{cor1} = Y_{cor11} + Y_{cor21}$$
$$Y_{cor2} = Y_{cor22} + Y_{cor12}$$

Substituting these terms into eq. (2.49):

$$\frac{|i_{stot}|^2}{4k_BT_0\Delta_f} = G_s + G_n + R_{n1}|Y_{s1} + Y_{cor1}|^2 + R_{n2}|Y_{s2} + Y_{cor2}|^2 \tag{2.50}$$

We solve for the noise figure, by considering the total power at the input, which is proportional to $|i_{s1} + i_{s2}|^2$ and includes any uncorrelated currents. So using the standard definition of noise figure for a two port devices (there is no strict IEEE definition for three port devices):

$$F = \frac{|i_stot|^2}{|i_{s1} + i_{s2}|^2} \tag{2.51}$$

Applying this definition to eq. (2.50),

$$F = 1 + \frac{G_n}{G_s} + \frac{R_{n1}}{G_s}|Y_{s1} + Y_{cor1}|^2 + \frac{R_{n2}}{G_s}|Y_{s2} + Y_{cor2}|^2 \tag{2.52}$$

This is now in the form of eq. (2.46). Theoretically differential amplifiers models require nine noise parameters [53], eq. (2.52) contains only seven. The missing terms are contained in the G_s term representing the correlation between the current sources.

In order to solve the differential, ${}^{\mathrm{d}F}/_{\mathrm{d}Y_s}$. We assume that the noise sources at the input are uncorrelated, ie $G_s = G_{s1} + G_{s2}$ as $|i_{s1} + i_{s2}|^2 = |i_{s1}|^2 + |i_{s2}|^2$. Also $\mathrm{Im}\{Y_{opt}, s_1\} = -\mathrm{Im}\{Y_{cor1}\}$ and $\mathrm{Im}\{Y_{opt}, s_2\} = -\mathrm{Im}\{Y_{cor2}\}$. As before:

$$Y_{opt,s_1} = G_{opt,s_1} - \mathrm{Im}\{Y_{cor1}\} \tag{2.53}$$
$$Y_{cor1} = G_{cor1} + \mathrm{Im}\{Y_{cor1}\} \tag{2.54}$$

Which allows us to solve for Y_{cor1}:

$$Y_{cor1} = G_{cor1} + G_{opt,s_1} - Y_{opt,s_1} \tag{2.55}$$

Similarly,

$$Y_{cor2} = G_{cor2} + G_{opt,s_2} - Y_{opt,s_2} \tag{2.56}$$

Substituting back into eq. (2.52) gives us

$$\begin{aligned} F =& 1 + \frac{G_n}{G_{s_1} + G_{s_2}} + \frac{R_{n1}}{G_{s_1} + G_{s_2}}|Y_{s_1} - Y_{opt,s_1} + G_{cor1} + G_{opt,s_1}|^2 \\ &+ \frac{R_{n2}}{G_{s_1} + G_{s_2}}|Y_{s_2} - Y_{opt,s_2} + G_{cor2} + G_{opt,s_2}|^2 \end{aligned} \tag{2.57}$$

As before because the terms here are now uncorrelated we can simplify:

$$
\begin{aligned}
F =& 1 + \frac{G_n}{G_{s_1} + G_{s_2}} + \frac{R_{n1}}{G_{s_1} + G_{s_2}} |G_{cor1} + G_{opt,s_1}|^2 \\
&+ \frac{R_{n2}}{G_{s_1} + G_{s_2}} |G_{cor2} + G_{opt,s_2}|^2 \\
&+ \frac{R_{n1}}{G_{s_1} + G_{s_2}} |Y_{s_1} - Y_{opt,s_1}|^2 \\
&+ \frac{R_{n2}}{G_{s_1} + G_{s_2}} |Y_{s_2} - Y_{opt,s_2}|^2
\end{aligned} \tag{2.58}
$$

Which gives us the final form:

$$
F = F_{min} + \frac{R_{n1}}{G_{s_1} + G_{s_2}} |Y_{s_1} - Y_{opt,s_1}|^2 + \frac{R_{n2}}{G_{s_1} + G_{s_2}} |Y_{s_2} - Y_{opt,s_2}|^2 \tag{2.59}
$$

If we set $Y_{s_1} = Y_{s_2} = {}^1\!/_2 Y_s$ this does not reduce back to the two port case, which suggests a slight error in modelling differential amplifiers in the standard way.

2.4.5 Maximum and minimum LNA noise temperature envelopes for wideband antenna design

LNA noise temperatures are modelled as the sum of a minimum temperature T_{min}, and a matching term, in terms of the input impedance (either Z_{act} or Γ_{act}). For some applications a variable line length or *ultra wide band* (UWB) applications, the phase of the input impedance is either unknown or cannot be matched across the whole of the band, which leads to an uncertainty in the LNA noise contribution. Formulas for the best and worst case are developed for any phase, and thus can be used to calculate a more general matching criteria, which might be more useful for these applications. General and specific examples are given, along with the impact to the system noise temperature.[3]

Maximum and minimum Cases The noise of a LNA, given a particular input impedance Γ_{act}, is modelled as [54]:

$$
T_{\text{LNA}} = T_{min} + 4\text{N}T_o \frac{|\Gamma_{act} - \Gamma_{opt}|^2}{(1 - |\Gamma_{act}|^2)\,(1 - |\Gamma_{opt}|^2)} \tag{2.60}
$$

If the amplifier parameters are fixed (generally the case for an antenna designer) and the phase of Γ_{act} is not tunable (often the case for wide bandwidth applications), then the maximum and minimum T_{LNA} contribution is calculated for a particular Γ_{opt}, by considering only the numerator in the matching term, $|\Gamma_{act} - \Gamma_{opt}|$. The rest of the expression is independent of the phase of Γ_{act} and acts only as a constant scaling factor. It is then easy to see that the maximum and minimum occur when $|\Gamma_{act} - \Gamma_{opt}| = |\Gamma_{act}| + |\Gamma_{opt}|$ and $|\Gamma_{act}| - |\Gamma_{opt}|$ respectively. Giving two new equations:

$$
T_{\text{LNA max}} = T_{min} + 4\text{N}T_o \frac{(|\Gamma_{act}| + |\Gamma_{opt}|)^2}{(1 - |\Gamma_{act}|^2)\,(1 - |\Gamma_{opt}|^2)} \tag{2.61}
$$

---

[3] The author is indebted to the late *Per S Kildal* for his supervision in developing the idea of LNA envelope curves.

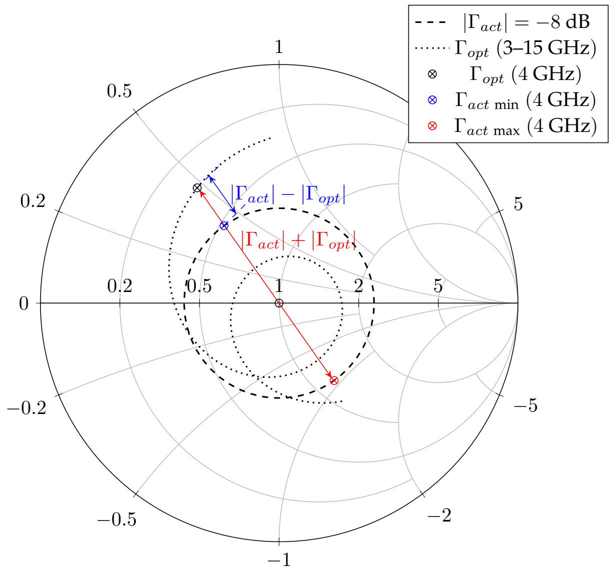

Figure 2.15: Maximum and minimum points at 4 GHz for a 66 K UWB LNA.

$$T_{\text{LNA min}} = T_{min} + 4\text{N}T_o \frac{(|\Gamma_{act}| - |\Gamma_{opt}|)^2}{(1 - |\Gamma_{act}|^2)\,(1 - |\Gamma_{opt}|^2)} \tag{2.62}$$

Using the standard impedance form of eq. (2.60):

$$T_{\text{LNA}} = T_{min} + \text{N}T_o \frac{|Z_{act} - Z_{opt}|^2}{R_{act} R_{opt}} \tag{2.63}$$

The impedance forms of eqs. (2.61) and (2.62) are:

$$T_{\text{LNA max}} = T_{min} + \text{N}T_o \frac{(R_{act} + R_{opt})^2}{R_{act} R_{opt}} \tag{2.64}$$

$$T_{\text{LNA min}} = T_{min} + \text{N}T_o \frac{(R_{act} - R_{opt})^2}{R_{act} R_{opt}} \tag{2.65}$$

It is easily shown that Γ_{act} is in and out of phase with Γ_{opt} at the two limits, for $|\Gamma_{act} - \Gamma_{opt}|$

$$\begin{aligned} &= ||\Gamma_{act}|e^{j\theta_{act}} - |\Gamma_{opt}|e^{j\theta_{opt}}| \\ &= |(|\Gamma_{act}| - |\Gamma_{opt}|)e^{j\theta_{opt}}| \text{ for } \theta_{act} = \theta_{opt} \\ &= |\Gamma_{act}| - |\Gamma_{opt}| \text{ (min) and for } \theta_{act} = \pi + \theta_{opt} \\ &= |\Gamma_{act}| + |\Gamma_{opt}| \text{ (max)} \end{aligned}$$

Visually shown in fig. 2.15 where a 66 K UWB LNA has been used to illustrate the principle, with $|\Gamma_{act}| = -8$ dB.

This is similarly expressible in terms of the LNA matching efficiency η_{miss} (defined in [55] and given by eq. (2.66) where T_{LNA} used here, is equivalent to T_{rec}). These efficiencies are plotted in fig. 2.16 (note that as this is an efficiency, and a maximum temperature corresponds with a minimum matching efficiency).

$$\begin{aligned} \eta_{miss} &= \frac{T_{min}}{T_{\text{LNA}}} \\ \eta_{miss\ \text{min}|\text{max}} &= \frac{T_{min}}{T_{\text{LNA max}|\text{min}}} \end{aligned} \tag{2.66}$$

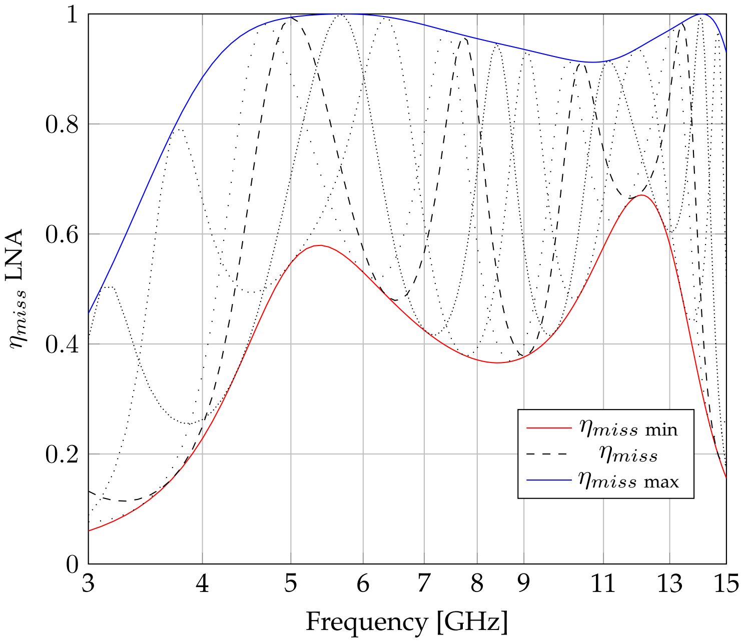

Figure 2.16: Multiple arbitrary phased LNA η_{miss} curves, with maximum and minimum envelopes, calculated for a $|\Gamma_{act}| = -8$ dB matching criteria and a UWB 66 K LNA.

From an antenna or system designer's perspective the worst case is normally of most interest, which can now easily be calculated for a general matching criteria. Plotted in fig. 2.17 are maximum LNA temperature contributions, and minimum LNA efficiencies for different $|\Gamma_{act}|$. The maximum ripple in the noise temperature $(T_{\text{LNA max}} - T_{\text{LNA min}})$ is plotted in fig. 2.18 which, along with the maximum curve characterise the LNA envelopes fully.

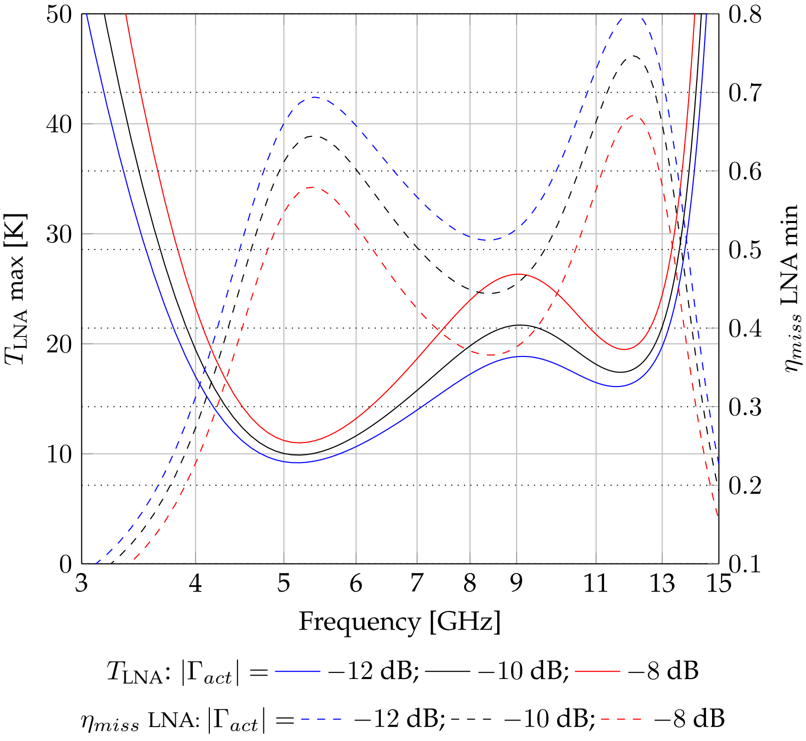

Figure 2.17: Maximum LNA temperature, and minimum LNA efficiency curves for different $|\Gamma_{act}|$ and a UWB 66 K LNA.

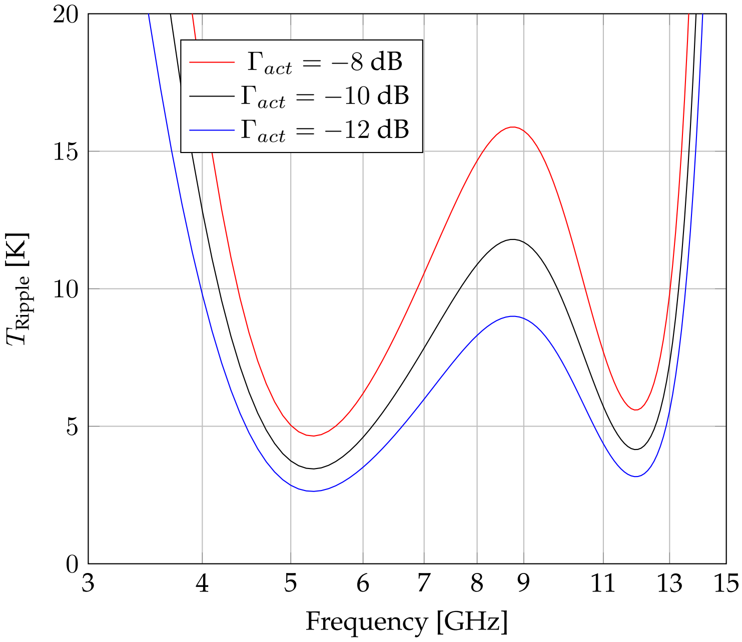

Figure 2.18: Maximum LNA ripple curves calculated for a various $|\Gamma_{act}|$ and a UWB 66 K LNA.

2.4.6 Noise wave modelling

Noise wave modelling was first introduced by *Bauer* and *Rothe* [56] (German), and called attention to by *Penfield* [57]. The method differs in that the noise sources are replaced by equivalent waves emanating from the ports shown in fig. 2.19. This theory has been applied extensively with the aid of computers by *Kanaglekar*, *McIntosh* and *Bryant* [58]. *Wedge* and *Rutledge* present this using the already known concept of a *characteristic noise matrix* [59]. Wave modelling relies on knowing the scattering parameters of the components, often only S_{21} is given for amplifiers, this can be measured or assumptions can be made ($S_{11} = 0$). The assumptions are already inherent in taking a simpler approach so does not degrade the simulated model.

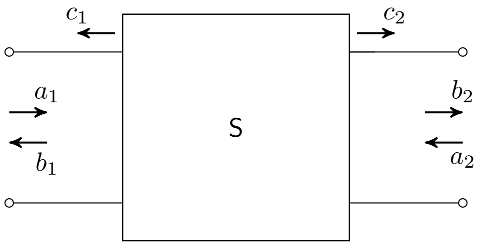

Figure 2.19: Equivalent S network, using noise wave sources, adapted from [59].

The noise contribution is then modelled by modifying the standard S–parameter model as follows:

$$\boldsymbol{b} = \mathsf{S}\boldsymbol{a} + \boldsymbol{c} \tag{2.67}$$

Where the characteristic noise matrix is:

$$\mathsf{C}_s = \overline{\boldsymbol{c}\boldsymbol{c}^\dagger} \tag{2.68}$$

Which is related to eq. (2.33) by [59, fig. 2]:

$$\mathsf{C}_s = \frac{1}{4}(\mathsf{I} + \mathsf{S})\overline{\mathsf{i}\mathsf{i}^\dagger}(\mathsf{I} + \mathsf{S})^\dagger \tag{2.69}$$

$$\mathsf{C}_s = \frac{1}{4}(\mathsf{I} - \mathsf{S})\overline{\mathsf{v}\mathsf{v}^\dagger}(\mathsf{I} - \mathsf{S})^\dagger \tag{2.70}$$

and to the noise temperature by [60, chp. 7].

$$|\boldsymbol{c}_i| = kT_i \tag{2.71}$$

$$\overline{\boldsymbol{c}_i\boldsymbol{c}_j^*} = k\sqrt{T_iT_j}\rho_{ij} \tag{2.72}$$

The reader is referred to [59–61] for the full multiport theory for scattering matrices, and noise waves.

Chapter 3

Noise modelling, applied to a wideband complex feed

3.1 Introduction

The theory in chapter 2 is applied to a wideband multiport feed with close coupling elements, the Eleven antenna. Demonstrating the theory and giving us confidence in the prediction critical to applying it to design and optimisation. Sections of this chapter are extracted from [62].

3.2 Noise modelling the Eleven antenna

The Eleven antenna (shown in fig. 3.1) is a compact form of a log periodic dipole array. It consists of eight single ended or four differential ports connected to two sets of two linearly polarised petals, the ports can be combined in multiple configurations. Y–factor measurements [3, chp. 10] have been carried out using two arrangements, eight single ended amplifiers, as illustrated in fig. 3.2, and using differential amplifiers illustrated in fig. 3.3. The modelling becomes complex because as can be seen the inter-element spacing is small, there is strong mutual coupling in the receiver which contributes to the system noise, referred to as *noise coupling*. In closely coupled antennas this contribution can be up to 30 %, a combined effect of changing the active impedance Γ_{act}, the noise properties of the LNAs and the beam forming weights.

The Eleven antenna although not an array, can be considered as an array of receiving ports and simplified to a single receiver chain using methods in [47] and presented in [62]. The methodology is analogous (when the coupling between unconnected elements are negligible and the amplifiers and channels identical) to methods presented in [64], a simple and useful method of modelling antenna receiver systems with multiple receiving chains and amplifiers. This reduces the system to a single receiver chain shown in fig. 3.4 below.

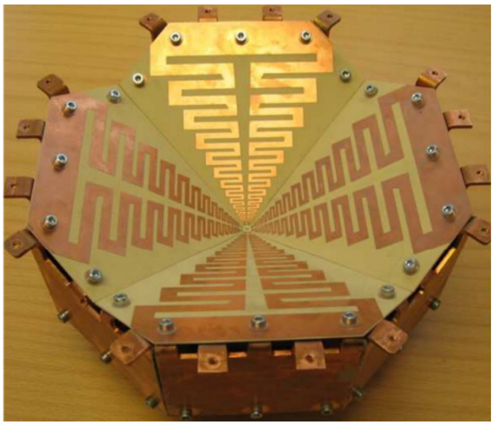

Figure 3.1: The Eleven Antenna, an ultra wideband, dual polarized antenna operating over a decade bandwidth from 1 GHz to 10 GHz, with a near constant gain of 11 dB.

3.2.1 Brightness temperature

When modelling system sensitivity it is important to understand the reflector used and feed illumination. The considered system and associated noise contributions, at zenith, are modelled as shown in fig. 3.5. The noise contribution of the atmosphere is calculated by integrating the sky brightness temperature across the antenna beam, modelling the ground as a constant 293 K visible from $\theta > \pi/2$, and the sky temperature distributed as shown in chapter 2 using eq. (2.6). Various calculated system brightness temperature, of an Eleven antenna pointing upwards, for different illumination tapers, is given in fig. 3.6. Where the antenna is assumed to be pointing at Zenith, the average and most commonly used case. For large reflector antennas where the feed sees the dish ($\theta < \theta_0$ in fig. 3.5) can be consider as pointing at zenith. For angles between this and the horizon the sky, as calculated from eq. (2.7), and $\theta > \pi/2$ the ground. Clearly from fig. 3.6, the greater the illumination angle the more the feed is shielded from ground noise. Increasing the illumination angle reduces the aperture efficiency as can be seen from fig. 3.7, resulting in a trade-off between noise and gain. The optimal point to place the feed depends on the total system temperature, if the overall system has a very low noise temperature it is better to reduce ground pick up, while if it is high, better to get more gain.

3.2.2 Ohmic and aperture efficiencies

The Eleven antenna is designed to illuminate a prime focused reflector, the aperture efficiencies are calculated from the measured beam patterns. The reader is referred to Appendix A for the calculations. The physical losses in the feed are given as an ohmic efficiency e_{ohmic}. The beam efficiencies and ohmic are plotted in fig. 3.8 where e_{rad} is the combined efficiencies of the radiation and ohmic efficiency.

3.2.3 LNA modelling

Various wideband LNAs are available and given in table 3.1, the choice of amplifier is critical to the noise matching. The optimal impedance Γ_{opt} of two possible amplifiers are plotted in fig. 3.9 and the impedance of the Eleven antenna in fig. 3.10. Clearly due to the wide

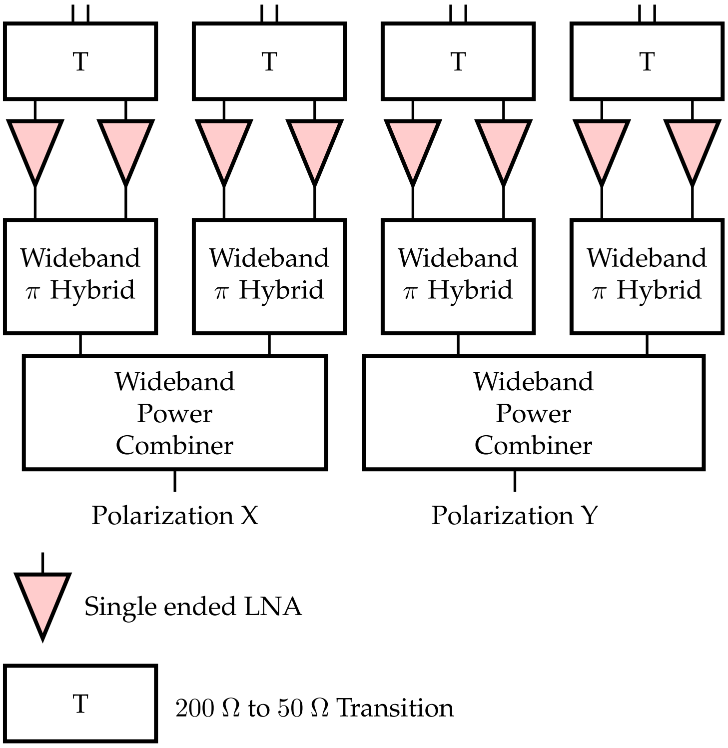

Figure 3.2: Descrambling solution using 8 single-ended amplifiers and 4 commercial wideband $180°$ hybrids and two 3 dB power combiners. The 200 to $50\,\Omega$ transition T, transforms a balanced twin-lead line to single-ended line, adapted from fig 11. [63].

frequency band of the system it is practically impossible to match the feed's impedance to the optimum amplifiers impedance. Instead a general matching criteria is developed that looks at the worst case. The envelope curves for the Chalmer's LNA (shown in fig. 3.9) are plotted in fig. 3.11. The Caltech differential amplifier is used in the cryogenic measurements and its noise temperature is plotted in section 3.2.4.

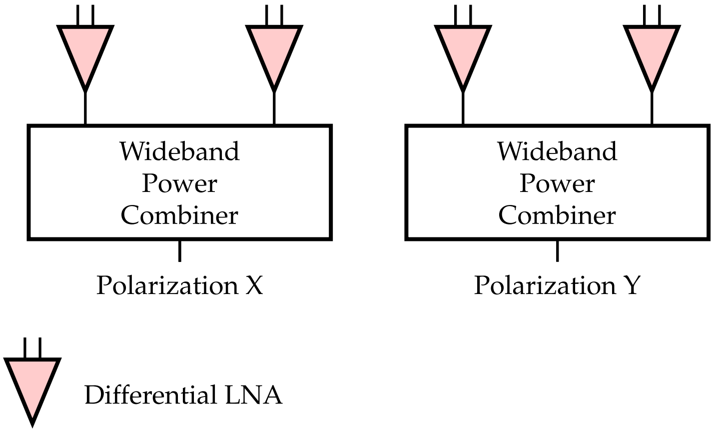

Figure 3.3: Descrambling solution using four active baluns, i.e. differential LNAs with single-ended outputs, adapted from fig 13. [63].

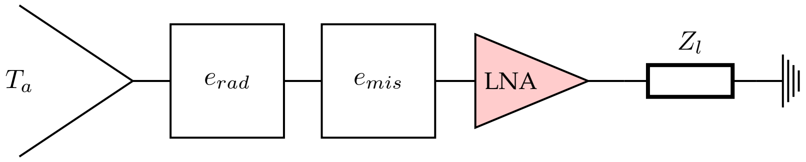

Figure 3.4: Equivalent single channel noise model.

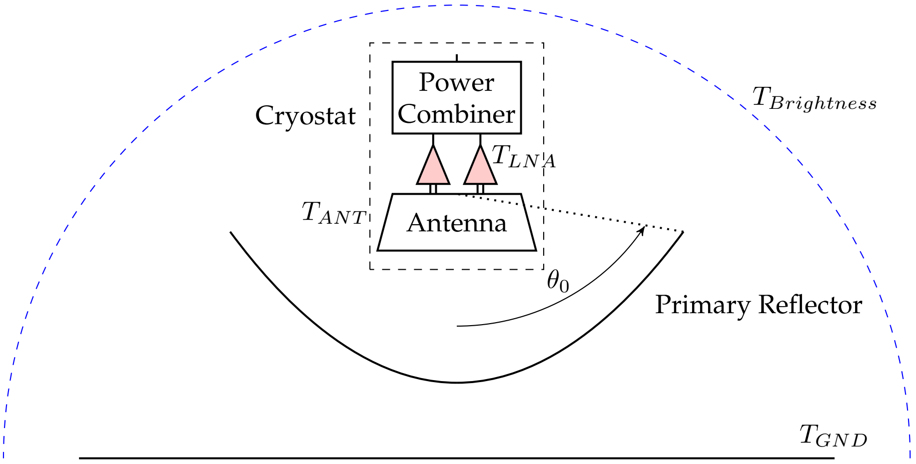

Figure 3.5: System model with associated noise contributions (right). There are assumed to be 4 LNAs with differential 200 Ω ports connected to the 8 Eleven antenna ports shown on the rear side of the feed.

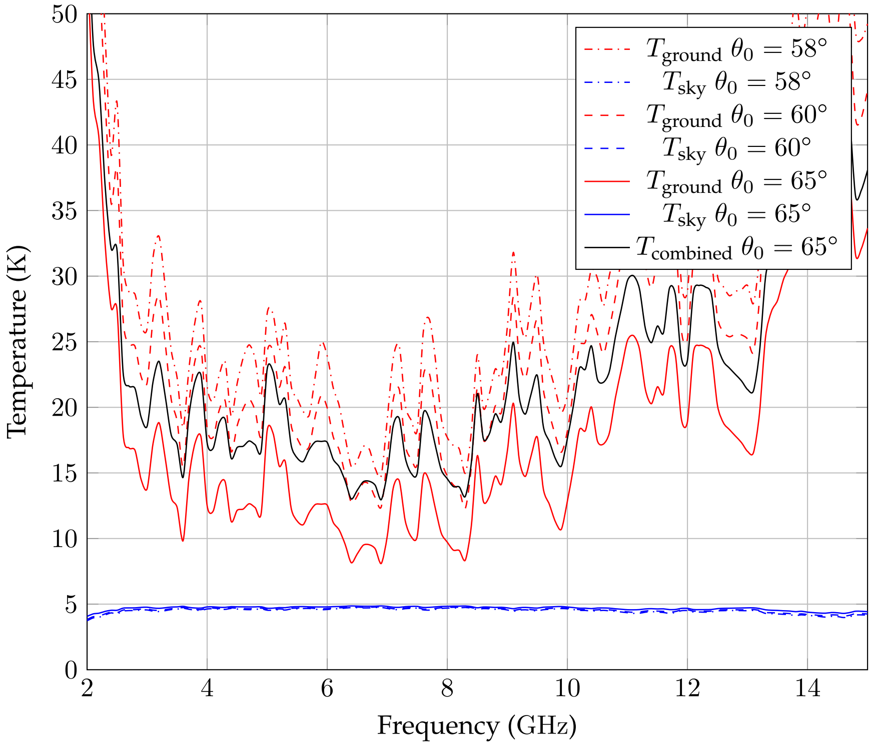

Figure 3.6: Integrated beam brightness temperatures vs Frequency, simulated for various illumination angles.

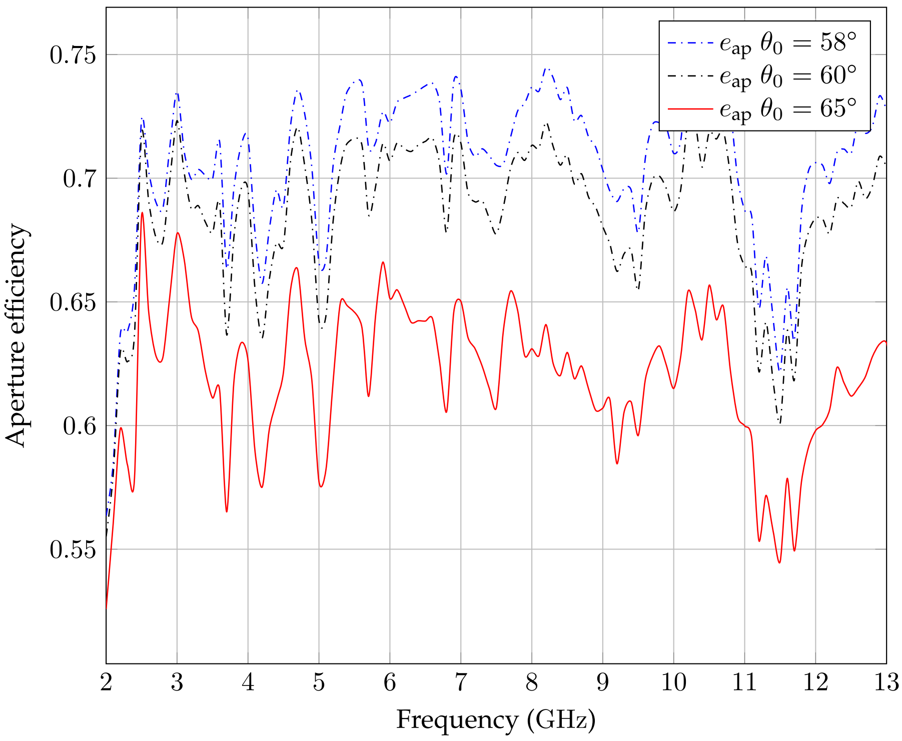

Figure 3.7: Aperture efficiency vs Frequency, simulated for various illumination angles.

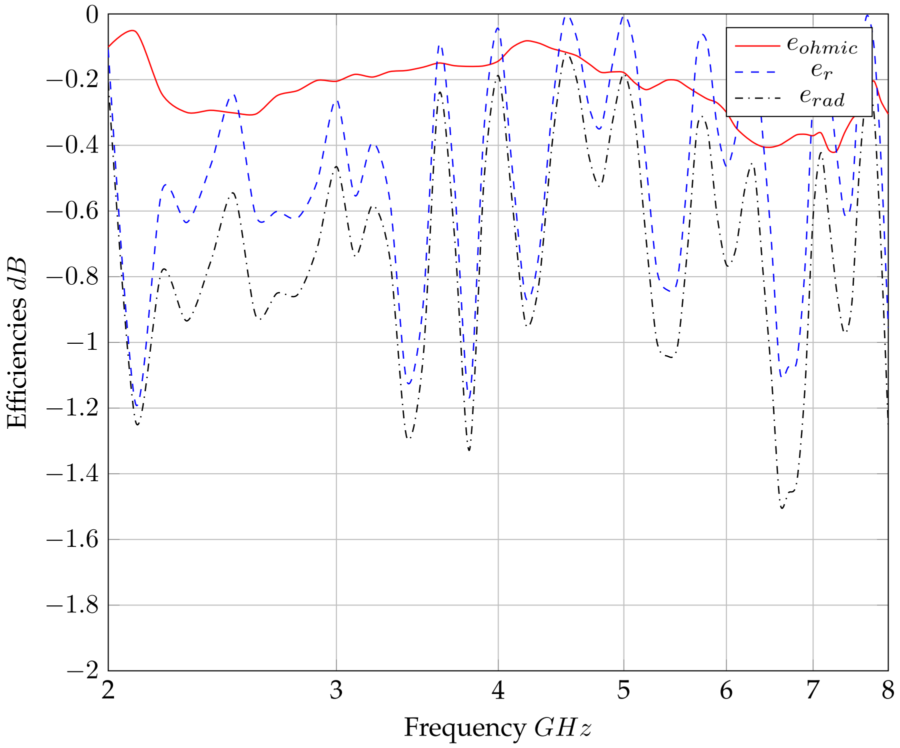

Figure 3.8: Ohmic and radiation efficiencies of the Eleven antenna, calculated on the beam patterns for an optimal illumination angle.

Table 3.1: Available wideband LNAs.

Techn.	Input Type	Physical Temperature	Source	Impedance	Frequency	Gain (11 GHz)	Noise Temperature (11 GHz)
lnp HEMT MMIC	single ended	20 K	Caltech	50 Ω	0.5 GHz to 11 GHz	40 dB	5 K
lnp HEMT MMIC	differential	20 K	Caltech	200 Ω	0.5 GHz to 11 GHz	37 dB	5 K
GaAS mHEMT MMIC	single ended	70 K	Low Noise Factory	50 Ω	1 GHz to 11 GHz	32 dB	16 K
GaAS mHEMT MMIC	single ended	298 K	Low Noise Factory	50 Ω	1 GHz to 11 GHz	31 dB	60 K
GaAS mHEMT MMIC	single ended	70 K	MC2	50 Ω	1 GHz to 11 GHz	32 dB	16 K
GaAS mHEMT MMIC	differential	298 K	MC2	150 Ω	1 GHz to 15 GHz	25 dB	75 K
discrete GaAS	single ended	20 K	GARD	50 Ω	4 GHz to 8 GHz	33 dB	5 K

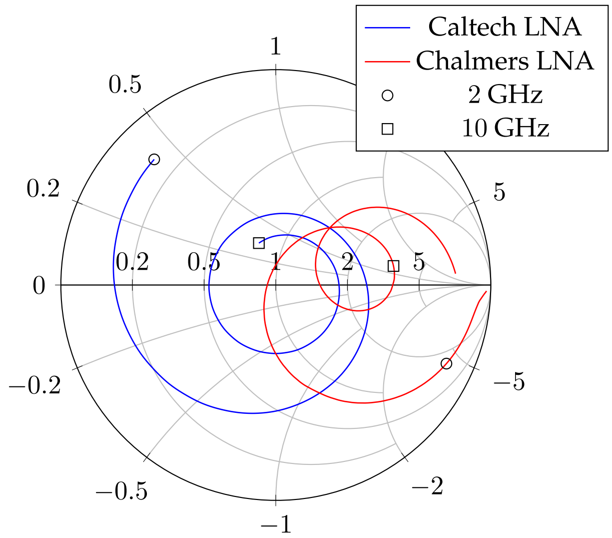

Figure 3.9: Optimum noise input impedances of Chalmers (ambient) and Caltech (cryogenic) LNAs as given by the manufactures, all charts matched to 200 Ω.

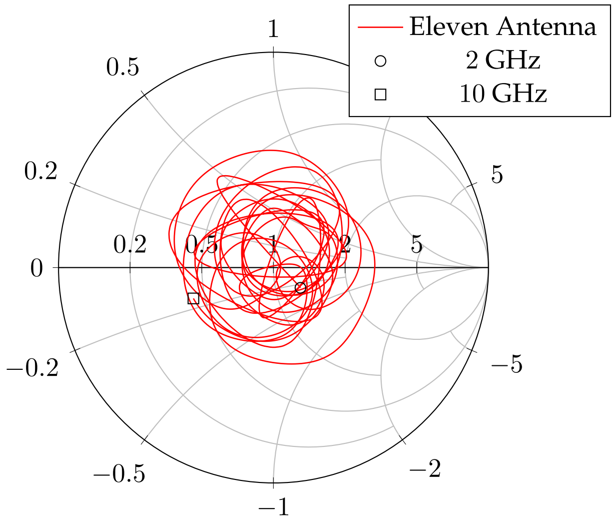

Figure 3.10: Measured input impedances of the Eleven Antenna, all charts matched to 200 Ω.

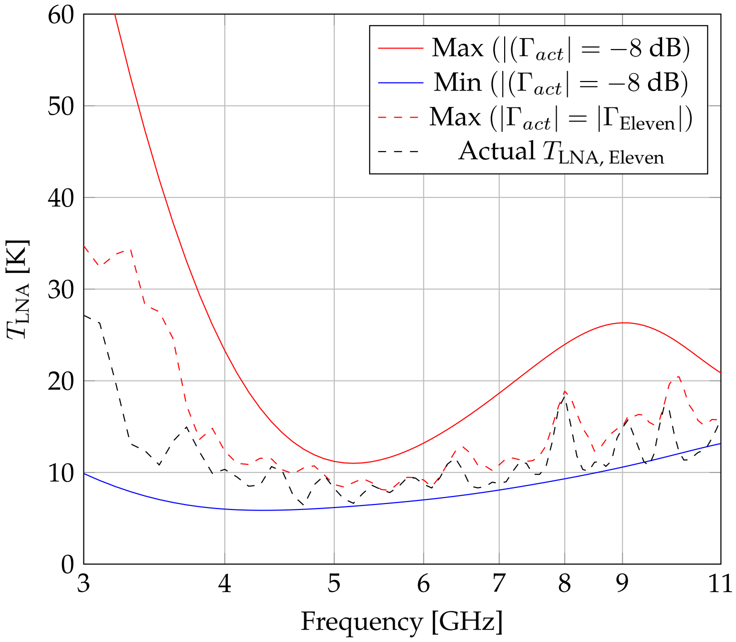

Figure 3.11: Simulated T_{LNA} curves calculated for a -8 dB, and specific antenna (Γ_{Eleven}) matching criteria and a UWB 66 K LNA.

3.2.4 Complete system temperature

Hot cold Y–factor measurements using the sky and Ecosorb for the loads were done at the Onsala space observatory. The Eleven antenna is placed inside a Dewar which is cryogenically cooled under vacuum, pictures of the measurements are given in fig. 3.12 and details are presented in [65]. The final predicted system noise temperature is plotted in fig. 3.13, the amplitude agreement is good with the average noise temperature within $0.3\,\mathrm{K}$ of the model. The model however does not capture the dynamics of the noise as should be expected with a simpler single channel model.

Figure 3.12: Cryogenically cooled Eleven antenna in Dewar, and measurement setup. Liquid Helium is used for the cooling, and the system is given several hours to stabilise. The amplifier voltages where monitored to control for gain fluctuations using a precision power supply.

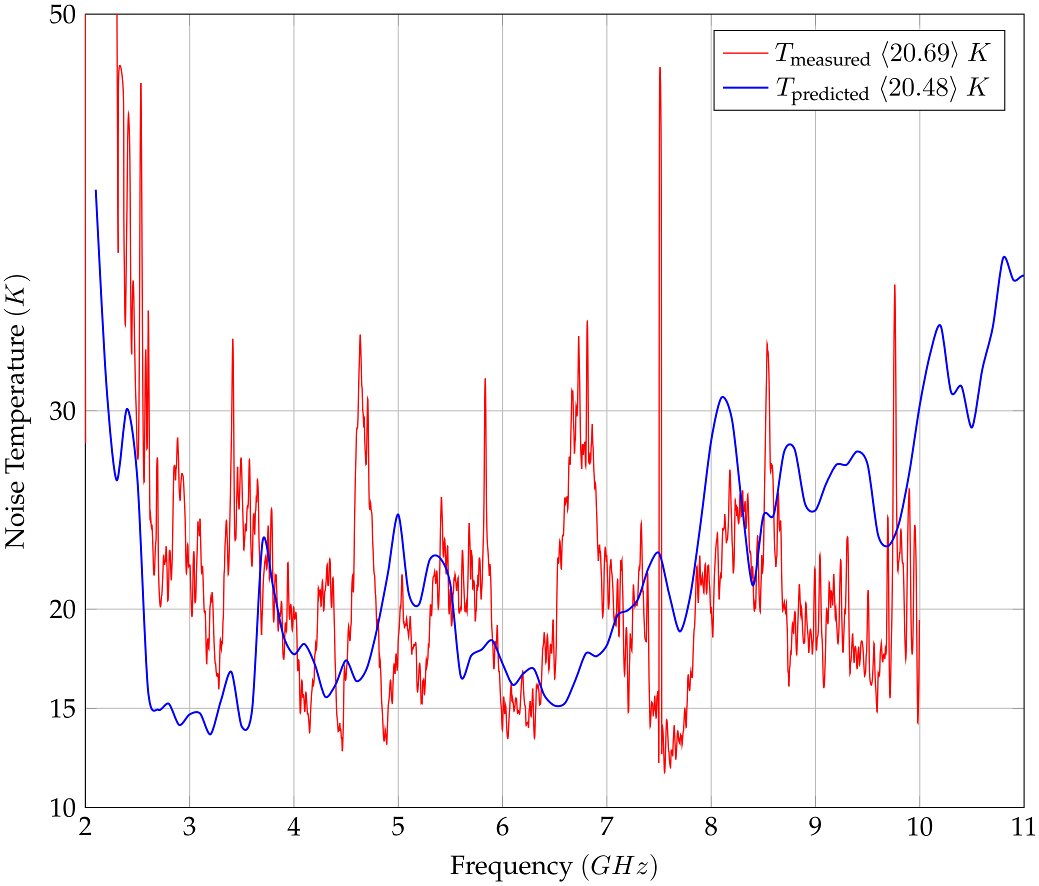

Figure 3.13: Measured vs. Simulated Noise Temperature for a cryogenic Eleven Antenna system using wideband Caltech amplifiers, note, the noise is plotted logarithmically so as not to lose the low temperature points, measurements where done at the MIT Haystack observatory.

3.3 System sensitivity

Combining environmental and receiver noise contributions, with the effective aperture calculations above (A/T $= \frac{e_{ap}e_{rad}A_{phy}}{T_a}$) the final A/T curve is plotted in fig. 3.14. This is the final desired goal function that represents the total system sensitivity and should be the goal of a final system optimisation function.

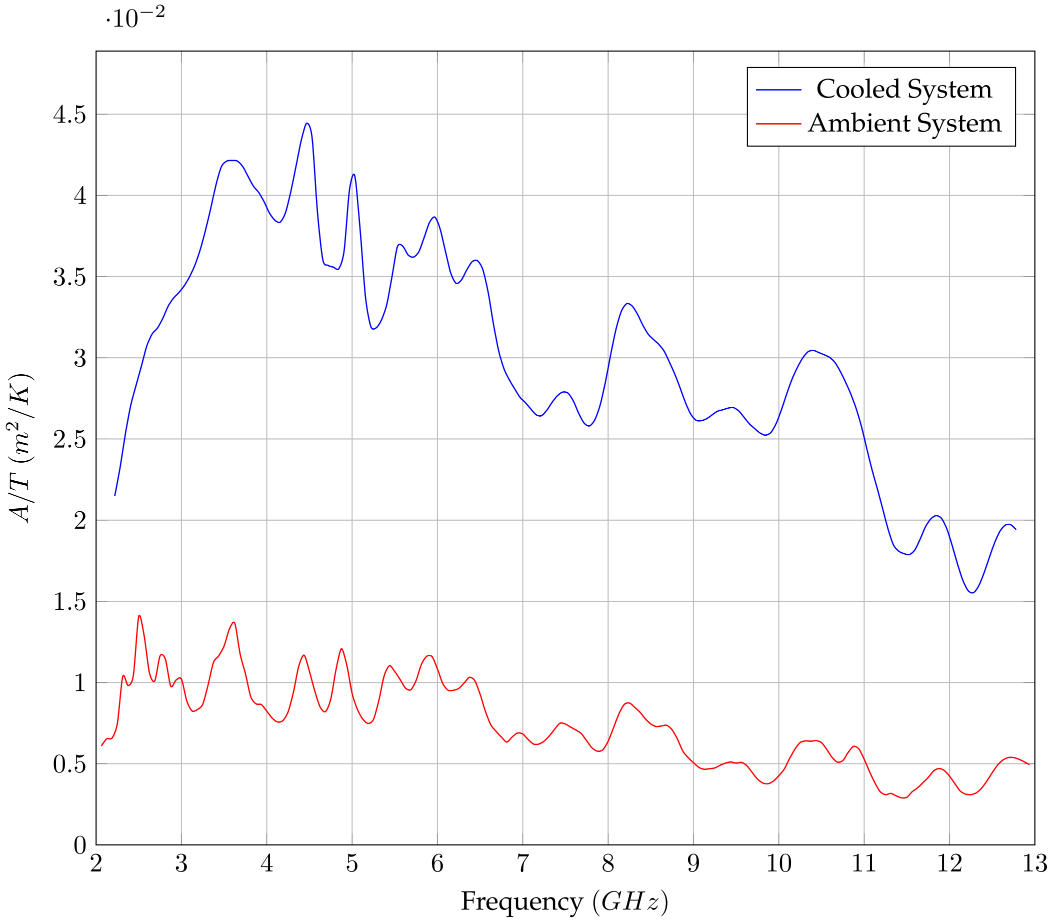

Figure 3.14: Maximum achievable A/T per m^2 physical aperture vs. Frequency f for cooled and uncooled systems(F/D $= 0.433$), when the Eleven antenna feeds a reflector with half subtended angle $\theta_0 = 60°$.

3.4 Conclusion

The application of equivalent single channel noise modelling theory to a complex feed gives a good prediction of the system noise, even if it does not capture all the dynamics as is expected. The modelling presented is sufficient to give Radio Astronomers a good expectation to the receiver's sensitivity and that the system is working correctly. For simpler systems the calculation of the overall system sensitivity gives us a goal function to compare and contrast possible systems, however for more complex and sensitive systems multiport modelling is required. The next chapter goes through the motivation and approach of more complex noise modelling calculations.

Chapter 4

Integration of Noise Modelling into EM design

4.1 Introduction

Next generation radio astronomy systems and Earth observation science rely largely on innovative antenna technologies (such as wideband dense arrays and multiport feeds for reflector antennas) and low noise receivers. Examples of on going developments are the SKA radio telescope and VLBI2012 network [28, 34]. Design and optimization of such high sensitivity wideband systems is challenging, due to the computationally intensive nature of the antenna simulations (over wide frequency and scan angle ranges) and strong interaction between antenna element mutual coupling, receiver noise and beam forming scenarios [66]. To tackle these problems a number of computationally efficient numerical approaches, combined antenna receiver characterization techniques and dedicated software tools have recently been developed [35, 37, 64]. One example is the `CAESAR` software, an advanced EM/MW solver for the analysis of large antenna array systems [35], and a newly developed phased array feed toolbox for the analysis of reflector antennas [37]. This software is tailored to solve for the noise response of receiver/antenna systems to external (ground and sky) and internal (LNAs, ohmic losses) noise sources. The necessary input parameters for the system noise performance calculation are: (i) antenna radiation patterns and radiation efficiencies and the antenna input impedance matrix; (ii) noise and S–parameters of LNAs and beam forming network; (iii) the external noise temperature distribution. Currently the software is not widely available, and the author should be directly contacted to obtain it.

Most antennas are designed using commercial software and it is not practical, nor efficient to resolve them using these specialised solvers. It is more useful to be able to use this specialised software in conjunction with the commercial solvers. The specific commercial solver considered here is `CST`, but it applies generally to any commercial solver.

The Problem is formulated as follows: The radiation patterns, efficiency and impedance of an antenna are simulated in `CST` and can be exported to `CAESAR` to construct the overall system model. The excitation conditions for antenna ports and formats of the simulation data of the radiated field as implemented in `CST` and `CAESAR` are however different. Our objective is therefore to develop a general procedure for calculating the necessary data for noise evaluation, from `CST` (or similar EM software) into the format required for modelling the system noise temperature in `CAESAR`.

The model is tested using a simple folded dipole. The dipole can be simulated completely in `CAESAR` and then compared to the hybrid `CST/CAESAR` solution. The solution is then applied to develop a detailed system model of the multiport Eleven antenna for a reflector antenna [67], and to perform the system noise analysis.

Sections of this chapter have been experted and adapted from [68].

4.2 A general multiport antenna model

4.2.1 Definitions

For convenience we compact the representation of a multiport antenna into a matrix vector formulation, shown in fig. 4.1.

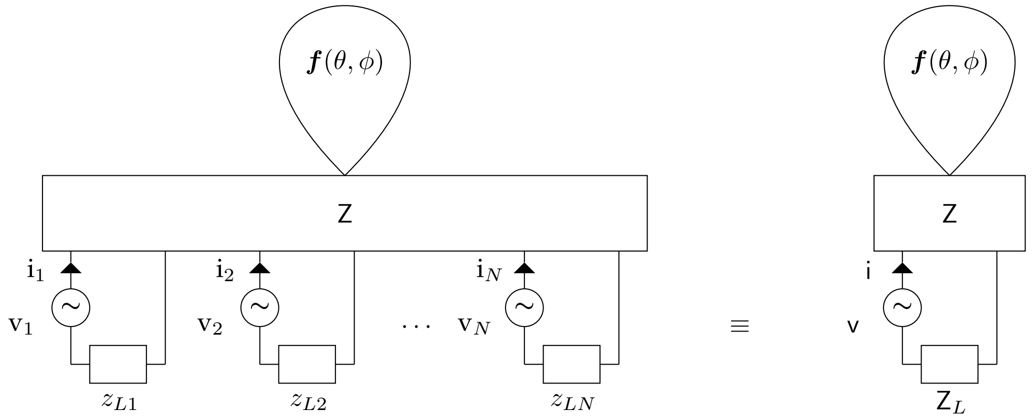

Figure 4.1: Equivalent single port antenna representation of a multiport antenna system.

In fig. 4.1 $\mathsf{v} = [\mathrm{v}_1, \mathrm{v}_2\ \dots\ \mathrm{v}_N]^{\mathrm{T}}$ a column vector of the port voltages (where T is the transpose operator), i, similarly defined, is the port currents, $\boldsymbol{f}$ is the total beam pattern defined as

$$\boldsymbol{f}(\theta,\phi) = \boldsymbol{E}_\theta(\theta,\phi) + \boldsymbol{E}_\phi(\theta,\phi)$$

Z is the antenna Z–matrix, and

$$\mathsf{Z}_L = \begin{bmatrix} z_{L1} & \cdots & 0 \\ \vdots & \ddots & \vdots \\ 0 & \cdots & z_{LN} \end{bmatrix}$$

is a diagonal matrix of the load impedances. To completely characterise a N–port antenna device we need M linearly independent voltage vectors corresponding to M antenna beam patterns, where $M \geq N$. Compactly expressed as:

$$\mathsf{V} = [\mathsf{v}_1 \ \vdots\ \mathsf{v}_2 \ \vdots\ \dots \ \vdots\ \mathsf{v}_M] \tag{4.1}$$

$$\mathsf{f} = [\boldsymbol{f}_1, \boldsymbol{f}_2\ \dots\ \boldsymbol{f}_M]^{\mathrm{T}} \tag{4.2}$$

Where V is a square $N \times M$ matrix and f is a $M \times 1$ column vector. For the case where each port is excited sequentially with $1\ V$, V is the identity matrix i.e. $\mathsf{V} = \mathsf{V}_0 = \mathsf{I}$. The corresponding f vector is defined as $\mathsf{f}_0 = [\boldsymbol{f}_{0,1}, \boldsymbol{f}_{0,2}\ \cdots\ \boldsymbol{f}_{0,N}]^{\mathrm{T}}$, where $\boldsymbol{f}_{0,n}$ is the embedded element pattern of the nth element when it is excited with $1\ V$ and the remaining elements are unexcited (there source voltages are equal to zero, but they are still loaded). Using the principles of superposition and that the antenna beam pattern contribution from a single port is directly scalable by the voltage at the same port, we can rewrite the general case as:

$$\begin{aligned}
\boldsymbol{f}_1 &= \mathrm{v}_{1,1}\boldsymbol{f}_{0,1} + \mathrm{v}_{1,2}\boldsymbol{f}_{0,2} + \dots \mathrm{v}_{1,N}\boldsymbol{f}_{0,N} \\
\boldsymbol{f}_2 &= \mathrm{v}_{2,1}\boldsymbol{f}_{0,1} + \mathrm{v}_{2,2}\boldsymbol{f}_{0,2} + \dots \mathrm{v}_{2,N}\boldsymbol{f}_{0,N} \\
&\vdots \\
\boldsymbol{f}_M &= \mathrm{v}_{M,1}\boldsymbol{f}_{0,1} + \mathrm{v}_{M,2}\boldsymbol{f}_{0,2} + \dots \mathrm{v}_{M,N}\boldsymbol{f}_{0,N}
\end{aligned}$$

Where:

$$\boldsymbol{f}_m = \sum_{n=1}^{N} \mathrm{v}_{m,n}\boldsymbol{f}_{0,n}$$

Or in matrix form:

$$\mathsf{f} = \mathsf{V}^{\mathrm{T}}\mathsf{f}_0 \tag{4.3}$$

If V is linearly independent $\mathsf{f}_0 = \mathsf{V}^{-\mathrm{T}}\mathsf{f}$. Note, when $M > N$ it is assumed that the pseudo–inverse is computed.

4.2.2 Beam pattern conversion due to different loading and excitation

The original known case is defined as "a", and the antenna beam patterns to be calculated, given a new loading and excitation defined as case "b". The port and circuit equivalents are given in fig. 4.2. To calculate the required beam patterns the scaling voltage is required. That is to calculate the excitation which would be required in order to produce the desired port voltage excitation in b. This is easily done using the equivalent circuits. The required port voltages to produce the required current is defined as v'_{a}, shown in fig. 4.3.

Using the equivalent circuit for case "b",

$$\mathsf{v}_{\mathsf{b}} = (\mathsf{Z}_{\mathsf{b}} + \mathsf{Z})\,\mathsf{i}_{\mathsf{b}}$$

Solving for the desired current i_{b} gives:

$$\mathsf{i}_{\mathsf{b}} = (\mathsf{Z}_{\mathsf{b}} + \mathsf{Z})^{-1}\,\mathsf{v}_{\mathsf{b}} \tag{4.4}$$

Similarly (from fig. 4.3) the corresponding voltage, which causes current i_{b} in circuit "a", v'_{a} is:

$$\mathsf{v}'_{\mathsf{a}} = (\mathsf{Z}_{\mathsf{a}} + \mathsf{Z})\,\mathsf{i}_{\mathsf{b}} \tag{4.5}$$

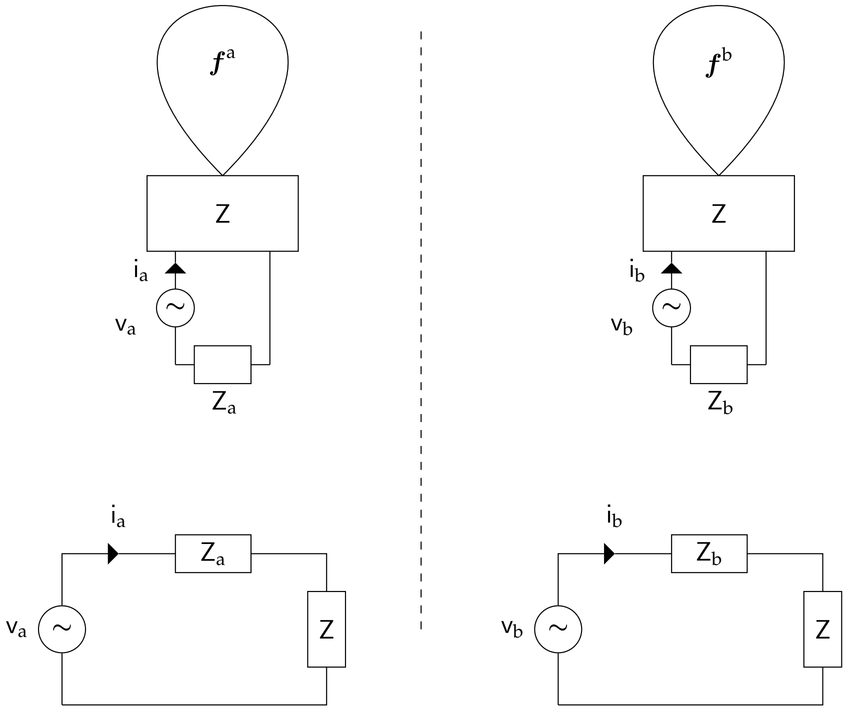

(a) Original solution

(b) New solution

Figure 4.2: Network and equivalent circuit representations.

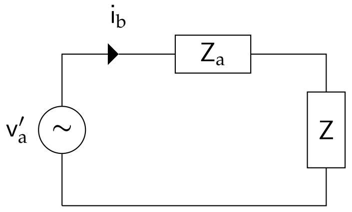

Figure 4.3: Equivalent voltage excitation for case "a" to realise current i_b in situation "b".

Substituting eq. (4.4) into eq. (4.5) gives:

$$v'_a = (Z_a + Z)\,(Z_b + Z)^{-1}\,v_b \tag{4.6}$$

For N linearly independent excitations this in matrix form is:

$$V'_a = (Z_a + Z)\,(Z_b + Z)^{-1}\,V_b \tag{4.7}$$

For the case where $V_b = V_0$,

$$V'_{a0} = (Z_a + Z)\,(Z_b + Z)^{-1}\,V_0 = (Z_a + Z)\,(Z_b + Z)^{-1} \tag{4.8}$$

In this case the beam patterns transformation is a simple scaling:

$$f_0^b = V'_{a0} f_0^a \tag{4.9}$$

The relations of the f_0 beam patterns to the required beam patterns f are calculated using eq. (4.3):

$$\mathsf{f}^{\mathsf{b}} = \mathsf{V}_{\mathsf{b}}^{\mathrm{T}}\mathsf{f}_0^{\mathsf{b}} \tag{4.10}$$

$$\mathsf{f}_0^{\mathsf{a}} = \mathsf{V}_{\mathsf{a}}^{-\mathrm{T}}\mathsf{f}^{\mathsf{a}} \tag{4.11}$$

Substituting eqs. (4.8), (4.9) and (4.11) into eq. (4.10) the required conversion equation can be formulated:

$$\begin{aligned}\mathsf{f}^{\mathsf{b}} &= \mathsf{V}_{\mathsf{b}}^{\mathrm{T}}\mathsf{V}'_{\mathsf{a}0}\mathsf{f}_0^{\mathsf{a}} \\ &= \mathsf{V}_{\mathsf{b}}^{\mathrm{T}}\mathsf{V}'_{\mathsf{a}0}\mathsf{V}_{\mathsf{a}}^{-\mathrm{T}}\mathsf{f}^{\mathsf{a}} \\ &= \mathsf{V}_{\mathsf{b}}^{\mathrm{T}}\left(\mathsf{Z}_{\mathsf{a}} + \mathsf{Z}\right)\left(\mathsf{Z}_{\mathsf{b}} + \mathsf{Z}\right)^{-1}\mathsf{V}_{\mathsf{a}}^{-\mathrm{T}}\mathsf{f}^{\mathsf{a}}\end{aligned} \tag{4.12}$$

Alternatively expressed for a single beam pattern as:

$$\boldsymbol{f}_m^{\mathsf{b}} = \sum_{n=1}^{N}\left(\mathsf{Z}_{\mathsf{a}} + \mathsf{Z}\right)\left(\mathsf{Z}_{\mathsf{b}} + \mathsf{Z}\right)^{-1}\frac{\mathsf{v}_{m,n}^{\mathsf{b}}}{\mathsf{v}_{m,n}^{\mathsf{a}}}\boldsymbol{f}_n^{\mathsf{a}} \tag{4.13}$$

Where $\boldsymbol{f}_m^{\mathsf{b}}$ is the beam pattern when the array is exited with voltages v_m, and loaded with Z_{b}. As expected the equations reduce to unity, (i.e $\mathsf{f}_{\mathsf{b}} = \mathsf{f}_{\mathsf{a}}$) when $\mathsf{Z}_{\mathsf{b}} = \mathsf{Z}_{\mathsf{a}}$, and $\mathsf{V}_{\mathsf{b}} = \mathsf{V}_{\mathsf{a}}$, as required.

eq. (4.12) can now be used to scale the beam patterns, however `CAESAR` also normalises the patterns (to an equivalent 1 W source) so this needs to be de–normalised so as to be re–normalised later.

4.2.3 De–normalisation

$$\begin{aligned} G &= \frac{P_r}{P_{in}/4\pi} \\ &\text{where:} \\ P_r &= \frac{1}{2}\frac{|\boldsymbol{f}|^2}{120\pi} \\ G &= \frac{|\boldsymbol{f}|^2}{2\;120\pi P_{in}/4\pi} \\ G &= \frac{|\boldsymbol{f}|^2}{60P_{in}} \\ &\text{rearranging:} \\ |\boldsymbol{f}| &= \sqrt{60P_{in}}\sqrt{G} \end{aligned} \tag{4.14}$$

From eq. (4.14), $\sqrt{60P_{in}}$ is the de–normalisation factor. Where the power, for `CST`, for the mth port is:

$$
\begin{aligned}
P_{in,m} &= \frac{1}{2} Re\{\mathsf{v}_0 \mathsf{i}_0^*\} \\
&= \frac{1}{2} Re\{\mathsf{i}_0^H \mathsf{v}_0\} \\
&= \frac{1}{2} Re\{\left(\mathsf{Z}^{-1}\mathsf{v}_0\right)^H \mathsf{v}_0\} \\
&= \frac{1}{2} Re\{\mathsf{v}_0^H \left(\mathsf{Z}^{-1}\right)^H \mathsf{v}_0\}
\end{aligned}
\tag{4.15}
$$

Where:

$$
\begin{aligned}
\mathsf{v}_\mathsf{a} &= \left(\mathsf{Z}_\mathsf{a} + \mathsf{Z}\right)\left(0 + \mathsf{Z}\right)^{-1} \mathsf{v}_0 \\
\mathsf{v}_0 &= \left(\mathsf{Z}_\mathsf{a} + \mathsf{Z}\right)^{-1} \left(\mathsf{Z}\right) \mathsf{v}_\mathsf{a}
\end{aligned}
$$

$$
|\boldsymbol{f}_m| = \sqrt{60 P_{in,m}} \sqrt{G_m}
$$

Where $\boldsymbol{V}$ can be calculated from the equivalent `CAESAR` excitation (see eq. (4.6)). The Gain Normalisation factor required for `CAESAR` is then finally $\sqrt{60 \mathsf{V} P_{in}}$. Where V is typically the identity matrix.

4.3 Testing and verification

To test the conversion a folded dipole with two ports simulated at a single frequency is used. Both `CST` and `CAESAR` models are produced and a comparison made between the converted `CST` pattern and actual `CAESAR` pattern. It is expected to vary slightly due to the different simulation methods and meshing. The modelled geometries are given in fig. 4.4.

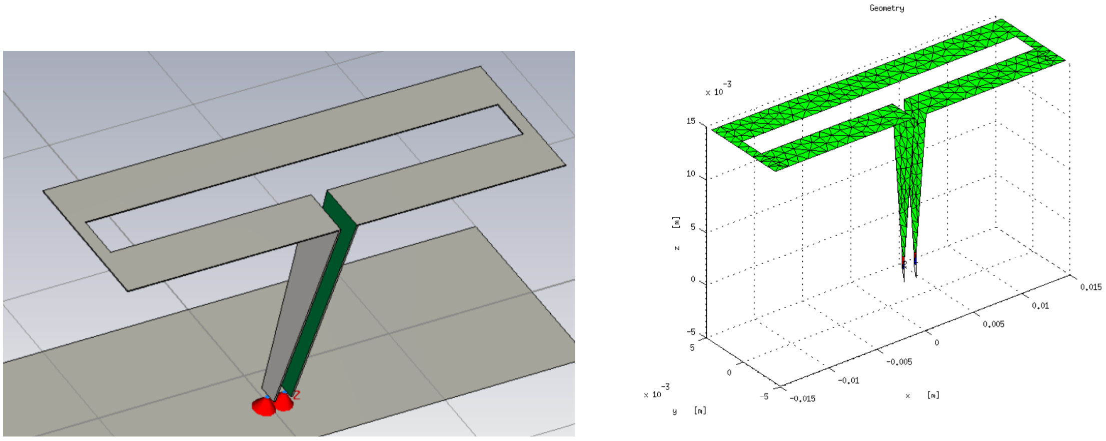

(a) `CST` model

(b) `CAESAR` model

Figure 4.4: Simple folded dipole geometries, for both `CST` and `CAESAR`, the ground plane for CAESAR is not shown.

The difference in the calculated Z matrices (as they are used directly in the translation) estimate the variations expected in the beam pattern. For `CAESAR` this is:

$$Re\{Z_{\text{CAE}}\} \approx \begin{pmatrix} 180 & 161 \\ 161 & 181 \end{pmatrix} \text{ and for } \texttt{CST}, \; Re\{Z_{\texttt{CST}}\} \approx \begin{pmatrix} 165 & 140 \\ 140 & 164 \end{pmatrix}$$

So the two beams patterns are expected to conform within 85%–95% of each other, which they do as shown in the original and converted beams plotted in fig. 4.5. The comparison, which is within the required accuracy, is given in fig. 4.6. The beams are symmetric and only port 1 is needed to be compared.

4.3.1 Conclusion

The converted beam patterns are within 2 % of the desired pattern, variations in the nulls are relatively to the total radiated power very small and so differences here are not problematic. This is considered within in the expected variation between the solvers. It is possible using this method to use `CAESAR` with `CST` and given the general approach to use it with any other commercial solver, as long as the form of the port excitations are known.

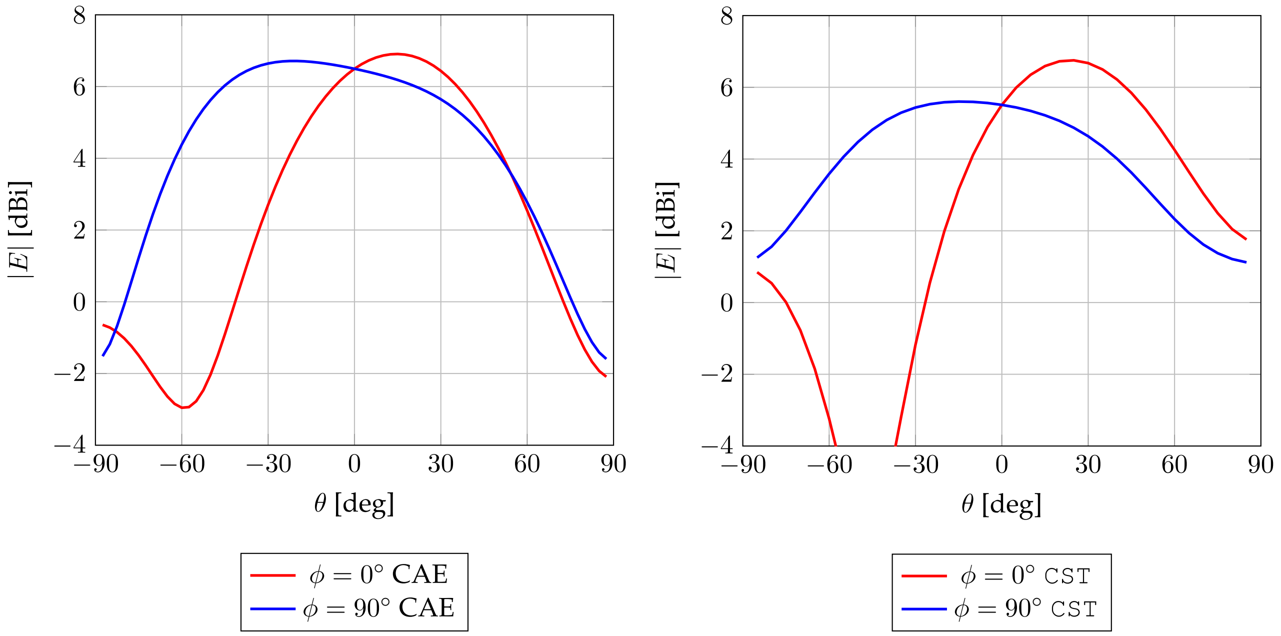

(a) `CAESAR` original

(b) `CST` original

Figure 4.5: Originally computed far field beam patterns for `CAESAR` and `CST`.

4.4 Modelling of multi-port antenna patterns

4.4.1 Description of the Eleven antenna system

The Eleven antenna is a decade-bandwidth log-periodic dual-dipole array developed at Chalmers University of Technology [67], consisting of eight single-ended ports connected

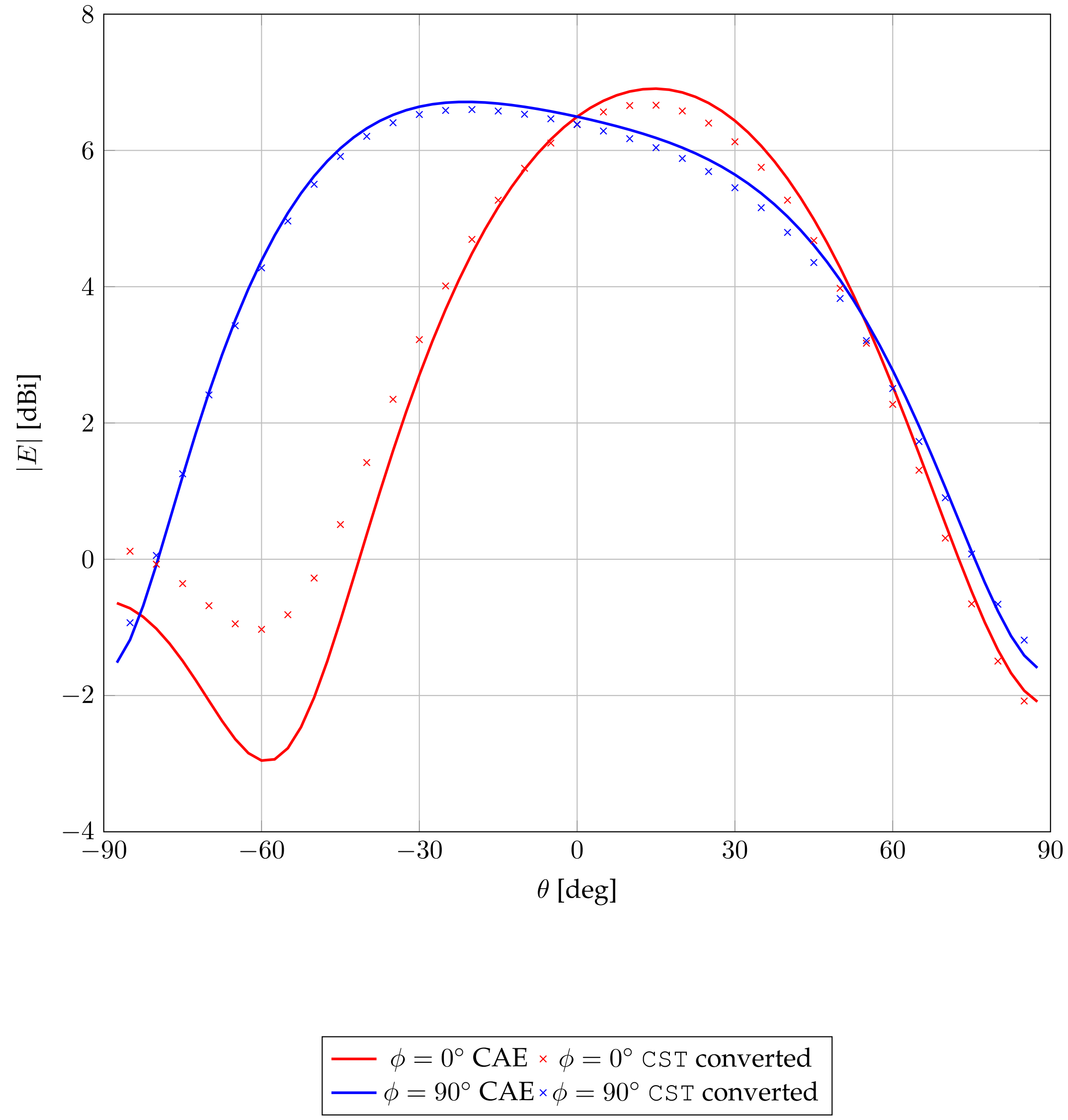

Figure 4.6: Comparison between original `CAESAR` and converted `CST` beam patterns.

to LNAs and a combining network as show in fig. 4.7. The noise performance of this receiver has previously been analysed with an approximate model (based on the equivalent system representation [64, 67]) and assuming identical LNAs (with no reflections at their ports) and an ideal combiner. The `CAESAR` model, presented here, is a full numerical approach which can be applied to perform a detailed study of the Eleven antenna performance and uses (where available) the measured noise and scattering parameters of LNAs and combiner components. The numerical results are compared to measurements carried out with the practical system.

The Eleven antenna is a symmetric structure and thus knowing the required combination network for the desired antenna beam pattern, means the simulation is typically done for only one eighth of the antenna using appropriate symmetry planes and associated boundary conditions for the fields [69]. Receiver noise however is coupled through all pattern correlations and so the `CAESAR` model requires the feed beam pattern to be modelled. From the inversion requirement in eq. (4.12), eight ports require eight unique

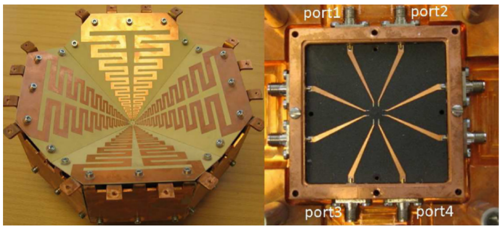

(a) Photos of the Eleven antenna consisting of four log-periodic dipole arrays and the descrambling board, realizing a transition to eight single-ended coaxial ports (on the rear side of the ground plane.

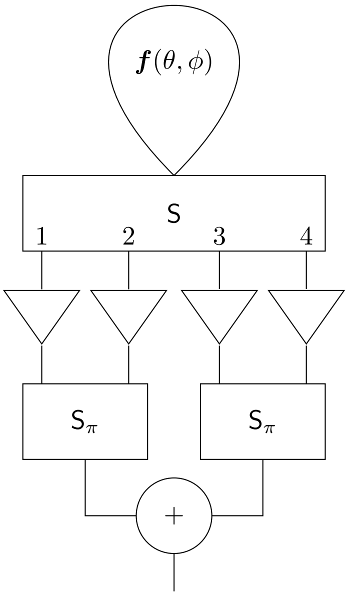

(b) The Eleven antenna receiver model, for one polarization, including two oppositely located dipole arrays, four single ended LNAs connected to the coaxial ports, two hybrids and combiner. The output ports of the other four LNAs are matched terminated.

Figure 4.7: Photos of the Eleven antenna, and the overall system model

excitation cases to be able to produce the case for any arbitrary excitation and port termination. This is impractical over the wide bandwidth of the Eleven antenna and so a single port is simulated instead, with all other ports terminated and then the simulated beam pattern is mathematically mirrored to produce the beam patterns for the equivalent single port excitations. This requires the full antenna to be simulated but only for one excitation. It is pointed out that it is computationally faster to simulate multiple smaller problems with varying E and H plane symmetries, as the number of mesh cells grows faster with a larger geometry than with the number of cases however, the single port pattern is chosen in this case as it is easier to verify the implemented code with a simple test cases, as discussed below.

4.4.2 Exploiting the rotation/translation symmetry

The mirroring is done using X, Y plane symmetries, and is tested using four simple folded dipoles configured to match the port configuration of the Eleven antenna, but simulated at one frequency (so all ports and combinations can be quickly simulated and compared

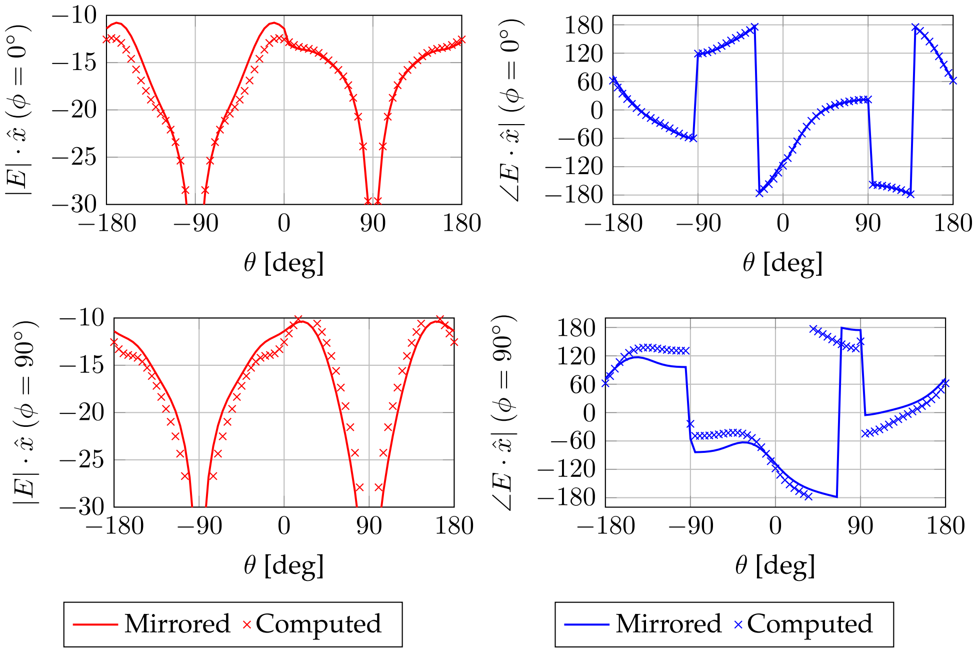

Figure 4.8: Comparisons between mirrored and directly computed beam pattern cuts for port 2 of four folded dipoles arranged in an identical port layout as shown in fig. 4.7, simulated at 5 GHz, (the phase has been wrapped for compactness).

to the mirrored patterns), shown in figs. 4.8, 4.10 and 4.10. The mirroring function shows only small variations (5–10^o) in the $\phi = 90^o$ plane. This accounts for similar variations in the summed patterns of the Eleven antenna case shown in fig. 4.11. Further verification is done by comparing the appropriately summed single port beam patterns with the previously simulated total antenna beam pattern used to characterise the feed. The comparison is plotted (at a single frequency for brevity) in fig. 4.11. The patterns are normalised and agree well with full port simulation (patterns within the simulated band, 1–12 GHz, show similar agreement given in Appendix B). The small differences between the results are primarily due to the fact that the two simulations are performed in `CST`; one for the entire Eleven antenna exciting a single port only, and another one for for one eighth of the antenna using symmetry planes for the fields.

4.5 System noise analysis

The beam patterns are transformed through eq. (4.12), and used directly in the `CAESAR` software. The method used is to compute the system gain using a 1 K sky noise temperature distribution and an otherwise noiseless system. The noise temperature of the noisy system is then modelled and normalised by dividing out the system available noise gain. Before doing so an ideal system (matched, lossless and reflection less beam former) was modelled in `CAESAR`, and compared to simpler modelling predictions.

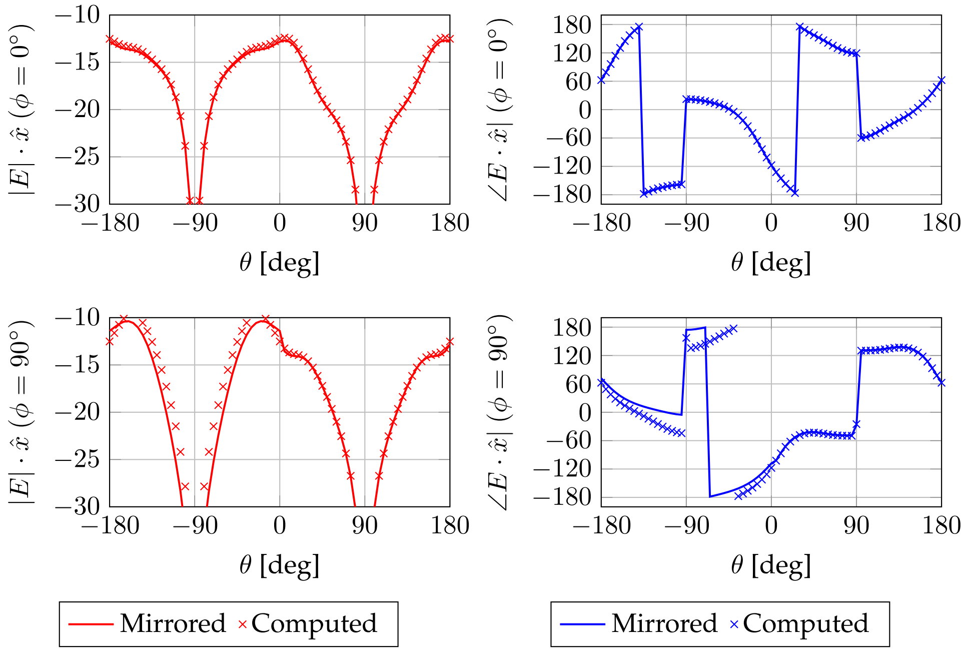

Figure 4.9: Comparisons between mirrored and directly computed beam pattern cuts for port 3 of four dipoles arranged in an identical port layout as shown in fig. 4.7, simulated at 5 GHz, (the phase has been wrapped for compactness).

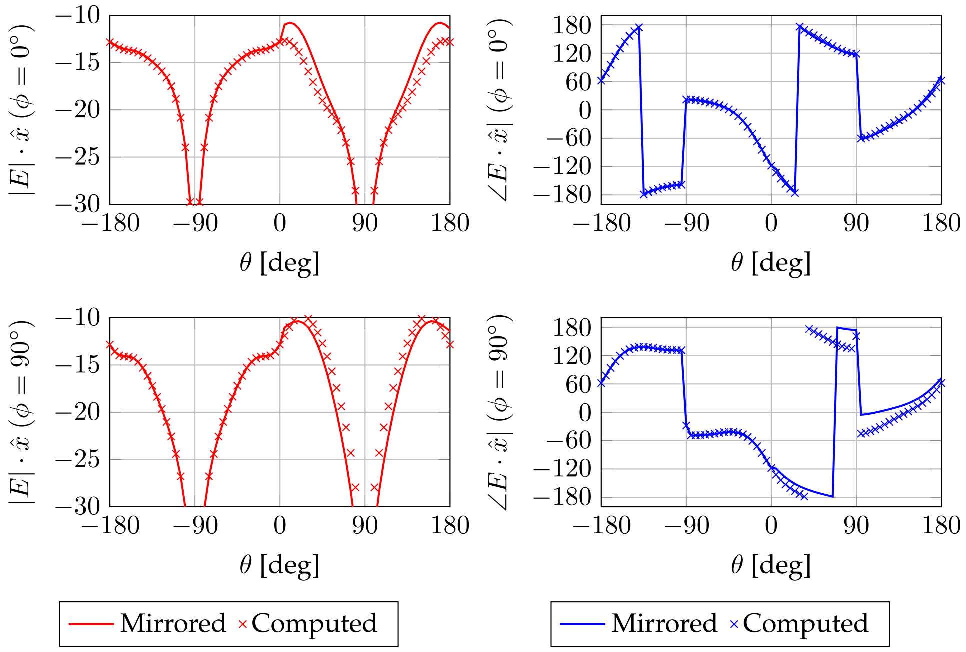

Figure 4.10: Comparisons between mirrored and directly computed beam pattern cuts for port 4 of four folded dipoles arranged in an identical port layout as shown in fig. 4.7, simulated at 5 GHz, (the phase has been wrapped for compactness).

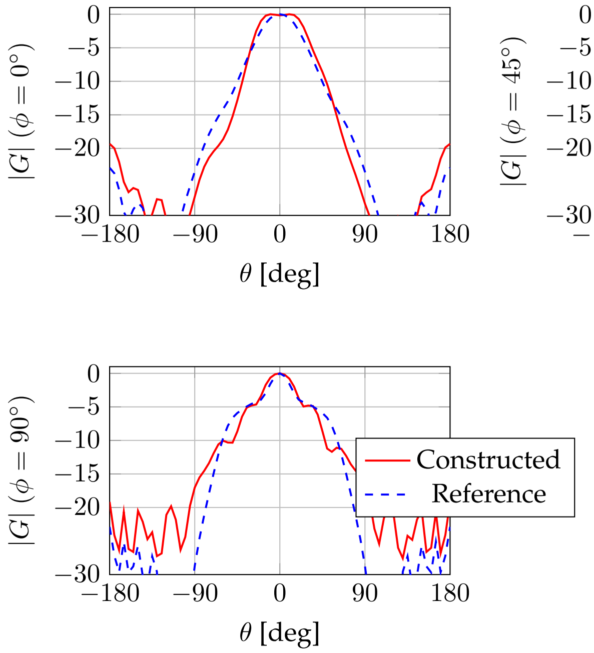

Figure 4.11: The Eleven antenna pattern cuts at 6 GHz, as obtained by simulating the entire antenna structure including the four folded dipoles, descrambling board and the power combining network (shown in fig. 4.7), and by simulating the eight part of the antenna with the following-up procedure for reconstructing the patterns of the other ports (see figs. 4.8 to 4.10).

4.5.1 Simpler Noise characterization models

An ideal hybrid and combiner network, with cryogenic wideband Caltech LNAs with an Eleven antenna can be modelled using a simple model assuming a perfect beam former that can be approximated as a single channel with only one amplifier modelled using the standard *Pospieszalski* model [70] or more accurately using an equivalent system representation [64]. The equivalent model assumes no isolation and reflection losses in the LNAs, hybrids and combiner. The comparison is plotted below in fig. 4.12. The variations between the `CAESAR` and the ideal model are due to approximation of the beam pattern which introduce small errors in the normalisation.

4.5.2 Numerical and experimental results

A single polarization of the Eleven antenna is modelled assuming a 7 K atmospheric contribution and 300 K ground contribution with and a 15^o tree line. The model accounts for; external sky and ground noise sources, ohmic losses in the feed, LNA noise sources, coupling between the dipole elements, reflections between all the beam forming elements including the LNAs. The predicted and measured system noise temperatures are plotted in fig. 4.13. All the measurements were taken at Onsala Space Observatory with the feed placed looking skyward and without a reflector. This setup increases the measured noise as it increases the measured noise temperature compared to a set including the reflector antenna, due to the additional ground noise pick-up component in the directions $\theta = 90$–180^o. Both the

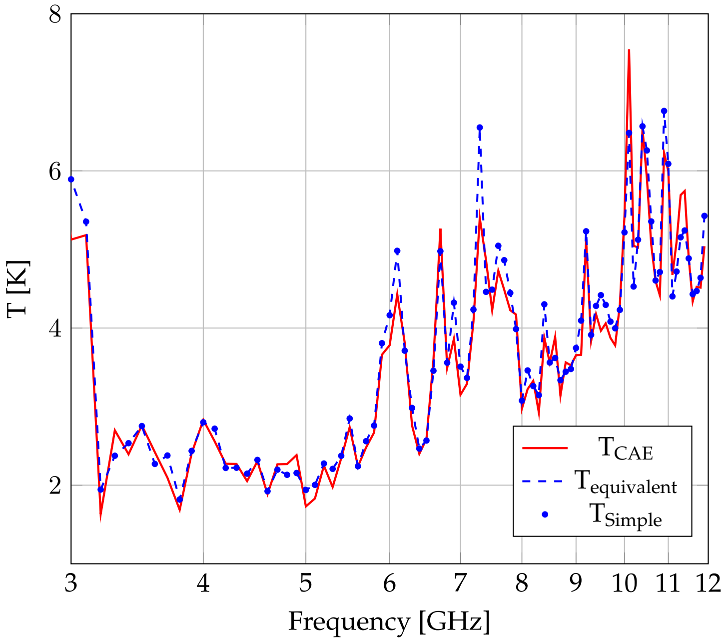

Figure 4.12: Noise temperature contributions due to the LNAs and antenna impedance noise mismatch, as obtained with the complete Eleven antenna receiver model (see fig. 4.7) and two simpler models: *equivalent model* assuming no isolation and reflection losses in the LNAs, hybrids and combiner and *simple model* assuming, additional to the *equivalent model*'s assumptions, identical beam former channels and LNAs.

measured and simulated data are smoothed using a moving average over 200 MHz in order to reduce random measurement noise. The model shows good correlation of ripples within the noise temperature especially at higher frequencies and is clearly closer than the single port model seen in fig. 3.13. The model underestimates the measured noise by 7.3 K averaged across the band, this underestimate is mainly due to using a uniform sky brightness temperature distribution where in reality it increases at the higher end of the band, as can be seen in fig. 4.13. This can be accounted for using a better atmospheric model but here a standard model is preferred. The estimated thermal noise component of the antenna due to the radiation efficiency loss (η_{rad}) is added onto to the `CAESAR` prediction based on measurements done of the Eleven antenna in the spherical near-field test range at DTU (Technical University of Denmark) [67]. Adding η_{rad} post modelling increases the prediction fractionally, η_{rad} is simulated close to 0.9 so the effect is small. The differences seen are considered accounted for or within the noise of the measurement.

4.6 Conclusion

The characterization of low-noise multi-port wideband receiving systems is a challenging problem requiring advanced modelling methods and measurement techniques. A system model has been developed in `CAESAR` incorporating data from `CST` by developing a mathematically general procedure to transform the antenna radiation and impedance characteristics between the `CST` and `CAESAR` software. This method and model has been validated for a simple system of folded dipoles and used with the Eleven antenna. The resonance

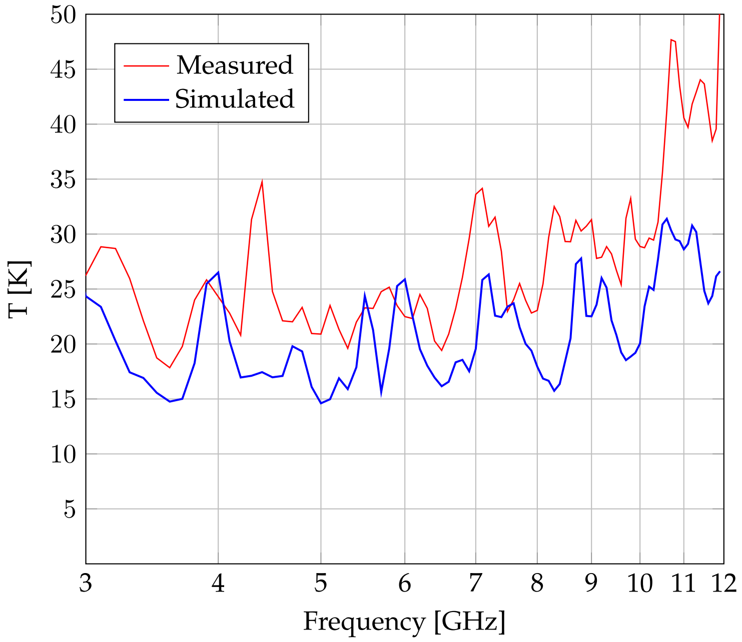

Figure 4.13: Predicted and measured system noise temperatures of the Eleven antenna receiver for one polarization, due to both the external and internal noise sources, including the sky background noise (7 K for $\theta = 0–75^o$), thermal ground noise (300 K for $\theta = 75–180^o$), antenna ohmic loss (at physical temperature of 25 K), noisy LNAs and power combining network.

structure of the system noise temperature reproduces well the measurements performed with the actual UWB LNAs, with differences between the simulations and measurements of 7 K on average over the frequency band. The model works well for predicting the resonance behaviour of the system. Future work on the model is focused on using a more accurate sky temperature distribution and beam patterns, which include the effect of the cooling cryostat's ring (which might produce ground reflections) and radome's window (which adds loss). The problem now is to incorporate this modelling into design and optimisation using commercial solvers, this is tackled in the next two chapters.

Chapter 5

Scripting of FEKO

5.1 Introduction

The integration of noise modelling goals into receiver design is typically tricky given that EM code focuses on antenna fundamentals, typical for industrial applications. Almost all software packages integrate analysis and optimisation for antenna design. This is convenient but limiting, it requires the optimisation variable to be a field within a geometric parameter of the CAD software and using the output parameters as a goal function. For instance aiming for a particular beamwidth, or Γ_{11} matching criteria based on antenna length. For designers the trade off is not always obvious and rules of thumb are typically used. Optimising for a VSWR of better than $2:1$ or an edge taper of -20 dB are typical examples. Noise analysis removes this uncertainty by designing for the exact system sensitivity or performance, allowing greater flexibility in antenna design and ease in setting an optimisation goal. For this we develop software to perform the following:

a) a low level interface with an EM solver, b) build and modify geometries based on a general mathematical description, c) run simulations and optimise based on noise criteria.

The latest version of the code used in this chapter is available here [71].

5.2 Code outline

EM solvers are for the most part carefully designed and relatively simple to use however, no matter how well written they are limited to the functions thought useful by the software engineers who wrote them. In general this is sufficient. The use of an EM's solvers low level interface requires the writing and coding of all the desired user functions, this is time consuming but does allow complete customisation. If done well it does allow reuse and the option to use multiple EM solvers.

The simplest way to use a Descriptive Language (DL) to code the design parameters then create wrapping code, which outputs this description to a readable format for the EM code run the code and then have reading functions to read in the basic files. The process is shown in fig. 5.1.

The chosen descriptive language is `GNU Octave` [72] an open source mathematical and scientific programming language written to be compatible with `MATLAB` code. It is cross

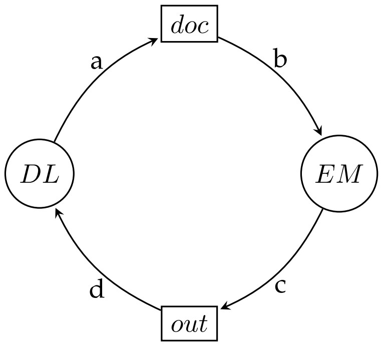

Figure 5.1: Basic software loop, where a) mathematical descriptive language, b) geometrical cards, c) source and field results, d) calculated noise and efficiencies.

platform and allows anyone to run it conveniently.

5.2.1 Incorporating meshing into Octave

Octave easily describes complex objects but it does not have built in meshing functionality critical for EM simulation. This has to be done by the chosen EM code after importing the geometry. Alternatively it can by performed by an external program. GMSH is an excellent option, focused purely on meshing 2 and 3D geometries [21]. It is open source and widely available.

The wrapping tool is written using an object orientated approach. Individual surfaces are described by `@gmshSurf` objects which can then be combined into a larger `@gmsh` object, allowing complex objects to be built up using simple ones. The individual triangles are easily available from `GMSH` and can be used directly in simulating software.

The `@gmshSurf` class definition `@gmshSurf` creates a file for the open source meshing program `GMSH`, the following assumes some knowledge of `GMSH`.

The `@gmshSurf` class creates an object with the following fields:

```
gms.dpath=dpath; % full path and filename /home/user/test.geo
gms.pnts=[];
gms.pntsC={};
gms.pN=0;
gms.pNC=0;
gms.lines=[];
gms.lineloops=[];
gms.surfaces=[];
gms.surfaceloops=[];
gms.volume=[];
gms.physicalline={};
gms.physicalsurface={};
gms.physicalvolume={};
gms.comments=[];
gms.pointINsurfaces=[];
gms.periodicpoints=[];
```

With associated functions:

`addlineloops.m`, `addpntsC.m`, `addsurfaceloops.m`, `addsurfC.m`, `addvolume.m`, `display.m`, `gmshSurf.m`, `rungmshSurf.m`, `translateSurf.m`, `writeComp.m`, `addlines.m`, `addpnts.m`, `addsurfaces.m`, `addsurf.m`, `createsurface.m`, `get.m`, `readmsh.m`, `set.m`, `writeC.m` and `write.m`.

It is simplest to demonstrate the usage through example.

Creating a `@gmshSurf` object

Creating the object:

```
$dpath=[pwd ’′basicobject.geo’]; %linux path stucture
$A=gmshSurf(dpath);
$mshv=0.5; % Set the general mesh resolution for all points
$mshvd=0.25; % Set the mesh resolution for point d
$sqz=2;
$a=[-sqz -sqz 0 mshv];
$b=[-sqz sqz 0 mshv];
$c=[ sqz sqz 0 mshv];
$d=[ sqz -sqz 0 mshvd];
$A=addpnts(A, [a]); % adds 1 point
$A=addpnts(A, [b; c; d]); % add multiple points
$write(A);% write out the object to the .geo file
```

This writes out the following to the `basicobject.geo` file:

```
// Variables
Point(1)={−2,−2,0,0.5};
Point(2)={−2,2,0,0.5};
Point(3)={2,2,0,0.5};
Point(4)={2,−2,0,0.25};
```

Finishing off creating the square:

```
% We now can add some lines
% Available linetypes:  Line, Spline, BSpline, Circle and Ellipse
$ltype=’Line’;
$[A lna]=addlines(A,[1 2],ltype); % line 1
$[A lnb]=addlines(A,[2 3],ltype); % line 2
$[A lnc]=addlines(A,[3 4],ltype); % line 3
$[A lnd]=addlines(A,[4 1],ltype); % line 4
% Now we can create a lineloop out of the lines
$[A lnloopa]=addlineloops(A,[lna lnb lnc lnd]); % lineloop 1
% and a surface from the lineloop
% Available surfacetypes:  Plane, Ruled, Compound and Physical
$stype=’Plane’;
$[A surfa]=addsurfaces(A,lnloopa,stype);
$write(A);
```

The additional code in the `basicobject.geo` file is:

```
// Lines, Splines, BSplines, Circles and Ellipses
Line(1)={1,2};
Line(2)={2,3};
Line(3)={3,4};
Line(4)={4,1};

// Line Loops
Line Loop(1)={1 ,2 ,3 ,4};

// Surfaces
Plane Surface(1)={1};
```

If desired `GMSH` can be run directly, creating the `.msh` file and returning a `meshout` object with fields: `meshout.v` *(Vertices)* `meshout.ed` *(Edges)* and `meshout.tr` *(Triangles)*, as described in the `GMSH` documentation.

```
$meshout=rungmshSurf(A);
```

The final outputed mesh is given in fig. 5.2.

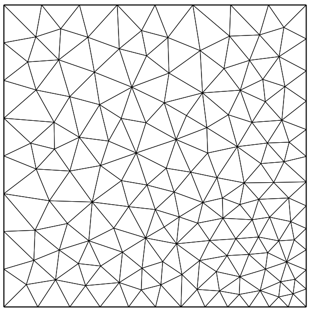

Figure 5.2: Simple meshed square example using `@gmshSurf` and `GMSH`, showing variable meshing for point `d`.

Creating a curved surface This allows complex shapes to be easily created:

```
$A=gmshSurf(dpath);
% Let's create a curved surface y=y0*sin2̂(x/x0) x:  0 -> x0*pi/2
$mshv=0.5; % Set the general mesh resolution for all points
$N=20;
$y0=4;
$x0=5;
$x=linspace(0,x0*pi/2,N);
$y=y0*sin(x/x0).2̂;
$pnts=[x' y' zeros(length(x),1) mshv*ones(length(x),1)];
$A=addpnts(A, pnts);
$endpnt=[x(end) y(1) 0 mshv];
$[A pN]=addpnts(A, endpnt);
$ltype='lines';
$lnum=1;
```

```
$for n=2:pN, A=set(A,ltype,lnum,[n-1 n],'l');lnum=lnum+1; end;
$A=set(A,'lines',lnum,[n 1],'l');lnum=lnum+1; % put in last point
$A=set(A,'lineloops',1:(lnum-1));
$snum=1;
$A=set(A,'surfaces',0,1,'p');snum=snum+1;
$write(A);
$meshout=rungmshSurf(A);
```

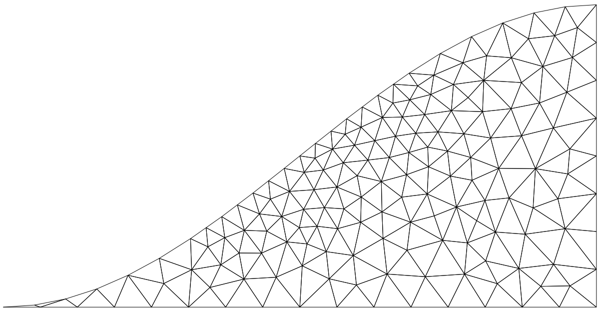

Figure 5.3: Simple meshed curved example using `@gmshSurf` and `GMSH`.

The `@gmsh` class definition The `@gmsh` class allows us combine several `@gmshSurf` objects, the class contains the following fields:

```
Gms.name = name;
Gms.gmsurfs = [];
```

With associated functions:

`addgmsh.m`, `addsurface.m`, `addsurfaceSimp.m`, `display.m`, `get.m`, `set.m`, `displaygmsh.m`, `getgmsh.m`, `getlineloops.m`, `getlines.m`, `getpnts.m`, `getsurfaces.m`, `gmsh.m`, `readmsh.m`, `rungmsh.m`, `setgmsh.m`, `translateGmsh.m`, `writeComp.m` and `write.m`.

Combining `@gmshSurf` objects A simple example combining two gmsh surfaces:

```
$G=gmsh(dpath);
$A=gmshSurf;
$mshv=0.5; % Set the general mesh resolution for all points
$mshvd=0.25; % Set the mesh resolution for point d
$sqz=2;
$a=[-sqz -sqz 0 mshv];
$b=[-sqz sqz 0 mshv];
$c=[ sqz sqz 0 mshv];
$d=[ sqz -sqz 0 mshvd];
$A=addpnts(A, [a; b; c; d]); % add multiple points
$ltype='Line';
$[A lna]=addlines(A,[1 2],ltype); % line 1
$[A lnb]=addlines(A,[2 3],ltype); % line 2
$[A lnc]=addlines(A,[3 4],ltype); % line 3
```

```
$[A lnd]=addlines(A,[4 1],ltype); % line 4
$[A lnloopa]=addlineloops(A,[lna lnb lnc lnd]); % lineloop 1
$stype='Plane';
$[A surfa]=addsurfaces(A,lnloopa,stype);
% Add surfaces A to the larger object
$G=addsurface(G,A);
$B=gmshSurf;
$a=a+[2*sqz 0 0 -mshvd];
$b=b+[2*sqz 0 0 0];
$c=c+[2*sqz 0 0 0];
$d=d+[2*sqz 0 0 mshvd];
$B=addpnts(B, [a; b; c; d]); % add multiple points
$ltype='Line';
$[B lna]=addlines(B,[1 2],ltype); % line 1
$[B lnb]=addlines(B,[2 3],ltype); % line 2
$[B lnc]=addlines(B,[3 4],ltype); % line 3
$[B lnd]=addlines(B,[4 1],ltype); % line 4
$[B lnloopa]=addlineloops(B,[lna lnb lnc lnd]); % lineloop 1
$stype='Plane';
$[B surfa]=addsurfaces(B,lnloopa,stype);
% Add surfaces B to the larger object
$G=addsurface(G,B);
% We can now write out the compisite object
$write(G);
% We can now directly run GMSH
$meshout=rungmsh(G);
```

The combined surfaces are shown in fig. 5.4:

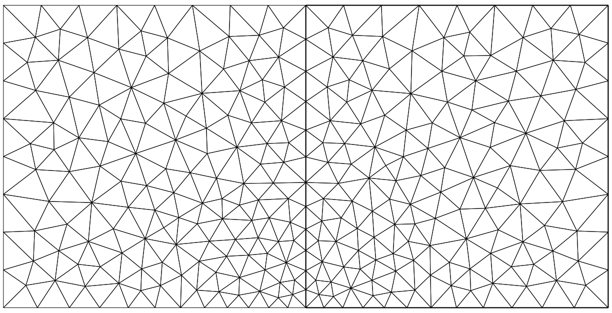

Figure 5.4: Simple meshed combined square example using `@gmsh` and `GMSH`.

5.2.2 Running EM code from Octave

`FEKO` is chosen as the EM software, as it was already available and contains good low level calling functions, specifically `EDITFEKO` [73].

The code as with `GMSH` is written using an object orientated approach to create a `FEKO` class which contains fields of all the available control and geometrical cards associated with

`EDITFEKO`. This allows anyone with a knowledge of `EDITFEKO` to easily be able to use the class. `EDITFEKO` is a card based code where an object is specified with fields arrayed along a line of code separated by colons. This makes it difficult to read and debug complex objects (it has some limited support for programming commands), it however makes it useful from a scripting perspective because it is has a text based input structure with all the geometry objects being described by primitives.

In the class structure each of these primitives or cards is called with a separate function and returns the `EDITFEKO` object, this is easy to read and debug. When its written the wrapping class takes care of all the tricky card based spaces. The code outline is given in fig. 5.5, and the `@WritePreFeko` object contains the following fields:

```
F.filename = [];
F.directory = [];
F.header = []; % comments
F.vars=[]; % define a variable
F.varsA=[]; % define an array
F.IP = []; % meshing parameters options
F.FM= []; % fast solver options (MLFMM)
F.DP=[]; % defines a point
F.ZY=[]; % cylindrical surface
F.KR=[]; % circular surface
F.KK=[]; % conical section
F.AW=[]; % waveport excitation
F.FF=[]; % far field calculation options
F.FE=[]; % near field calculation options
F.OS=[]; % current calculation options
F.SP=[]; % s-parameter calculation options
F.FR=[]; % frequency calculation options
F.PW=[]; % source power options
F.DA=[]; % data out options
F.SY=[]; % symmetry settings
F.BQ=[]; % flat quadrangle surface
F.BP=[]; % flat parallelogram surface
F.PM=[]; % flat polygon surface
F.DZ=[]; % cylindrical shell
F.PH=[]; % quadrangle plate, with circular hole or ellipse
F.TG=[]; % translation, or rotation of triangles
F.BT=[]; % flat triangle shape
F.RM=[]; % set remeshing rules
F.DI=[]; % frequency dependant material options (dielectrics)
F.SF=[]; % scaling of geometrical data
F.LE=[]; % conical section, with varying angles
F.MB=[]; % modal port boundary condition
F.PB=[]; % parabolic reflector
```

With associated functions:

`AW.m`, `BP.m`, `BQ.m`, `BT.m`, `CS.m`, `DA.m`, `DI.m`, `display.m`, `DPA.m` `DPAxyz.m`, `DP.m`, `DZ.m`, `FE.m`, `FF.m`, `FM.m`, `FR.m`, `header.m`, `IP.m`, `KK.m`, `KKxy.m`, `KKxz.m`, `KR.m`, `LA.m`, `LE.m`, `MB.m` `nodes2tri.m`, `notes.m`, `OS.m`, `PB.m`, `PH.m`, `PHsq.m`, `PM.m`, `PW.m`, `read.m`, `RM.m`, `SF.m`, `SP.m`, `SY.m`, `TG.m`, `varsA.m`, `vars.m`, `write.m`, `WritePreFeko.m` and `ZY.m`.

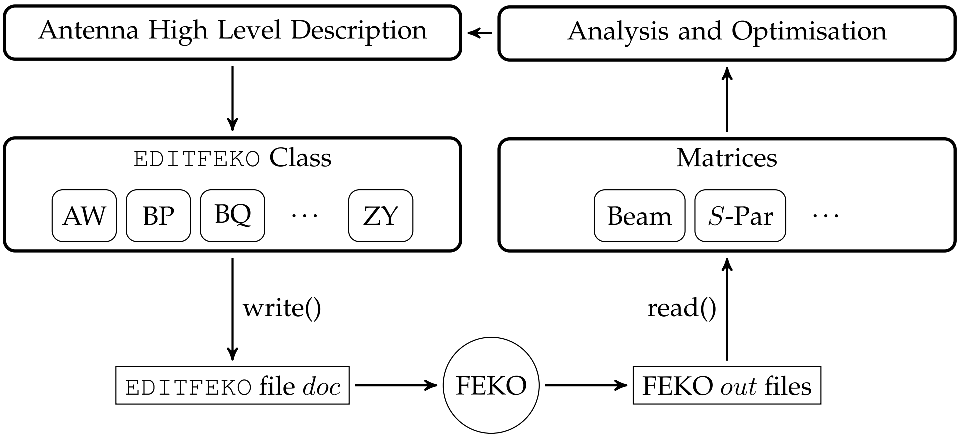

Figure 5.5: GNU Octave class structure

Further details are provided in Appendix C. A simple horn is used to demonstrate the class functionality.

5.2.3 Smooth walled horn example

Let’s start with a simple smooth walled conical horn. The geometry frequency and the simulated requirements are specified in a `Shorn` structure. This makes it natural to script and modify it.

```
% Variables
c0=physical_constant(’speed of light in vacuum’);
rot_ang=360;
lambda=c0/Shorn.freq;

% Create the class object
Cone=WritePreFeko(Shorn.filename, Shorn.directory);
Cone=header(Cone, ’Simple Horn Function’);

% Set the simulated frequency
Cone=FR(Cone,’s’,Shorn.freq);

% Set the meshing rules, as per FEKO requirements
Cone=IP(Cone,[],Shorn.maxTrimesh*lambda,[],[],[]);

% Define points to creates the inner waveguide section
Cone=DP(Cone, ’origin’,0,0,0,[]);
```

```
Cone=DP(Cone, 'Gin_StrtTop',Shorn.Gin_rad*lambda,0,0,[]);
Cone=DP(Cone, 'Gin_EndCent',0,0,Shorn.Gin_len*lambda,[]);
Cone=DP(Cone, 'OrgPforG', 0, 0, 0+1, []);

% Create the waveguide section using the ZY card (Cylinder)
Cone=ZY(Cone,'origin','Gin_EndCent','Gin_StrtTop',rot_ang,...
 Shorn.Gin_msh*lambda,[],0, 'Waveguide');

% Create the waveguide port section using the KR card (Ellipse)
Cone=KR(Cone,'origin','OrgPforG','Gin_StrtTop', [], rot_ang,...
 Shorn.Gin_msh*lambda, Shorn.Gin_msh*lambda,[], 'WGPort');

%Create a waveguide excitation incident on the KR section
Cone=AW(Cone, 'circ','WGport',[], 0, 'origin', 'Gin_StrtTop',...
 'Gin_EndCent',1, 0, 'FUN', 0, [], [], {1 1},[]);

% Remesh just the port
Cone=RM(Cone,'localpoint',Shorn.maxTrimesh*lambda/10,...
 'origin',Shorn.Gin_rad*lambda,1);

% Define points to specify the cone section
Cone=DP(Cone, 's1cone',0,0,...
 (Shorn.Gin_len+Shorn.Conelength)*lambda,[]);
Cone=DP(Cone, 's2cone',0,0,(Shorn.Gin_len)*lambda,[]);
Cone=DP(Cone, 's3cone',Shorn.ConeHeight*lambda,0,...
 (Shorn.Gin_len+Shorn.Conelength)*lambda,[]);
Cone=DP(Cone, 's4cone',Shorn.Gin_rad*lambda,0,...
 (Shorn.Gin_len)*lambda,[]);

% Create the inner waveguide section using the KK card (cone)
Cone=KK(Cone,'s1cone','s2cone','s3cone','s4cone',0,rot_ang,0,...
 rot_ang,Shorn.Gin_msh*lambda,Shorn.Gin_msh*lambda,[],[], 'cone');

% Set the simulation parameters for the far field
Cone=FF(Cone, 'stand', 1,[],'gain', Shorn.numphi,Shorn.numtheta
    ,...
 Shorn.phi0,Shorn.theta0,       Shorn.iphi, Shorn.itheta);

% Set the requested files
Cone = DA(Cone, 'fo', 'fo', 'fo','fo', 's' , 1);

% write the prefeko file
write(Cone);
```

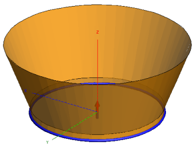

Figure 5.6: Simple horn created by `GNU Octave` and `EDITFEKO`.

5.2.4 Corrugated horn example

`FEKO` is an excellent and powerful commercial EM solver with wide applicability and design options. It is possible with a little effort to produce a satisfactory smooth walled horn. It takes substantial additional effort to produce a corrugated horn. It is perhaps due to the difficulty of producing a corrugated horn that `FEKO` now includes a corrugated horn in the Antenna Magus design toolbox [74]. Scripting this in Octave is much simpler, replacing the single `KK` cone function with a loop.

```
for Cnum = 1:CNUM-1
 % Find the starting and ending X and Z co-ordinates for the
    corrugation.
 % Ct is a vector with the corrugation teeth widths
 xzS = xzE; xzE = [xzS(1)+Ct(Cnum)*sin(alphar(Cnum)) xzS(2)+Ct(
    Cnum)*cos(alphar(Cnum))]; xR = org(1);
 % Create a single label, so do this only for the 1st corrugation
 if(abs(Cnum-1)<tol)
  [ch ind] = KKxz(ch, xzS, xzE, xR, org(2), angV, mshV,ind, ’
     Corrugations’);
 else
  [ch ind] = KKxz(ch, xzS, xzE, xR, org(2), angV, mshV,ind);
 end

 % Cd is a vector of the corrugation left depths
 xzS = xzE; xzE = [xzS(1)+Cd(Cnum)*cos(alphar(Cnum)) xzS(2)-Cd(
    Cnum)*sin(alphar(Cnum))]; xR = org(1);
 [ch ind] = KKxz(ch, xzS, xzE, xR, org(2), angV, mshV,ind);

 % Cw is a vector of the corrugation widths
 xzS = xzE; xzE =[xzS(1)+Cw(Cnum)*sin(alphar(Cnum)) xzS(2)+Cw(Cnum
    )*cos(alphar(Cnum))]; xR = org(1);
 [ch ind] = KKxz(ch, xzS, xzE, xR, org(2), angV, mshV,ind);

 % Cdd is a vector of the corrugation right depths
 xzS = xzE; xzE =[xzS(1)-Cdd(Cnum)*cos(alphar(Cnum)) xzS(2)+Cdd(
    Cnum)*sin(alphar(Cnum))]; xR = org(1);
 [ch ind] = KKxz(ch, xzS, xzE, xR, org(2), angV, mshV,ind);
 if (Lmax-xzE(2))<tol, msg = [’Maximium length reached after ’
    num2str(Cnum) ’ Corrugations’]; disp(msg); break; end
end
```

Where the horn is specified in terms of a series of vectors where the corrugations are specified using; w for width, d for depth (back), df for depth (front) and t for tooth width, as shown in fig. 5.7.

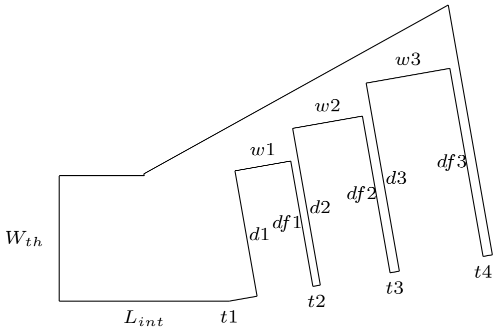

Figure 5.7: Cross section of a simple linear horn.

Arranging the code in this manner any horn can quickly and easily be produced, for example consider the design of a dual mode horn shown in fig. 5.8. Produced by changing the vector properties.

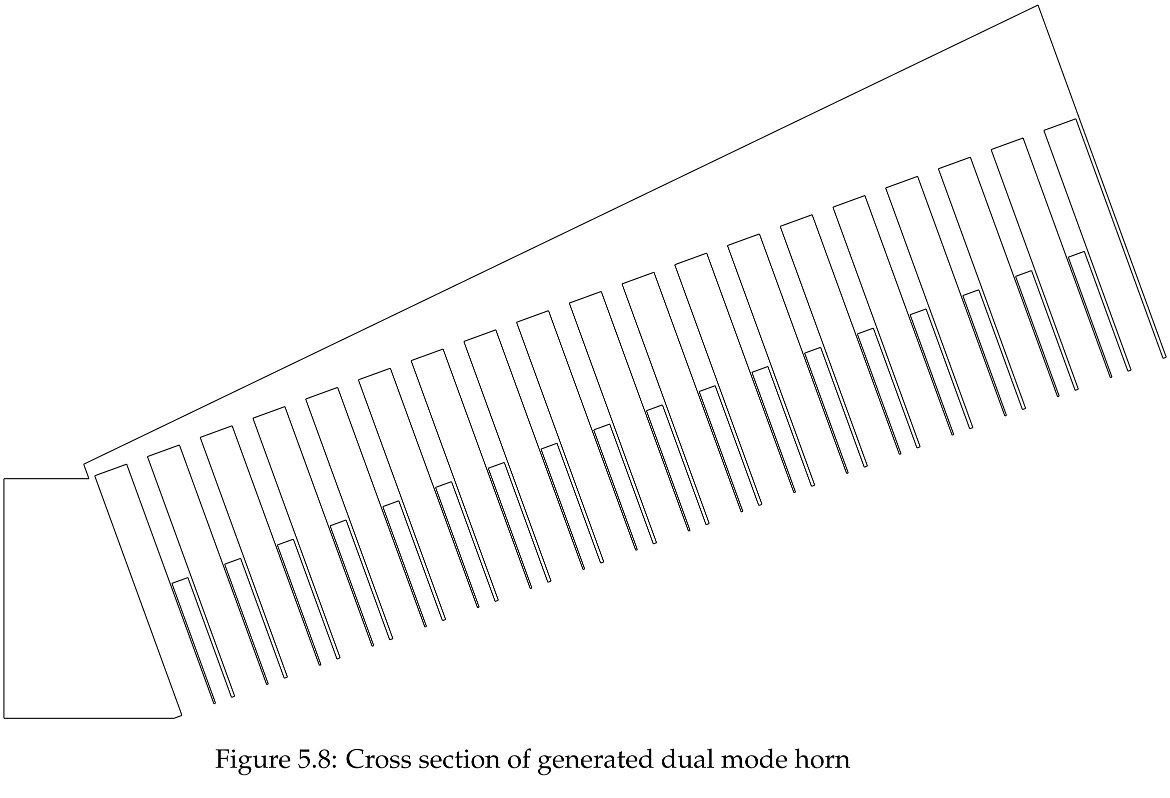

Figure 5.8: Cross section of generated dual mode horn

Or a logarithmic horn shown in fig. 5.9, where all the vectors are spaced logarithmically across standarad corrugated octave band horn. A truncated version built in `FEKO` is shown fig. 5.10.

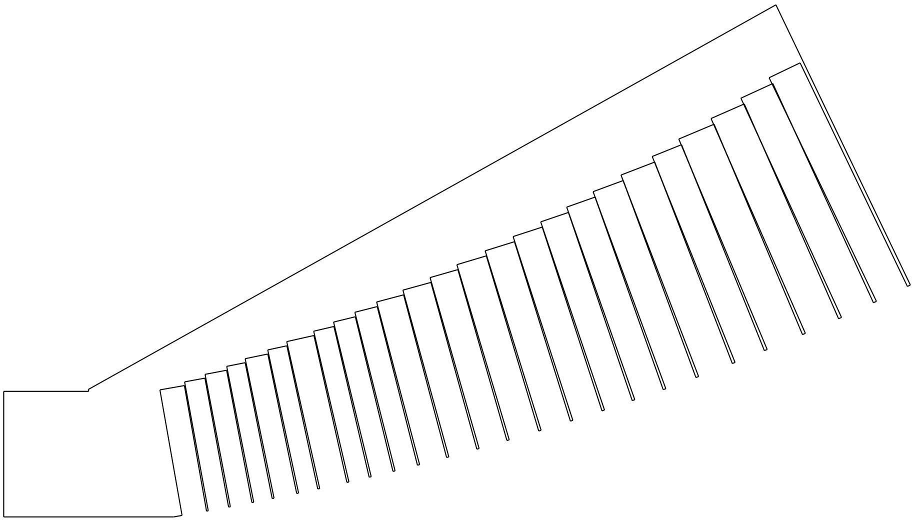

Figure 5.9: Cross section of generated logarithmic horn.

5.2.5 Exporting `GMSH` geometries into `FEKO`

If the antenna is specified in `gmsh` it is now possible to import the mesh directly into `FEKO` using the `@WritePreFeko` class. It is a simple matter of reading in the mesh and writing it into `EDITFEKO` as series of triangles. This allows us to create curved edges and surfaces without having to use `EDITFEKO` cards. A simple example is to take the curved surface shown in fig. 5.3 and import it into `FEKO`. Following directly from the example in section 5.2.1.

```
% First we get the nodes out of the mesh
                $nodes=readmsh(A,’mesh’);

% Create the @WritePreFeko object to write to
                $filename=[ ’curvedobjectimport.pre’];
                $C=WritePreFeko(filename, [CurrentDirectory ’/
                   geofiles/’]);
                $C=header(C, ’Testing gmsh to feko’);
                $C=notes(C, ’Testing of gmsh to feko’);

% Convert the nodes to triangles, and add them to the FEKO object
                $C=nodes2tri(C,nodes,’test’,1,’PEC’);
                $C=IP(C,[],1,[],[],[]);

% Write out the file
                $write(C);
```

The final curve is shown in fig. 5.11 identical to the Gmsh version in fig. 5.3.

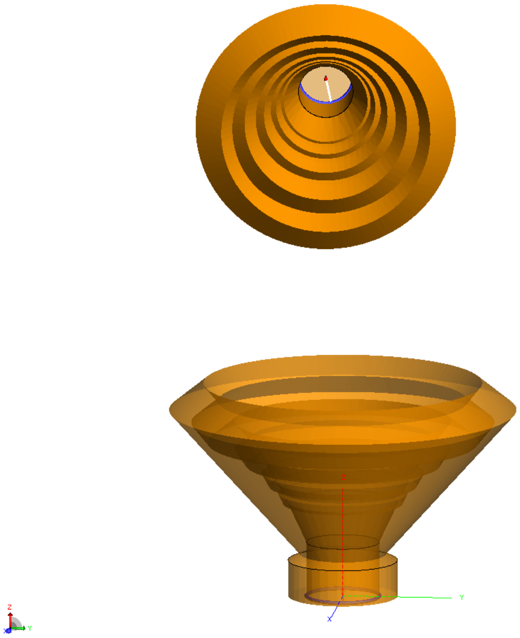

Figure 5.10: Logarithmic corrugated horn, side and front views.

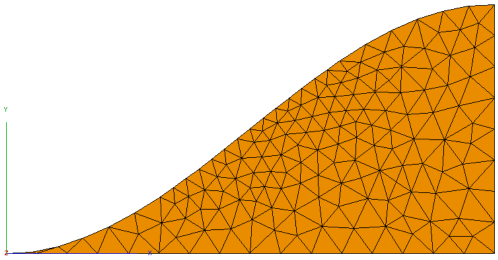

Figure 5.11: Imported curved surface.

5.3 Optimisation

The combination of `GNU Octave` and `GMSH` allows complex shapes to be created from primitive elements within `FEKO`. This flexibility means it is possible to build antennas based on any descriptive parameter. The EM solver can be run using text based commands issued by Octave and the solutions written to external files which can be easily read using standard `IO` libraries [75].

It is now possible to implement a custom optimisation with the system sensitivity linked to noise modelling. The implemented process for a single antenna with a simple feeding system is shown in fig. 5.12. Where:

Hi Horn and excitation description.

Oc Octave build, control and optimisation code.

Fi FEKO input files (`.pre`).

Fe FEKO.

Fo FEKO output files (`.ffe .sNp`).

Op Optimisation routines, can be within FEKO or Octave.

Re Reflector geometry, environmental variables and amplifier parameters.

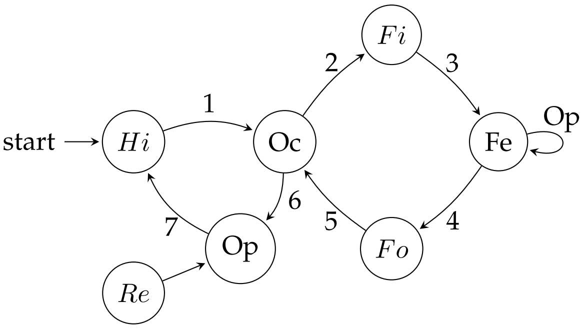

Figure 5.12: Design and optimisation code structure.

The procedure referring to fig. 5.12 is:

1. script the horn description with relevant variables for optimisation.
2. create a `.pre` file FEKO to run.
3. pass this to FEKO to run and locally optimise if required.
4. write out the relevant far field and S–parameter files.
5. read these into Octave.
6. solve the cost function for the specific input parameters.
7. based on an optimisation function modify the horn variables.

This method gives the user much more control by separating out the horn description and cost function to Octave and the EM modelling to `FEKO`. The optimisation routines in `FEKO` are still available along with any other routines the user wishes to run.

5.3.1 Simple system test

In order to test the code a simple narrow band single polarised receiver system is used, the advantage is that this does not need large amounts of simulation time and is quickly verified. The system is a $3\,\mathrm{m}$ dish that required a feed to image the Hydrogen Line at $1420\,\mathrm{MHz}$ for a physics laboratory. Choke horns with flat corrugations have been shown to be a good choice for shallow parabolic dishes ($F/D < 0.35$). Starting with the suggested design by *Wohlleben*, *Mattes* and *Lochner* [76] shown in fig. 5.13. The scripting of the design process allows for much greater freedom in the optimisation, as the antenna is free to be designed across almost any parameter. This however is not the focus of the research here and rather the setting up of the goal function and the modelling of the entire system is researched, rather than the specific optimisation routine to use a few key parameters are chosen and a simple gradient based search chosen. It should be noted that the goal here is not to verify the design of an antenna or the simulation tools, but to show that the simulation tools can be run and optimised by octave.

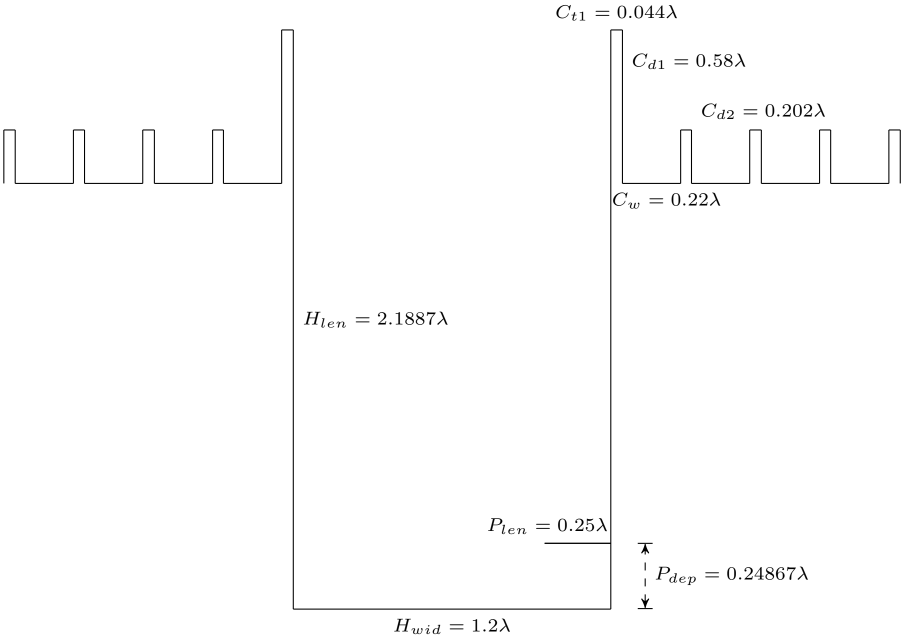

Figure 5.13: Cross section of standard choke horn design.

The ambient noise amplifier *ZX60-P162LN+* from Mini-Circuits is chosen with a noise figure of $0.5\,\mathrm{dB}$ [77]. The noise matching is not available for this model but given the sensitivity not critical to model, instead a simple single channel model is sufficient. The cost function is the final system sensitivity A/T, based on the aperture efficiency calculated from the dish and simulated beam parameters. Given that the system is ambient the noise figure is sufficient to simulate the system temperature T. The amplifier noise temperate spill over efficiency and known connector ohmic losses are summed. The matching criteria is solved by optimising the S_{11} a second time over the length the excitation stub.

Results A cross section of the simulated horns are plotted in fig. 5.14, demonstrating the progression of the optimisation.

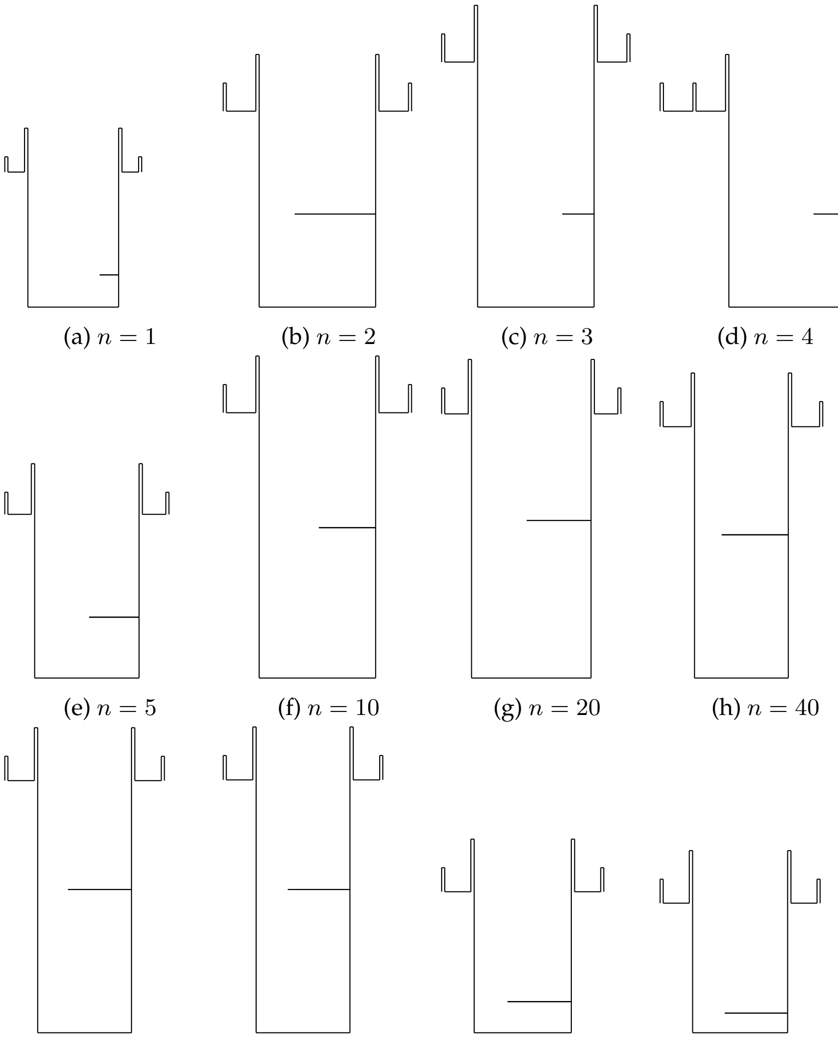

(a) $n = 1$ (b) $n = 2$ (c) $n = 3$ (d) $n = 4$

(e) $n = 5$ (f) $n = 10$ (g) $n = 20$ (h) $n = 40$

(i) $n = 80$ (j) $n = 100$ (k) $n = 120$ (l) $n = 136$

Figure 5.14: Selection of iterated simple choke horn sections.

The convergence of the first optimisation loop is shown in fig. 5.15, the individual components are shown in fig. 5.16a and fig. 5.16b. The second optimisation loop, focusing on improving the S_{11} matching is shown in fig. 5.16c.

Final design The final optimised design is shown in fig. 5.17.

The final optimised beam pattern along with the measured beam with the standard design for comparison is shown in fig. 5.18. The original horn's performance is only slightly changed as it is an optimised design. The back lobes in the single corrugations as is expected are higher but still below -10 dB and not significant to the system performance. The optimised design is simpler requiring only a single corrugation and has lower side lobes corresponding to a reduced brightness temperature. The measured beam is $\approx 10°$ wider than the simulated beam at the $-10\,\mathrm{dB}$ point. This is within expected tolerances given measurement and rough construction accuracies of the prototype.

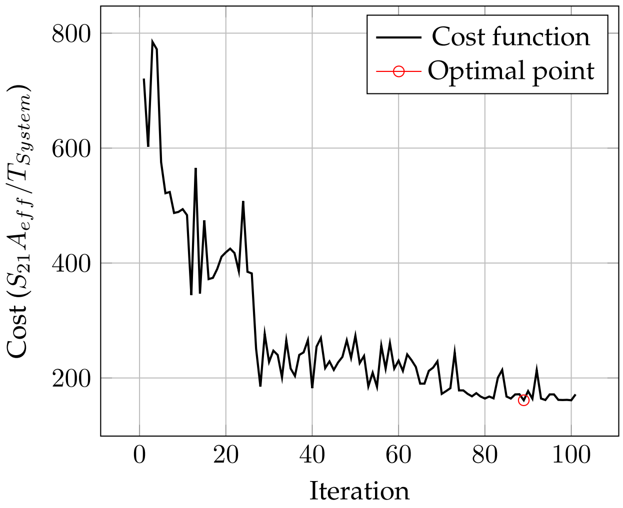

Figure 5.15: Convergence of `fminsearch()` function for a simple choke horn.

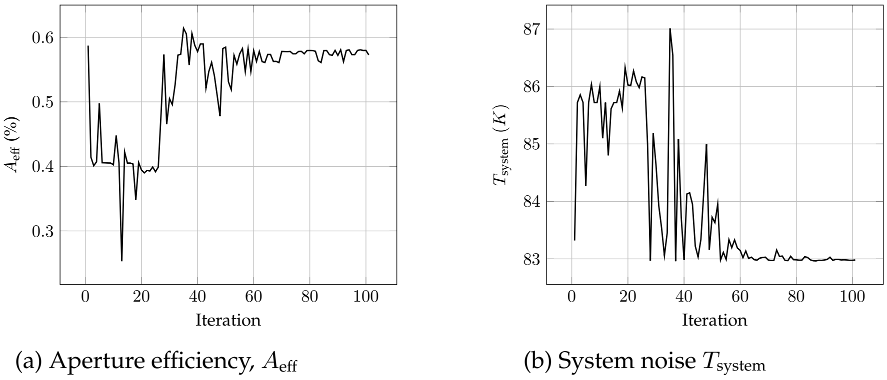

(a) Aperture efficiency, A_{eff}

(b) System noise T_{system}

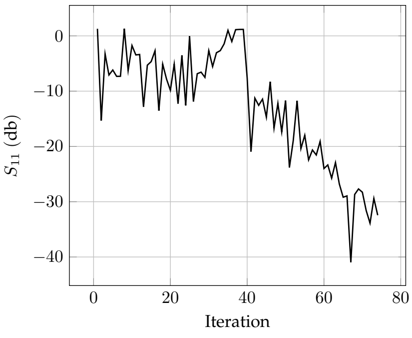

(c) System matching, S_{11}

Figure 5.16: Components of the used `fminsearch()` cost function.

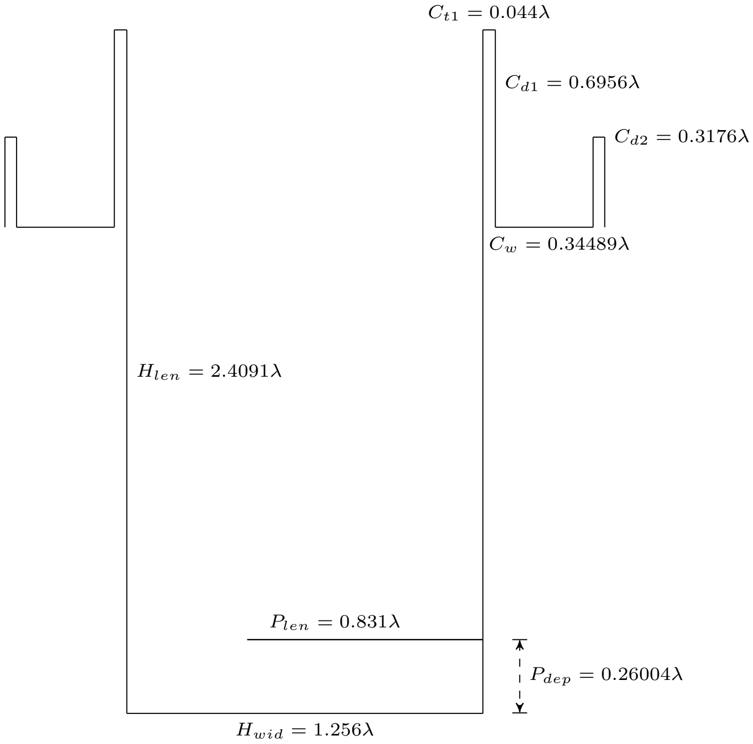

Figure 5.17: Final optimised corrugated horn.

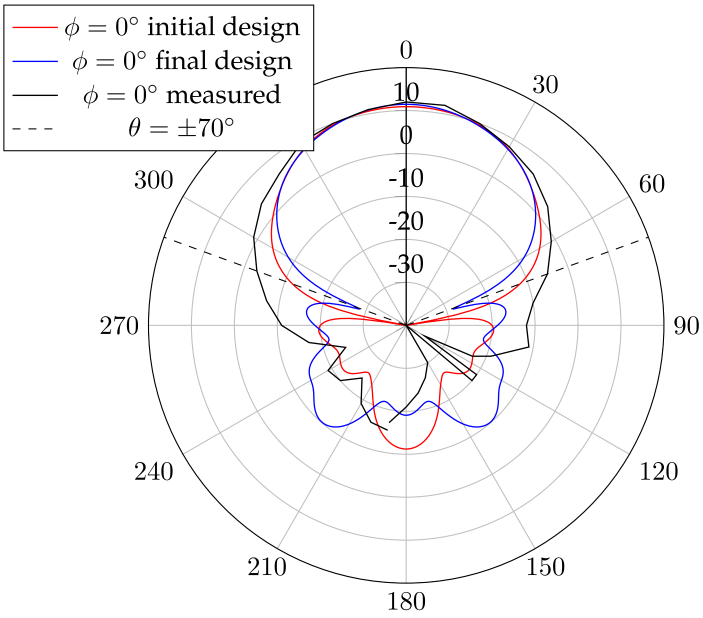

Figure 5.18: Theta cuts of the original choke horn, final design and measured horn ($\phi = 0°$).

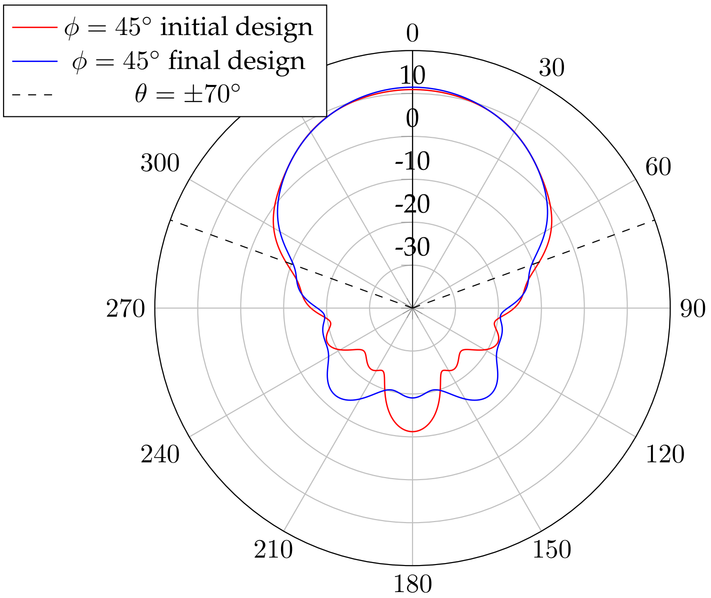

Figure 5.19: Theta cuts of initial and final designs ($\phi = 45°$).

5.3.2 System wide optimisation

For more complex designs with orthogonal and wideband feeding it is required to simulate the system components separately and combine later. A total system optimisation routine is given below in fig. 5.20. It is now possible to use multiple different specialised programs to produce a single optimisation routine and final design. A component based method can still be used as an initial point for the optimisation.

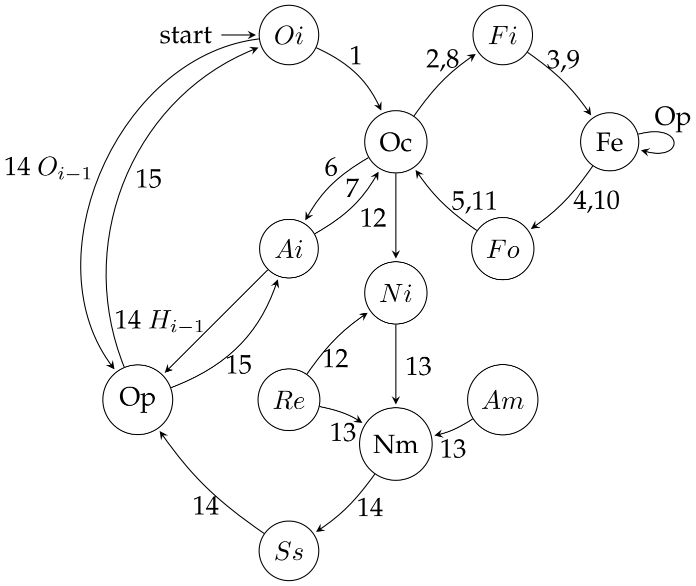

Figure 5.20: Complex system design and optimisation code structure.

Where:

Oi Orthogonal feeding section.

Ai Antenna geometry.

Oc Octave build, control and optimisation code.

Fi FEKO input files (`.pre`).

Fe FEKO.

Fo FEKO output files (`.ffe .sNp`).

Re Reflector geometry and environmental variables.

Am Amplifier noise and S–parameters.

Nm Noise modelling software.

Ni Noise input.

Ss Predicted total system sensitivity.

Op Optimisation routines, can be within FEKO or Octave.

Referring to fig. 5.20 the software now runs as follows:

1. script the feeding description, with relevant variables for optimisation.
2. create a `.pre` file FEKO to run.
3. pass this to FEKO to run, and locally optimise if required.
4. write out the relevant S–parameter files, and mode or voltage excitations.
5. read these into Octave.
6. write the excitation into the antenna description, such that it is this excitation that is simulated.
7. pass this as an object to Octave for scripting.
8. create a `.pre` file FEKO to run.
9. pass this to FEKO to run, and locally optimise if required.
10. write out the relevant S–parameter and far field files.
11. read these into Octave.
12. pass the relevant information for noise modelling, combined with the environmental data.
13. combine the amplifier, antenna and environmental data.
14. run the optimisation and derive the modify the feeding and antenna parameters.
15. update the model parameters ready for the next iteration.

This scheme is beyond just incorporating noise parameters into the optimisation, it is possible to perform full system design as required.

5.4 Conclusion

It is been demonstrated that complex structures can be built up from primitive elements and imported into an EM solver. This is applied successfully to a choke horn based on an existing reflector geometry, and optimised based on a simple noise model for the goal function. The next chapter looks at a more typical design.

Chapter 6

System Design

6.1 Introduction

In chapter 5 the principles of the design approach have been solved but there are still problems to solve for more complex receivers. We now look at a practical wideband design. This crucially relies on the ability to separate out components and simulate them separately, this is first verified and then a real world system is considered.

Given time and resource limitations the final design is left to future work. This means that the final optimisation loop could not be implemented but rather the initial design, local optimisation and incorporating of certain components is presented.

Wideband microwave receiver systems are in generally complex and difficult to simulate and global optimisation impossible. Instead separate optimisation of components of the system is done and matched, for example the antenna is optimised for the correct beam pattern given a certain input impedance and excitation. Practically this is a good approach and is taken as a first step here. By altering the simulation approach slightly and goal functions it is possible to take further steps to tune the optimisation to be more sensitive to noise considerations. First we will verify this approach and then apply it to a practical corrugated horn design.

6.2 Approach and verification

The feeding system in fig. 6.1a is modelled as the S–matrix S such that the input and output voltage amplitude vectors, $\mathbf{v}_a$ and $\mathbf{v}_b$ are related by $\mathbf{v}_b = \mathsf{S}\mathbf{v}_a$. The voltages here are the field strength imposed and reflected in $[V/m]$ across the waveguide, the associated currents $\mathbf{i}$ are given in $[A/m]$ and are related by the mode impedances Z. Useful as TE and TM modes are imposed differently in our simulations. The horn is modelled as a series of beam patterns associated with the modes. So the final beam $\boldsymbol{f} = \sum \boldsymbol{f}_k^{\mathrm{b}}$. This requires simulating the antenna with a pure mode for every significant mode, but this only needs to be done once after which the effect of changes in the feeding section are immediately calculable. The weightings for each of the modes is calculated from the power within the modes. The

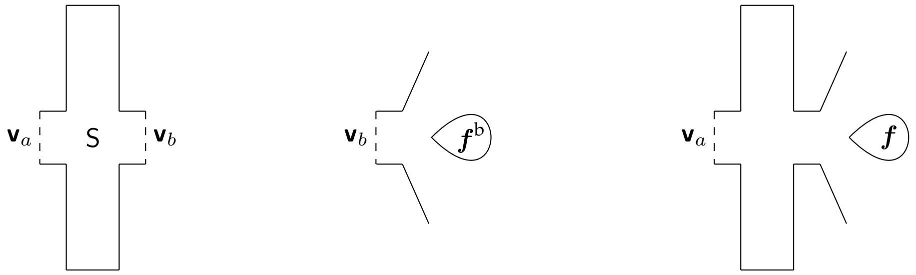

(a) (b) (c)

Figure 6.1: Verification of the approach of breaking up the designed receiver, into a feeding section (a) and horn section (b), with the complete simulation (c).

power in each circular waveguide mode is given by [78, 79]:

$$P_{TE_{mn}} = \pi a^4 \frac{\epsilon_{0m}}{4} k\beta \left[\frac{J_m(p'_{mn})}{p'_{mn}}\right]^2 \left(1 - \frac{m^2}{p'_{mn}}\right) \eta |H|^2 \tag{6.1}$$

$$P_{TM_{mn}} = \pi a^4 \frac{\epsilon_{0m}}{4} k\beta \left[\frac{J'_m(p_{mn})}{p_{mn}}\right]^2 \frac{|E|^2}{\eta} \tag{6.2}$$

Where:

k $= 2\pi f$
a $=$ waveguide radius
p_{mn} $=$ the mth root of the J_n function
p'_{mn} $=$ the mth root of the J'_n function
kc $= \frac{p'_{mn}}{a}$ for TE modes and $\frac{p_{mn}}{a}$ for TM
β $= \sqrt{k^2 - kc^2}$
H $=$ magnetic field strength in $[\mathrm{A/m}]$
E $=$ electric field strength in $[\mathrm{V/m}]$
η $= \sqrt{\frac{\mu}{\epsilon}}$ intrinsic impedance
ϵ_{0m} $= 2$, for $m = 0$ else 1

The power into the converter can be calculated by summing up the power in the input modes given by eqs. (6.1) and (6.2), where E and H fields are associated with $\mathbf{v}_a$ and $\mathbf{i}_a$ respectively. The power transferred to each mode is related by the S matrix. The coefficients of the S matrix relate the voltage waves so the relationship to the power is given by $|\mathrm{S}|^2$. The basic assumption in this method is that the beam pattern is separable into a linear combination of modal beam patterns. This is seems obviously true following directly from the fact that modes are orthogonal, but it is worth checking. It is noted that even for normal antenna simulations, splitting the beam is useful to better take advantage of magnetic and electric symmetries in the simpler mode patterns.

Truncating the horn to a single corrugation and simulating with three cases: i. TE_{11}, ii. $TM_{11}\angle 90°$, and iii. HE_{11}. The weighting is for the TE mode is $1\,\mathrm{A\,m^{-1}}$ and $1\,\mathrm{V\,m^{-1}}$ for the TM mode. The plots of the simulated and later calculated by summing the directivity patterns is plotted in fig. 6.2a. The approach is clearly valid, the error in the directivity is within $0.01\,\mathrm{dB}$.

This approach also allows us to simulate a single horn and by scaling the input modes, dependent on a variation in the TE to HE transition predict the directivity pattern, without

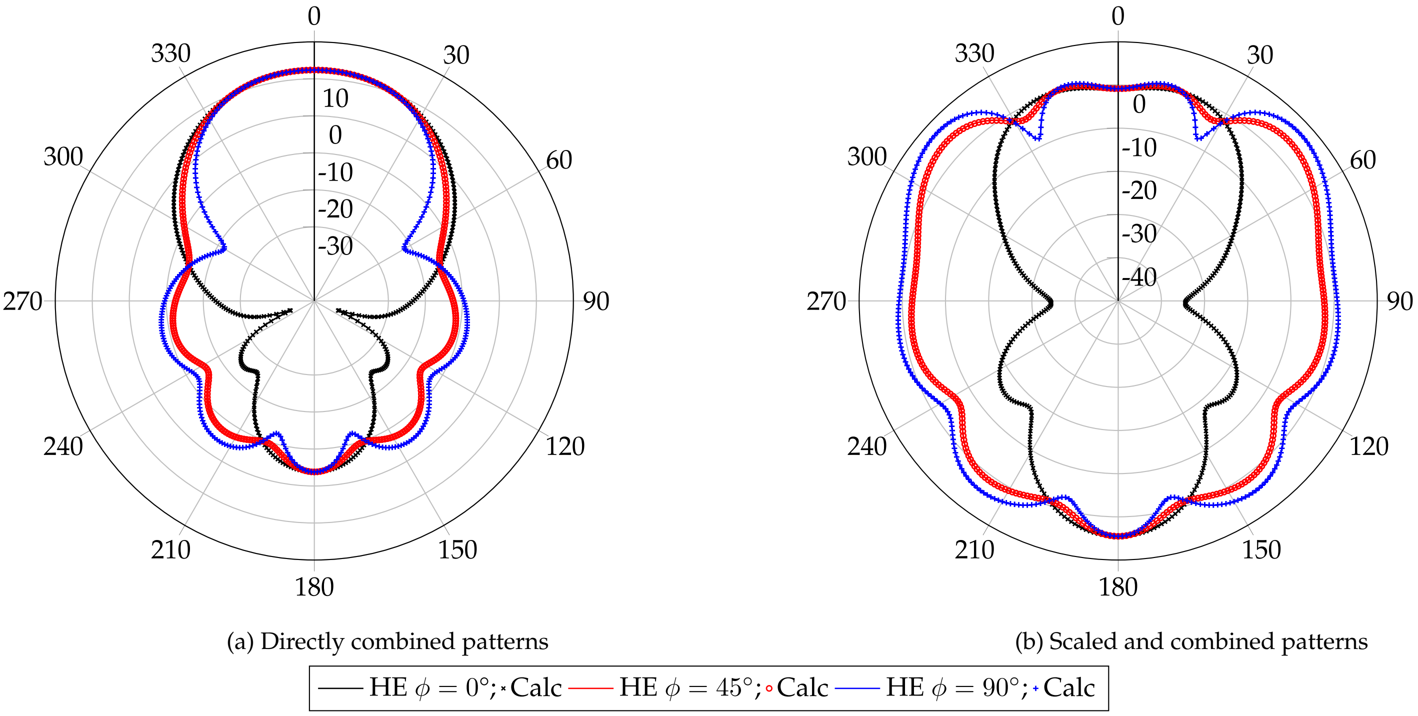

(a) Directly combined patterns

(b) Scaled and combined patterns

Figure 6.2: Comparisons between simulated and calculated directivity patterns for a simple truncated horn for a scaled HE mode.

having to run the larger more complex simulation. A more complex case, where we have scaled the weightings is plotted in fig. 6.2b. It is also within $0.01\,\mathrm{dB}$.

Considering a single reflection in well matched systems ($\mathrm{S}_{11} < -10\,\mathrm{dB}$) this assumption is sufficient. The power then into each mode is given by:

$$P_{bi} = \sum_{j}^{N} P(v_{aij}) |S_{ij}|^2 \angle S_{ij} \tag{6.3}$$

The voltage or current of the excited mode is then calculated from this power. The matching criteria assures that any reflected power sums to less than $-20\,\mathrm{dB}$ of the beam sum. If this is insufficient the sum can be modified to:

$$P_{bi} = \sum_{j}^{N} P(v_{aij}) \left(|S_{ij}|^2 \angle S_{ij} + |S_{ij} S_{ji} S_{ii}^2|^2 \angle S_{ij} S_{ji} S_{ii}^2 \right) \tag{6.4}$$

Which can be expanded indefinitely, it is noted that an exact solution is available [80] but for our purposes is considered overly complex to implement. A simple example is useful to test and verify this approach using a small simplistic example, a single corrugation and a simple horn are simulated together and separately, the later and former beam patterns are compared. We simulate with a single TE_{11} mode such that $\boldsymbol{v}_a = [0\ 0\ 1\ 0\ \cdots\ 0]$. The two most significant modes are the $TM_{11\angle 90°}$ and TE_{11}. The patterns for these modes are simulated the unaccounted modes introduce a small error, but we can calculated exactly the effect by considering the amount of power in the modes not considered.

Considering a circular waveguide corrugation with an input radius of $0.65\,\lambda$, to allow for the TE_{11} mode to propagate. The input power, per A/m is then calculated as $434.11\ mW$, and $S_{TE_{11}} = -20\,\mathrm{dB}$, as required. The power transferred directly to the TE_{11} mode is now calculated. $S_{TE_{21}} = -0.91\,\mathrm{dB}\angle{-110.34}°$ so using eq. (6.3) we calculated the power in the output mode $P_{bTE_{11}} = 351.91\,\mathrm{mW}\angle{-110.34}°$. Given an output radius of $0.667\,\lambda$, the associated current $\mathrm{i}_{TE_{11}} = 0.9\,\mathrm{A\,m^{-1}}\angle{-110.34}°$. For the next most important mode $TM_{11\angle 90°}$, $S_{TM_{21}} = -0.317$ dB$\angle{-86.469}°$, so using eq. (6.3) we calculated the power in the output mode $P_{bTM_{11}} = 43.609\,\mathrm{mW}\angle{-86.469}°$. Given an output radius of $0.667\,\lambda$ the associated current $\mathrm{i}_{TM_{11}} = 454.45\,\mathrm{V\,m^{-1}}\angle{-86.469}°$. Given that the simulation is lossless the power accounted for is $\approx 91\,\%$. The simulations in fig. 6.3 show good agreement which can be improved by including more modes, given this increases the number of required simulations it should only be done if required for the resolution of the noise calculation.

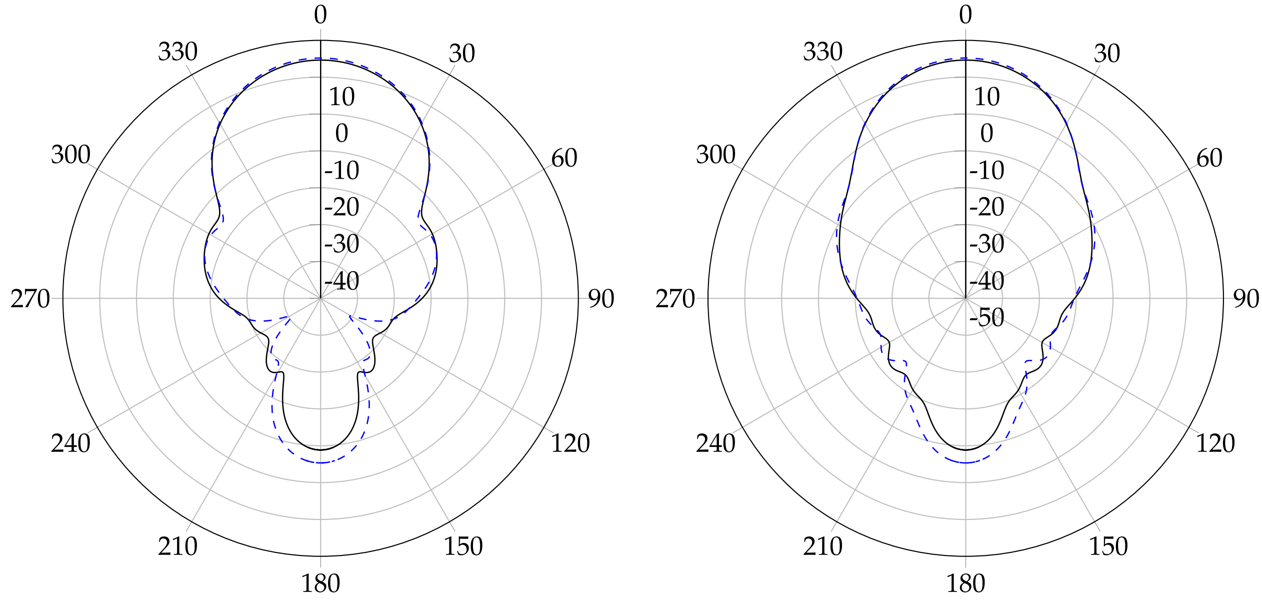

(a) $\phi = 0^\circ$

(b) $\phi = 15^\circ$

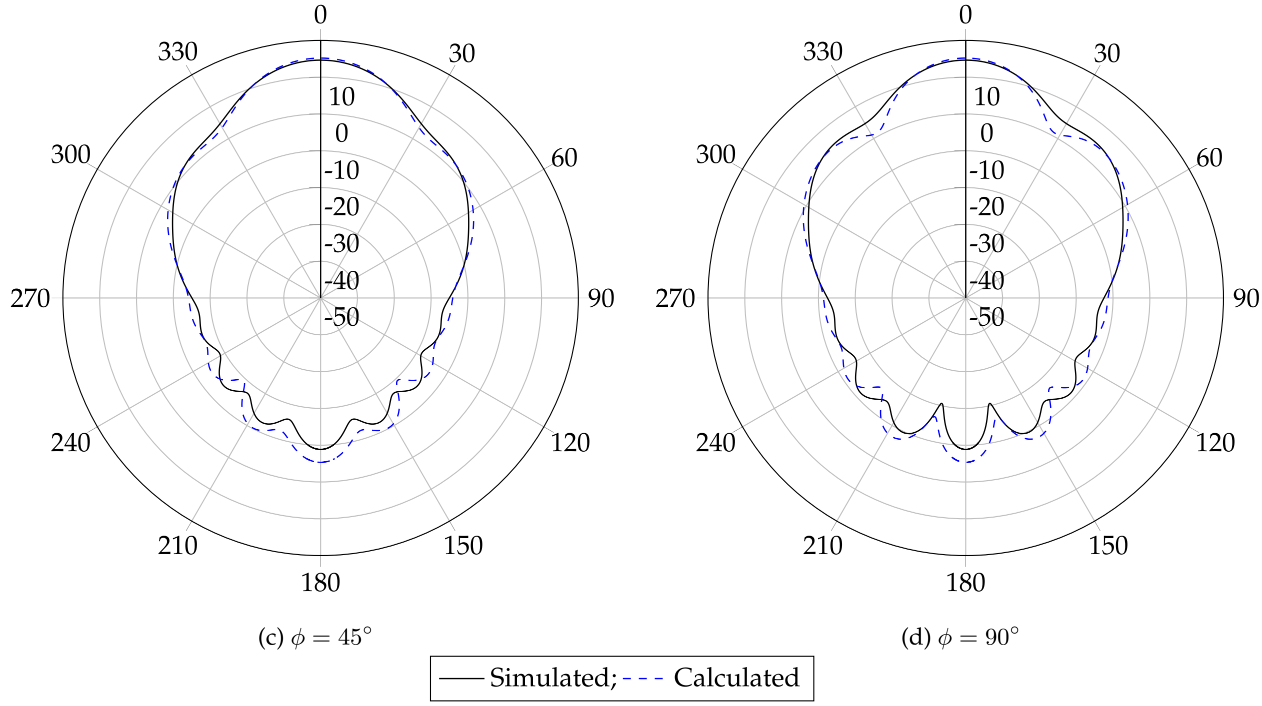

(c) $\phi = 45^\circ$

(d) $\phi = 90^\circ$

Figure 6.3: Comparisons between simulated and calculated directivity patterns for a simple truncated horn for scaled TE and TM modes.

6.3 Practical wideband system

The HartRAO observatory is currently upgrading their receiver systems on their $26\,\mathrm{m}$ cassegrain reflector. The objective is replace several narrow band Potter Horns (around $10\,\%$) receivers with wider band systems $(2:1)$. This allows the use of wider band lower noise LNAs without the need for isolators, increases simultaneous observing, frees up space on the antenna for higher frequency receivers and reduces running costs (fewer Cryogenic packages). The following section details the initial design, simulations and optimisation. The current status and future work is discussed.

6.3.1 System specifications and chosen design

Given the optics of the dish at this stage are being kept the same, the existing Potter Horn receivers give the initial design specification:

a) frequency range of $4.5\,\mathrm{GHz}$ to $9\,\mathrm{GHz}$. b) Dual Polarization ($< -20\,\mathrm{dB}$ isolation, typical $-30\,\mathrm{dB}$) c) Feed illumination angle $13.771°$, $-20\,\mathrm{dB}$ edge taper. d) $S_{11} < -10\,\mathrm{dB}$, typical $-15\,\mathrm{dB}$. e) Optimised for system sensitivity [A/T].

The design presents numerous problems for system wide optimisation, the main limiting factor is the computationally intensive simulations required for implementing the goal function. The existing reflector geometry is given in fig. 6.4.

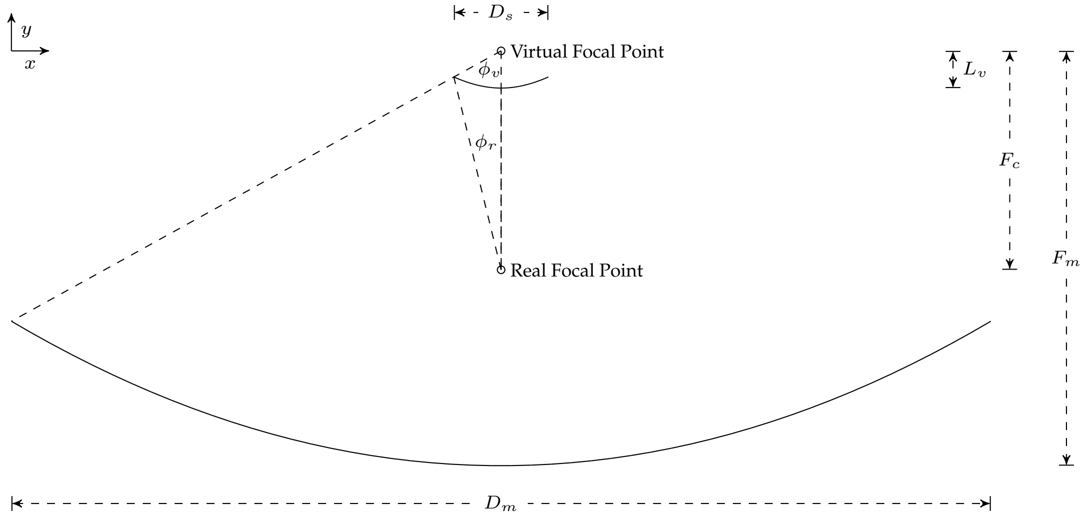

Figure 6.4: Cross section of the HartRAO's $26\,\mathrm{m}$ telescope's geometry.

Where, for HartRAO:

D_m = Diameter of the main reflector $(25.9\,\mathrm{m})$
D_s = Diameter of the subreflector $(2.5\,\mathrm{m})$
L_v = Height from centre of subreflector to Virtual Focal Point $(0.984\,\mathrm{m})$
F_m = Height from centre of main reflector to Virtual Focal Point $(10.973\,\mathrm{m})$
F_c = Distance between Real and Virtual Focal Points $(5.791\,\mathrm{m})$
ϕ_r = Illumination angle for feed $(13.771°)$
ϕ_v = Illumination angle for the main reflector $(61.089°)$

Cassegrain systems can be simplified by using the concept of a virtual feed and deriving an equivalent parabola with illumination angle ϕ_r [81]:

$$F_e = F_m \frac{F_c - L_v}{L_v} \tag{6.5}$$

$$\phi_r = 2 \arctan \left(\frac{D_m}{4F_e} \right) \tag{6.6}$$

Assuming the antenna is pointed at zenith, and using a ray tracing approach the brightness distribution can be simplified for the noise modelling. The beam sees the sky at zenith for angles to the edge of the subreflector, sky to the horizon for angles greater than this to $90°$ and the ground for angles greater than this. The chosen antenna is a corrugated horn. Corrugated horns have: high bandwidth (3:1), high gain, low peak cross polarisation and low sidelobes [82], making them a common choice for Radio Telescope applications [83, 84], and a satisfy the requirement to replace the narrower band Potter horns. A good initial horn can be found using design curves. First the feeding system is considered.

6.3.2 Orthomode transducer

The horn requires dual polarized feeding and consequently is excited by an Orthomode Transducer (OMT), which converts the dual circular from the horn to dual linear. Quadruple Ridged Waveguides [85] have a sufficiently wide bandwidth, and have been used for similar designs. Several variations are given in the literature, eg. *Coutts* or *de Villiers*, *Meyer* and *Palmer* [86, 87]. The simpler design of *Skinner* and *James* is chosen [88] as the starting point. A cut of the design is shown in fig. 6.5.

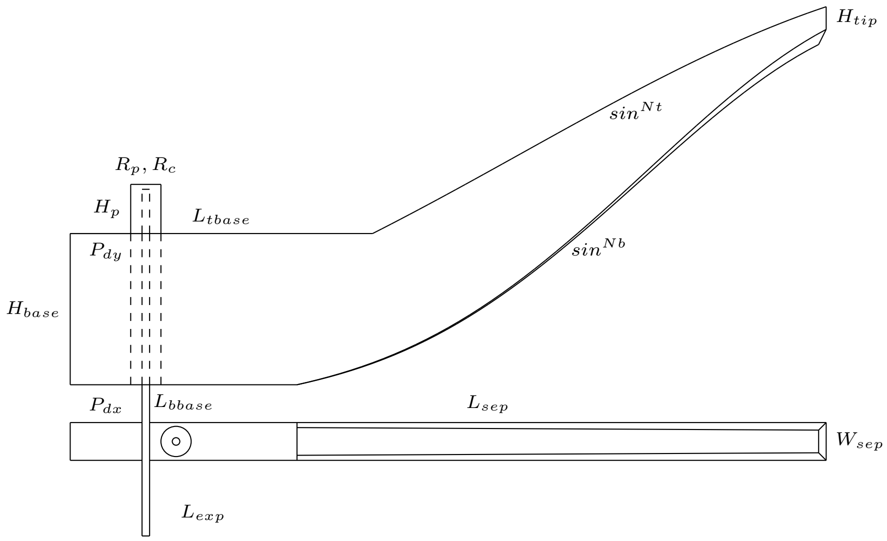

Figure 6.5: Upper cross section of half an OMT, adapted from [88].

Building the OMT The OMT in fig. 6.5 is a complex structure and given the specific function of the curve difficult to build. Scripting this simplifies the process using `GMSH` and the `@WritePreFeko`, the approach is to break the structure into individual surfaces that are later combined. This allows us to easily construct any new version based on the descriptive variable, some simple examples are shown in fig. 6.6. The generated `FEKO` model is shown in fig. 6.7. It is now possible to optimise the OMT based on any combination of variables and for any output parameters.

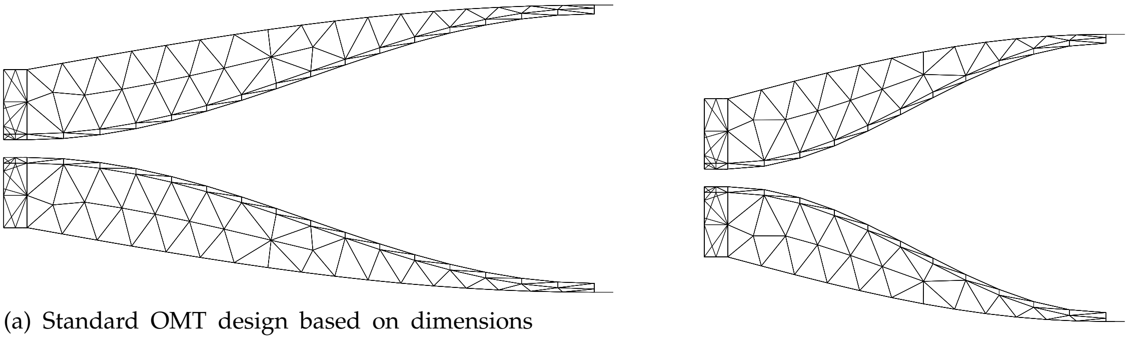

(a) Standard OMT design based on dimensions from [88].

(b) Changing the length, L_{sep}.

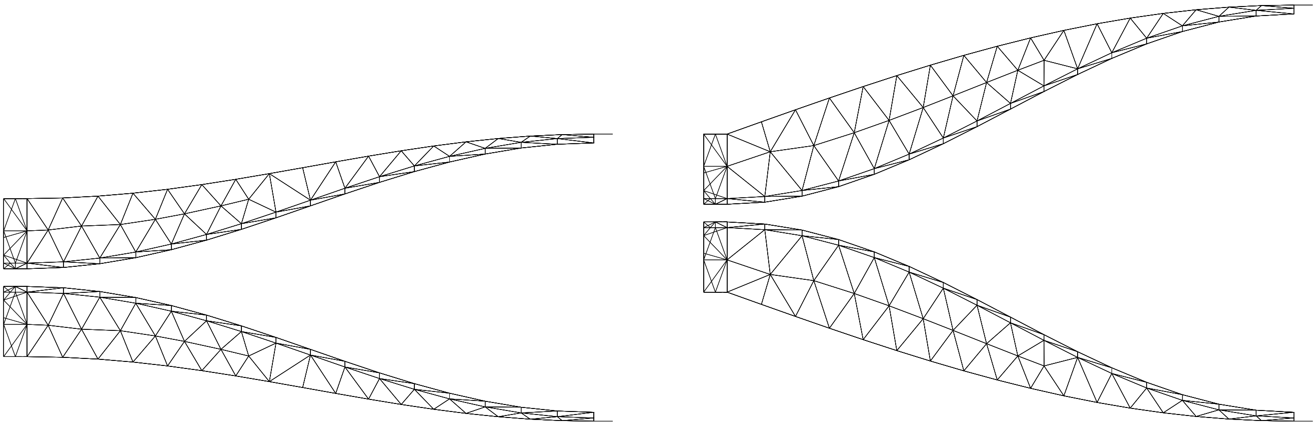

(c) Changing the wall curve function, N_t.

(d) Changing the waveguide size, H_{tip}.

Figure 6.6: OMT designs based on varying single design parameters, the walls, rear matching cone and y–axis septum are not shown.

Optimising the OMT Given the large number of possible variables it is impossible to optimise over all of them. Initial optimisation focused on just the matching criteria and determining the important parameters. For the matching the parameters are found to be the separation between the septum and the port length. The initial optimisation cost functions are shown in fig. 6.8, where the individual frequency and total cost functions are shown. It is clear that the low and high frequency cost functions start to diverge and further optimisation is not useful here. The associated S–parameters are shown in fig. 6.9.

Results and future work The simulated OMT does not meet the requirement across the band so it is decided to change the design to the one given by *Coutts*. It is a more complex but is currently being used on the Very Large Array (VLA) in similar frequency bands with good results. This is left to future work.

Figure 6.7: Quadridge orthomode transducer modelled in `FEKO`, front and back view including coaxial feeding arrangement. The back matching cone is not shown so as not to obscure the feeding arrangement.

6.3.3 TE$_2$HE transition

Corrugated horns require a hybrid HE mode and so the second step is to transform the TE mode produced by the OMT. The transition creates the Hybrid mode (HE_{11}) where HE_{11} is a mix of TE_{11} and TM_{11} modes. Following the work by *B. Thomas*,*G. James* and *K. Greene* [89] for a frequency range from $4.5 - 8.7\,\mathrm{GHz}$ we can specify and initial design given in fig. 6.11.

Table 6.1: Dimensions in mm of precise TE$_2$HE converter fig. 6.11

n	1	2	3	4	5	6	7	8	9	10	11
a_n	27.81	28.76	29.71	30.66	31.61	32.55	33.5	34.45	35.4	36.35	37.3
b_n	0.9	1.56	2.21	2.87	3.52	4.17	4.83	5.48	6.14	6.79	
w_n	7.44	7.44	7.44	7.44	7.44	7.44	7.44	7.44	7.44	7.44	
d_{2n-1}	14.43	14.43	14.42	14.42	14.42	14.42	14.41	14.41	14.41	14.41	
t_n	8.12	7.47	6.81	6.16	5.5	4.85	4.2	3.54	2.89	2.23	
h_{2n}	9.62	9.62	9.61	9.61	9.61	9.61	9.61	9.61	9.6	9.6	
h_{2n-1}	9.62	9.62	9.62	9.61	9.61	9.61	9.61	9.61	9.61	9.6	

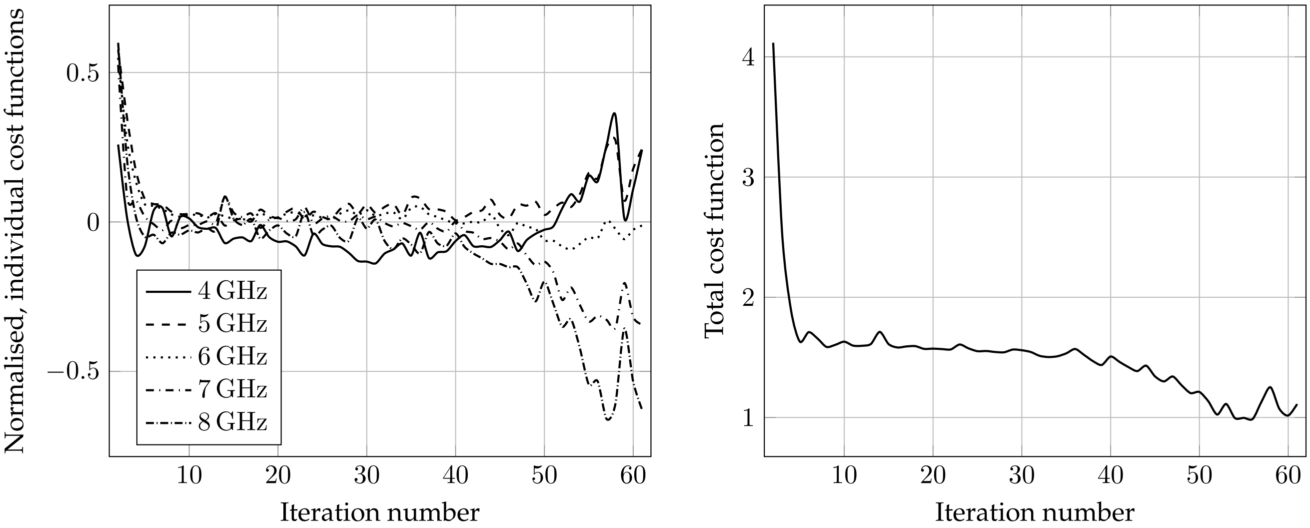

(a) Individual matching criteria cost function.

(b) Total matching criteria cost function.

Figure 6.8: Individual cost functions for initial optimisation for matching criteria, for initial OMT design, RG402 connectors.

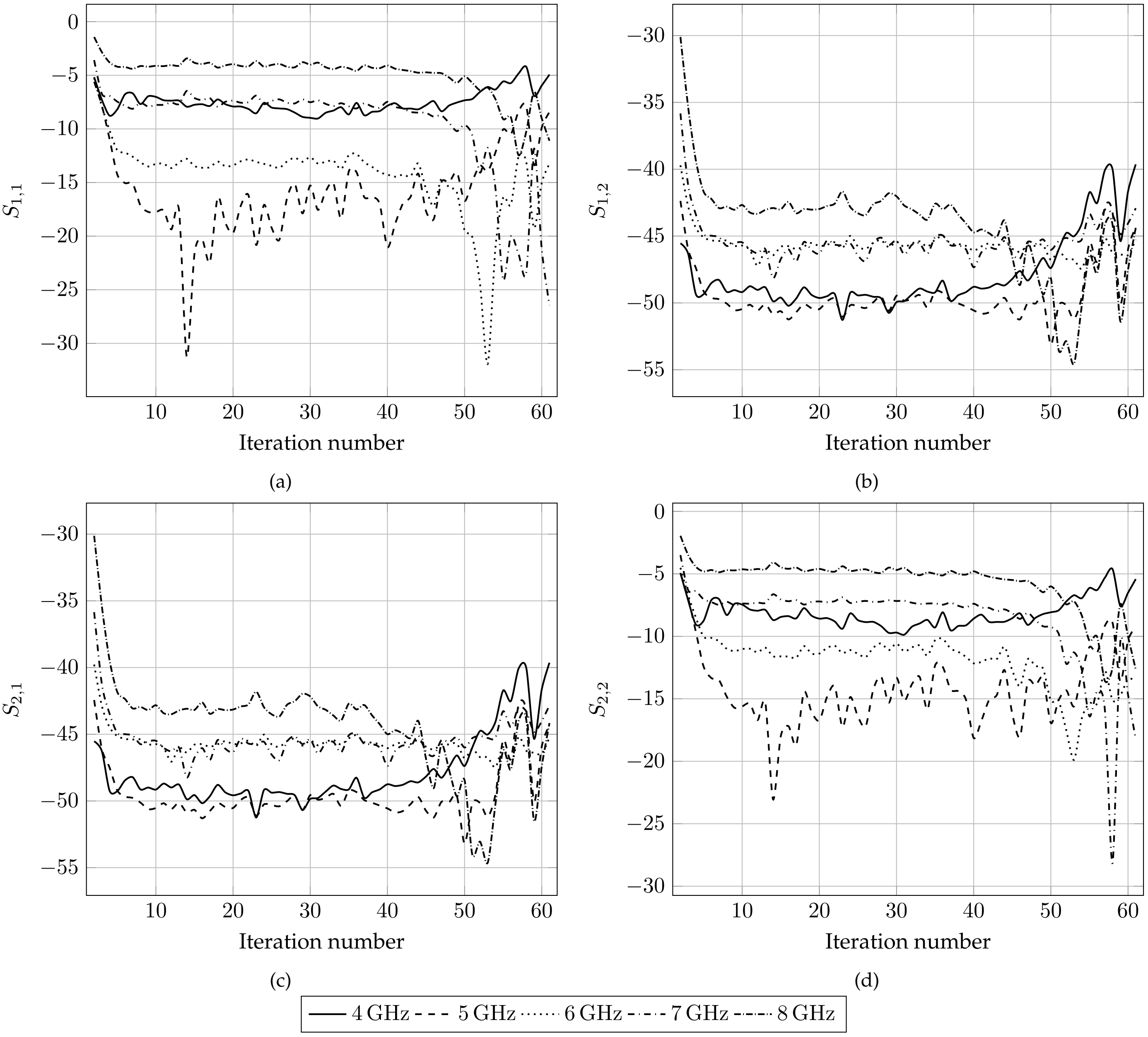

Figure 6.9: Varied S–parameters, initial optimisation for matching criteria, for initial OMT design, RG402 connectors.

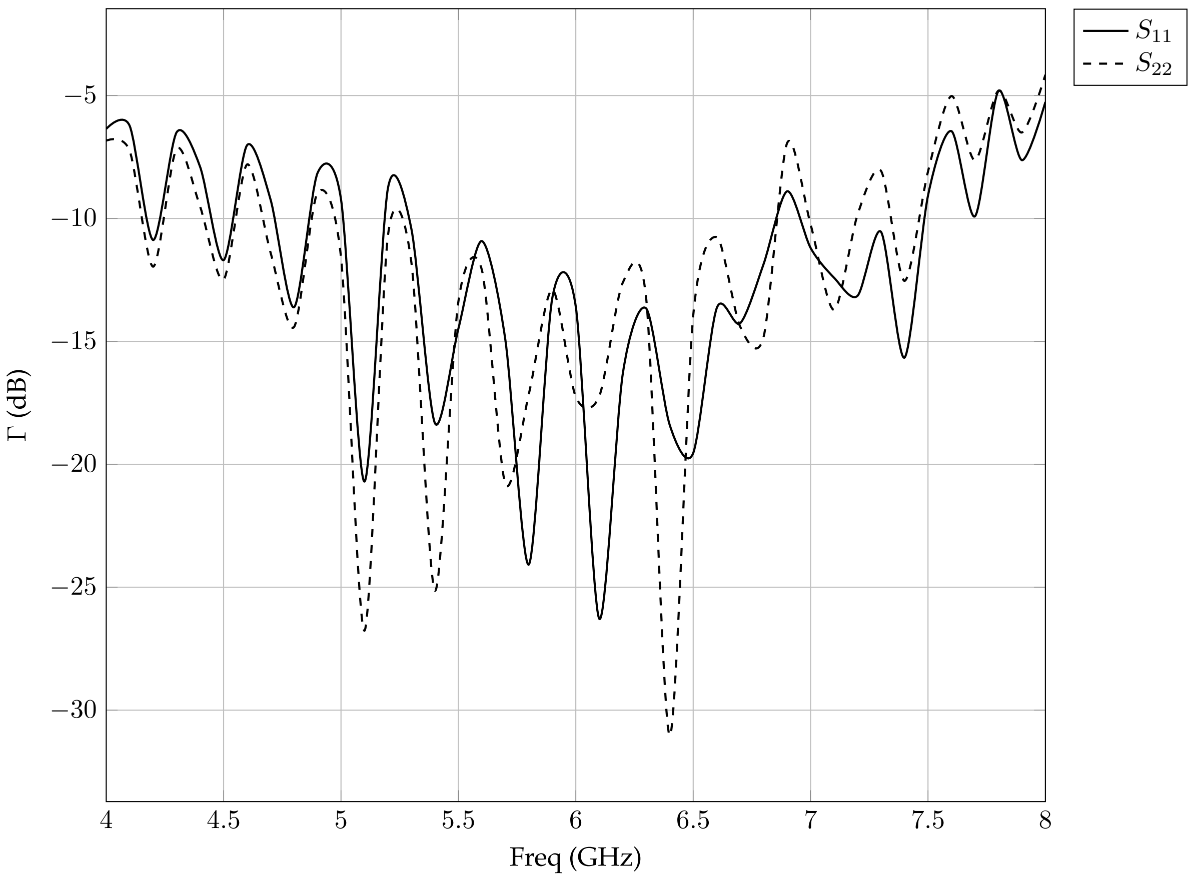

Figure 6.10: Initial OMT design, RG402 connectors.

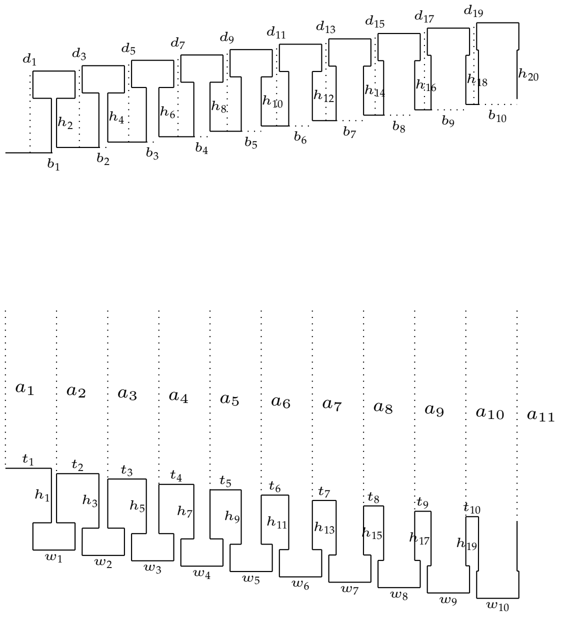

Figure 6.11: Ten ring loaded slot TE_2HE converter (to scale) with dimensions given in table 6.1.

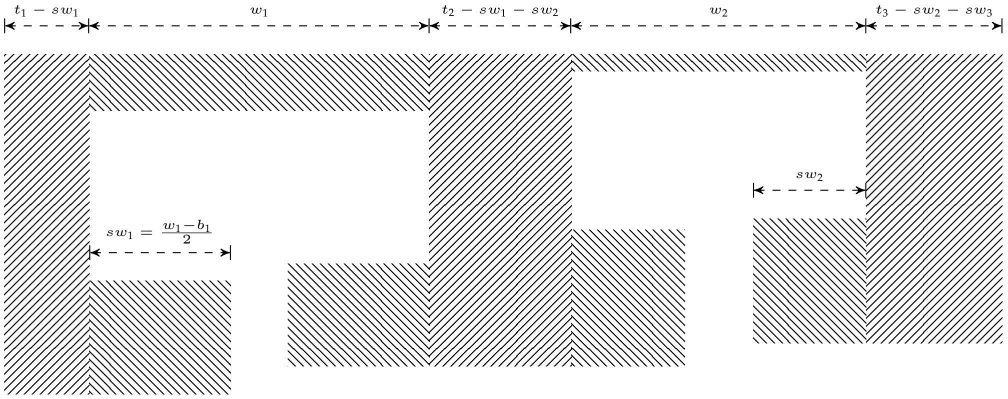

Figure 6.12: Widths required for discretization of transition shown in fig. 6.11 by using Al sheeting.

The exact transition can be machined out of solid Al however this is expensive especially for prototyping. A much cheaper method is to use standard sheeting and cut out rings that are stacked together. Given available sheeting of $1, 1.2, 1.6, 2.0, 2.4, 3.0, 3.2, 4.0$ and $5\,\mathrm{mm}$, and allowing for stacking of different sheets we can get a transition which is close to the design. The rings can still be cut out to any value so only the widths need to be considered, referring to fig. 6.11, the relevant widths are given in fig. 6.12 and the prototype in fig. 6.13. The required sheeting is given in table 6.2.

Table 6.2: Al thickness's required for prototype, dimensions in mm of the TE_2HE section given in fig. 6.11

w_n	7.4	7.4	7.4	7.4	7.4	7.4	7.4	7.4	7.4	7.4
sw_n	3.2	3	2.6	2.2	2	1.6	1.2	1	1	0
$t_n - sw_{n-1} - sw_n$	5	1.2	1.2	1.2	1.2	1.2	1.2	1.2	1	1.2

Table 6.3: Dimensions in mm of the discretised TE_2HE section given in table 6.2

n	1	2	3	4	5	6	7	8	9	10	11
a_n	27.81	28.76	29.71	30.66	31.61	32.55	33.5	34.45	35.4	36.35	37.3
b_n	1	1.4	2.2	3	3.4	4.2	5	5.4	5.4	7.4	
w_n	7.4	7.4	7.4	7.4	7.4	7.4	7.4	7.4	7.4	7.4	
d_{2n-1}	14.43	14.43	14.42	14.42	14.42	14.42	14.41	14.41	14.41	14.41	
t_n	8.2	7.4	6.8	6	5.4	4.8	4	3.4	3	2.2	
h_{2n}	9.62	9.62	9.61	9.61	9.61	9.61	9.61	9.61	9.6	9.6	
h_{2n-1}	9.62	9.62	9.62	9.61	9.61	9.61	9.61	9.61	9.61	9.6	

The transition is built in the same way as the corrugated horn and the final `FEKO` model is shown in fig. 6.14.

The Simulated reflection coefficients of the discrete and initial design is given in fig. 6.15. The mode transmissions are given in fig. 6.16 including the unwanted 12 modes. As expected the discretisation has only a small effect and the transition is well matched across the band. The horn can now be designed based on the S–parameters of the transition assuming an ideal TE_{11} excitation.

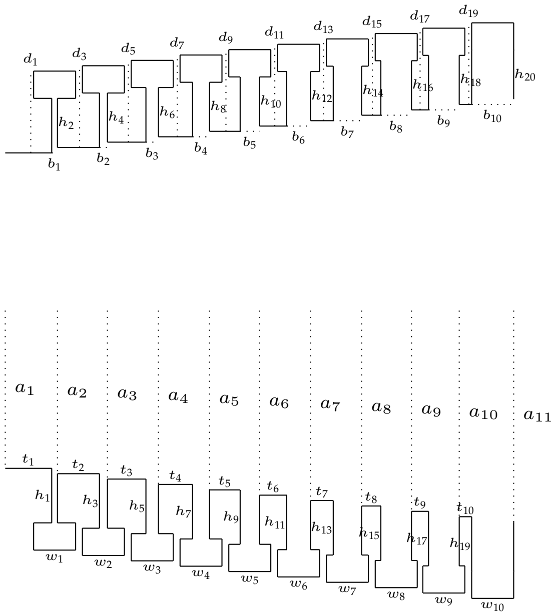

Figure 6.13: Ten ring loaded slots TE_2HE converter (to scale).

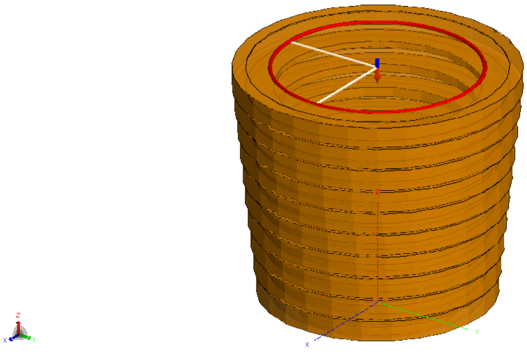

Figure 6.14: TE_2HE transition modeled in FEKO.

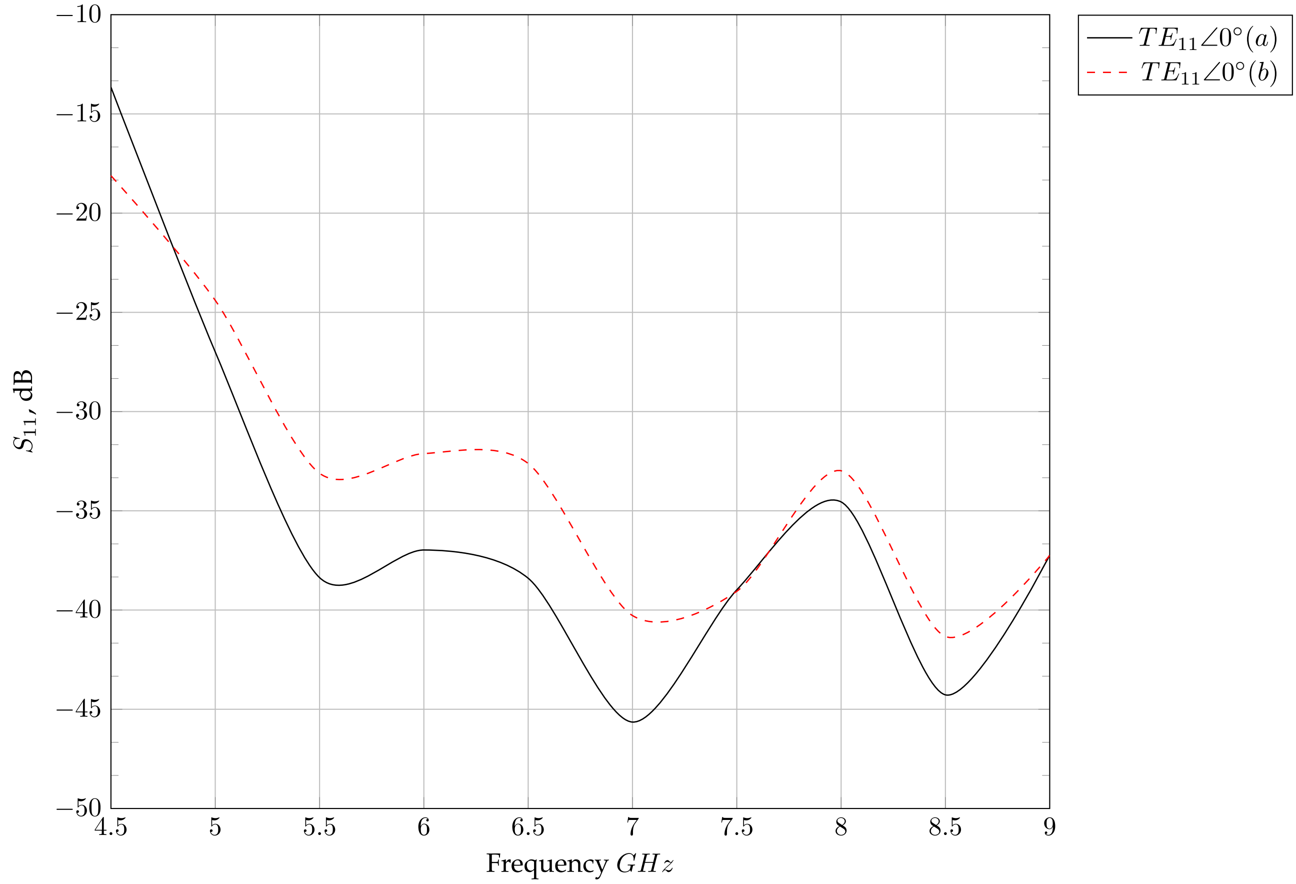

Figure 6.15: Reflection coefficient of the input TE_{11} mode for (a) ideal and (b) discrete cases.

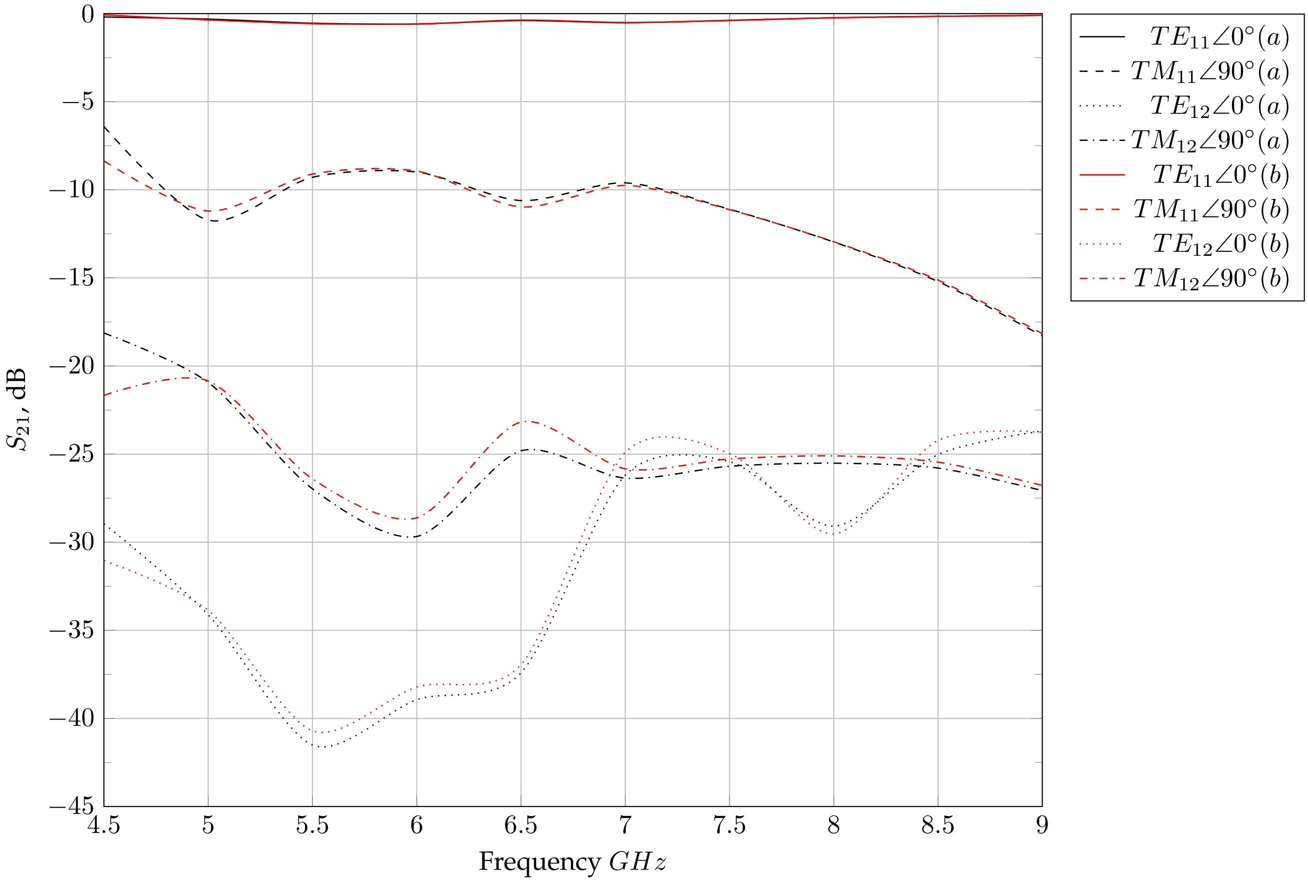

Figure 6.16: Transmission coefficients for the desired TE_{11}, TM_{11} and undesired TE_{12},TM_{12} modes, for (a) ideal and (b) discrete cases.

6.3.4 Corrugated horn design

A good initial horn can be designed by using a Gaussian beam model as detailed by *Kildal* [90]. Traditionally the horn design begins by finding out the gain and beam angle for a given taper which is matched to the existing Potter Horn and ideally can be seen in fig. 6.18. For wide band horns the ideal is a flare controlled horn, a geometrical characteristic which remains invariant over the band. This however results in a long horn with a large aperture. The cassegrain dish has a relatively small cone section with multiple receivers placed inside and a given these physical space requirements a compact design is required. This reverses the design procedure. We begin by considering the largest horn we can fit and work out the optimal flare for the required beam taper and phase centre location.

Given an aperture limitation of $400\,\mathrm{mm}$ which translates to $D = 6\,\lambda$ at $4.5\,\mathrm{GHz}$. From fig. 6.18 it is calculated that the if we want Feed illumination angle $(13.771°)$, $-20\,\mathrm{dB}$ edge taper. This means we need a gain of $23.5\,\mathrm{dB}$. The possible beam angles are plotted in fig. 6.17.

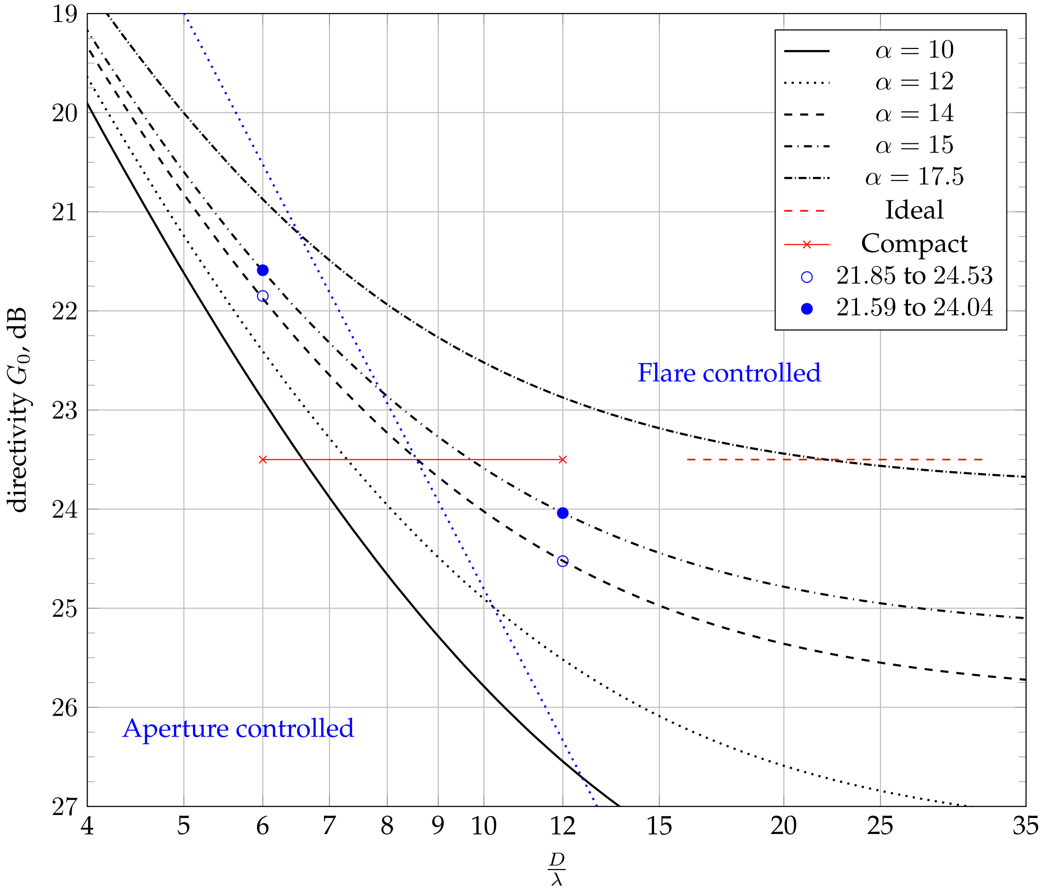

Figure 6.17: Possible horns, dotted line show boundary between flare and Aperture controlled horns.

If we choose $14°$ then we get a directivity of between 21.85 to $24.54\,\mathrm{dB}$ or if we choose $15°$ then we get a directivity of between 21.59 to $24.04\,\mathrm{dB}$. The associated edge taper of these two choices is plotted in fig. 6.18 and the phase centre variation in fig. 6.19.

Considering a beam angle α of $14°$ to $15°$. This gives us a horn of between 746 to $802\,\mathrm{mm}$

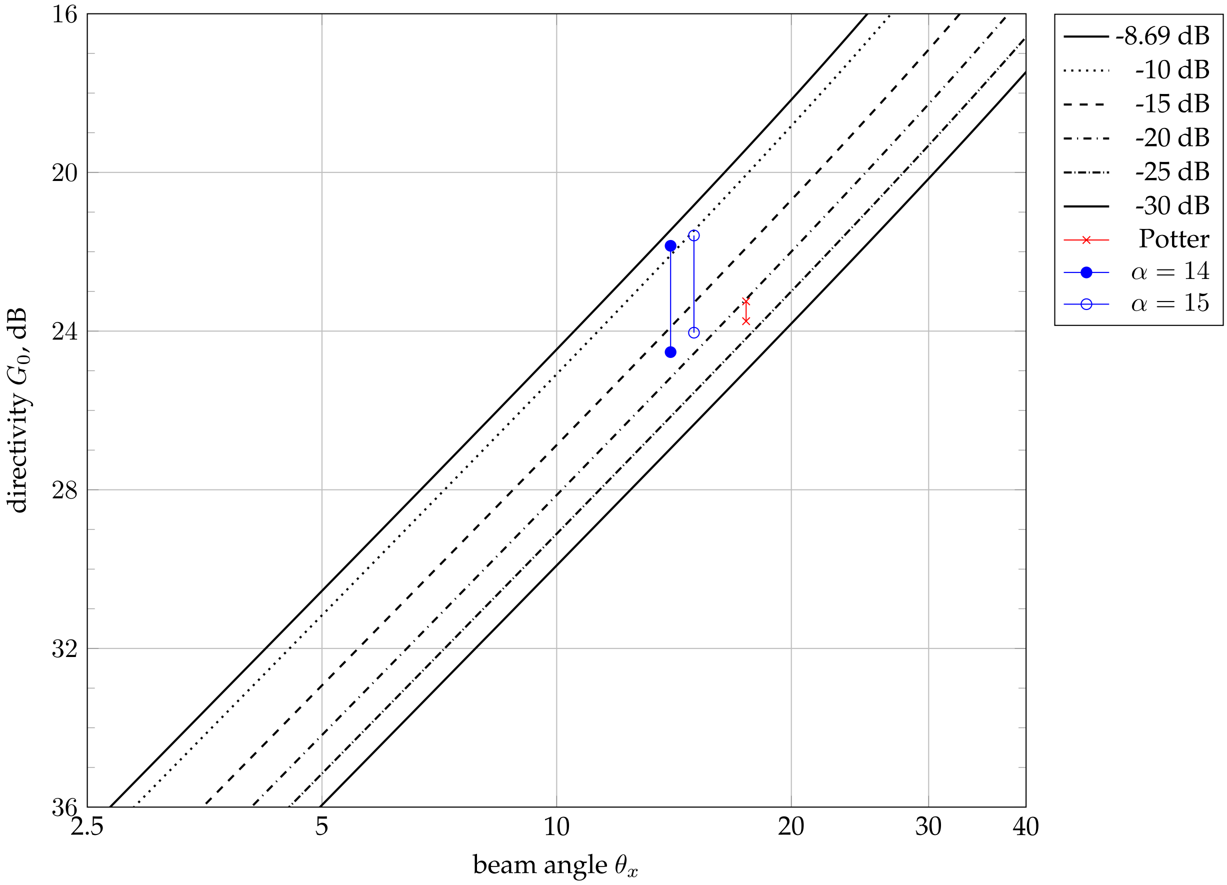

Figure 6.18: Required Directivity, for various beam tapering.

and a phase center variation of between 313 to 602 mm. This gives us a good starting point for the design.

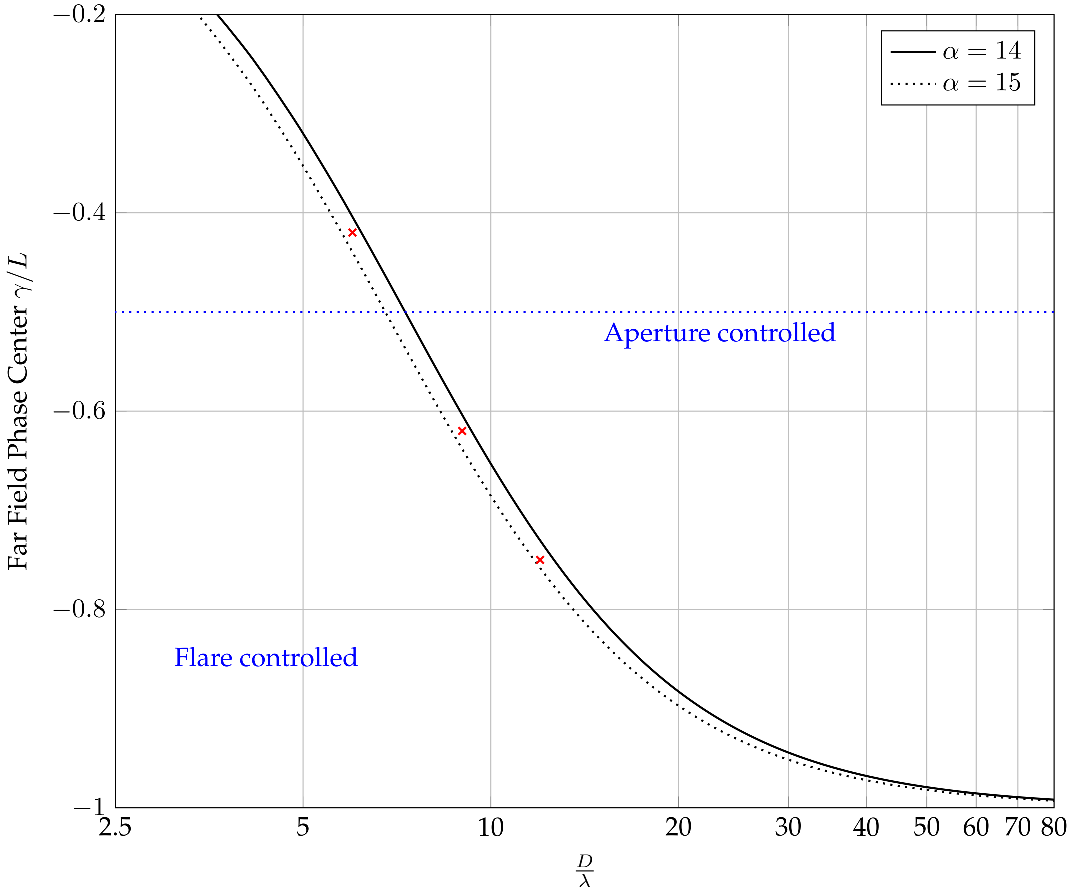

Figure 6.19: Phase variation for corrugated horns.

The design curves assume that the horn is exctied by a pure HE_{11} mode and an ideal corrugated surface. Corrugated surfaces to be effective need to fullfill the following conditions: a) at least 10 corrugations long, b) slot depth $\lambda_0/4 < d < \lambda_0/2$, c) slot width $w < \lambda_0/10$ and d) tooth width $t < w/10$ [91]. This slot depth gives corrugated surface a bandwidth of $2:1$.

The horn is simulated seperately for both TE_{11} and TM_{11} modes and the final beam pattern calculated using the S–parameters from the TE$_2$HE transition. Several variations where simulated and a horn with the following parameters, in wavelengths at the lower frequency, is found to give good performance:

G_{in} = Inner radius $0.715\,\lambda$ matched to the TE$_2$HE section
L = Horn length $11.582\,\lambda$
α = flare angle $14°$
C_w = Corrugation width $0.1\,\lambda$
C_t = Corrugation teeth width $0.01\,\lambda$
C_d = Corrugation initial depth $0.25\,\lambda$
C_{dd} = Corrugation second depth $0.25\,\lambda$

The beam patterns including the modal patterns are plotted in fig. 6.20 and a composite plot is given in section 6.3.4. The phase centre optimised over the whole and main beams is given in fig. 6.22, further plots and details of this calculation is given in Appendix E.

The beam patterns meet the specifications as required and the phase centre matches exactly the range expected from the design curves. It is noted that at the higher end of the band the sidelobes begin to rise, this is due to a field distribution not being well tapered at the edge of the apeture. The reason is that the corrugated surface is starting to no longer act as a perfect magnetic conductor and is conducting some current.

6.4 Conclusions and future work

Corrugated surfaces and mode converters in particular are well modelled using mode matching code [92]. More complex horns can be designed and simulations significantly sped up using this numerical method. Initial work has been done on producing this code but has been left to future work. The method and approach are detailed in Appendix D.

The horn as designed and simulated can be used to optimise any part of the system as any variation in the feeding system only changes the mode weightings and so the new beam pattern and noise consequences is easily calculated without the need for further simulation. Therefore the effect of a non-ideal OMT is easily calculated by adding the weighted modal patterns. The system is optimised within Octave and so the noise temperatures can as is shown previously in the simpler design, be directly incorporated into the design.

The scripting and simulation approach works, it allows the design to be broken up and the final system sensitivity to be calculated based on simulating each component separately. This has the great advantage that no other components need to be simulated except for the one being locally optimised. For example once the horn is optimised, further optimisation of the OMT or transition does not need the horn to be resimulated to determine the effect on the beam pattern. Given the large number of meshes required for the horn this is a significant saving.

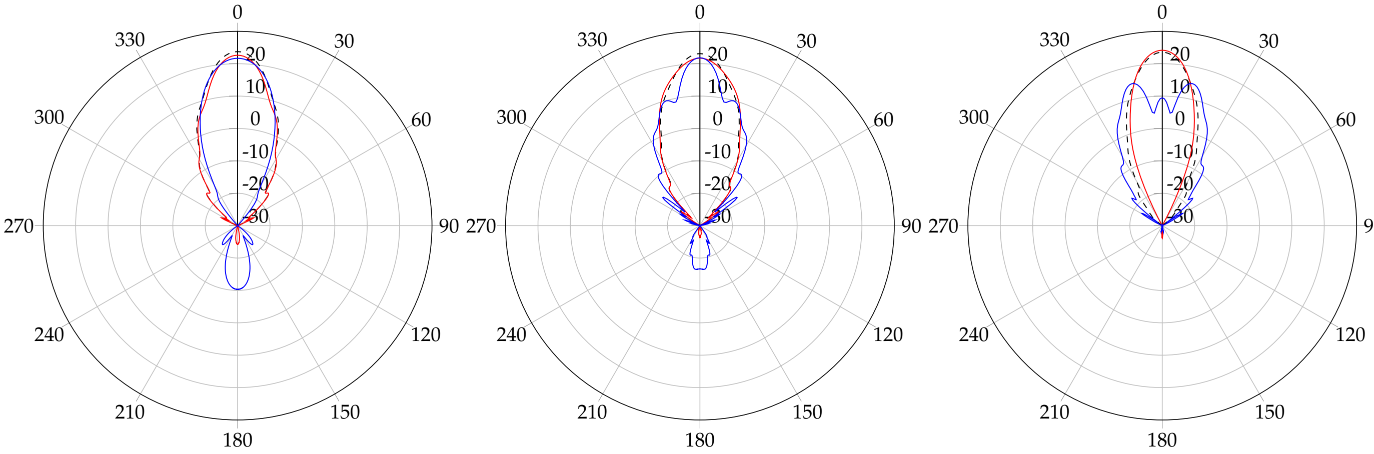

(a) 4500 MHz

(b) 5000 MHz

(c) 5500 MHz

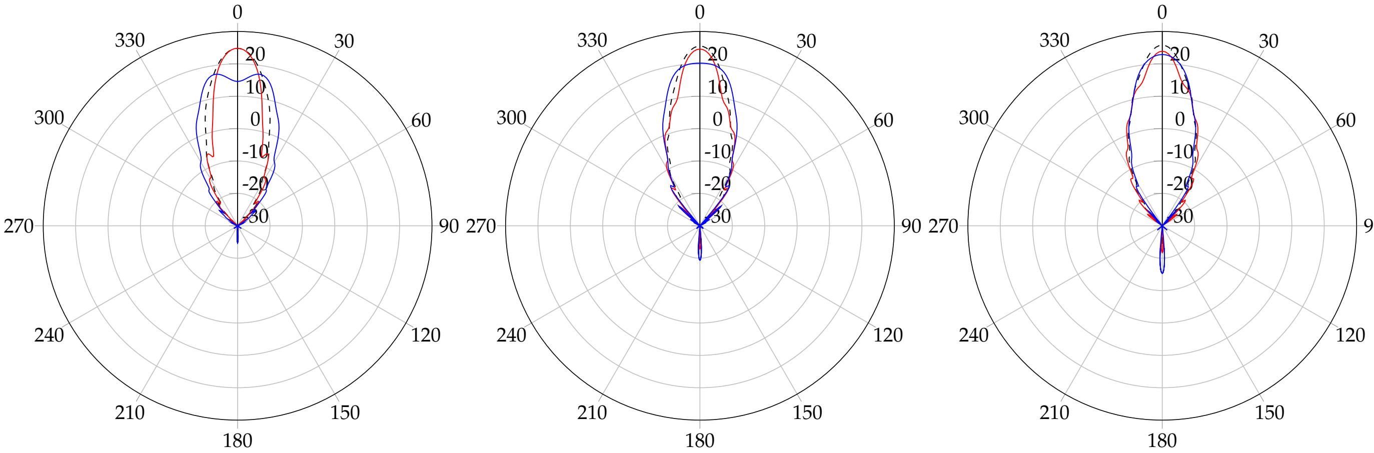

(d) 6000 MHz

(e) 6500 MHz

(f) 7000 MHz

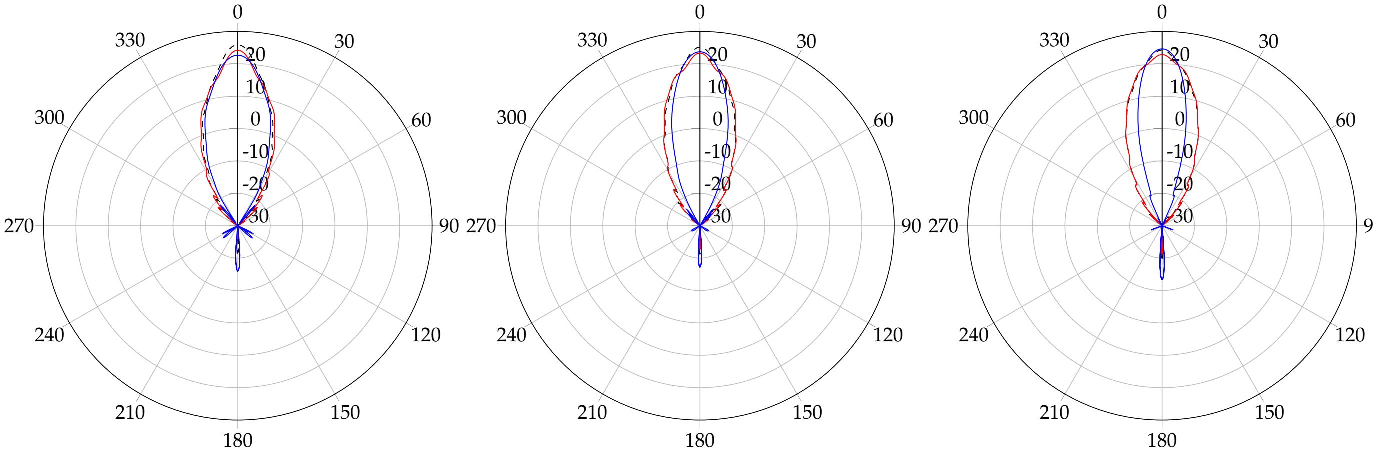

(g) 7500 MHz

(h) 8000 MHz

(i) 8500 MHz

Figure 6.20: Final corrugated horn design beam patterns, based on the summation of TE_2HE modes.

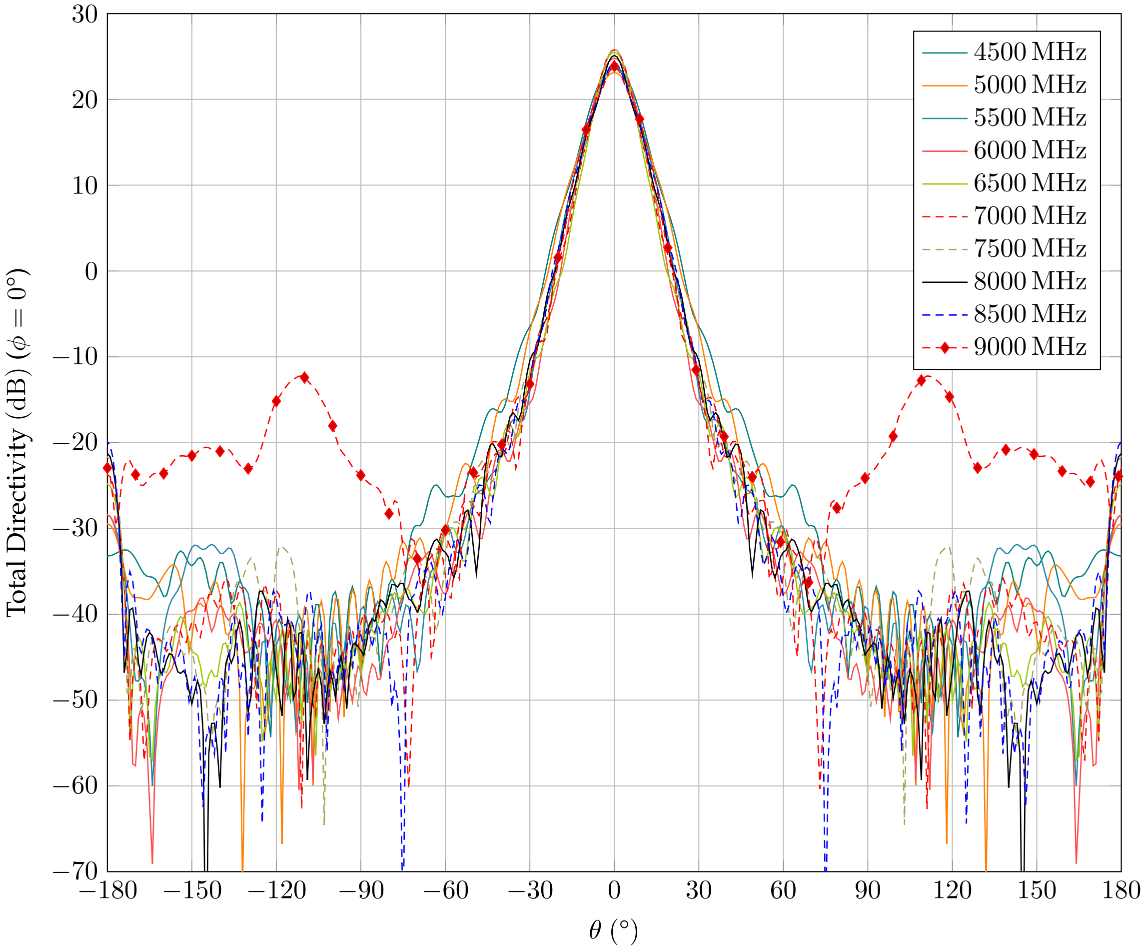

Figure 6.21: Combined final corrugated horn design beam patterns, based on the summation of TE_2HE modes.

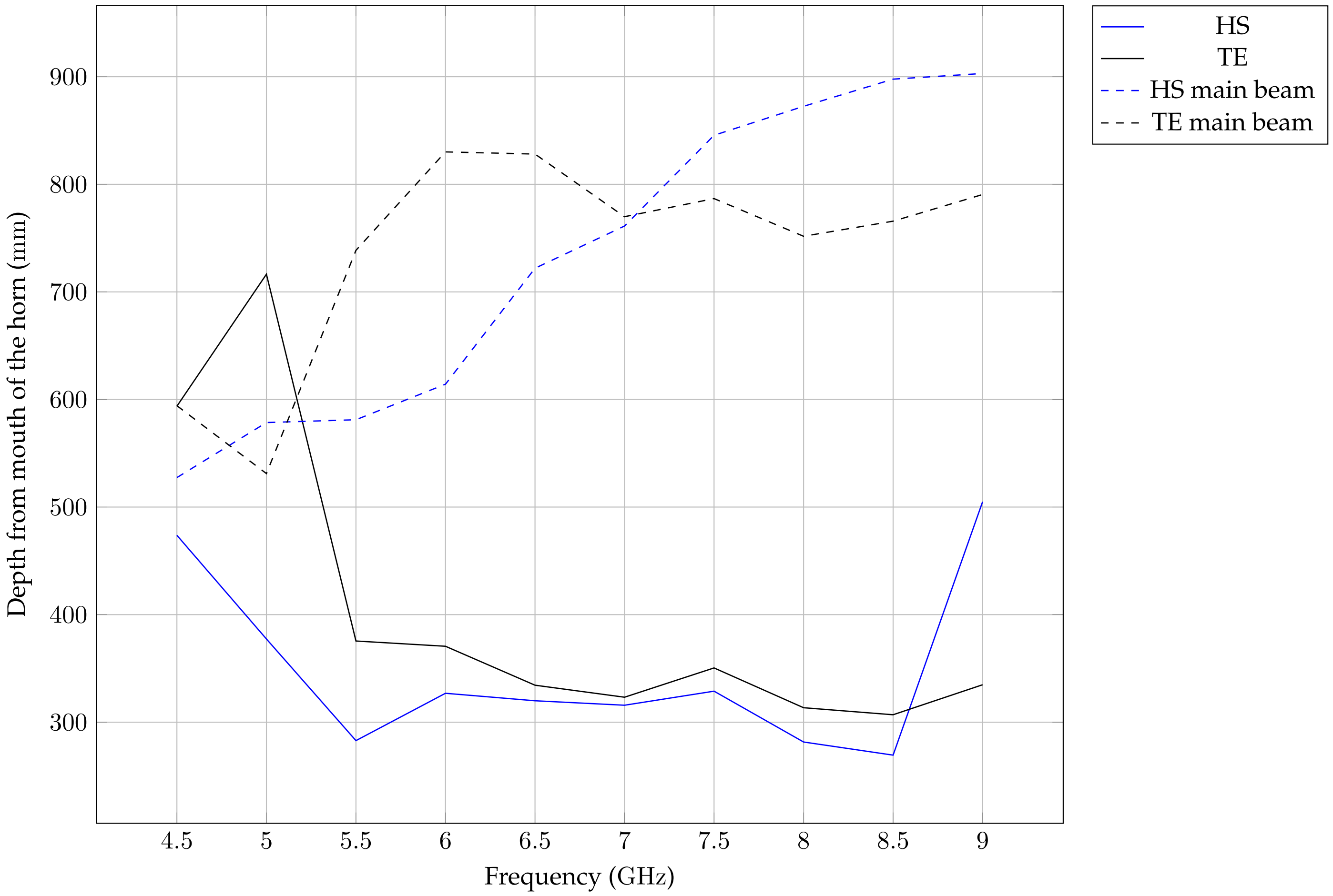

Figure 6.22: Optimal phase centre for corrugated horn.

Currently a higher frequency horn and transition is planned to be built and excited by narrow band TE feeding sections to verify the design. Once this is complete the OMT can be designed and optimised based on the existing transition, antenna and chosen amplifier. Therefore directly incorporating the system sensitivity into the receiver design as required. The system performance based on changing the OMT is a numerical calculation requiring no further EM simulation, adding very little simulation time to any optimisation loop.

Chapter 7

Conclusion

Many future Radio Astronomy systems are required to be wideband, compact, highly sensitive and consisting of arrayed elements. Their modelling and design requires the incorporation of noise modelling and overall sensitivity. Multiport noise theory is well developed and good models are possible as confirmed with modelling and measurements. Commercial solvers do not however for good practical reasons include this theory. Given the usefulness and power of commercial solvers this is a problem for designers of very low noise critical receivers.

It is possible to use commercial solvers to design and optimise receivers for low noise applications however it requires considerable effort. One approach is to use specialised software with the outputs of commercial solvers. Specifically it is shown using a test folded dipole simulation that `CAESAR` can be incorporated with `CST`. The theory to combine any of the commercial solvers is developed, as long as the input port definitions of the original simulation is known. Given that the original simulation does have to simulate each port individually this does add a cost to the simulation. If the structure is symmetrical around the feeding ports however it is shown that the symmetry of the problem can be recovered by mirroring the beam patterns, even if it is not possible to use this in the original simulation.

Using an Eleven antenna and ultra wideband low noise Caltech LNAs, multiport noise modelling is tested and given the highly sensative nature of the system the theory gives excellent agreement with measurement validating the approach.

The optimisation of structures outside of the commercial solvers framework is significantly more complex. It requires the development of a software outside of commercial solvers to run the simulation. Using the open source program `GNU Octave` and the commercial solver `FEKO` this is done using a class based scripting approach. The added complexity of this approach however has three main advantages. Firstly it allows the incorporation of any output variable such as sensitivity as part of the criteria for the optimisation goal function. In principle this could include any variable, for example the cost of the materials and weight to be optimised for. Secondly it is a convenient mathematical approach to describing designs, complex three dimensional elements are easily described and replicated. This allows for easy modelling of, for example complex waveguide structures, Self-complementary and Fractal antennas. Thirdly given the modular nature of this approach it allows almost any variable of the design to be used as the input parameter for the optimisation, for instance the number of corrugations in a horn or whole sections in a waveguide transformer.

Traditionally this type of optimisation is difficult or impossible. It is typically never done. The complexity of using multiple different software languages and programs is more than made up for by the simplification in design and flexibility in optimisation.

The application and utility of the approach and software is demonstrated with a basic example and a more complex design. The simple example proves that this approach is possible and works. It is clear that the use of scripting and modularisation improves the ability to design Radio Telescope receiver systems. This leads to cheaper, more sensitive systems and better designs for specialised problems.

Appendices

Appendix A

Antenna efficiencies

We can directly calculate the beam efficiencies follow the form given in [47], where the antenna is approximated as a Body of Revolution–Type 1 (BOR1) antenna and the efficiencies, of the BOR1 components, calculated. The actual efficiency is then a product of the approximate e_{ant} efficiency and the BOR1 efficiency e_{BOR1}, giving the overall antenna efficiency. The calculations are:

$$e_{ap} = \frac{4\pi \cot^2\left(\frac{\theta_0}{2}\right)\left|\int_0^{\theta_0} G_{\text{co45}}\left(\theta_f\right)\tan\left(\frac{\theta_f}{2}\right)d\theta_f\right|^2}{2\pi\int_0^{\pi}\left[\left|G_{\text{co45}}\left(\theta_f\right)\right|^2+\left|G_{\text{xp45}}\left(\theta_f\right)\right|^2\right]\sin\left(\frac{\theta_f}{2}\right)d\theta_f} \tag{A.1}$$

$$e_{sp} = \frac{2\pi\int_0^{\theta_0}\left(\left|G_{\text{co45}}\left(\theta_f\right)\right|^2+\left|G_{\text{xp45}}\left(\theta_f\right)\right|^2\right)\sin\theta_f d\theta_f}{2\pi\int_0^{\pi}\left(\left|G_{\text{co45}}\left(\theta_f\right)\right|^2+\left|G_{\text{xp45}}\left(\theta_f\right)\right|^2\right)\sin\theta_f d\theta_f} \tag{A.2}$$

$$e_{ill} = 2\cot^2\left(\frac{\theta_0}{2}\right)\frac{\left|\int_0^{\theta_0}\left|G_{\text{co45}}\left(\theta_f\right)\tan\left(\frac{\theta_f}{2}\right)d\theta_f\right|\right|^2}{\int_0^{\theta_0}\left|G_{\text{co45}}\left(\theta_f\right)\right|^2\sin\theta_f d\theta_f} \tag{A.3}$$

$$e_{\phi} = \frac{\left|\int_0^{\theta_0} G_{\text{co45}}\left(\theta_f\right)\tan\left(\frac{\theta_f}{2}\right)d\theta_f\right|^2}{\left[\int_0^{\theta_0}\left|G_{\text{co45}}\left(\theta_f\right)\right|\tan\left(\frac{\theta_f}{2}\right)d\theta_f\right]^2} \tag{A.4}$$

$$e_{BOR1} = \frac{2\pi\int_0^{\pi}(\left|G_{\text{co45}}\left(\theta_f\right)\right|^2+\left|G_{\text{xp45}}\left(\theta_f\right)\right|^2)\sin\theta d\theta}{P_{tot}} \tag{A.5}$$

Appendix B

Testing port combinations

B.1 Testing of mirroring function

The Eleven Antenna consists of four differential ports, defined, with coordinate system, as simulated in fig. B.1. The verification of mirroring and combining these eight ports is plotted here. Considering just single petal patterns, that is we excite a single port and terminate all the other ports, we do this for all eight ports and compare the simulated to analytically mirroring and rotating the pattern from port 1.

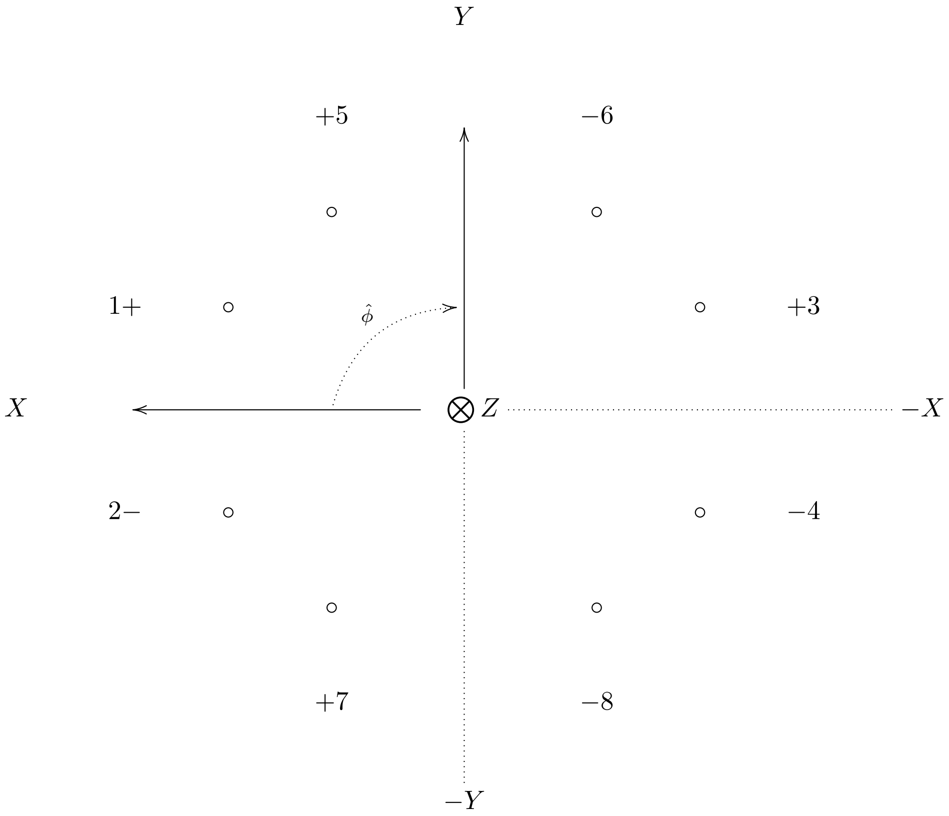

Figure B.1: `CST` ports definition.

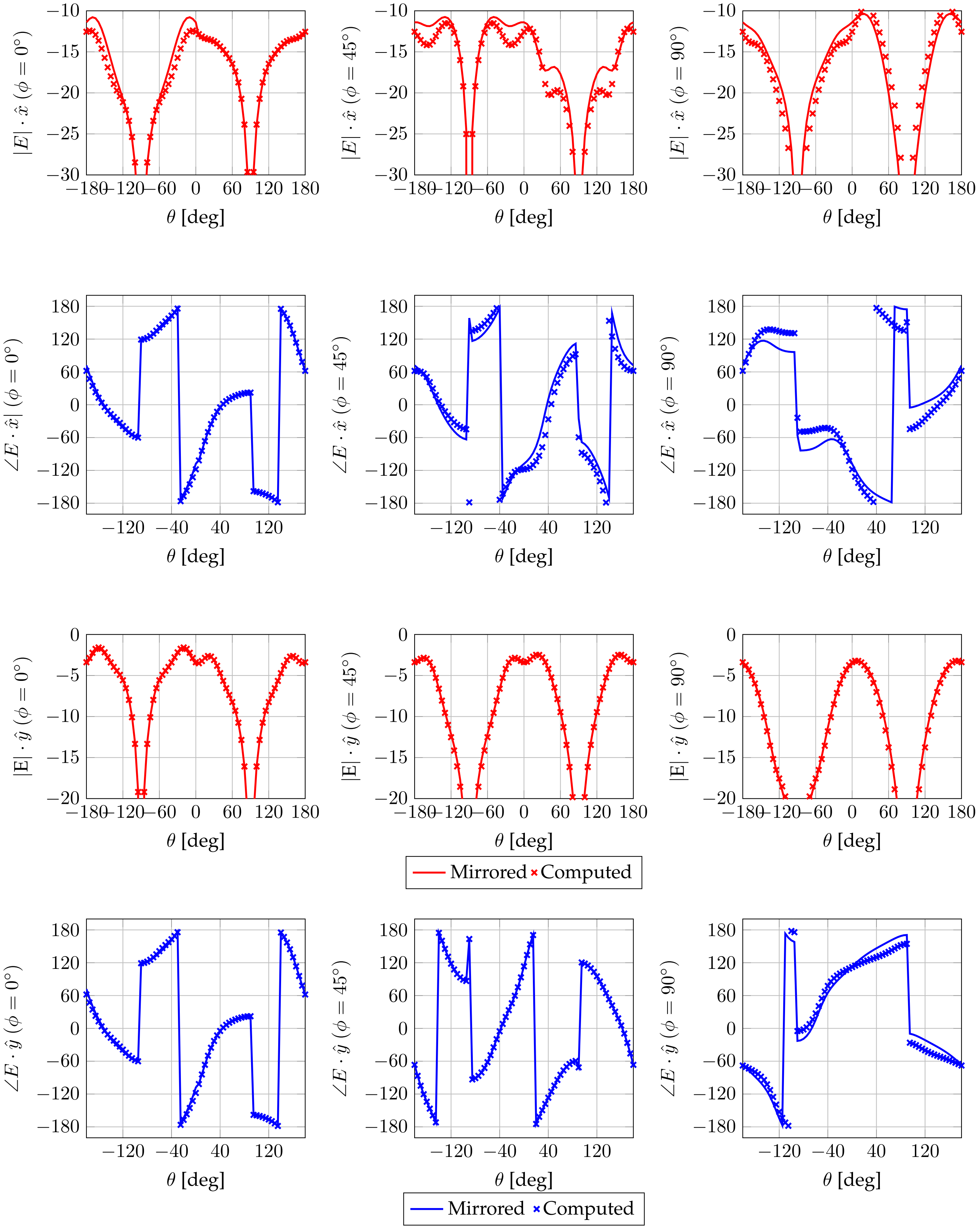

Figure B.2: Comparisons between mirrored and directly computed beam pattern cuts for port 2.

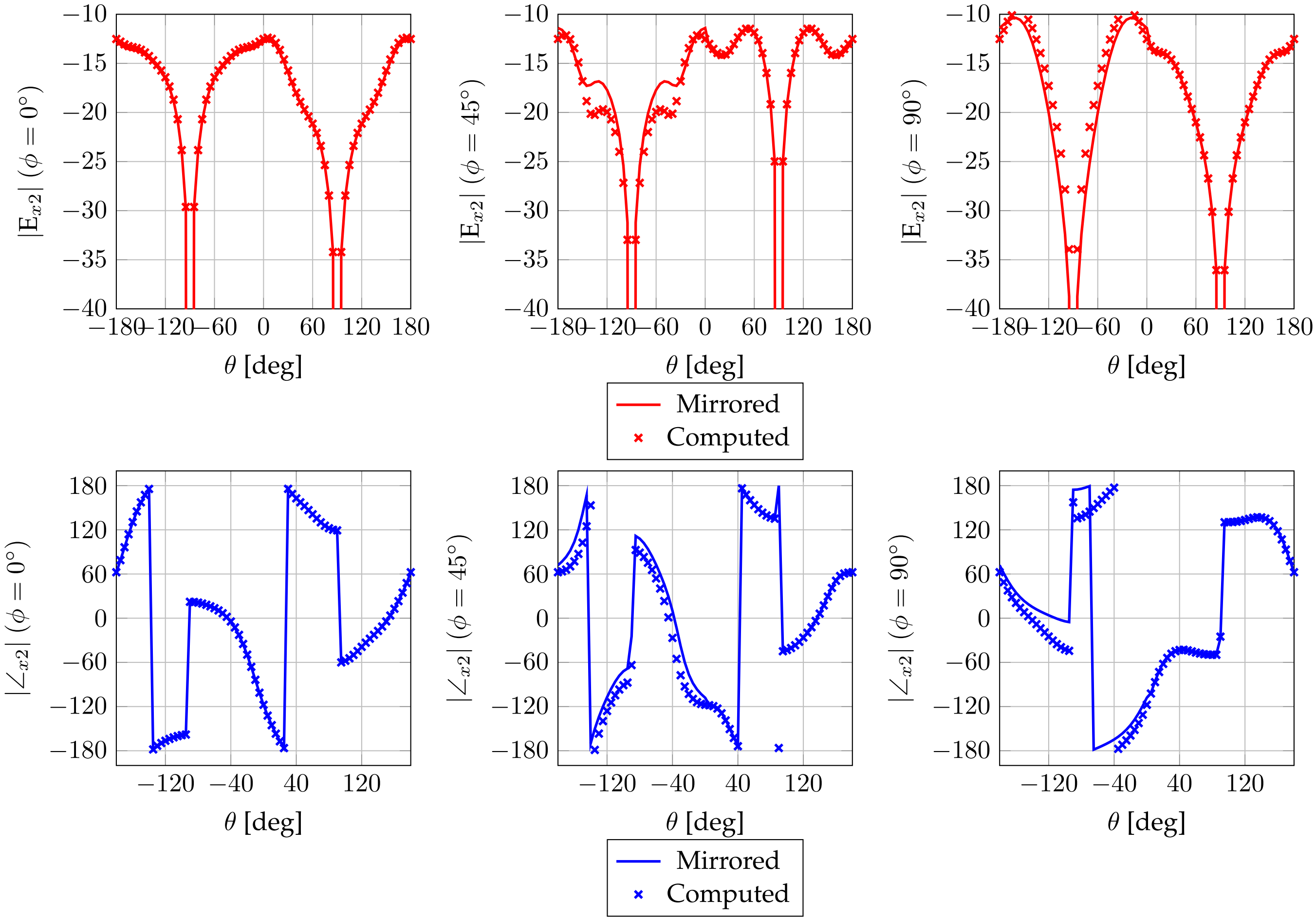

Figure B.3: Comparisons between mirrored and directly computed beam pattern cuts for port 3.

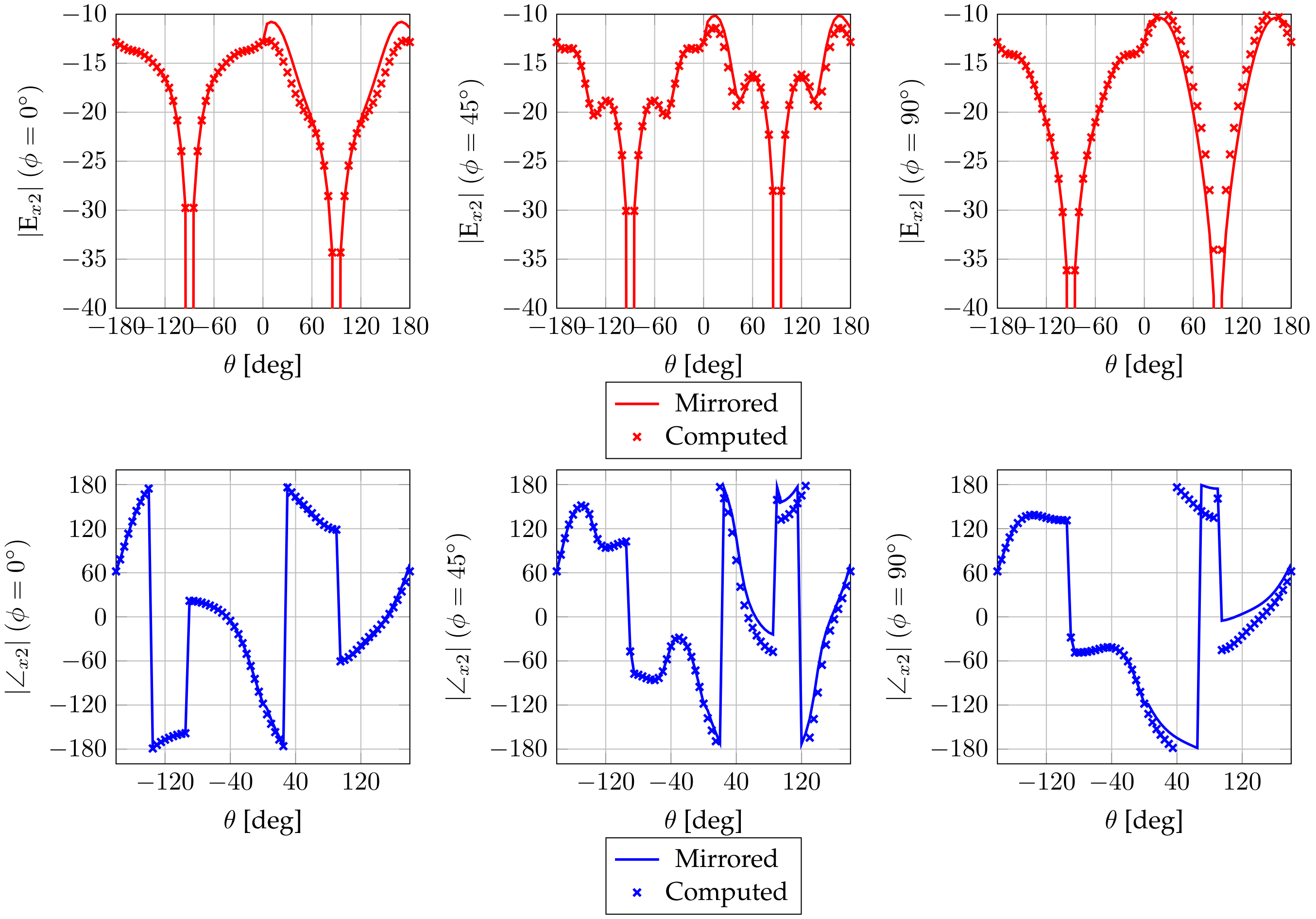

Figure B.4: Comparisons between mirrored and directly computed beam pattern cuts for port 4.

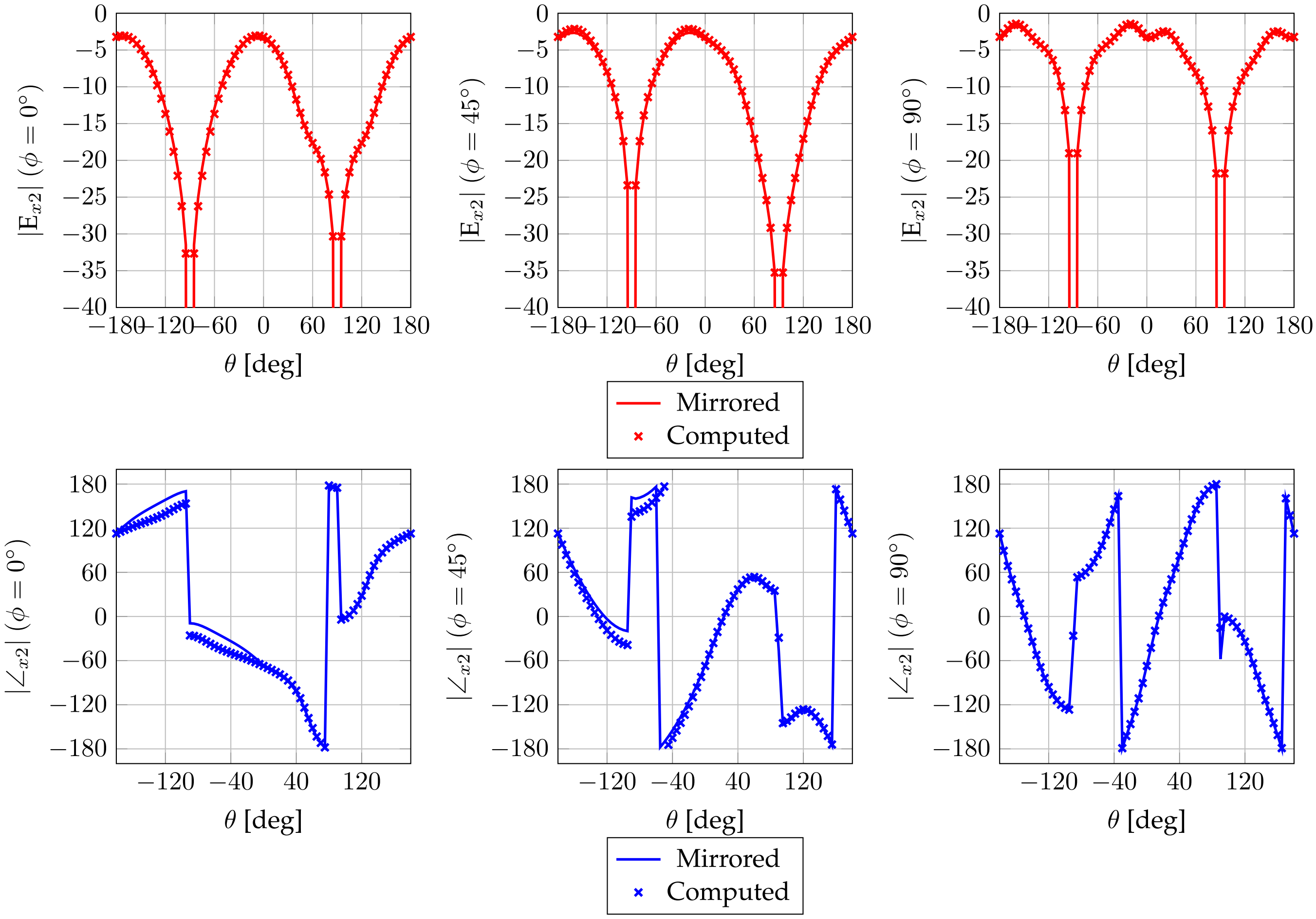

Figure B.5: Comparisons between mirrored and directly computed beam pattern cuts for port 5.

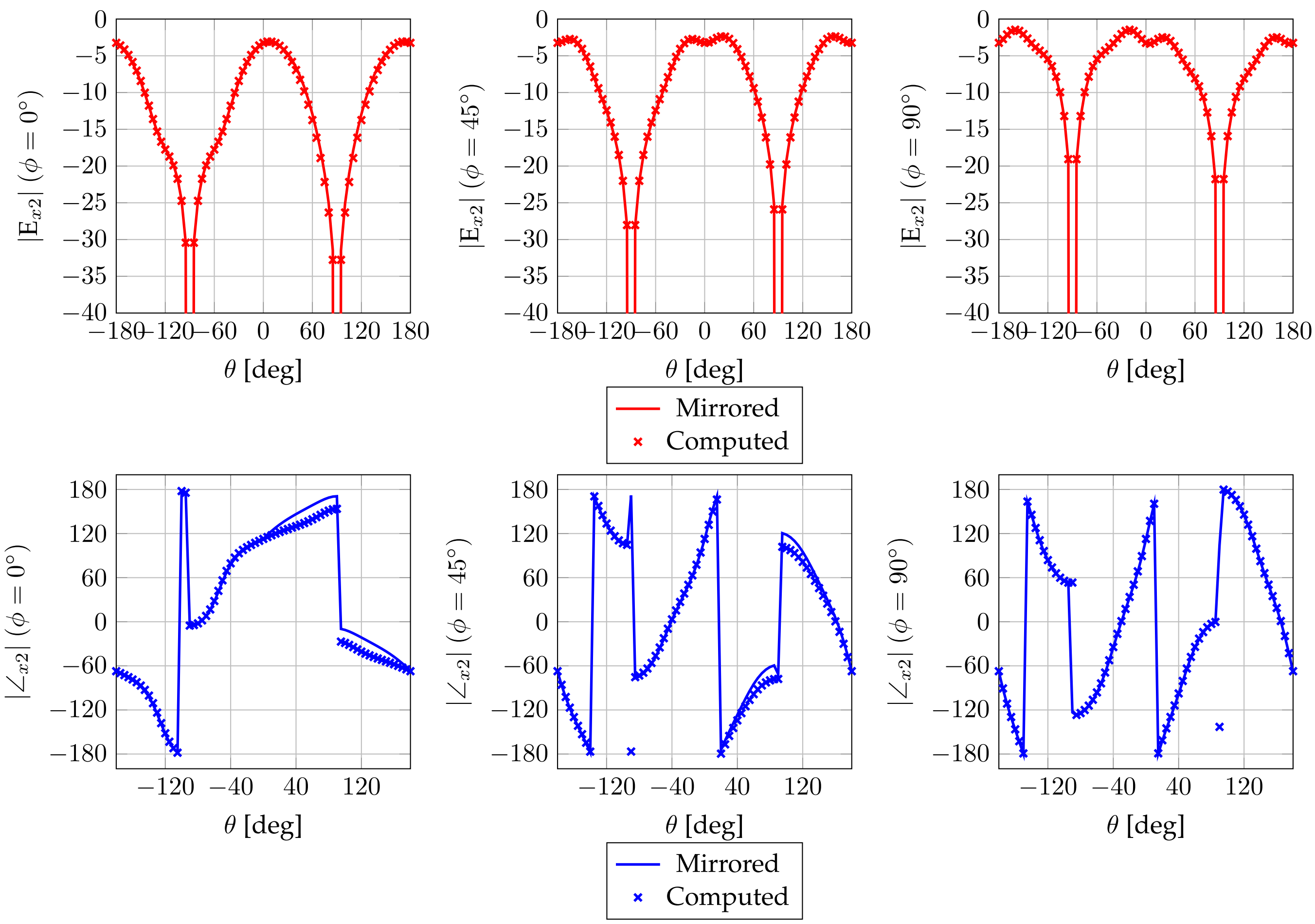

Figure B.6: Comparisons between mirrored and directly computed beam pattern cuts for port 6.

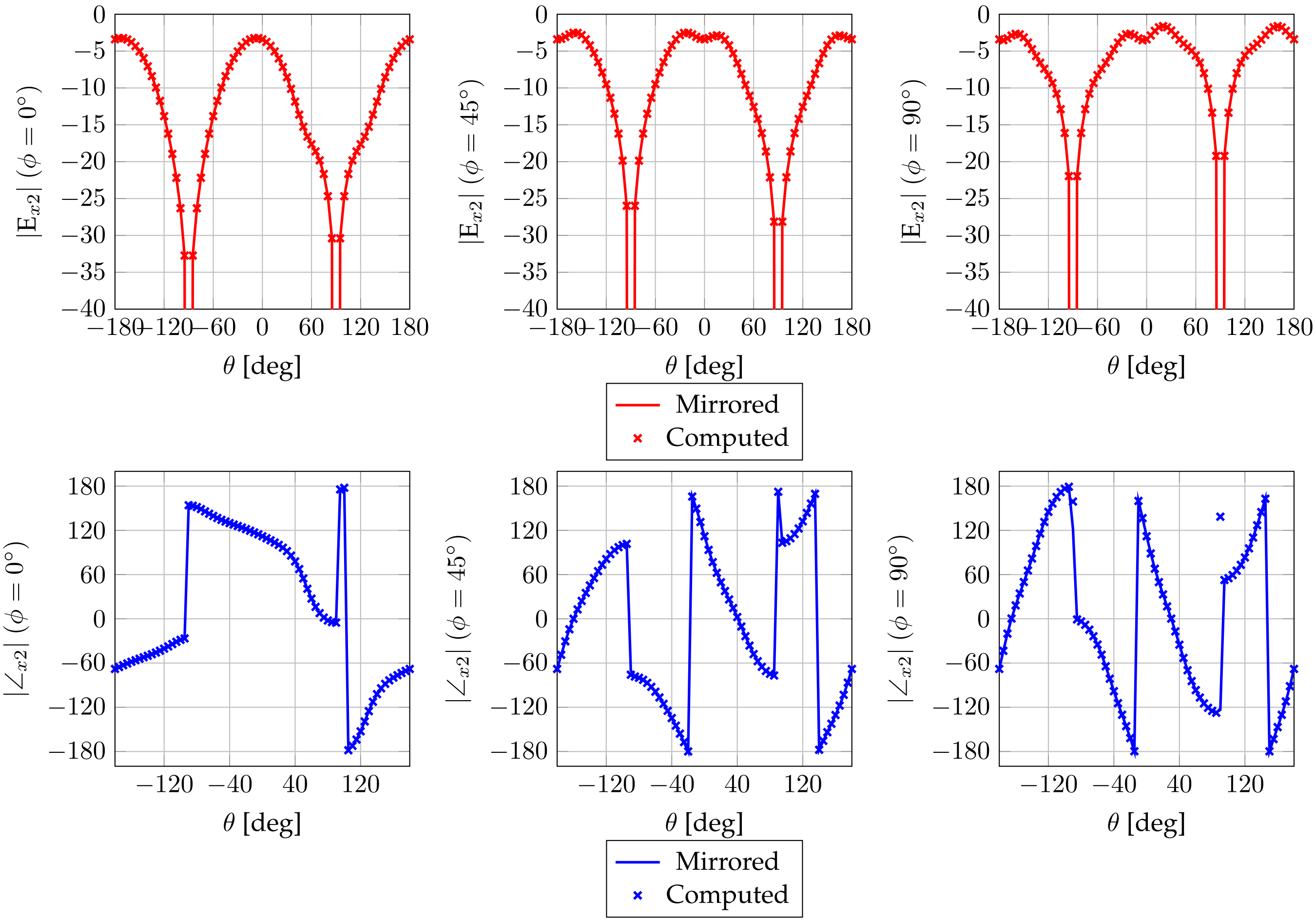

Figure B.7: Comparisons between mirrored and directly computed beam pattern cuts for port 7.

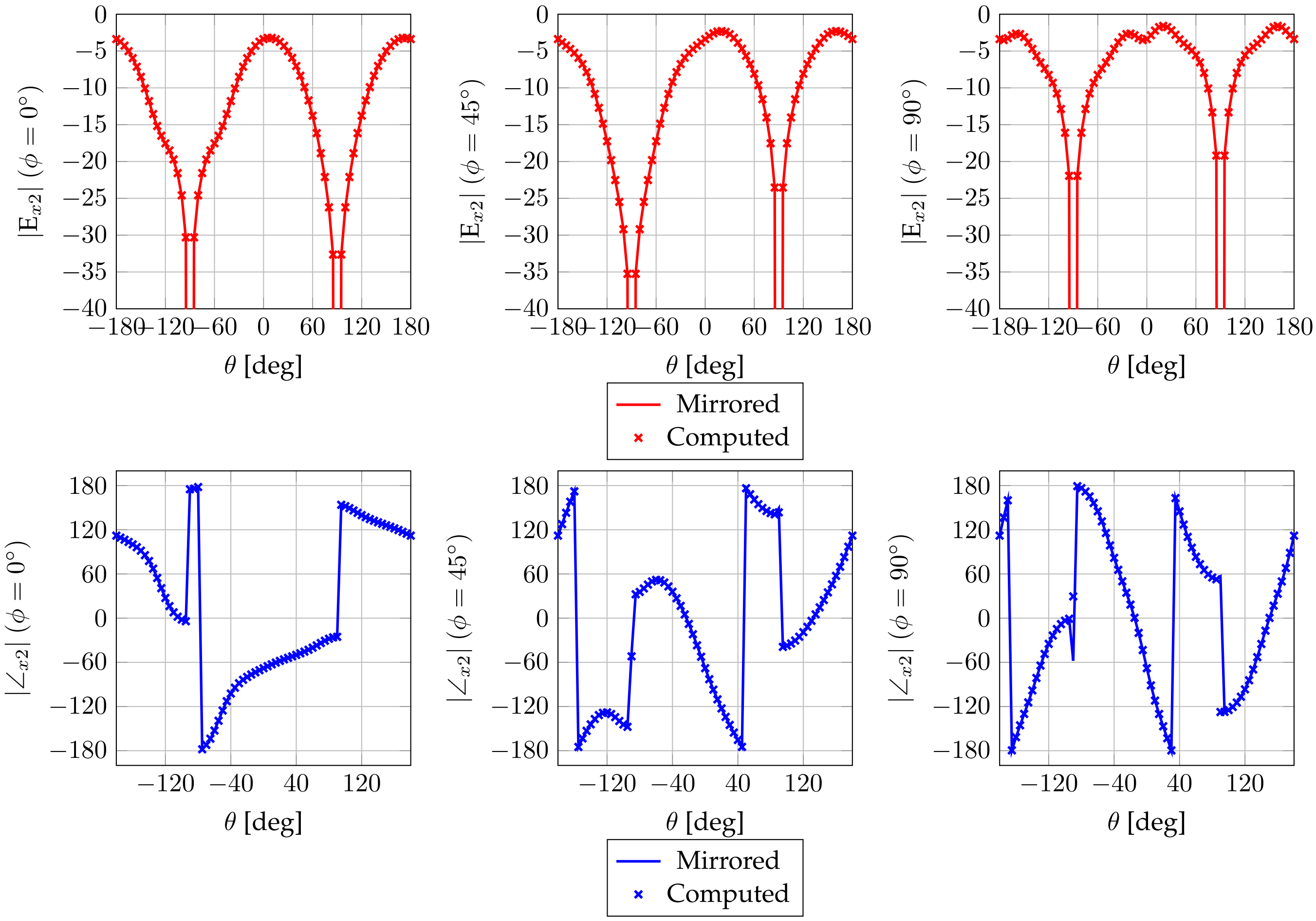

Figure B.8: Comparisons between mirrored and directly computed beam pattern cuts for port 8.

B.2 Testing of computing full beam from single port measurements

The following are plots testing the combining of single port patterns to produce a combined beam pattern. The phase is left wrapped for compactness.

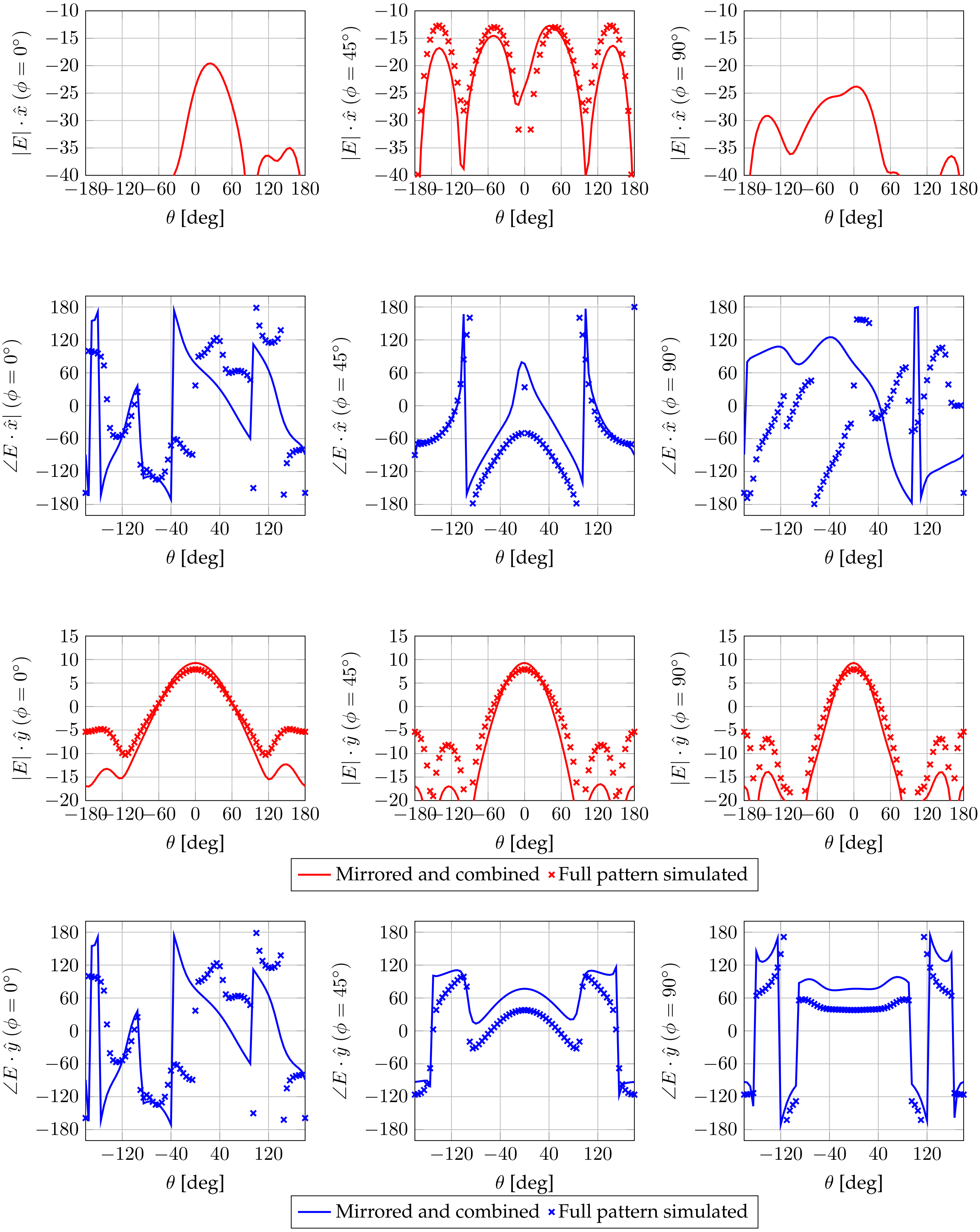

Figure B.9: Comparisons between mirrored patterns at 2 GHz and directly computed beam pattern cuts at 2 GHz.

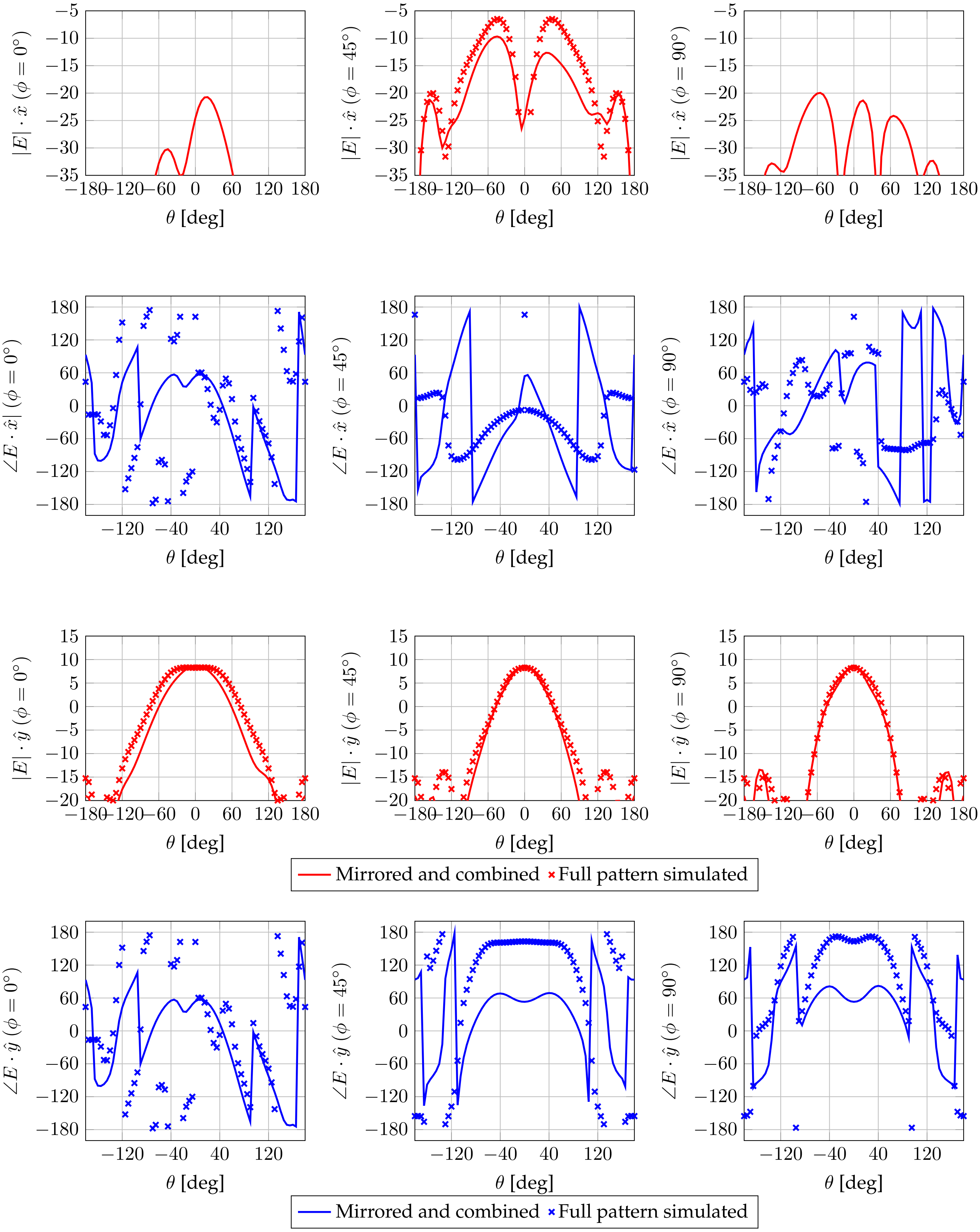

Figure B.10: Comparisons between mirrored patterns at 3.1 GHz and directly computed beam pattern cuts at 3.08 GHz.

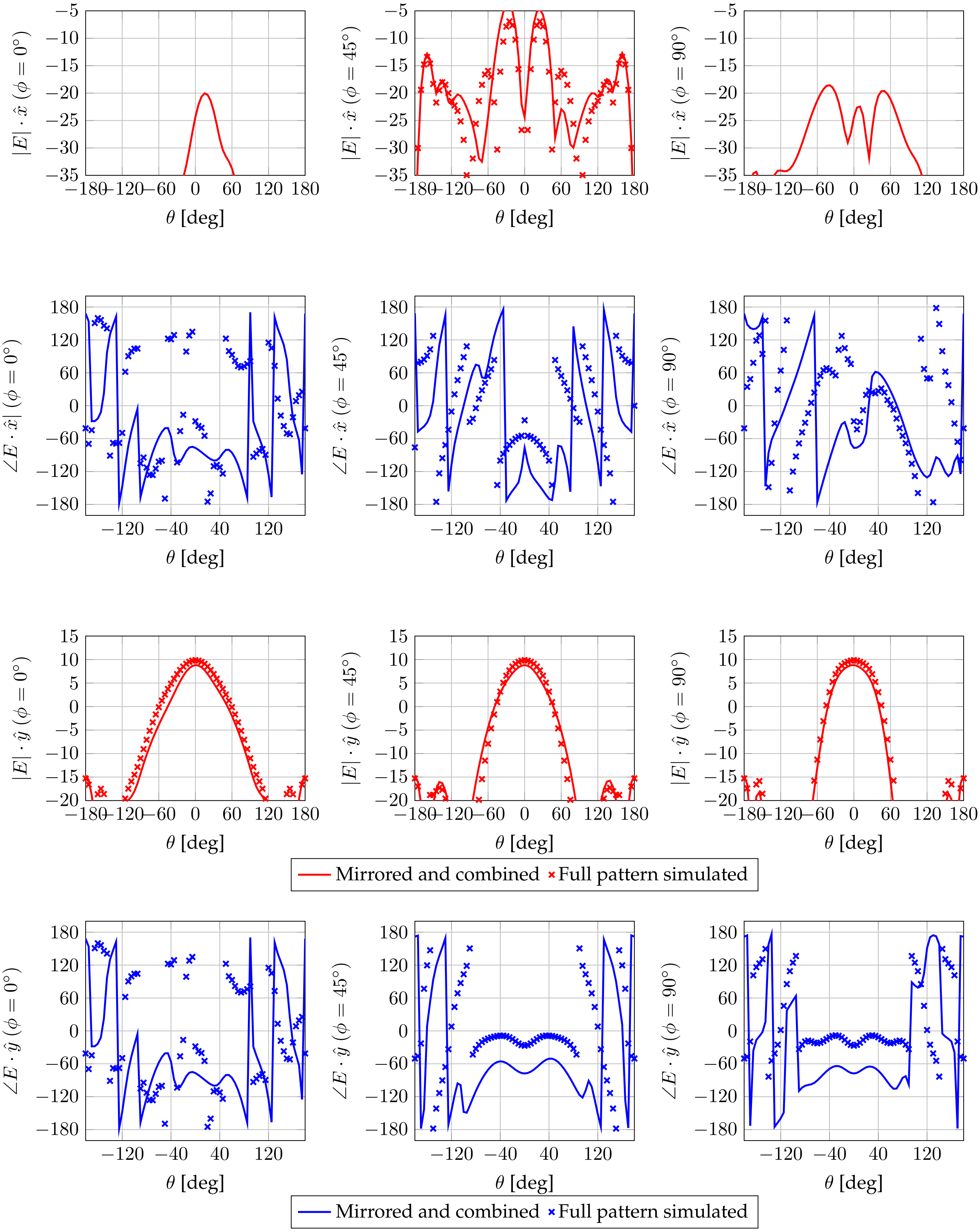

Figure B.11: Comparisons between mirrored patterns at 4 GHz and directly computed beam pattern cuts at 4.01 GHz.

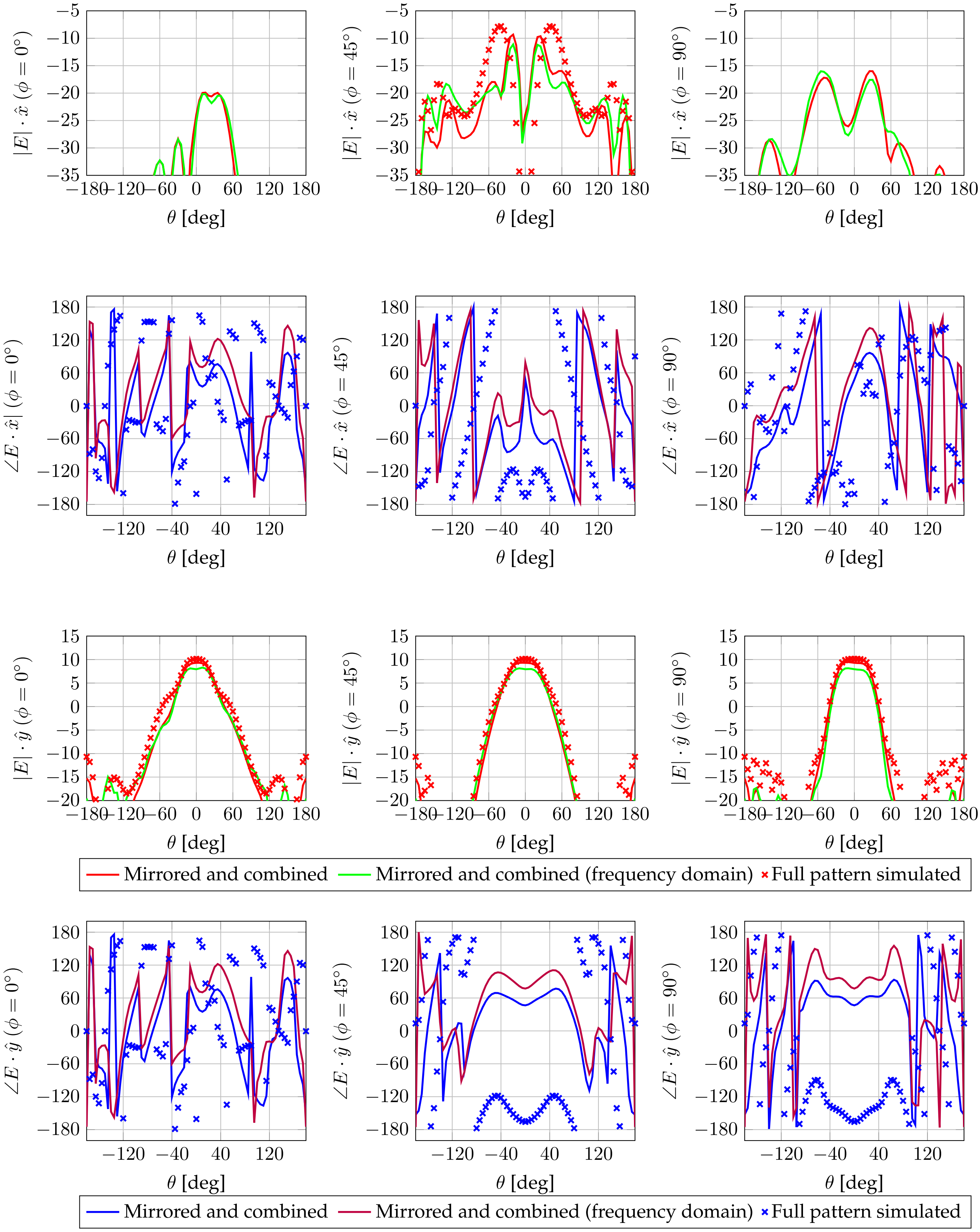

Figure B.12: Comparisons between mirrored patterns at 5 GHz and directly computed beam pattern cuts at 5.2 GHz (simulated in frequency domain).

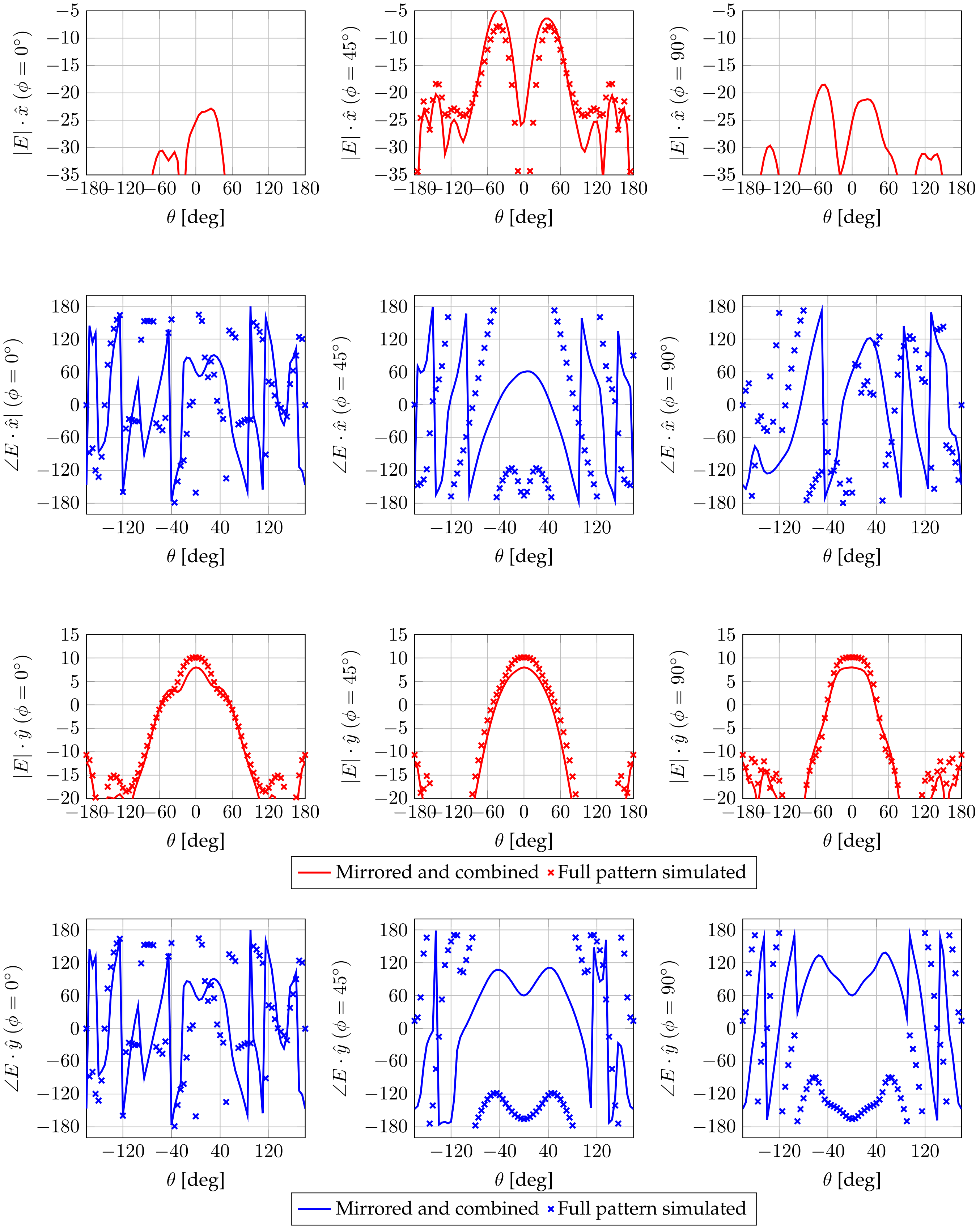

Figure B.13: Comparisons between mirrored patterns at 5.2 GHz and directly computed beam pattern cuts at 5.2 GHz.

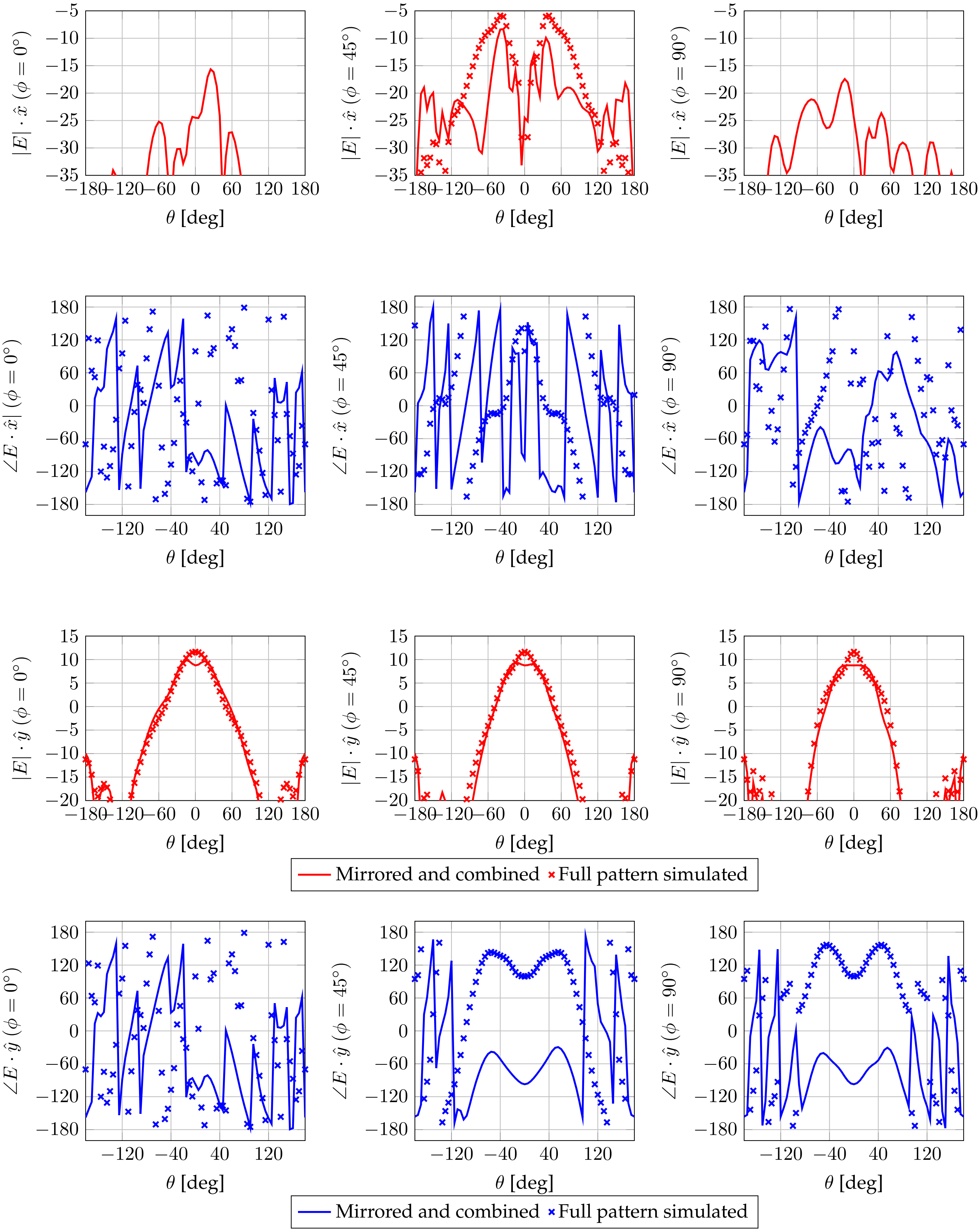

Figure B.14: Comparisons between mirrored patterns at 6.2 GHz and directly computed beam pattern cuts at 6.2 GHz.

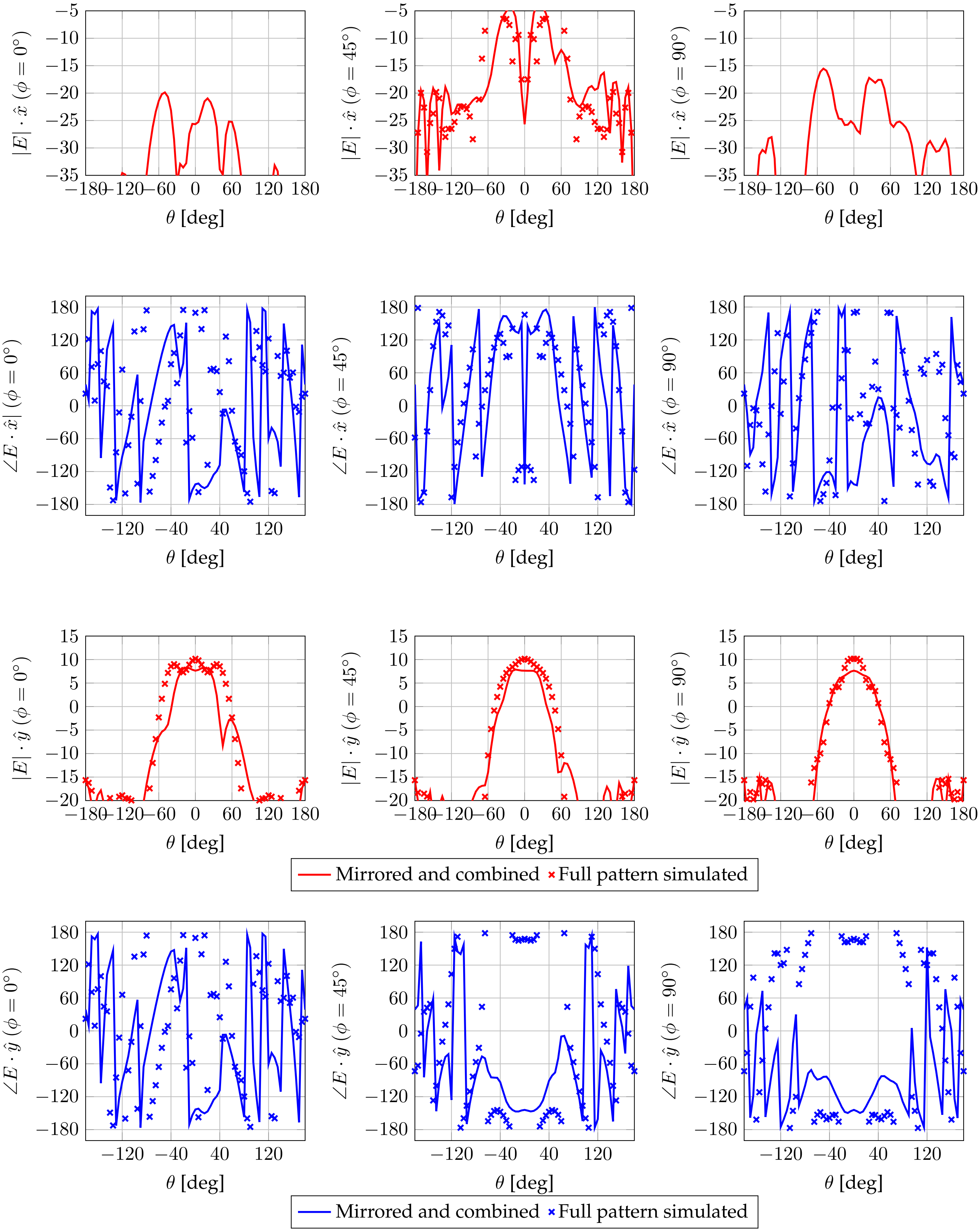

Figure B.15: Comparisons between mirrored patterns at 7.4 GHz and directly computed beam pattern cuts at 7.370 GHz.

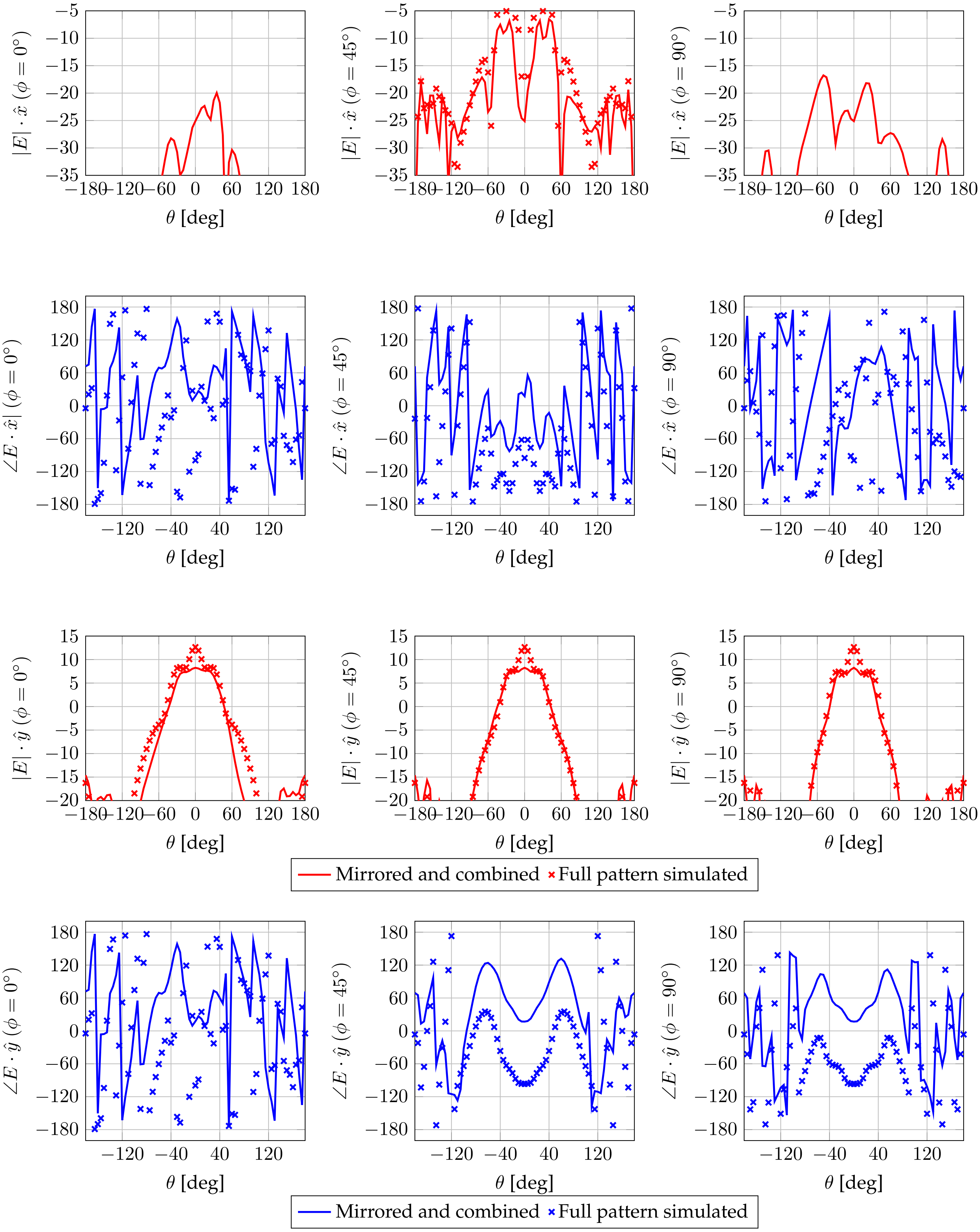

Figure B.16: Comparisons between mirrored patterns at 8 GHz and directly computed beam pattern cuts at 8.040 GHz.

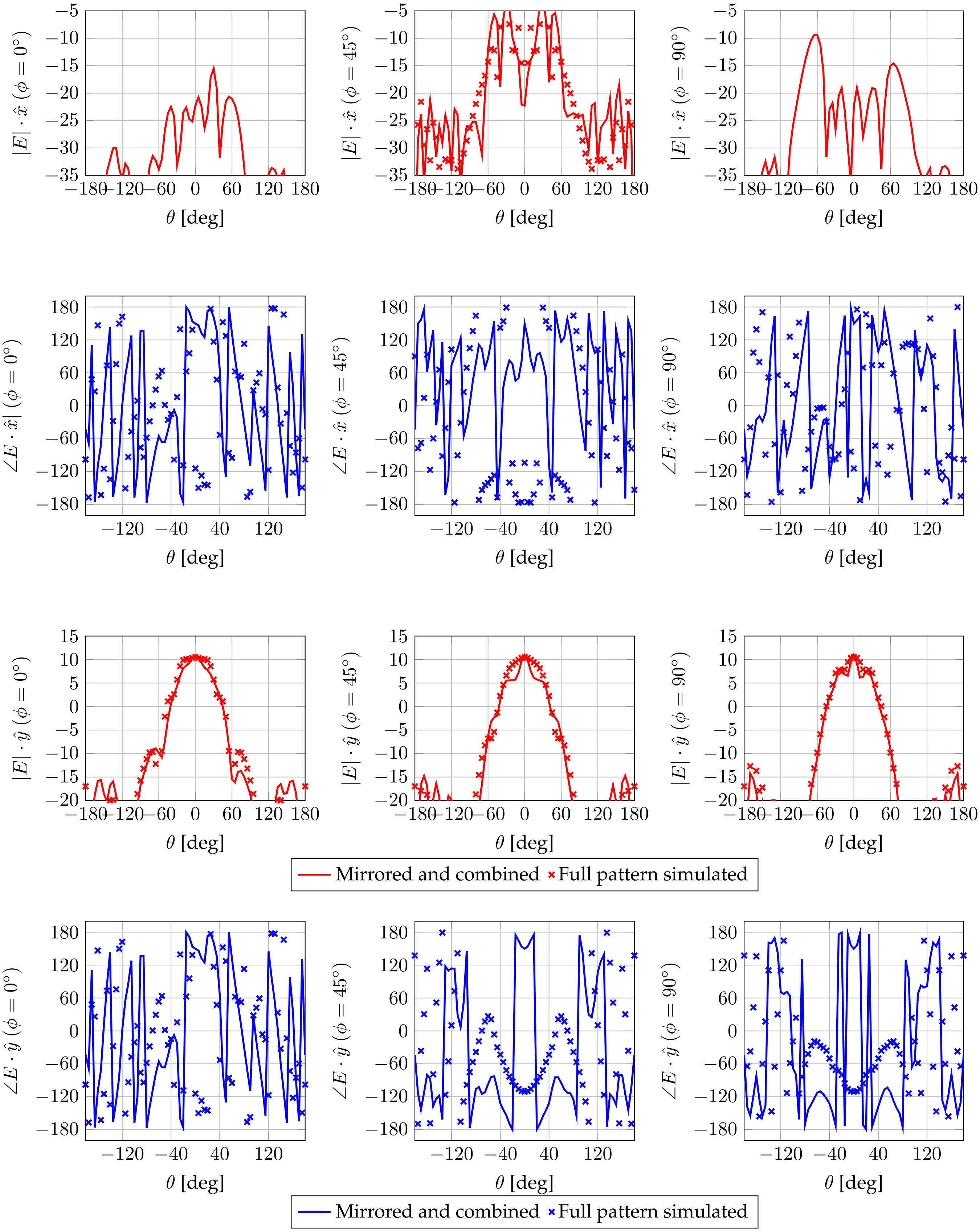

Figure B.17: Comparisons between mirrored patterns at 9.6 GHz and directly computed beam pattern cuts at 9.570 GHz.

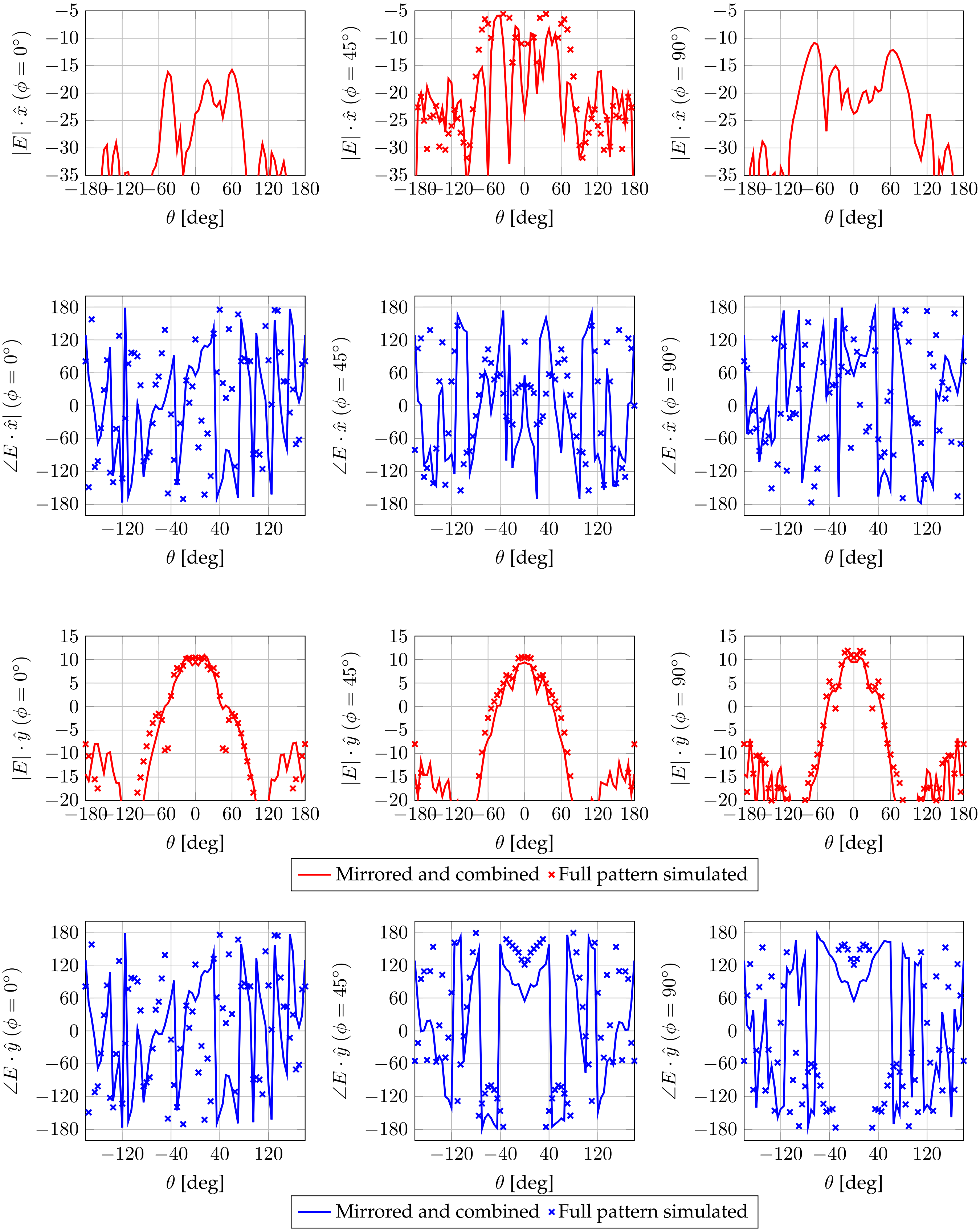

Figure B.18: Comparisons between mirrored patterns at 10.4 GHz and directly computed beam pattern cuts at 10.430 GHz.

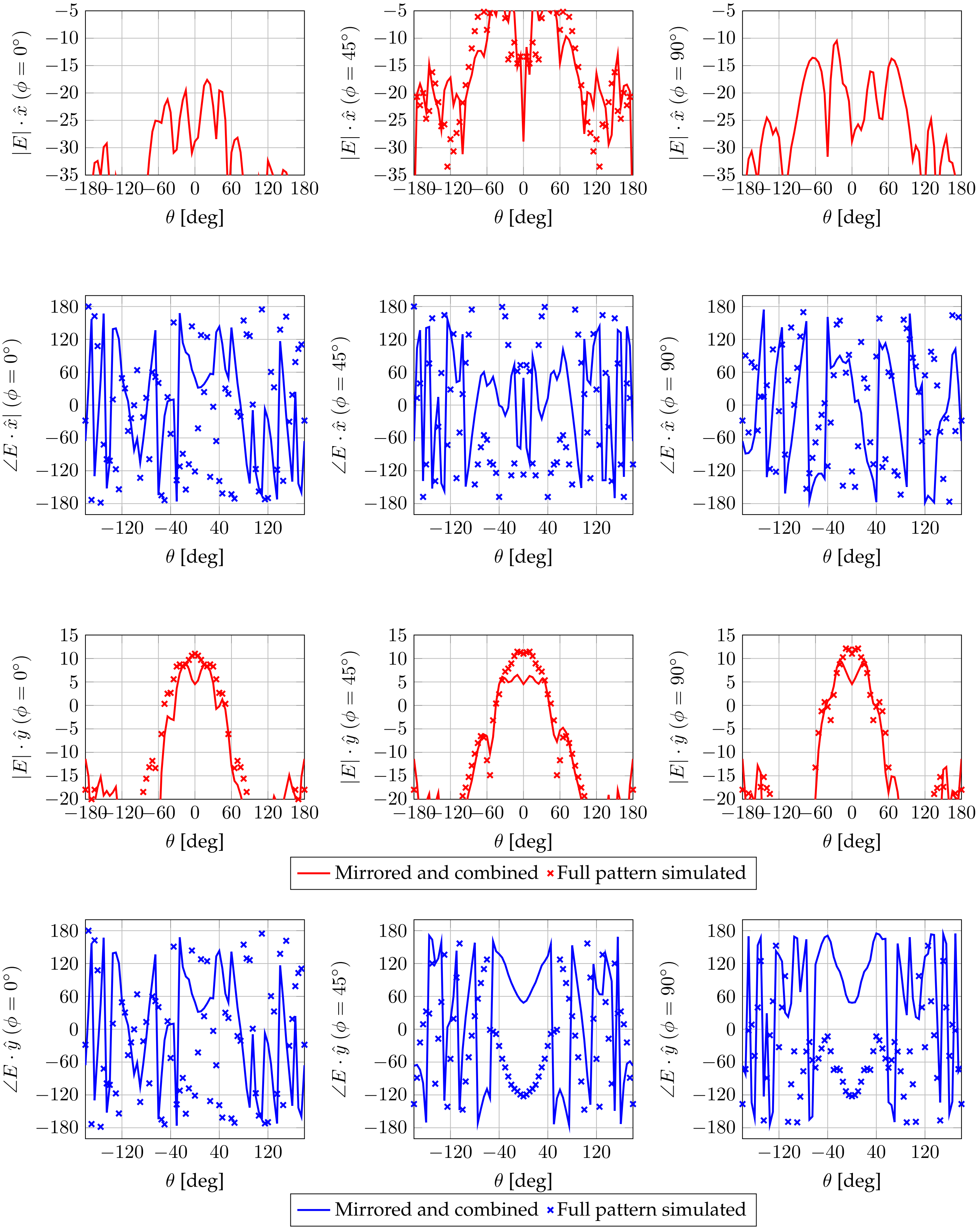

Figure B.19: Comparisons between mirrored patterns at 11.4 GHz and directly computed beam pattern cuts at 10.390 GHz.

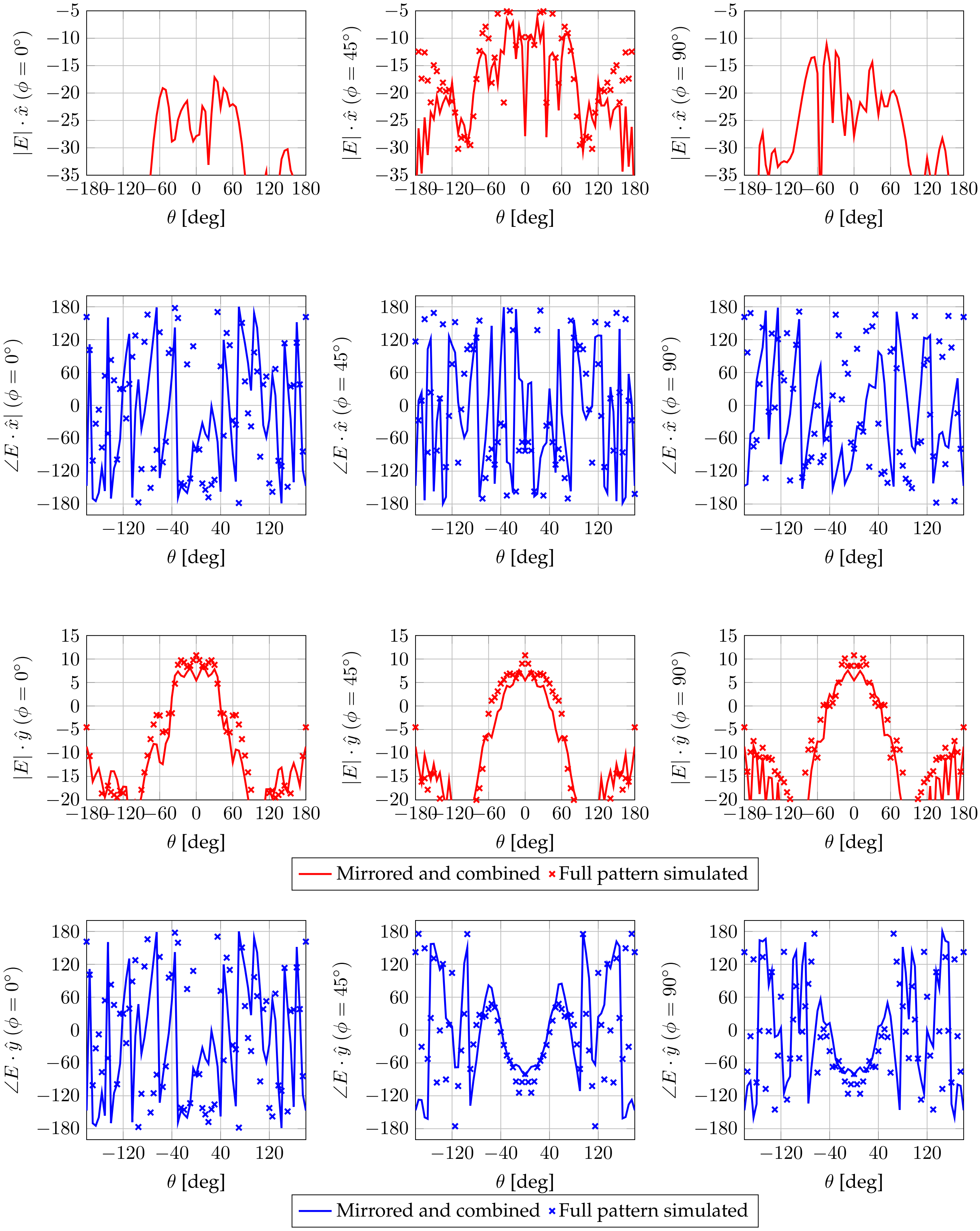

Figure B.20: Comparisons between mirrored patterns at 12 GHz and directly computed beam pattern cuts at 12.420 GHz.

Appendix C

Class function definitions

For the usage the readers is refered to the individual m–files.

C.1 `@gmsh` class

```
function Gms=addgmsh(Gms,Gmsa)

function Gms=addsurface(Gms,gms)

function Gms=addsurfaceSimp(Gms,gms)

function display(Gms)

function sv = get(Gms, prop)

function Gms = set(Gms, varargin)

function display(Gms)

function sv = getgmsh(Gms, prop)

function [lineloops lln] = getlineloops(Gms,lines)

function [lines linenums] = getlines(Gms,pnts)

function [xyz pnts] = getpnts(Gms)

function [surfaces] = getsurfaces(Gms,lineloops)

function mesh=readmsh(Gms,form)

function [meshout]=rungmsh(gms)

function Gms = set(Gms, varargin)
```

```
function Gms = translateGmsh(Gms, vect)

function write(Gms,compound)

function write(Gms,compound)
```

C.2 **`@gmshSurf`** class

```
function [gms pLl] = addlineloops(gms, lines)

function [gms pNC]=addpntsC(gms,xyzm ,msh)

function [gms pSL] = addsurfaceloops(gms, surfaces)

function gms = addsurfC(gms,gmsn, type ,vrb);

function [gms pV] = addvolume(gms, surfaceloops)

function display(gms)

function [meshout]=rungmshSurf(gms)

function gmsn = translateSurf(gms, vect)

function write(gms, initvalues)

function [gms pL] = addlines(gms, pnts ,ltype)

function [gms pN]=addpnts(gms,xyzm ,msh)

function [gms pS] = addsurfaces(gms, lineloops ,stype)

function gms = addsurf(gms,gmsn, type ,vrb);

function gms = createsurface(gms, xyzt ,xyzb)

function gms = getgmshSurf(gms,prop);

function mesh=readmsh(gms, form)

function gms = setgmshSurf(gms, varargin)

function writeC(gms, initvalues)

function write(gms, initvalues)
```

C.3 **`@WritepreFeko`** class

```
function [F ind] = AW(F, varargin)% s1, s2, s3, s4, ns, as, lpt,
    medt, aptgeom, ecfm,tem, tm, temm, mind, nind, mag, ph, rotang,
         % mexp, pasp)

function F = BP(F, s1,s2,s3,s4,msha,mshb,La)

function F = BQ(F,s1,s2,s3,s4,LA, varargin)

function F = BT(F, s1,s2,s3,a,b,c,La)

function F = CS(F, s1,s2,s3,s4,angBotStrt,angBotEnd,angTopStrt,
    angTopEnd,edgelenBot,edgelenTop, inflag, scale, LA)

function [F ind] = DA(F,Eopt, Hopt, FFopt, Copt, files, ind)

function F = DI(F, varargin) %, s1,s2,s3,s4,angBotStrt,angBotEnd,
    angTopStrt,angTopEnd,edgelenBot,edgelenTop,      inflag, scale,
    LA)

function displayWritePreFeko(a)

function F = DP(F, name, x, y, z, NurbW)

function F = DZ(F, s1,s2,s3,s4,ang, maxarc, med, LA, varargin)

function [F ind] = FE(F, calculation, ind, varargin)

function [F ind] = FF(F, fieldpos, ind, varargin)

function F = FM(F, varargin)

function F = FR(F, modes ,varargin)

function F = header(F, header, ign)

function F = IP(F, Wr, Tl, Ws, Cbl, Ttl)

function F = KK(F, s1,s2,s3,s4,angBotStrt,angBotEnd,angTopStrt,
    angTopEnd,edgelenBot,edgelenTop, inflag, scale, La, MEkr)

function [ch ind] = KKxy(ch, xzS, xzE, xR, y, angV, mshC,ind, La)

function [ch ind] = KKxz(ch, xzS, xzE, xR, y, angV, mshC,ind, La)

function F = KR(F, s1,s2,s3,s4, ang, edgelenOut,edgelenIn, scale,
    LA, MEkr)

function F = LA(F,string, ind)

function F = LE(F, Mode, varargin)
```

```
function [F ind] = MB(F,name,s1,s2,s3)

function F=nodes2tri(F,nodes,name,msh,La);

function F = notes(F, notes)

function [F ind] = OS(F, calculation, ind, varargin)

function F = PB(F, s1,s2,s3,s4,subang,maxtri,LA,MEkr)

function F = PH(F, s1,s2,s3,s4,s5, maxedge, scale, LA)

function F = PHsq(F, cornp, rad, pname, maxedge, LA)

function F = PM(F,pnts, msh, varargin)

function F = PW(F, modes, varargin)

function [y] = read(F,typ)

function F = RM(F, RMmode, mshsize, varargin)

function F = SF(F, scale)

function [F ind] = SP (F, A, R, Z0, ind)

function F = SY(F,xyz,label)

function F = TG(F, numcopies, labelstr, labelend, incr, rot, tran,
    mirror, scale, includes)

function F = varsA(F, varName, varValues)

function F = vars(F, varName, varValue)

function write(F)

function F = ZY(F, s1,s2,s3,ang,edgelen,scale,inflag,LA,MEzy)
```

Appendix D

Mode matching theory

D.1 Introduction

The principles of Mode Matching where first formally presented in the late 1960s and the early 70s, and, with the increase in available computational power, have become a very useful numerical technique. Existing software is available, but due to a desire for flexibility and user understanding custom code is preferred.

The operating principle is to describe a section of waveguide, by decomposing the EM waves within it into the constituent modes. The steps required to solve for the modes is to solve for the waves, given the geometry and fields, assuming a potential function. The boundary conditions are used to solve for the mode coefficients. Depending on the discretization, sometimes evanescent modes are required.

Once the form of the modes is known, the behaviour of the guide is solved for by step by step solving for the coupling coefficients between sections of the guide, most often straight planar sections are used as an approximation for the guide. Spherical propagation is possible, but is very guide specific.

D.2 Theory

The theory of Mode Matching has been extensively covered in many papers and text books, starting in the 1960s to the present day. The theory here is based on the general case as described by *Masterman* and *Clarricoats* [93]. The advantage of this formulation is it avoids the need to normalise the mode terms. The theory is presented here for completeness and so that their is no confusion of later use of terms and implementation. The problem is shown in fig. D.1.

If we consider that surface S contains k apertures described by a surface S_k. The fields within waveguide one can be described as a series of orthogonal modes. Given the condition of orthogonality, this means that:

$$\int_S \boldsymbol{e}_i \times \boldsymbol{h}_j \,\mathrm{d}s = 0 \text{ and } \int_{S'} \boldsymbol{e}'_i \times \boldsymbol{h}'_j \,\mathrm{d}s = 0 \;;\; i \neq j \tag{D.1}$$

The fields in each waveguide can be expressed as a sum of these orthogonal fields such that, the transverse fields $\boldsymbol{E}_T$ are given by:

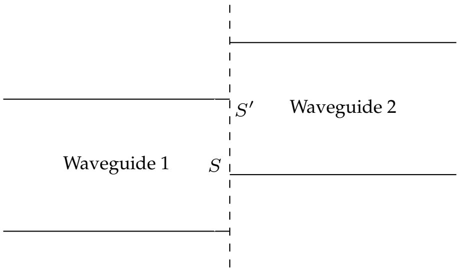

Figure D.1: General waveguide discontinuity

Waveguide 1:

$$\boldsymbol{E}_T = \sum_{m=1}^{\infty} (a_{im} + a_{rm}) \boldsymbol{e}_m \tag{D.2a}$$

$$\boldsymbol{H}_T = \sum_{m=1}^{\infty} (a_{im} - a_{rm}) \boldsymbol{h}_m, \tag{D.2b}$$

Waveguide 2:

$$\boldsymbol{E}'_T = \sum_{n=1}^{\infty} (a'_{in} + a'_{rn}) \boldsymbol{e}'_n \tag{D.3a}$$

$$\boldsymbol{H}'_T = \sum_{n=1}^{\infty} (a'_{in} - a'_{rn}) \boldsymbol{h}'_n, \tag{D.3b}$$

Where the i modes indicate incident and r the reflected waves. The goal is to calculate these coefficients. To solve this, we introduce an expression for the fields at the discontinuity. We can represent the fields within the apertures, in a similar manner, such that, for the kth aperture:

$$\boldsymbol{E}_{Tk} = \sum_{i=1}^{\infty} b_{ki} \boldsymbol{e}_{ki} \text{ and } \boldsymbol{H}_{Tk} = \sum_{i=1}^{\infty} c_{ki} \boldsymbol{h}_{ki} \tag{D.4}$$

Where, as before the modes are orthogonal:

$$\int_{S_k} \boldsymbol{e}_{ki} \times \boldsymbol{h}_{kj} \, \mathrm{d}s = 0 \; ; \; ki \neq kj \tag{D.5}$$

If we can solve for the b and c coefficients, we can solve for the desired a and a' coefficients. It is noted that the fields expressed in eq. (D.4) do not represent the actual fields, but rather are used as a mathematical tool to solve for the real fields in the waveguides. The fields must be continuous. Considering the kth aperture:

Over the kth apeture:

$$\boldsymbol{E}_{Tk} = \sum_{m=1}^{\infty} (a_{im} + a_{rm}) \boldsymbol{e}_m = \sum_{i=1}^{\infty} b_{ki} \boldsymbol{e}_{ki} = \sum_{n=1}^{\infty} (a'_{im} + a'_{rm}) \boldsymbol{e}'_n \tag{D.6a}$$

$$\boldsymbol{H}_{Tk} = \sum_{m=1}^{\infty} (a_{im} - a_{rm}) \boldsymbol{h}_m = \sum_{i=1}^{\infty} c_{ki} \boldsymbol{h}_{ki} = \sum_{n=1}^{\infty} (a'_{im} - a'_{rm}) \boldsymbol{h}'_n, \tag{D.6b}$$

Using eq. (D.6a), if we obtain the cross product with h_M and integrate over the kth aperture we get the set of equations:

$$\sum_{m=1}^{\infty}(a_{im}+a_{rm})\int_{S_k}\boldsymbol{e}_m\times\boldsymbol{h}_M\ \mathrm{d}s=\sum_{i=1}^{\infty}b_{ki}\int_{S_k}\boldsymbol{e}_{ki}\times\boldsymbol{h}_M\ \mathrm{d}s\ ;\ M=1,2,3\cdots\infty \tag{D.7}$$

If we define the surface around P apertures as $S_0=S-\sum_{k=1}^{P}S_k$. Then as the field must vanish across this surface:

$$\sum_{m=1}^{\infty}(a_{im}+a_{rm})\int_{S_0}\boldsymbol{e}_m\times\boldsymbol{h}_M\ \mathrm{d}s=0 \tag{D.8}$$

We can sum over all P apertures in eq. (D.7), and apply the orthogonality condition given by eq. (D.1), to give:

$$a_{iM}+a_{rM}=\frac{\sum_{k=1}^{P}\sum_{i=1}^{\infty}b_{ki}\int_{S_k}\boldsymbol{e}_{ki}\times\boldsymbol{h}_M\ \mathrm{d}s}{\int_{S}\boldsymbol{e}_M\times\boldsymbol{h}_M\ \mathrm{d}s} \tag{D.9}$$

And similarly for waveguide 2:

$$a'_{iN}+a'_{rN}=\frac{\sum_{k=1}^{P}\sum_{i=1}^{\infty}b_{ki}\int_{S_k}\boldsymbol{e}_{ki}\times\boldsymbol{h}'_N\ \mathrm{d}s}{\int_{S'}\boldsymbol{e}'_N\times\boldsymbol{h}'_N\ \mathrm{d}s} \tag{D.10}$$

Using eq. (D.6b), we can similarly obtain the cross product with e_I and integrate over the kth aperture we get the set of equations:

$$\sum_{m=1}^{\infty}(a_{im}-a_{rm})\int_{S_k}\boldsymbol{e}_{kI}\times\boldsymbol{h}_m\ \mathrm{d}s=\sum_{i=1}^{\infty}c_{ki}\int_{S_k}\boldsymbol{e}_{kI}\times\boldsymbol{h}_i\ \mathrm{d}s\ ;\ I=1,2,3\cdots\infty \tag{D.11}$$

As before applying eq. (D.5), all but the $i=I$ term disappears, gives us:

$$c_{kI}=\frac{\sum_{m=1}^{\infty}(a_{im}-a_{rm})\int_{S_k}\boldsymbol{e}_{kI}\times\boldsymbol{h}_m\ \mathrm{d}s}{\int_{S_k}\boldsymbol{e}_{kI}\times\boldsymbol{h}_i\ \mathrm{d}s} \tag{D.12}$$

Similarly for the other terms in eq. (D.6b).

$$c_{kI}=\frac{\sum_{n=1}^{\infty}(a'_{in}-a'_{rn})\int_{S_k}\boldsymbol{e}_{kI}\times\boldsymbol{h}'_n\ \mathrm{d}s}{\int_{S_k}\boldsymbol{e}_{kI}\times\boldsymbol{h}_{kI}\ \mathrm{d}s} \tag{D.13}$$

We are now in the position to solve eqs. (D.9), (D.10), (D.12) and (D.13). The series are truncated, to p and p' modes in waveguide 1 and 2 respectively and the modes in aperture k is truncated to q_k, so that:

$$\begin{aligned}m&\leq p, M\leq p\\ n&\leq p', N\leq p'\\ i&\leq q_k, I\leq q_k\end{aligned}$$

We can now write out eq. (D.9) in matrix form:

$$\begin{bmatrix} a_{i1} \\ a_{i2} \\ \vdots \\ a_{ip} \end{bmatrix} + \begin{bmatrix} a_{r1} \\ a_{r2} \\ \vdots \\ a_{rp} \end{bmatrix} = \begin{bmatrix} R_1(1,1) & \cdots & R_1(1,q_1) & & R_P(1,1) & \cdots & R_P(1,q_P) \\ \vdots & & \vdots & \cdots & \vdots & & \vdots \\ R_1(p,1) & \cdots & R_1(p,q_1) & & R_P(p,1) & \cdots & R_P(p,q_P) \end{bmatrix} \begin{bmatrix} b_{11} \\ \vdots \\ b_{1q_1} \\ \vdots \\ b_{P1} \\ \vdots \\ b_{Pq_P} \end{bmatrix} \tag{D.14}$$

Where:

$$R_k(i,j) = \frac{\int_{S_k} \boldsymbol{e}_{kj} \times \boldsymbol{h}_i \, \mathrm{d}s}{\int_S \boldsymbol{e}_i \times \boldsymbol{h}_i \, \mathrm{d}s} \tag{D.15}$$

For ease eq. (D.14) is written compactly as:

$$\mathsf{a}_i + \mathsf{a}_r = \mathsf{R}\mathsf{b} \tag{D.16}$$

Setting $q_T = \sum_{k=1}^{P} q_k$, R has dimensions $p \times qT$, and b has dimensions $qT \times 1$. Similarly from eq. (D.10):

$$\mathsf{a}'_i + \mathsf{a}'_r = \mathsf{R}'\mathsf{b} \tag{D.17}$$

Similarly R' has dimensions $p' \times qT$ elements, and

$$R'_k(i,j) = \frac{\int_{S_k} \boldsymbol{e}_{kj} \times \boldsymbol{h}'_i \, \mathrm{d}s}{\int_{S'} \boldsymbol{e}'_i \times \boldsymbol{h}'_i \, \mathrm{d}s} \tag{D.18}$$

Putting eq. (D.12) in matrix form gives:

$$\begin{bmatrix} c_{11} \\ \vdots \\ c_{1q_1} \\ \vdots \\ c_{P1} \\ \vdots \\ c_{Pq_P} \end{bmatrix} = \begin{bmatrix} S_1(1,1) & \cdots & S_1(1,p) \\ \vdots & & \vdots \\ S_1(q_1,1) & \cdots & S_1(q_1,p) \\ \vdots & & \vdots \\ S_P(1,1) & \cdots & S_P(1,p) \\ \vdots & & \vdots \\ S_P(q_P,1) & \cdots & S_P(q_P,p) \end{bmatrix} \begin{bmatrix} a_{i1} - ar1 \\ \vdots \\ \vdots \\ \vdots \\ \vdots \\ a_{iP} - a_{rP} \end{bmatrix} \tag{D.19}$$

Where:

$$S_k(i,j) = \frac{\int_{S_k} \boldsymbol{e}_{ki} \times \boldsymbol{h}_j \, \mathrm{d}s}{\int_{Sk} \boldsymbol{e}_{ki} \times \boldsymbol{h}_{ki} \, \mathrm{d}s} \tag{D.20}$$

Matrix eq. (D.19) in compact form:

$$\mathsf{c} = \mathsf{S}\mathsf{a}_i - \mathsf{S}\mathsf{a}_r \tag{D.21}$$

The c has qT elements, S has dimensions $qT \times p$. Similarly for eq. (D.13):

$$\mathsf{c} = \mathsf{S}'\mathsf{a}_i' - \mathsf{S}'\mathsf{a}_r' \tag{D.22}$$

Where:

$$S_k'(i,j) = \frac{\int_{S_k} \boldsymbol{e}_{ki} \times \boldsymbol{h}_j' \, \mathrm{d}s}{\int_{Sk} \boldsymbol{e}_{ki} \times \boldsymbol{h}_{ki} \, \mathrm{d}s} \tag{D.23}$$

It is now possible to solve for a_r given an excitation a_i. Multiply eq. (D.16) by S:

$$\mathsf{S}\mathsf{a}_i + \mathsf{S}\mathsf{a}_r = \mathsf{SRb}$$

and substituting eq. (D.21):

$$\begin{aligned} \mathsf{S}\mathsf{a}_i + [\mathsf{S}\mathsf{a}_i - \mathsf{c}] &= \mathsf{SRb} \\ \mathsf{c} &= 2\mathsf{S}\mathsf{a}_i - \mathsf{SRb} \end{aligned} \tag{D.24}$$

Similarly from eqs. (D.17) and (D.22):

$$\mathsf{c} = \mathsf{S}'\mathsf{R}'\mathsf{b} - 2\mathsf{S}'\mathsf{a}_i' \tag{D.25}$$

By eqs. (D.24) and (D.25) we get the equation relating a_i and a_r to b:

$$\begin{aligned} 2\mathsf{S}\mathsf{a}_i - \mathsf{SRb} &= \mathsf{S}'\mathsf{R}'\mathsf{b} - 2\mathsf{S}'\mathsf{a}_i' \\ [\mathsf{SR} + \mathsf{S}'\mathsf{R}']\mathsf{b} &= 2\mathsf{S}\mathsf{a}_i + 2\mathsf{S}'\mathsf{a}_i' \\ \mathsf{b} &= [\mathsf{SR} + \mathsf{S}'\mathsf{R}']^{-1}[2\mathsf{S}\mathsf{a}_i + 2\mathsf{S}'\mathsf{a}_i'] \end{aligned} \tag{D.26}$$

Once b has been solved for, it can be substituted into eqs. (D.16) and (D.17), to find the desired reflected coefficients a_r and a_r', as follows:

$$\mathsf{a}_r = \mathsf{R}[\mathsf{SR} + \mathsf{S}'\mathsf{R}']^{-1}[2\mathsf{S}\mathsf{a}_i + 2\mathsf{S}'\mathsf{a}_i'] - \mathsf{a}_i \tag{D.27}$$

$$\mathsf{a}_r' = \mathsf{R}'[\mathsf{SR} + \mathsf{S}'\mathsf{R}']^{-1}[2\mathsf{S}\mathsf{a}_i + 2\mathsf{S}'\mathsf{a}_i'] - \mathsf{a}_i' \tag{D.28}$$

These represent the set of simultaneous equations to be solved.

D.3 Rectangular modes

Solving for the classic case where:

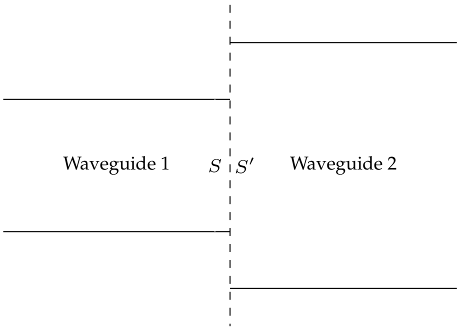

Figure D.2: Rectangual waveguide discontinuity

The equations for the square waveguides are given by, for TE modes:

$$e_{TEx} = \frac{j\mu w k_{\mathrm{y}}}{k_{\mathrm{c}}^2} \cos(x k_{\mathrm{x}}) \sin(y k_{\mathrm{y}}) \tag{D.29}$$

$$e_{TEy} = \frac{-j\mu w k_{\mathrm{x}}}{k_{\mathrm{c}}^2} \sin(x k_{\mathrm{x}}) \cos(y k_{\mathrm{y}}) \tag{D.30}$$

$$e_{TEz} = 0 \tag{D.31}$$

$$h_{TEx} = \frac{\gamma k_{\mathrm{x}}}{k_{\mathrm{c}}^2} \sin(x k_{\mathrm{x}}) \cos(y k_{\mathrm{y}}) \tag{D.32}$$

$$h_{TEy} = \frac{\gamma k_{\mathrm{y}}}{k_{\mathrm{c}}^2} \cos(x k_{\mathrm{x}}) \sin(y k_{\mathrm{y}}) \tag{D.33}$$

$$h_{TEz} = \cos(x k_{\mathrm{x}}) \sin(y k_{\mathrm{y}}) \tag{D.34}$$

and for TM modes,

$$e_{TMx} = \frac{\gamma k_{\mathrm{x}}}{k_{\mathrm{c}}^2} \cos(x k_{\mathrm{x}}) \sin(y k_{\mathrm{y}}) \tag{D.35}$$

$$e_{TMy} = \frac{\gamma k_{\mathrm{y}}}{k_{\mathrm{c}}^2} \sin(x k_{\mathrm{x}}) \cos(y k_{\mathrm{y}}) \tag{D.36}$$

$$e_{TMz} = \sin(x k_{\mathrm{x}}) \cos(y k_{\mathrm{y}}) \tag{D.37}$$

$$h_{TMx} = \frac{-j\varepsilon w k_{\mathrm{y}}}{k_{\mathrm{c}}^2} \sin(x k_{\mathrm{x}}) \cos(y k_{\mathrm{y}}) \tag{D.38}$$

$$h_{TMy} = \frac{\varepsilon j w k_{\mathrm{x}}}{k_{\mathrm{c}}^2} \cos(x k_{\mathrm{x}}) \sin(y k_{\mathrm{y}}) \tag{D.39}$$

$$h_{TMz} = 0 \tag{D.40}$$

Where $\gamma^2 = k_{\mathrm{c}}^2 - k^2$, $k_{\mathrm{c}}^2 = k_{\mathrm{x}}^2 + k_{\mathrm{y}}^2$, $k_{\mathrm{x}} = \frac{m\pi}{a}$, $k_{\mathrm{y}} = \frac{n\pi}{b}$ and $k^2 = w^2 \mu_0 \varepsilon_0$.

D.4 Solving the cross products

Separating eq. (D.23) into the top and bottom terms, the top term we need to integrate is given as:

$$\begin{aligned} S'_{top_{i,j}} &= \boldsymbol{e}_{iL} \times \boldsymbol{h}_{jR} \cdot \hat{z} && \text{(D.41)} \\ &= \begin{vmatrix} \hat{x} & \hat{y} & \hat{z} \\ e_{iLx} & e_{iLy} & e_{iLz} \\ h_{jRx} & h_{jRy} & h_{jRz} \end{vmatrix} \cdot \hat{z} && \text{(D.42)} \\ &= e_{iLx} h_{jRy} - e_{iLy} h_{jRx} && \text{(D.43)} \end{aligned}$$

Dropping the i, j indices for conciseness and splitting this into; TETE, TMTM, TETM and TMTE.

Starting with TETE:

$$\begin{aligned} S_{TETE_{i,j}} =& e_{x_L} h_{y_R} - e_{y_L} h_{x_R} \\ =& e_{TEx_L} h_{TEy_R} - e_{TEy_L} h_{TEx_R} \\ =& \frac{j\mu w \gamma_R}{k_{c_R}^2 k_{c_L}^2} \big[k_{y_L} k_{y_R} \cos(x k_{x_L}) \cos(x k_{x_R}) \sin(y k_{y_L}) \sin(y k_{y_R}) \\ & + k_{x_L} k_{x_R} \sin(x k_{x_L}) \sin(x k_{x_R}) \cos(y k_{y_L}) \cos(y k_{y_R}) \big] && \text{(D.44)} \end{aligned}$$

For TMTM:

$$\begin{aligned} S_{TMTM_{i,j}} =& e_{x_L} h_{y_R} - e_{y_L} h_{x_R} \\ =& e_{TMx_L} h_{TMy_R} - e_{TMy_L} h_{TMx_R} \\ =& \frac{\varepsilon j w \gamma_L}{k_{c_L}^2 k_{c_R}^2} \big[k_{x_L} k_{x_R} \cos(x k_{x_L}) \cos(x k_{x_R}) \sin(y k_{y_L}) \sin(y k_{y_R}) \\ & + k_{y_L} k_{y_R} \sin(x k_{x_L}) \sin(x k_{x_R}) \cos(y k_{y_L}) \cos(y k_{y_R}) \big] && \text{(D.45)} \end{aligned}$$

For TETM:

$$\begin{aligned} S_{TETM_{i,j}} =& e_{x_L} h_{y_R} - e_{y_L} h_{x_R} \\ =& e_{TEx_L} h_{TMy_R} - e_{TEy_L} h_{TMx_R} \\ =& \frac{\varepsilon \mu w^2}{k_{c_L}^2 k_{c_R}^2} \big[k_{x_L} k_{y_R} \sin(x k_{x_L}) \sin(x k_{x_R}) \cos(y k_{y_L}) \cos(y k_{y_R}) \\ & - k_{y_L} k_{x_R} \cos(x k_{x_L}) \cos(x k_{x_R}) \sin(y k_{y_L}) \sin(y k_{y_R}) \big] && \text{(D.46)} \end{aligned}$$

For TMTE:

$$\begin{aligned} S_{TMTE_{i,j}} =& e_{x_L} h_{y_R} - e_{y_L} h_{x_R} \\ =& e_{TMx_L} h_{TEy_R} - e_{TMy_L} h_{TEx_R} \\ =& \frac{\gamma_L \gamma_R}{k_{c_L}^2 k_{c_R}^2} \big[k_{x_L} k_{y_R} \cos(x k_{x_L}) \cos(x k_{x_R}) \sin(y k_{y_L}) \sin(y k_{y_R}) \\ & - k_{y_L} k_{x_R} \sin(x k_{x_L}) \sin(x k_{x_R}) \cos(y k_{y_L}) \cos(y k_{y_R}) \big] && \text{(D.47)} \end{aligned}$$

To solve the method, we need to solve the integral $\int_S S_{mn}\mathrm{d}s = \int_0^{a_L}\int_0^{b_L} S_{mn}(x,y)\mathrm{d}x\mathrm{d}y$. Clearly we can separate variables and rearrange the integrals so the only integrals we need to solve are: $\int \cos(b_1 u)\cos(b_2 u)\mathrm{d}u$ and $\int \sin(b_1 u)\sin(b_2 u)\mathrm{d}u$, which can be solved using common integral tables:

$$\int \sin b_1 u \sin b_2 u \ \mathrm{d}u = \frac{\sin((b_2-b_1)u)}{2(b_2-b_1)} - \frac{\sin((b_1+b_2)u)}{2(b_1+b_2)} \qquad \text{(for } |b_1| \neq |b_2|\text{)}$$

$$\int \sin^2 bu \ \mathrm{d}u = \frac{u}{2} - \frac{1}{4b}\sin 2bu \qquad \text{(for } |b_1| = |b_2| = |b|\text{)}$$

$$\int \cos a_1 u \cos a_2 u \ \mathrm{d}u = \frac{\sin((a_2-a_1)u)}{2(a_2-a_1)} + \frac{\sin((a_2+a_1)u)}{2(a_2+a_1)} \qquad \text{(for } |a_1| \neq |a_2|\text{)}$$

$$\int \cos^2 au \ \mathrm{d}u = \frac{u}{2} + \frac{1}{4a}\sin 2au \qquad \text{(for } |a_1| = |a_2| = |a|\text{)}$$

Putting in the limits $[0, L]$ we can define the functions:

$$S_\int(b_1, b_2, L) = \begin{cases} \frac{\sin((b_2-b_1)L)}{2(b_2-b_1)} - \frac{\sin((b_1+b_2)L)}{2(b_1+b_2)} & \text{for } |b_1| \neq |b_2| \\ \frac{L}{2} - \frac{1}{4b}\sin 2bL & \text{for } |b_1| = |b_2| = |b| \end{cases} \tag{D.48}$$

$$C_\int(a_1, a_2, L) = \begin{cases} \frac{\sin((a_2-a_1)L)}{2(a_2-a_1)} + \frac{\sin((a_2+a_1)L)}{2(a_2+a_1)} & \text{for } |a_1| \neq |a_2| \\ \frac{L}{2} + \frac{1}{4a}\sin 2aL & \text{for } |a_1| = |a_2| = |a| \end{cases} \tag{D.49}$$

Integrating Equations (D.44) to (D.47), by substituting eqs. (D.48) and (D.49), and reintroducing the i, j indices gives us:

$$\begin{aligned} \int_{S_k} S_{TETE_{i,j}} \ \mathrm{d}s = & \frac{j\mu w \gamma_{R_j}}{k^2_{c_{R_j}} k^2_{c_{L_i}}} \Big[k_{y_{L_i}} k_{y_{R_j}} C_\int\big(k_{x_{L_i}}, k_{x_{R_j}}, a_L\big) S_\int\big(k_{y_{L_i}}, k_{y_{R_j}}, b_L\big) \\ & + k_{x_{L_i}} k_{x_{R_j}} S_\int\big(k_{x_{L_i}}, k_{x_{R_j}}, a_L\big) C_\int\big(k_{y_{L_i}}, k_{y_{R_j}}, b_L\big) \Big] \end{aligned} \tag{D.50}$$

$$\begin{aligned} \int_{S_k} S_{TMTM_{i,j}} \ \mathrm{d}s = & \frac{\varepsilon j w \gamma_{L_i}}{k^2_{c_{L_i}} k^2_{c_{R_j}}} \Big[k_{x_{L_i}} k_{x_{R_j}} C_\int\big(k_{x_{L_i}}, k_{x_{R_j}}, a_L\big) S_\int\big(k_{y_{L_i}}, k_{y_{R_j}}, b_L\big) \\ & + k_{y_{L_i}} k_{y_{R_j}} S_\int\big(k_{x_{L_i}}, k_{x_{R_j}}, a_L\big) C_\int\big(k_{y_{L_i}}, k_{y_{R_j}}, b_L\big) \Big] \end{aligned} \tag{D.51}$$

$$\begin{aligned} \int_{S_k} S_{TETM_{i,j}} \ \mathrm{d}s = & \frac{\varepsilon \mu w^2}{k^2_{c_{L_i}} k^2_{c_{R_j}}} \Big[k_{x_{L_i}} k_{y_{R_j}} S_\int\big(k_{x_{L_i}}, k_{x_{R_j}}, a_L\big) C_\int\big(k_{y_{L_i}}, k_{y_{R_j}}, b_L\big) \\ & - k_{y_{L_i}} k_{x_{R_j}} C_\int\big(k_{x_{L_i}}, k_{x_{R_j}}, a_L\big) S_\int\big(k_{y_{L_i}}, k_{y_{R_j}}, b_L\big) \Big] \end{aligned} \tag{D.52}$$

$$\begin{aligned} \int_{S_k} S_{TMTE_{i,j}} \ \mathrm{d}s = & \frac{\gamma_{L_i} \gamma_{R_j}}{k^2_{c_{L_i}} k^2_{c_{R_j}}} \Big[k_{x_{L_i}} k_{y_{R_j}} C_\int\big(k_{x_{L_i}}, k_{x_{R_j}}, a_L\big) S_\int\big(k_{y_{L_i}}, k_{y_{R_j}}, b_L\big) \\ & - k_{y_{L_i}} k_{x_{R_j}} S_\int\big(k_{x_{L_i}}, k_{x_{R_j}}, a_L\big) C_\int\big(k_{y_{L_i}}, k_{y_{R_j}}, b_L\big) \Big] \end{aligned} \tag{D.53}$$

Considering all the desired, $S_{i,j}, S'_{i,j}, R_{i,j}$ and $R'_{i,j}$ terms, we alter eqs. (D.50) to (D.53) to solve all the possibilities. If we define eqs. (D.50) to (D.53) as the function $S_{c\int}\big(i, j, a, b\big)$, where i, j index all the possible modes.

So if we consider eqs. (D.15), (D.18), (D.20) and (D.23):

$$\begin{aligned}
R_k(i,j) =& \frac{\int_S \boldsymbol{e}_j \times \boldsymbol{h}_i \, \mathrm{d}s}{\int_S \boldsymbol{e}_i \times \boldsymbol{h}_i \, \mathrm{d}s} = \frac{S_{c\int}\big(j_L, i_L, a_L, b_L\big)}{S_{c\int}\big(i_L, i_L, a_L, b_L\big)} \\
R'(i,j) =& \frac{\int_S \boldsymbol{e}_j \times \boldsymbol{h}'_i \, \mathrm{d}s}{\int_{S'} \boldsymbol{e}'_i \times \boldsymbol{h}'_i \, \mathrm{d}s} = \frac{S_{c\int}\big(j_L, i_R, a_L, b_L\big)}{S_{c\int}\big(i_R, i_R, a_R, b_R\big)} \\
S(i,j) =& \frac{\int_S \boldsymbol{e}_i \times \boldsymbol{h}_j \, \mathrm{d}s}{\int_S \boldsymbol{e}_i \times \boldsymbol{h}_i \, \mathrm{d}s} = \frac{S_{c\int}\big(i_L, j_L, a_L, b_L\big)}{S_{c\int}\big(i_L, i_L, a_L, b_L\big)} \\
S'(i,j) =& \frac{\int_S \boldsymbol{e}_i \times \boldsymbol{h}'_j \, \mathrm{d}s}{\int_S \boldsymbol{e}_i \times \boldsymbol{h}_i \, \mathrm{d}s} = \frac{S_{c\int}\big(i_L, j_R, a_L, b_L\big)}{S_{c\int}\big(i_L, i_L, a_L, b_L\big)}
\end{aligned}$$

So we need to solve for: $S_{c\int}\big(j_L, i_L, a_L, b_L\big)$, $S_{c\int}\big(i_L, i_L, a_L, b_L\big)$, $S_{c\int}\big(j_L, i_R, a_L, b_L\big)$, $S_{c\int}\big(i_R, i_R, a_R, b_R\big)$, $S_{c\int}\big(i_L, j_L, a_L, b_L\big)$, $S_{c\int}\big(i_L, j_R, a_L, b_L\big)$. These are analytical functions that don't require integration so can be very quickly solved and substituted into eq. (D.28).

Appendix E

Phase Centre Calculations

In order to correctly find the phase centre we solve for the point at which the phase is optimally flat in the far field. In two dimensions the wave distance Z_{lp} calculated from placing the antenna dZ from the origin in the θ plane can be calculated geometrically as:

$$Z_{lp} = \sqrt{r\sin^2(\theta) + r\cos^2(\theta) - dZ} \tag{E.1}$$

The phase centre can be defined as the point dZ at which the phase remains flat across the beam for all ϕ. The code is tested against an existing FEKO script, which is found to be limiting due to its restriction to beams orientated along the z–axis [94]. For the designed corrugated horn the phase variation for various depths is plotted in figs. E.1 to E.3. For a reflector antenna the phase across the aperture is critical so it makes more sense to optimise across the aperture, plotted in figs. E.4 to E.6.

E.1 Optimised over the whole beam

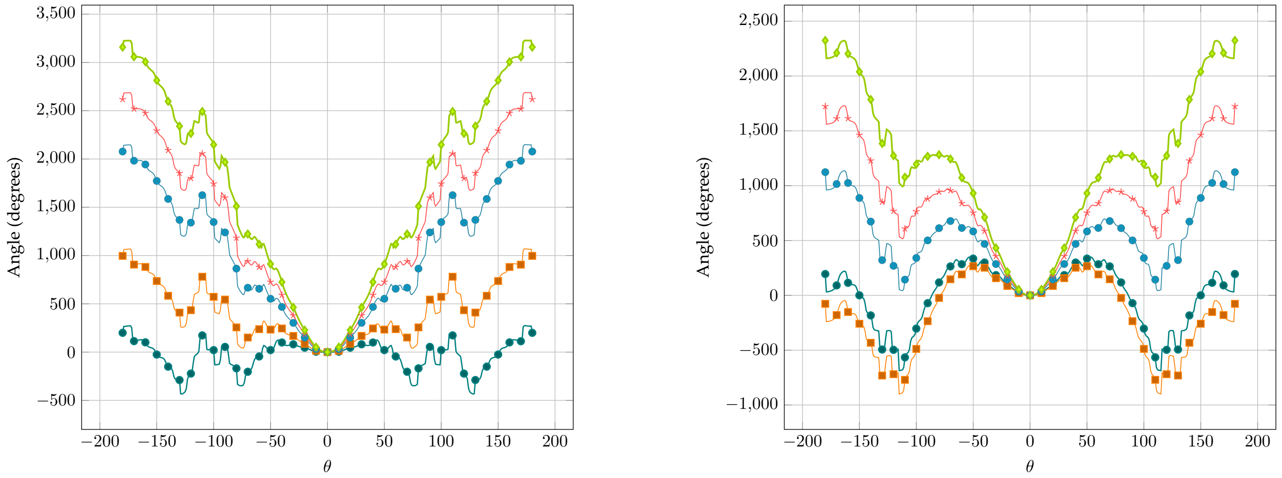

(a) 4.5 GHz,optimal depth 475 mm.

(b) 5 GHz,optimal depth 377 mm.

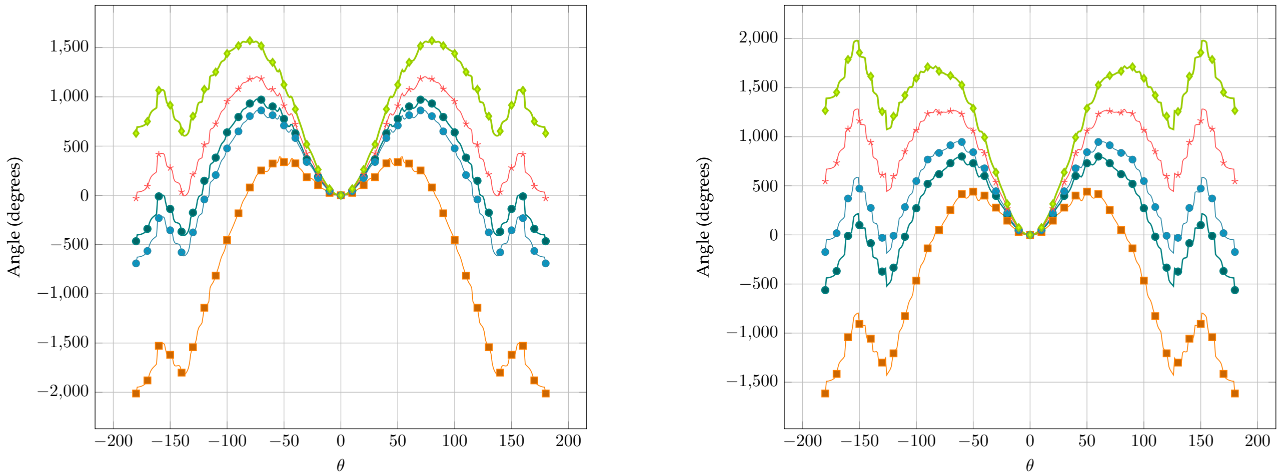

(c) 5.5 GHz,optimal depth 283 mm.

(d) 6 GHz,optimal depth 327 mm.

● Optimal ■ 400 ● 300 ☆ 250 ◆ 200

Figure E.1: Phase plots from 4.5 GHz to 6 GHz for the designed corrugated horn for various depths, optimised over the whole beam pattern.

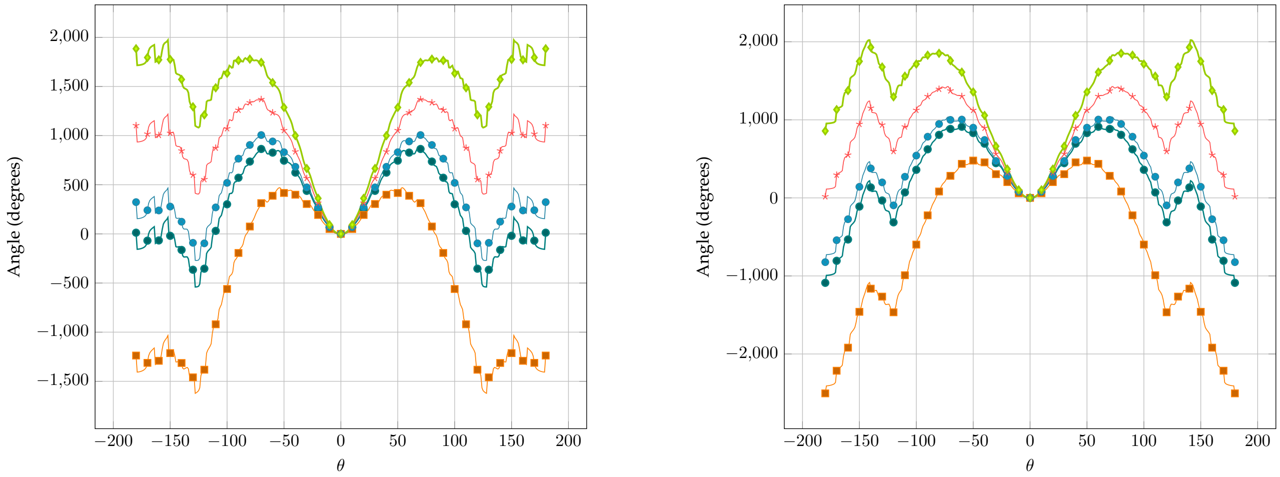

(a) 6.5 GHz,optimal depth 320 mm.

(b) 7 GHz,optimal depth 316 mm.

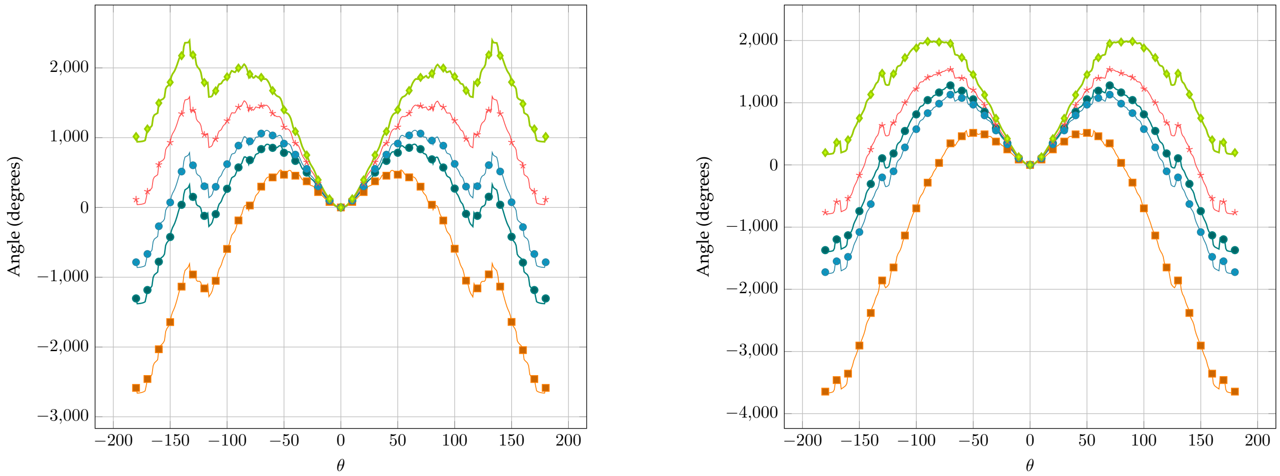

(c) 7.5 GHz,optimal depth 329 mm.

(d) 8 GHz,optimal depth 281 mm.

Figure E.2: Phase plots from 6.5 GHz to 8 GHz for the designed corrugated horn for various depths, optimised over the whole beam pattern.

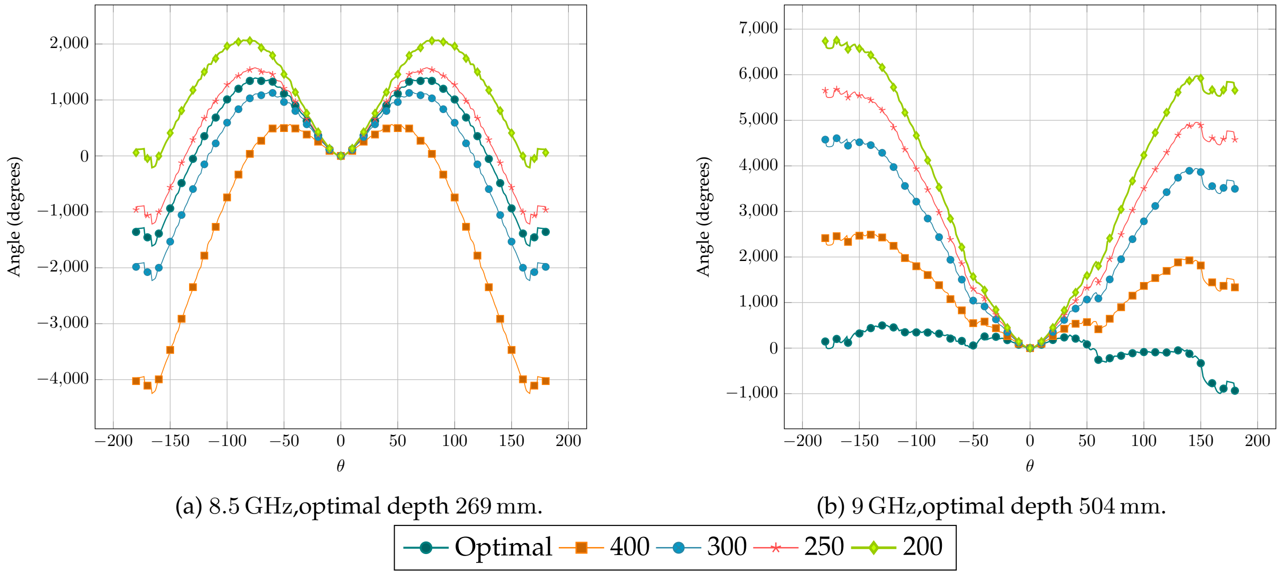

(a) 8.5 GHz,optimal depth 269 mm.

(b) 9 GHz,optimal depth 504 mm.

Figure E.3: Phase plots from 8.5 GHz to 9 GHz for the designed corrugated horn for various depths, optimised over the whole beam pattern.

E.2 Optimised over the main beam

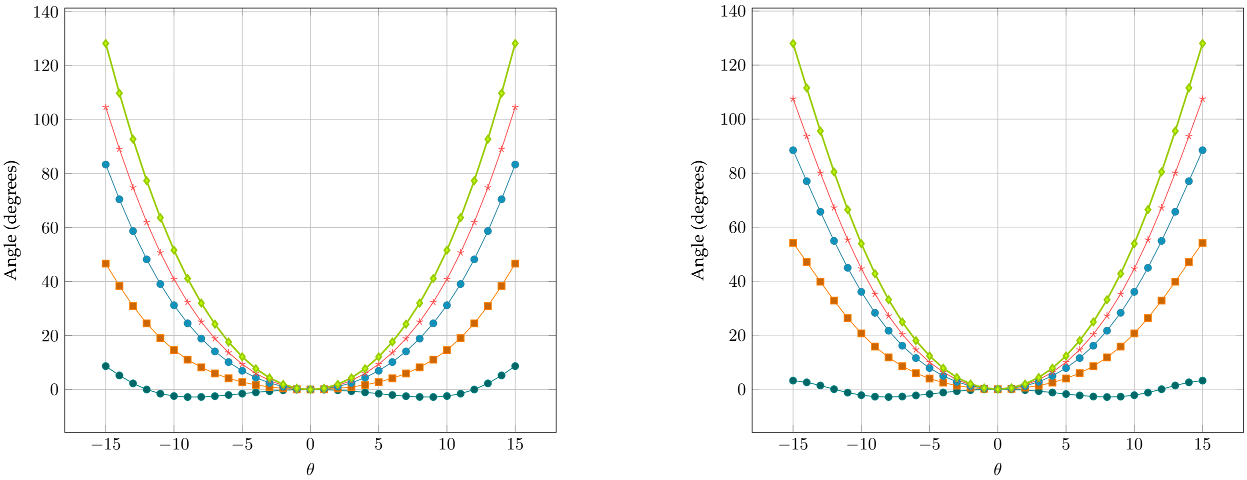

(a) 4.5 GHz,optimal depth 569 mm.

(b) 5 GHz,optimal depth 579 mm.

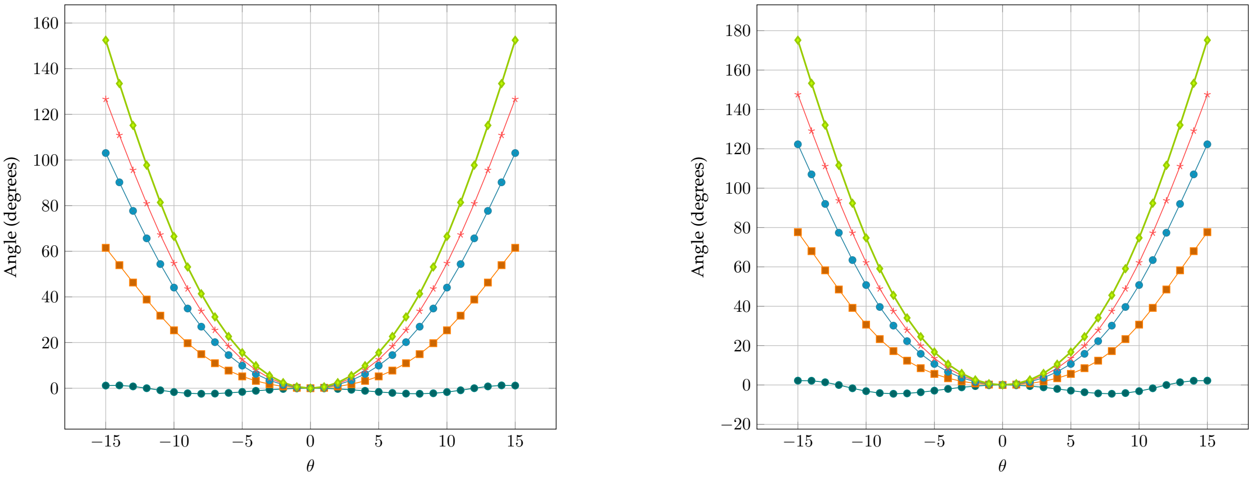

(c) 5.5 GHz,optimal depth 577 mm.

(d) 6 GHz,optimal depth 621 mm.

Figure E.4: Phase plots from 4.5 GHz to 6 GHz for the designed corrugated horn for various depths, optimised over the main beam pattern.

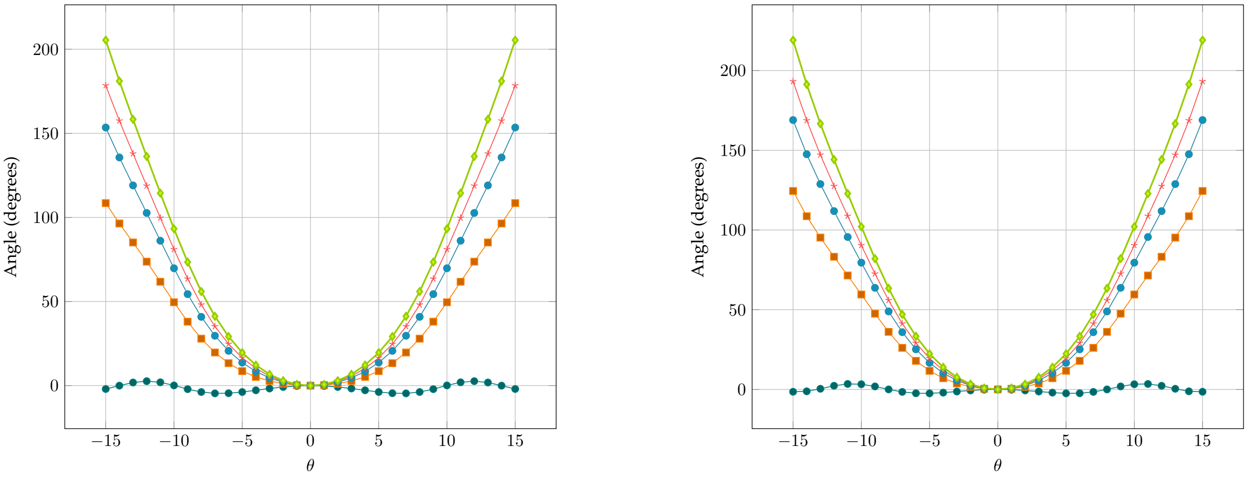

(a) 6.5 GHz,optimal depth 718 mm.

(b) 7 GHz,optimal depth 756 mm.

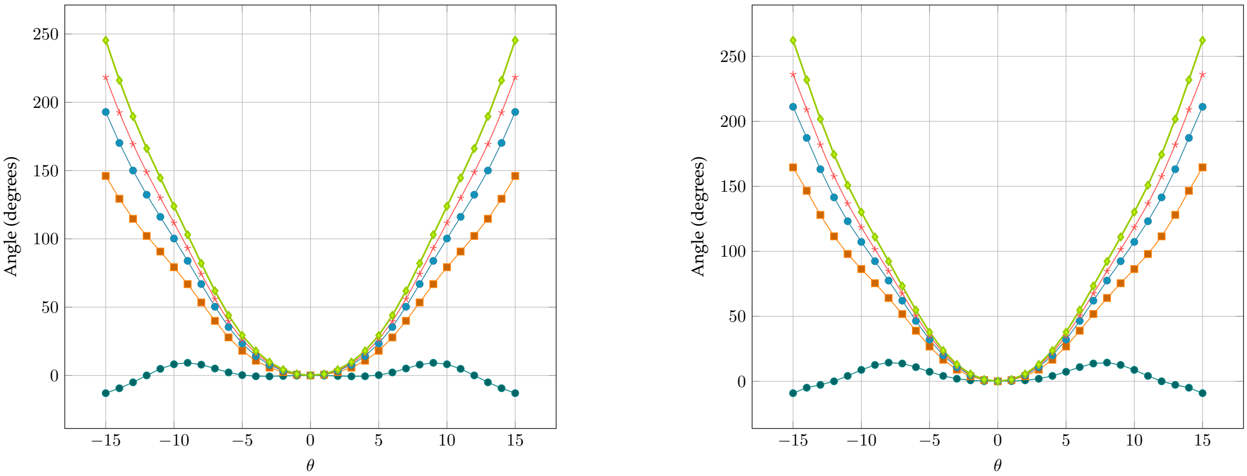

(c) 7.5 GHz,optimal depth 793 mm.

(d) 8 GHz,optimal depth 814 mm.

Optimal ■ 400 ● 300 ∗ 250 ◆ 200

Figure E.5: Phase plots from 6.5 GHz to 8 GHz for the designed corrugated horn for various depths, optimised over the main beam pattern.

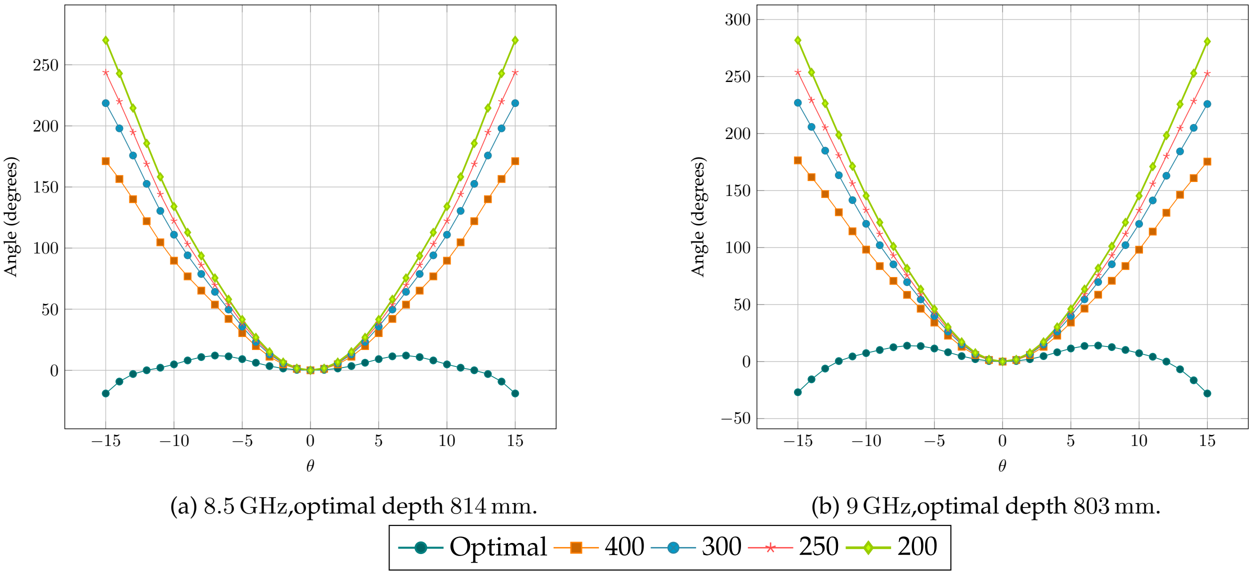

(a) 8.5 GHz,optimal depth 814 mm.

(b) 9 GHz,optimal depth 803 mm.

Figure E.6: Phase plots from 8.5 GHz to 9 GHz for the designed corrugated horn for various depths, optimised over the main beam pattern.

References

[1] J. D. Kraus, *Antennas*. New York, Toronto, London: McGraw-Hill Book Company, INC., August 1950.

[2] P.-S. Kildal, *Foundations of Antennas: A unified Approach*. Student Literature, Lund, 2000.

[3] D. Pozar, *Microwave Engineering, 4th Edition*. John Wiley & Sons, 2011.

[4] C. A. Balanis, *Antenna theory: analysis and design*, 3rd ed. John Wiley & Sons, 2016.

[5] R. S. Elliot, *Antenna theory and design*. John Wiley & Sons, 2006.

[6] M. N. Sadiku and A. F. Peterson, “A comparison of numerical methods for computing electromagnetic fields,” in *Southeastcon'90. Proceedings., IEEE*. IEEE, 1990, pp. 42–47.

[7] “Feko, Altair HyperWorks,” https://www.feko.info/, accessed: 2016-12-07.

[8] “CST, Computer Simulation Technology,” https://www.cst.com/, accessed: 2016-12-07.

[9] “ANSYS HFSS, High Frequency Electromagnetic Field Simulation,” http://ansys.com/, accessed: 2016-12-07.

[10] G. J. Burke, E. K. Miller, and A. J. Poggio, “The numerical electromagnetics code (nec)-a brief history,” in *Antennas and Propagation Society International Symposium, 2004. IEEE*, vol. 3. IEEE, 2004, pp. 2871–2874.

[11] A. Fourie and D. Nitch, “Supernec: Antenna and indoor-propagation simulation program,” *IEEE Antennas and Propagation Magazine*, vol. 42, no. 3, pp. 31–48, 2000.

[12] T. C. A. Molteno and N. Kyriazis, *NEC2++: An NEC-2 compatible Numerical Electromagnetics Code*. Department of Physics, University of Otago, New Zealand. Available at Debians necpp package documentation, http://packages.debian.org/testing/science/necpp, 2014.

[13] L. Dabbish, C. Stuart, J. Tsay, and J. Herbsleb, “Social coding in github: transparency and collaboration in an open software repository,” in *Proceedings of the ACM 2012 conference on Computer Supported Cooperative Work*. ACM, 2012, pp. 1277–1286.

[14] A. Logg, K.-A. Mardal, G. N. Wells *et al.*, *Automated Solution of Differential Equations by the Finite Element Method*. Springer, 2012.

[15] M. S. Alnæs, J. Blechta, J. Hake, A. Johansson, B. Kehlet, A. Logg, C. Richardson, J. Ring, M. E. Rognes, and G. N. Wells, “The fenics project version 1.5,” *Archive of Numerical Software*, vol. 3, no. 100, 2015.

[16] T. Dupont, J. Hoffman, C. Johnson, R. C. Kirby, M. G. Larson, A. Logg, and L. R. Scott, “The fenics project,” Tech. Rep. 2003–21, Chalmers Finite Element Center Preprint Series, Tech. Rep., 2003.

[17] A. Otto, N. Marais, E. Lezar, and D. Davidson, “Using the fenics package for fem solutions in electromagnetics,” *IEEE Antennas and Propagation Magazine*, vol. 54, no. 4, pp. 206–223, 2012.

[18] P. Dular and C. Geuzaine, “GetDP reference manual: the documentation for GetDP, a general environment for the treatment of discrete problems,” http://getdp.info.

[19] C. Geuzaine, “GetDP: a general finite-element solver for the de Rham complex,” in *PAMM Volume 7 Issue 1. Special Issue: Sixth International Congress on Industrial Applied Mathematics (ICIAM07) and GAMM Annual Meeting, Zürich 2007*, vol. 7. Wiley, 2008, pp. 1 010 603–1 010 604.

[20] P. Dular, C. Geuzaine, F. Henrotte, and W. Legros, “A general environment for the treatment of discrete problems and its application to the finite element method,” *IEEE Transactions on Magnetics*, vol. 34, no. 5, pp. 3395–3398, Sep. 1998.

[21] C. Geuzaine and J.-F. Remacle, “Gmsh: A 3-d finite element mesh generator with built-in pre-and post-processing facilities,” *International Journal for Numerical Methods in Engineering*, vol. 79, no. 11, pp. 1309–1331, 2009.

[22] J. Pont, *Le destin douloureux de Walther Ritz (1878-1909), physicien théoricien de génie*, ser. Cahiers de Vallesia. Archives de l’état du Valais, 2012.

[23] C. Geuzaine and B. Klein, “2d and 3d models of metallic waveguides,” http://onelab.info/wiki/Waveguides, Dec. 2016.

[24] R. Ierusalimschy, L. H. De Figueiredo, and W. Celes Filho, “Lua-an extensible extension language,” *Softw., Pract. Exper.*, vol. 26, no. 6, pp. 635–652, 1996.

[25] J. Stenarson, “Hftools-an open source python package for microwave engineering,” in *Microwave Measurement Conference (ARFTG), 2014 83rd ARFTG*. IEEE, 2014, pp. 1–4.

[26] D. H. Werner and S. Ganguly, “An overview of fractal antenna engineering research,” *IEEE Antennas and propagation Magazine*, vol. 45, no. 1, pp. 38–57, 2003.

[27] Y. Mushiake, *Self-Complementary Antennas: Principle of Self-Complementarity for Constant Impedance*. Springer Science & Business Media, 2012.

[28] A. Whitney, A. Niell, B. Corey, H. Hase, E. Himwich, H. Hinteregger, T. Kondo, Y. Koyama, C. Ma, Z. Malkin, B. Petrachenko, W. Schlueter, H. Schuh, D. Shaffer, G. Tuccari, and N. Vandenberg, “VLBI2010: Current and future requirements for geodetic VLBI systems, IVS WG3 report,” IVS WG3 Report, http://ivscc.gsfc.nasa.gov/about/wg/wg3/, Tech. Rep., 2005.

[29] R. Olsson, P.-S. Kildal, and S. Weinreb, "The eleven antenna: A compact low-profile decade bandwidth dual polarized feed for reflector antennas," *IEEE Transactions on Antennas and Propagation*, vol. 54, no. 2, pp. 368–375, Febuary 2006.

[30] G. Cortes-Medellin, "Novel non planar ultra wide band quasi self-complementary antenna," *Proc. of IEEE AP-S Symposium, Honolulu, Hawaii*, vol. 48, p. 5733 5736, 9-15 June 2007.

[31] A. Akgiray, S. Weinreb, and W. Imbriale, "Design and measurements of dual-polarized wideband constant-beamwidth quadruple-ridged flared horn," in *Antennas and Propagation (APSURSI), 2011 IEEE International Symposium on*. IEEE, 2011, pp. 1135–1138.

[32] R. Grundbacher, R. Lai, M. Barsky, R. Tsai, T. Gaier, S. Weinreb, D. Dawson, J. J. Bautista, J. F. Davis, N. Erickson, T. Block, and A. Oki, "0.1 mu;m inp hemt devices and mmics for cryogenic low noise amplifiers from x-band to w-band," in *Conference Proceedings. 14th Indium Phosphide and Related Materials Conference (Cat. No.02CH37307)*, 2002, pp. 455–458.

[33] W. A. Imbriale, S. Weinreb, and H. Mani, "Design of a wideband radio telescope," in *2007 IEEE Aerospace Conference*, March 2007, pp. 1–12.

[34] P. Hall, *The SKA: An Engineering Perspective*. Singer, 2005.

[35] R. Maaskant, "Analysis of large antenna systems," Ph.D. dissertation, Eindhoven Univ. of Technology, The Netherlands, 2010.

[36] M. Ivashina, O. Iupikov, and W. van Cappellen, "Extending the capabilities of the grasp and caesar software to analyze and optimize active beamforming array feeds for reflector systems," in *Electromagnetics in Advanced Applications (ICEAA), 2010 International Conference on*, Sept. 2010, pp. 197 –200.

[37] M. Ivashina, O. Iupikov, R. Maaskant, W. van Cappellen, and T. Oosterloo, "An optimal beamforming strategy for wide-field surveys with phased-array-fed reflector antennas," *Antennas and Propagation, IEEE Transactions on*, vol. 59, no. 6, pp. 1864 –1875, June 2011.

[38] H. Nyquist, "Thermal agitation of electric charge in conductors," *Physical review*, vol. 32, no. 1, pp. 110–113, 1928.

[39] J. B. Johnson, "Thermal agitation of electricity in conductors," *Physical review*, vol. 32, no. 1, p. 97, 1928.

[40] H. T. Friis, "Noise figures of radio receivers," *Proceedings of the IRE*, vol. 32, no. 7, pp. 419–422, 1944.

[41] R. Twiss, "Nyquist's and thevenin's theorems generalized for nonreciprocal linear networks," *Journal of Applied Physics*, vol. 26, no. 5, pp. 599–602, 1955.

[42] H. Rothe and W. Dahlke, "Theory of noisy fourpoles," *Proceedings of the IRE*, vol. 44, no. 6, pp. 811–818, 1956.

[43] H. A. Haus and J. R. Melcher, *Electromagnetic fields and energy*. Prentice Hall Englewood Cliffs, 1989.

[44] H. A. Haus, *Electromagnetic noise and quantum optical measurements*. Springer, 2000.

[45] H. Haus, W. Atkinson, G. Branch, W. Davenport, W. Fonger, W. Harris, S. Harrison, W. McLeod, E. Stodola, and T. Talpey, "Representation of noise in linear twoports," *Proceedings of the IRE*, vol. 48, no. 1, pp. 69–74, 1960.

[46] C. A. Balanis, *Antenna theory analysis and design*, 3rd ed. Hoboken, New Jersey: John Wiley & Sons, Inc., 2005.

[47] P.-S. Kildal, *Foundations of Antennas*. Chalmers University of Technology, 2010.

[48] X. Chen, "Study of system noise temperatures from 50 mhz to 15 mhz," Master's thesis, Chalmers University of Technology, 2009.

[49] G. C. Medellin, "Memo 95 : Antenna noise temperaute calculation," SKA, Tech. Rep., 07.

[50] M. V. Ivashina, R. Maaskant, and B. Woestenburg, "Equivalent system representation to model the beam sensitivity of receiving antenna arrays," *IEEE Antennas and Wireless Propagation Letters*, vol. 7, pp. 733–737, 2008.

[51] H. A. Haus and R. B. Adler, *Circuit theory of linear noisy networks*. The MIT Press, 1959.

[52] S. A. Maas, *Noise in linear and nonlinear circuits*. Artech House Publishers, 2005.

[53] J. Randa, "Noise characterization of multiport amplifiers," *IEEE Transactions on Microwave Theory and Techniques*, vol. 49, no. 10, pp. 1757–1763, 2001.

[54] M. W. Pospieszalski, "Modeling of noise paramaters," *IEEE Antennas and Wireless Propogation Letters*, vol. 2, January 1989.

[55] K. Warnick, M. Ivashina, R. Maaskant, and B. Woestenburg, "Unified definitions of efficiencies and system noise temperature for receiving antenna arrays," *Antennas and Propagation, IEEE Transactions on*, vol. 58, no. 6, pp. 2121 –2125, june 2010.

[56] H. Bauer and H. Rothe, "Der aquivalente rauschvierpol als wellenvierpol," *AEU*, vol. 10, pp. 241–252, 1956.

[57] P. Penfield, "Wave representation of amplifier noise," *IRE Transactions on Circuit Theory*, vol. 9, no. 1, pp. 84–86, 1962.

[58] R. G. Kanaglekar, R. E. Mcintosh, and W. E. Bryant, "Wave analysis of noise in interconnected multiport networks," *Microwave Theory and Techniques, IEEE Transactions on*, vol. 35, no. 2, pp. 112–116, 1987.

[59] S. W. Wedge and D. B. Rutledge, "Wave techniques for noise modeling and measurement," *Microwave Theory and Techniques, IEEE Transactions on*, vol. 40, no. 11, pp. 2004–2012, 1992.

[60] J. Dobrowolski, *Microwave Network Design Using the Scattering Matrix*, ser. Artech House microwave library. Artech House, 2010.

[61] J. A. Dobrowolski, “A CAD-oriented method for noise figure computation of two-ports with any internal topology,” *IEEE Transactions on Microwave Theory and Techniques*, vol. 37, no. 1, pp. 15–20, Jan 1989.

[62] B. Klein and P.-S. Kildal, “System noise calculations over the decade bandwidth of the eleven feed for radio telescope applications (apsursi 2010),” jul. 2010, pp. 1 –4.

[63] J. Yang, M. Pantaleev, P. S. Kildal, B. Klein, Y. Karandikar, L. Helldner, N. Wadefalk, and C. Beaudoin, “Cryogenic 2–13 ghz eleven feed for reflector antennas in future wideband radio telescopes,” *IEEE Transactions on Antennas and Propagation*, vol. 59, no. 6, pp. 1918–1934, June 2011.

[64] M. V. Ivashina, R. Maaskant, and B. Woestenburg, “Equivalent system representation to model the beam sensitivity of receiving antenna arrays,” *IEEE Antennas and Wireless Propogation Letters*, vol. 7, pp. 733–737, 2008.

[65] M. Pantaleev, J. Yang, Y. B. Karandikar, L. Helldner, B. Klein, R. Haas, A. U. Zaman, M. Zamani, and P.-S. Kildal, “Cryogenic integration of 2-14 ghz eleven feed in wideband receiver for vlbi 2010,” in *Sixth IVS General Meeting (International VLBI Service for Geodesy and Astrometry), February 7-13, 2010, Hobart, TAS, Australia*, 2010, pp. 415–419.

[66] K. F. Warnick, M. V. Ivashina, and S. G. Hay, “Guest editorial for the special issue on antennas for next generation radio telescopes,” *Antennas and Propagation, IEEE Transactions on*, vol. 59, no. 6, pp. 1786 – 1789, June 2011.

[67] J. Yang, M. Pantaleev, P.-S. Kildal, B. Klein, Y. Karandikar, L. Helldner, N. Wadefalk, and C. Beaudoin, “Cryogenic 2–13 GHz eleven feed for reflector antennas in future wideband radio telescopes,” *Antennas and Propagation, IEEE Transactions on*, vol. 59, no. 6, pp. 1918 – 1934, June 2011.

[68] B. Klein, M. V. Ivashina, R. Maaskant, A. R. Clark, and M. Panteleev, “Development of a detailed system model of the eleven feed receiver using the caesar software,” in *Antennas and Propagation (EUCAP), 2012 6th European Conference on*. IEEE, 2012, pp. 3416–3420.

[69] J. Yang and P.-S. Kildal, “Optimization of reflection coefficient of large log-periodic array by computing only a small part of it,” *Antennas and Propagation, IEEE Transactions on*, vol. 59, no. 6, pp. 1790 – 1797, June 2011.

[70] M. W. Pospieszalski, “Modeling of noise paramaters of mesfets and modfets and their frequency and temperature dependence,” *IEEE Transactionson on Microwave Theory and Techniques*, vol. 9, pp. 1340–1349, September 1989.

[71] B. Klein, “Octave–2–Feko GitHub repository,” https://github.com/B-Klein/Octave-2-Feko, Dec. 2016.

[72] J. W. Eaton, D. Bateman, and S. oren Hauberg, *GNU Octave version 3.0.1 manual: a high-level interactive language for numerical computations*. CreateSpace Independent Publishing Platform, 2009, ISBN 1441413006. [Online]. Available: http://www.gnu.org/software/octave/doc/interpreter

[73] EM Software Syst.(SA)(Pty), Ltd., Stellenbosch, South Africa, "Manual, feko users, suite 7.0," 2014.

[74] "Antenna magnus," http://www.antennamagus.com/, accessed: 2016-12-07.

[75] "Octave-Forge - Extra packages for GNU Octave, io," https://octave.sourceforge.io/io/index.html, accessed: 2016-12-07.

[76] R. Wohlleben, H. Mattes, and O. Lochner, "Simple small primary feed for large opening angles and high aperture efficiency," *Electronics Letters*, vol. 8, no. 19, pp. 474–476, 1972.

[77] "ZX60-P162LN+ data sheet," www.minicircuits.com, Mini-Circuits, P.O. Box 350166, Brooklyn, NY 11235-0003.

[78] B. Sequeira, "Properties of modes in a circular waveguide," http://www.rfcafe.com/references/electrical/circular-waveguide-modes.htm, Dec. 2016.

[79] R. E. Collin, *Foundations for microwave engineering*. John Wiley & Sons, 2007.

[80] A. Belenguer, E. D. Caballero, H. Esteban, A. L. Borja, and J. Cascón, "Krylov's solver based technique for the cascade connection of multiple n-port multimodal scattering matrices," *IEEE Transactions on Microwave Theory and Techniques*, vol. 61, no. 2, pp. 720–726, 2013.

[81] P. Hannan, "Microwave antennas derived from the cassegrain telescope," *IRE Transactions on Antennas and Propagation*, vol. 9, no. 2, pp. 140–153, 1961.

[82] A. D. Olver, *Microwave horns and feeds*. IET, 1994, vol. 39.

[83] J. Teniente, R. Gonzalo, and C. Del-Rio, "Superb gaussian beam efficiency corrugated horn antennas," in *Antennas and Propagation (EuCAP), 2010 Proceedings of the Fourth European Conference on*, April, pp. 1–4.

[84] ——, "Ultra-wide band corrugated gaussian profiled horn antenna design," *Microwave and Wireless Components Letters, IEEE*, vol. 12, no. 1, pp. 20–21, Jan.

[85] W. Sun and C. A. Balanis, "Analysis and design of quadruple-ridged waveguides," *Microwave Theory and Techniques, IEEE Transactions on*, vol. 42, no. 12, pp. 2201–2207, 1994.

[86] D. de Villiers, P. Meyer, and K. Palmer, "Broadband offset quad-ridged waveguide orthomode transducer," *Electronics Letters*, vol. 45, no. 1, pp. 60 –62, 1 2009.

[87] G. Coutts, "Octave bandwidth orthomode transducers for the expanded very large array," *Antennas and Propagation, IEEE Transactions on*, vol. 59, no. 6, pp. 1910 –1917, june 2011.

[88] S. J. Skinner and G. L. James, "Wide-band orthomode transducers," *Microwave Theory and Techniques, IEEE Transactions on*, vol. 39, no. 2, pp. 294–300, 1991.

[89] B. Thomas, G. James, and K. Greene, "Design of wide-band corrugated conical horns for cassegrain antennas," *IEEE Transactions on Antennas and Propagation*, vol. 34, no. 6, pp. 750–757, 1986.

[90] P.-S. Kildal, "Gaussian beam model for aperture-controlled and flareangle-controlled corrugated horn antennas," in *IEE Proceedings H-Microwaves, Antennas and Propagation*, vol. 135, no. 4. IET, 1988, pp. 237–240.

[91] C. A. Balanis, *Antenna theory: analysis and design*, 3rd ed. John Wiley & Sons, 2016, ch. 13, pp. 785–791.

[92] G. L. James, "Analysis and design of te 11-to-he 11 corrugated cylindrical waveguide mode converters," *Microwave Theory and Techniques, IEEE Transactions on*, vol. 29, no. 10, pp. 1059–1066, 1981.

[93] P. Masterman and P. Clarricoats, "Computer field-matching solution of waveguide transverse discontinuities," in *Proceedings of the Institution of Electrical Engineers*, vol. 118, no. 1. IET, 1971, pp. 51–63.

[94] Altair, Hyperworks, "Feko, calculate the far field phase centre," https://www.feko.info/support/lua-scripts/phase-center-determination/phase-center-determination, Dec. 2016.

Bibliography

Complete list of resources useful to the research, both cited and uncited.

A. Akgiray, S. Weinreb, and W. Imbriale. Design and measurements of dual-polarized wideband constant-beamwidth quadruple-ridged flared horn. In *Antennas and Propagation (APSURSI), 2011 IEEE International Symposium on*, pages 1135–1138. IEEE, 2011.

U. Balaji and R. Vahldieck. Mode-matching analysis of circular-ridged waveguide discontinuities. *Microwave Theory and Techniques, IEEE Transactions on*, 46(2):191–195, 1998.

C. A. Balanis. *Antenna theory analysis and design*. John Wiley & Sons, Inc., Hoboken, New Jersey, 3 edition, 2005.

C. A. Balanis. *Antenna theory: analysis and design*. John Wiley & Sons, third edition, 2016.

H. Bauer and H. Rothe. Der aquivalente rauschvierpol als wellenvierpol. *AEU*, 10:241–252, 1956.

A. T. Becking, H. Groendijk, and K. Knol. The noise factor of four-terminal networks. *Philips Res. Rep*, 10:349–357, 1955.

A. Belenguer, E. D. Caballero, H. Esteban, A. L. Borja, and J. Cascón. Krylov's solver based technique for the cascade connection of multiple n-port multimodal scattering matrices. *IEEE Transactions on Microwave Theory and Techniques*, 61(2):720–726, 2013.

G. J. Burke, E. K. Miller, and A. J. Poggio. The numerical electromagnetics code (nec)-a brief history. In *Antennas and Propagation Society International Symposium, 2004. IEEE*, volume 3, pages 2871–2874. IEEE, 2004.

X. Chen. Study of system noise temperatures from 50 mhz to 15 mhz. Master's thesis, Chalmers University of Technology, 2009.

P. Clarricoats, R. Dubrovka, and A. Olver. High performance compact corrugated horn. *IEE Proceedings-Microwaves, Antennas and Propagation*, 151(6):519–524, 2004.

R. E. Collin. *Foundations for microwave engineering*. John Wiley & Sons, 2007.

G. Cortes-Medellin. Novel non planar ultra wide band quasi self-complementary antenna. *Proc. of IEEE AP-S Symposium, Honolulu, Hawaii*, 48:5733 5736, 9-15 June 2007.

G. Coutts. Octave bandwidth orthomode transducers for the expanded very large array. *Antennas and Propagation, IEEE Transactions on*, 59(6):1910 –1917, june 2011a. ISSN 0018-926X. doi: 10.1109/TAP.2011.2122220.

G. M. Coutts. Octave bandwidth orthomode transducers for the expanded very large array. *Antennas and Propagation, IEEE Transactions on*, 59(6):1910–1917, 2011b.

L. C. da Silva. A method of analysis of te11-to-he11 mode converters. *IEEE Transactions on Microwave Theory and Techniques*, 36(3):480–488, Mar 1988. ISSN 0018-9480. doi: 10.1109/22.3538.

L. Dabbish, C. Stuart, J. Tsay, and J. Herbsleb. Social coding in github: transparency and collaboration in an open software repository. In *Proceedings of the ACM 2012 conference on Computer Supported Cooperative Work*, pages 1277–1286. ACM, 2012.

D. de Villiers, P. Meyer, and K. Palmer. Broadband offset quad-ridged waveguide orthomode transducer. *Electronics Letters*, 45(1):60 –62, 1 2009. ISSN 0013-5194. doi: 10.1049/el:20092887.

J. Dobrowolski. *Microwave Network Design Using the Scattering Matrix*. Artech House microwave library. Artech House, 2010. ISBN 9781608071302.

J. A. Dobrowolski. A CAD-oriented method for noise figure computation of two-ports with any internal topology. *IEEE Transactions on Microwave Theory and Techniques*, 37(1):15–20, Jan 1989. ISSN 0018-9480. doi: 10.1109/22.20016.

T. Dupont, J. Hoffman, C. Johnson, R. C. Kirby, M. G. Larson, A. Logg, and L. R. Scott. The fenics project. Technical report, Tech. Rep. 2003–21, Chalmers Finite Element Center Preprint Series, 2003.

J. W. Eaton, D. Bateman, and S. oren Hauberg. *GNU Octave version 3.0.1 manual: a high-level interactive language for numerical computations*. CreateSpace Independent Publishing Platform, 2009. URL `http://www.gnu.org/software/octave/doc/interpreter`. ISBN 1441413006.

R. S. Elliot. *Antenna theory and design*. John Wiley & Sons, 2006.

EM Software Syst.(SA)(Pty), Ltd., Stellenbosch, South Africa. Manual, feko users, suite 7.0, 2014.

A. Fourie and D. Nitch. Supernec: Antenna and indoor-propagation simulation program. *IEEE Antennas and Propagation Magazine*, 42(3):31–48, 2000.

H. T. Friis. Noise figures of radio receivers. *Proceedings of the IRE*, 32(7):419–422, 1944.

C. Geuzaine and J.-F. Remacle. Gmsh: A 3-d finite element mesh generator with built-in pre-and post-processing facilities. *International Journal for Numerical Methods in Engineering*, 79(11):1309–1331, 2009.

R. Grundbacher, R. Lai, M. Barsky, R. Tsai, T. Gaier, S. Weinreb, D. Dawson, J. J. Bautista, J. F. Davis, N. Erickson, T. Block, and A. Oki. 0.1 mu;m inp hemt devices and mmics for cryogenic low noise amplifiers from x-band to w-band. In *Conference Proceedings. 14th Indium Phosphide and Related Materials Conference (Cat. No.02CH37307)*, pages 455–458, 2002. doi: 10.1109/ICIPRM.2002.1014466.

P. Hall. *The SKA: An Engineering Perspective*. Singer, 2005.

P. Hannan. Microwave antennas derived from the cassegrain telescope. *IRE Transactions on Antennas and Propagation*, 9(2):140–153, 1961.

K. Hartmann. Noise characterization of linear circuits. *IEEE Transactions on circuits and systems*, 23(10):581–590, 1976.

H. Haus, W. Atkinson, G. Branch, W. Davenport, W. Fonger, W. Harris, S. Harrison, W. McLeod, E. Stodola, and T. Talpey. Representation of noise in linear twoports. *Proceedings of the IRE*, 48(1):69–74, 1960.

H. A. Haus. *Electromagnetic noise and quantum optical measurements*. Springer, 2000.

H. A. Haus and R. B. Adler. *Circuit theory of linear noisy networks*. The MIT Press, 1959.

H. A. Haus and J. R. Melcher. *Electromagnetic fields and energy*. Prentice Hall Englewood Cliffs, 1989.

R. P. Hecken. Analysis of linear noisy two-ports using scattering waves. *IEEE Transactions on Microwave Theory and Techniques*, 29(10):997–1004, 1981.

R. Ierusalimschy, L. H. De Figueiredo, and W. Celes Filho. Lua-an extensible extension language. *Softw., Pract. Exper.*, 26(6):635–652, 1996.

W. A. Imbriale, S. Weinreb, and H. Mani. Design of a wideband radio telescope. In *2007 IEEE Aerospace Conference*, pages 1–12, March 2007. doi: 10.1109/AERO.2007.352858.

W. A. Imbriale, S. Weinreb, G. Jones, and H. Mani. Rf performance of the gavrt wideband radio telescope (eucap 2010). pages 1 –4, apr. 2010.

M. Ivashina, O. Iupikov, and W. van Cappellen. Extending the capabilities of the grasp and caesar software to analyze and optimize active beamforming array feeds for reflector systems. In *Electromagnetics in Advanced Applications (ICEAA), 2010 International Conference on*, pages 197 –200, Sept. 2010. doi: 10.1109/ICEAA.2010.5652962.

M. Ivashina, O. Iupikov, R. Maaskant, W. van Cappellen, and T. Oosterloo. An optimal beamforming strategy for wide-field surveys with phased-array-fed reflector antennas. *Antennas and Propagation, IEEE Transactions on*, 59(6):1864 –1875, June 2011. ISSN 0018-926X. doi: 10.1109/TAP.2011.2123865.

M. V. Ivashina, R. Maaskant, and B. Woestenburg. Equivalent system representation to model the beam sensitivity of receiving antenna arrays. *IEEE Antennas and Wireless Propogation Letters*, 7:733–737, 2008a.

M. V. Ivashina, R. Maaskant, and B. Woestenburg. Equivalent system representation to model the beam sensitivity of receiving antenna arrays. *IEEE Antennas and Wireless Propagation Letters*, 7:733–737, 2008b.

G. L. James. Analysis and design of te 11-to-he 11 corrugated cylindrical waveguide mode converters. *Microwave Theory and Techniques, IEEE Transactions on*, 29(10):1059–1066, 1981.

J. B. Johnson. Thermal agitation of electricity in conductors. *Physical review*, 32(1):97, 1928.

R. C. Johnson and H. Jasik, editors. *Antenna Engineering Handbook*. McGraw-Hill Book Company, INC., second edition, 1984.

R. G. Kanaglekar, R. E. Mcintosh, and W. E. Bryant. Wave analysis of noise in interconnected multiport networks. *Microwave Theory and Techniques, IEEE Transactions on*, 35(2): 112–116, 1987.

P.-S. Kildal. Gaussian beam model for aperture-controlled and flareangle-controlled corrugated horn antennas. In *IEE Proceedings H-Microwaves, Antennas and Propagation*, volume 135, pages 237–240. IET, 1988.

P.-S. Kildal. *Foundations of Antennas: A unified Approach*. Student Literature, Lund, 2000.

P.-S. Kildal. *Foundations of Antennas*. Chalmers University of Technology, 2010.

A. Kishk and P.-S. Kildal. Modelling of soft and hard surfaces using ideal perfect electric conducting/perfect magnetic conducting strip grids. *Microwaves, Antennas Propagation, IET*, 3(2):296–302, March. ISSN 1751-8725. doi: 10.1049/iet-map:20070365.

B. Klein and P.-S. Kildal. System noise calculations over the decade bandwidth of the eleven feed for radio telescope applications (apsursi 2010). pages 1 –4, jul. 2010. doi: 10.1109/APS.2010.5561071.

J. D. Kraus. *Antennas*. McGraw-Hill Book Company, INC., New York, Toronto, London, August 1950.

A. Logg, K.-A. Mardal, and G. Wells. *Automated solution of differential equations by the finite element method: The FEniCS book*, volume 84. Springer Science & Business Media, 2012.

S. A. Maas. *Noise in linear and nonlinear circuits*. Artech House Publishers, 2005.

R. Maaskant. *Analysis of large antenna systems*. PhD thesis, Eindhoven Univ. of Technology, The Netherlands, 2010.

T. S. M. Maclean. *Principles of antennas: wire and apeture*. Cambridge University Press, 1986.

P. Masterman and P. Clarricoats. Computer field-matching solution of waveguide transverse discontinuities. In *Proceedings of the Institution of Electrical Engineers*, volume 118, pages 51–63. IET, 1971.

G. C. Medellin. Memo 95 : Antenna noise temperaute calculation. Technical report, SKA, 07.

R. Meys. A wave approach to the noise properties of linear microwave devices. *IEEE Transactions on Microwave Theory and Techniques*, 26(1):34–37, 1978.

T. C. A. Molteno and N. Kyriazis. *NEC2++: An NEC-2 compatible Numerical Electromagnetics Code*. Department of Physics, University of Otago, New Zealand. Available at Debians necpp package documentation, `http://packages.debian.org/testing/science/necpp`, 2014.

H. Nyquist. Thermal agitation of electric charge in conductors. *Physical review*, 32(1):110–113, 1928.

R. Olsson, P.-S. Kildal, and S. Weinreb. The eleven antenna: A compact low-profile decade bandwidth dual polarized feed for reflector antennas. *IEEE Transactions on Antennas and Propagation*, 54(2):368–375, Febuary 2006.

A. D. Olver. *Corrugated horns for microwave antennas*. Number 18. Iet, 1984.

A. D. Olver. *Microwave horns and feeds*, volume 39. IET, 1994.

A. D. Olver and J. Xiang. Design of profiled corrugated horns. *IEEE Transactions on Antennas and Propagation*, 36(7):936–940, July 1988. ISSN 0018-926X. doi: 10.1109/8.7198.

M. Pantaleev, J. Yang, Y. B. Karandikar, L. Helldner, B. Klein, R. Haas, A. U. Zaman, M. Zamani, and P.-S. Kildal. Cryogenic integration of 2-14 ghz eleven feed in wideband receiver for vlbi 2010. In *Sixth IVS General Meeting (International VLBI Service for Geodesy and Astrometry), February 7-13, 2010, Hobart, TAS, Australia*, pages 415–419, 2010.

P. Penfield. Wave representation of amplifier noise. *IRE Transactions on Circuit Theory*, 9(1): 84–86, 1962.

B. Petrachenko, A. Niell, D. Behrend, B. Corey, J. Böhm, P. Chralot, A. Collioud, J. Gipson, R. Haas, T. Hobiger, et al. Design aspects of the vlbi2010 system-progress report of the ivs vlbi2010 committee. 2009.

M. W. Pospieszalski. Modeling of noise paramaters of mesfets and modfets and their frequency and temperature dependence. *IEEE Transactionson on Microwave Theory and Techniques*, 9:1340–1349, September 1989a.

M. W. Pospieszalski. Modeling of noise paramaters. *IEEE Antennas and Wireless Propogation Letters*, 2, January 1989b.

D. Pozar. *Microwave Engineering, 4th Edition*. John Wiley & Sons, 2011. ISBN 9781118213636.

J. Randa. Noise characterization of multiport amplifiers. *IEEE Transactions on Microwave Theory and Techniques*, 49(10):1757–1763, 2001.

V. Rizzoli and A. Lipparini. Computer-aided noise analysis of linear multiport networks of arbitrary topology. *IEEE Transactions on Microwave Theory and Techniques*, 33(12):1507–1512, 1985.

V. Rodriguez. An open-boundary quad-ridged guide horn antenna for use as a source in antenna pattern measurement anechoic chambers. *IEEE Antennas and Propagation Magazine*, 48(2):157–160, April 2006.

K. Rohlfs and T. L. Wilson. *Tools of Radio Astronomy*, volume 4. Springer-Verlag Heidelberg, New York, 2004.

H. Rothe and W. Dahlke. Theory of noisy fourpoles. *Proceedings of the IRE*, 44(6):811–818, 1956.

W. V. T. Rusch and P. D. Potter. *Analysis of Reflector Antennas*. Academic Press, Inc. (London) Ltd., Berkley Square House, London, WIX 6BA, 1970.

M. N. Sadiku and A. F. Peterson. A comparison of numerical methods for computing electromagnetic fields. In *Southeastcon'90. Proceedings., IEEE*, pages 42–47. IEEE, 1990.

S. Silver. *Microwave Antenna Theory and Design*. McGraw-Hill Book Company, INC., 1949.

S. J. Skinner and G. L. James. Wide-band orthomode transducers. *Microwave Theory and Techniques, IEEE Transactions on*, 39(2):294–300, 1991.

J. Stenarson. Hftools-an open source python package for microwave engineering. In *Microwave Measurement Conference (ARFTG), 2014 83rd ARFTG*, pages 1–4. IEEE, 2014.

W. Sun and C. A. Balanis. Analysis and design of quadruple-ridged waveguides. *Microwave Theory and Techniques, IEEE Transactions on*, 42(12):2201–2207, 1994.

J. Teniente, R. Gonzalo, and C. Del-Rio. Superb gaussian beam efficiency corrugated horn antennas. In *Antennas and Propagation (EuCAP), 2010 Proceedings of the Fourth European Conference on*, pages 1–4, April.

J. Teniente, R. Gonzalo, and C. Del-Rio. Ultra-wide band corrugated gaussian profiled horn antenna design. *Microwave and Wireless Components Letters, IEEE*, 12(1):20–21, Jan. ISSN 1531-1309. doi: 10.1109/7260.975722.

B. Thomas, G. James, and K. Greene. Design of wide-band corrugated conical horns for cassegrain antennas. *IEEE Transactions on Antennas and Propagation*, 34(6):750–757, 1986.

A. R. Thomson, J. M. Moran, and J. George W. Swenson. *Interferometry and Synthesis in Radio Radio Astronomy*. John Wiley and Sons, New York, Chichester, Brisbane, Toronto and Singapore, 1986.

R. Twiss. Nyquist's and thevenin's theorems generalized for nonreciprocal linear networks. *Journal of Applied Physics*, 26(5):599–602, 1955.

B. Visser, P. P. Krüger, and O. C. O. C. De Jager. Theory and design of low-noise multipath amplifiers. 2011.

K. Warnick, M. Ivashina, R. Maaskant, and B. Woestenburg. Unified definitions of efficiencies and system noise temperature for receiving antenna arrays. *Antennas and Propagation, IEEE Transactions on*, 58(6):2121 –2125, june 2010. ISSN 0018-926X. doi: 10.1109/TAP.2010.2046859.

K. F. Warnick, M. V. Ivashina, and S. G. Hay. Guest editorial for the special issue on antennas for next generation radio telescopes. *Antennas and Propagation, IEEE Transactions on*, 59 (6):1786 – 1789, June 2011. ISSN 0018-926X. doi: 10.1109/TAP.2011.2156510.

S. W. Wedge and D. B. Rutledge. Wave techniques for noise modeling and measurement. *Microwave Theory and Techniques, IEEE Transactions on*, 40(11):2004–2012, 1992.

D. H. Werner and S. Ganguly. An overview of fractal antenna engineering research. *IEEE Antennas and propagation Magazine*, 45(1):38–57, 2003.

H. P. Westman, editor. *Reference data for radio engineers*, chapter 23. Howard W. Sams and CO., 1974.

A. Wexler. Solution of waveguide discontinuities by modal analysis. *Microwave Theory and Techniques, IEEE Transactions on*, 15(9):508–517, 1967.

A. Whitney, A. Niell, B. Corey, H. Hase, E. Himwich, H. Hinteregger, T. Kondo, Y. Koyama, C. Ma, Z. Malkin, B. Petrachenko, W. Schlueter, H. Schuh, D. Shaffer, G. Tuccari, and N. Vandenberg. VLBI2010: Current and future requirements for geodetic VLBI systems, IVS WG3 report. Technical report, IVS WG3 Report, `http://ivscc.gsfc.nasa.gov/about/wg/wg3/`, 2005.

J. Yang, X. Chen, N. Wadefalk, and P.-S. Kildal. Design and realization of a linearly polarized eleven feed for 1-10 ghz. *IEEE Antennas and Wireless Propagation letters (AWPL)*, 8: 64–68, 2009.

J. Yang, M. Pantaleev, P. S. Kildal, B. Klein, Y. Karandikar, L. Helldner, N. Wadefalk, and C. Beaudoin. Cryogenic 2–13 ghz eleven feed for reflector antennas in future wideband radio telescopes. *IEEE Transactions on Antennas and Propagation*, 59(6):1918–1934, June 2011. ISSN 0018-926X. doi: 10.1109/TAP.2011.2122229.